Design and Application of a Cellular, Piezoelectric, Artificial Muscle Actuator for Biorobotic Systems

by

Thomas William Secord

Master of Science in Mechanical Engineering
Massachusetts Institute of Technology, 2007

Bachelor of Mechanical Engineering
University of Minnesota, 2005

Submitted to the Department of Mechanical Engineering
in partial fulfillment of the requirements for the degree of

Doctor of Philosophy

at the

MASSACHUSETTS INSTITUTE OF TECHNOLOGY

June 2010

Author .....
Department of Mechanical Engineering
May 18, 2010

Certified by .....
H. Harry Asada
Professor of Mechanical Engineering
Thesis Supervisor

Accepted by .....
David E. Hardt
Chairman, Department Committee on Graduate Students

Design and Application of a Cellular, Piezoelectric, Artificial Muscle Actuator for Biorobotic Systems

by

Thomas William Secord

Submitted to the Department of Mechanical Engineering
on May 18, 2010, in partial fulfillment of the
requirements for the degree of
Doctor of Philosophy

Abstract

One of the foremost challenges in robotics is the development of muscle-like actuators that have the capability to reproduce the smooth motions observed in animals. Biological muscles have a unique cellular structure that departs from traditional electromechanical actuators in several ways. A muscle consists of a vast number of muscle fibers and, more fundamentally, sarcomeres that act as cellular units or building blocks. A muscle's output force and displacement are the aggregate effect of the individual building blocks. Thus, without using gearing or transmissions, muscles can be tailored to a range of loads, satisfying specific force and displacement requirements. These natural actuators are desirable for biorobotic applications, but many of their characteristics have been difficult to reproduce artificially.

This thesis develops and applies a new artificial muscle actuator based on piezoelectric technology. The essential approach is to use a subdivided, cellular architecture inspired by natural muscle. The primary contributions of this work stem from three sequential aims. The first aim is to develop the operating principles and design of the actuator cellular units. The basic operating principle of the actuator involves nested flexural amplifiers applied to piezoelectric stacks thereby creating an output length strain commensurate with natural muscle. The second aim is to further improve performance of the actuator design by imparting tunable stiffness and resonance capabilities. This work demonstrates a previously unavailable level of tunability in both stiffness and resonance. The final aim is to showcase the capabilities of the actuator design by developing an underwater biorobotic fish system that utilizes the actuators for resonance-based locomotion. Each aspect of this thesis is supported by rigorous analysis and functional prototypes that augment broadly applicable design concepts.

Thesis Supervisor: H. Harry Asada
Title: Professor of Mechanical Engineering

Acknowledgments

First I would like to thank my thesis advisor, Professor H. Harry Asada, for his mentorship, consultation, and guidance during my research. His passion for robotics and knowledge of mechanical engineering is a special source of inspiration to me. His unfailing dedication to his students has been the foundation of my development as an engineer and a researcher.

I would also like to thank my thesis committee members: Professor Kamal Youcef-Toumi, Professor Michael Triantafyllou, and Professor Sangbae Kim. You have all provided valuable guidance during the preparation of this thesis and I am grateful for your enthusiastic support.

I am very grateful to my corporate sponsor, Sumitomo Heavy Industries, for their financial support of this research.

I must profusely thank all of my fellow lab members for their friendship, support, and mentorship. It has been a tremendous privilege to work with and learn from so many talented engineers. The d'Arbeloff Laboratory is nothing short of a family. A million thanks to Waleed Farahat, Lael Odhner, Dan Burns, Manas Menon, Levi Wood, Ani Mazumdar, Dan Cunningham, Patrick Barragán, Devin Neal, Alisha Schor, Geoff Karasic, and Javier Ramos.

I would also like to thank my parents, Mike and Eileen, for their omnipresent support and inspiration. As parents, they support me in all of my decisions. As engineers, they inspire me to always pursue knowledge and excellence. Without them, none of what follows would have been possible.

Finally, I would like to thank my wonderful wife Erin. You are a constant source of inspiration for all that I do and this thesis would not have been possible without your love and support. It would take a thesis in itself to describe how much you mean to me. I dedicate this thesis to you.

Thomas W. Secord

Cambridge, Massachusetts

May 18, 2010

Contents

List of Figures

List of Tables

Chapter 1

Introduction

This thesis provides a unique approach to the challenge of artificial muscle development. This chapter begins with a survey of the importance of actuator development for the advancement of robotics and mechatronics. The motivating research challenges are addressed in Section 1.2, which provides the foundation for the research objectives presented in Section 1.3. The chapter concludes with an overview of the remaining thesis chapters.

1.1 The Importance of Actuators in Robotics and Mechatronics

Actuators are fundamental building blocks for engineered systems that transform energy from one domain to another in order to impart motion within a system. This role places actuators at the heart of many research challenges in robotics and mechatronics. In robotics, actuators are applied to a variety of systems ranging from multi-link arms to autonomous underwater vehicles. The range of mechatronic systems utilizing actuator technology is equally vast. In the majority of actuated systems, desired motions are achieved through use of one or more feedback loops.

Fig. 1-1 illustrates a typical feedback loop consisting of a controller, actuator, mechanism, and sensor. Within the context of such feedback systems, actuators may be viewed as the crucial link between a controller and the mechanism to be controlled. Each of the loop elements shown in Fig. 1-1 has received considerable research attention, although actuators largely remain an "off-the-shelf" item. In particular, electromagnetic actuators (DC motors, AC motors, brushless motors, voice coil actuators) are the most commonly employed class of actuators, while numerous devices are employed for the other elements within the feedback loop. This lack of diversity in actuator designs creates a performance gap, particularly for specialized areas of robotics such as biorobotics as is discussed in the next section.

The consistent advancement of semiconductor technology and control theory have propelled control algorithms, control hardware, and sensor technology to higher levels of performance than those observed in actuator technology. The advancement of semiconductors has been described by the well known Moore's law [76] while the advancement of control theory is chronicled in the expansive handbooks such as [66]. Actuators, however, have no such analogous history. The trends of these areas are

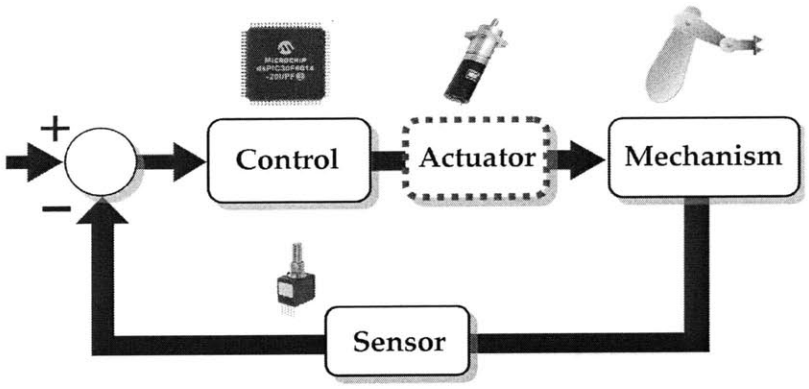

Figure 1-1: A typical feedback loop and the role of actuators.

shown qualitatively in Fig. 1-2, which clearly illustrates the technological gap and the importance of actuator research in the advancement of robotics and mechatronic systems. The actuators of tomorrow must redefine performance boundaries in terms of speed, efficiency, scalability, versatility, and safety. In the next section, the role of actuators is examined within the scope of biorobotics. In biorobotics, the goal of actuator research is the development of artificial muscle actuators that can retain some of the characteristics of natural muscle and improve upon others.

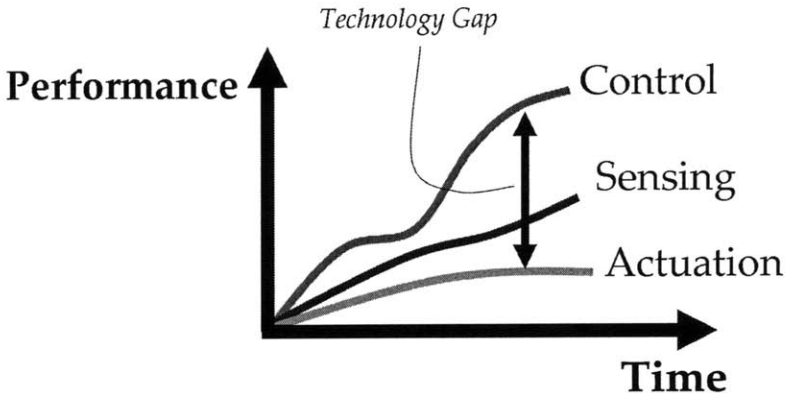

Figure 1-2: The technological gap between actuators and other control loop elements.

1.2 Challenges in Developing Artificial Muscle Actuators

Biological muscles have a unique cellular structure that departs from traditional electromechanical actuators in several ways. A muscle consists of a vast number of muscle fibers and, more fundamentally, sarcomeres that act as cellular units or building blocks. A muscle's output force and displacement are the aggregate effect of the

individual building blocks. Moreover, the force and strain characteristics are tuned to specific loads by combining cellular building blocks in series and parallel [68]. Rather than using gearing and transmission for load matching, muscles can be tailored to a range of loads, satisfying specific force and displacement requirements [23]. These natural actuators are desirable for biorobotics applications, but many of their characteristics have been difficult to reproduce artificially.

Electromechanical devices (DC motors, AC motors, brushless motors, etc.) form the most common class of actuators that are used in biorobotics. Since their inception, motors have remained largely unchanged although higher energy densities are continually being realized [97]. And despite their wide availability and ease of use, traditional motors are not well suited to biorobotic systems because they produce pure rotary motion, require bulky and inefficient gear trains, and exhibit high power dissipation (especially during high torque stalls).

The first major step towards artificial muscle design came in the 1950's when Joseph McKibben invented the pneumatic muscle actuator (PMA) [16]. Within the last two decades, several companies such as Toshiba, Bridgestone, and Shadow Robot have commercialized versions of the PMA (e.g. Rubbertuator) and feedback control of these actuators is still an active area of research [62]. The major drawbacks of McKibben artificial muscles are that they have pronounced nonlinearities and a limited bandwidth. Another major disadvantage of PMAs is that they require a source of compressed air. Although the actuator membrane is extremely lightweight, these actuators require several ancillary components in order to produce useful work as an artificial muscle, which illustrates why actuator power density and muscle performance mimicry are unsuitable as stand-alone metrics for design.

Most of the current research in artificial muscle actuators is centered on the materials science of polymeric materials and shape memory materials. Many of the current artificial muscles are particle driven, meaning that these actuators have response speeds that are often limited by the nature of the chemical, thermal, or intercalation stimuli. One notable exception is the electric field driven dielectric elastomer actuator, which has achieved some success in robotics [85], but has limited utility because of high voltages, low fatigue life, and fragility. Convenient summaries of many novel actuators have been compiled by the members of the Bio-Instrumentation group at MIT [54], [73].

Despite the current research efforts in artificial muscle design, an actuator having low power, large output strain, variable stiffness, high reliability, and a cellular architecture has not yet been developed. This thesis addresses the need for such an actuator by using a novel design based on piezoelectric stack actuators. The basic actuator design approach is an extension of the flextensional approach first described by Newnham [80] and later summarized in [82].

1.3 Research Objectives

The left portion of Fig. 1-3 shows three key performance issues associated with applying traditional actuators to biorobotic systems. The right hand portion of the figure shows the three corresponding performance goals for the actuators developed in this thesis.

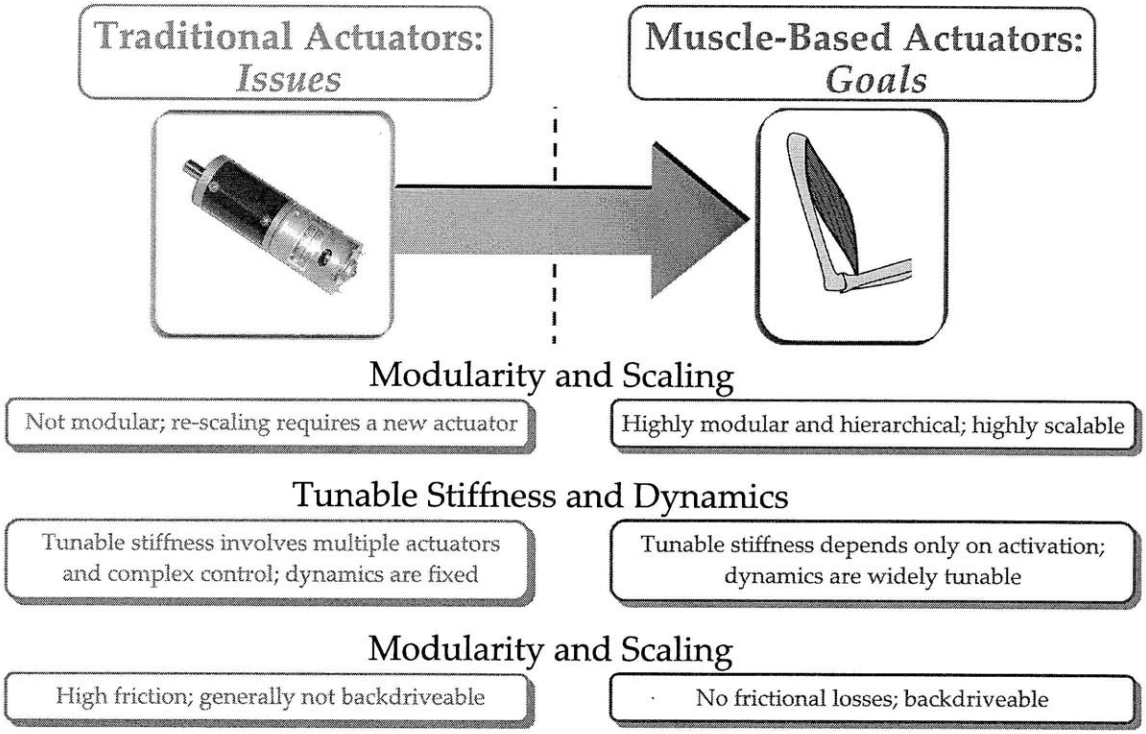

Figure 1-3: Artificial muscle research challenges and the corresponding research goals.

Modularity and Scaling: The first issue in applying traditional actuators to biorobotic systems involves the lack of modularity and scalability. For example, typical biorobotic systems have a single integrated actuator for each degree of freedom in the system. If the force, torque, or displacement requirements of the joint are modified, then an entirely new actuator, transmission, and joint system may be required. Alternatively, with muscle-like actuators based on a subdivided and hierarchical architecture, a joint's force and displacement requirements can be addressed through adjustment of the actuator subunit size or adjustment of the subunit arrangement. Furthermore, traditional actuators are typically rotary devices that do not apply linear tensile forces as required for muscle-based linear actuators.

The first aim of this research is to design a modular actuator that can be readily scaled to meet the demands of biorobotic systems. This work addresses the scaling and modularity through the use of a subdivided architecture inspired by the cellular nature of natural muscles. In natural muscles, the most fundamental building block within a muscle cell or muscle fiber is the sarcomere. The structure and size of muscle sarcomeres is nearly identical in all animal species, which implies that animals rely on a universal actuator solution that is readily scaled to meet the demands of individual animal species [31]. The creation of a unified actuator building block has numerous advantages that will be illustrated throughout this thesis. Each actuator building block is referred to as an actuator cell. The parallels between natural muscles and the artificial muscles developed in this thesis are illustrated in Fig. 1-4.

Tunable Stiffness and Dynamics: The second major issue in applying tra-

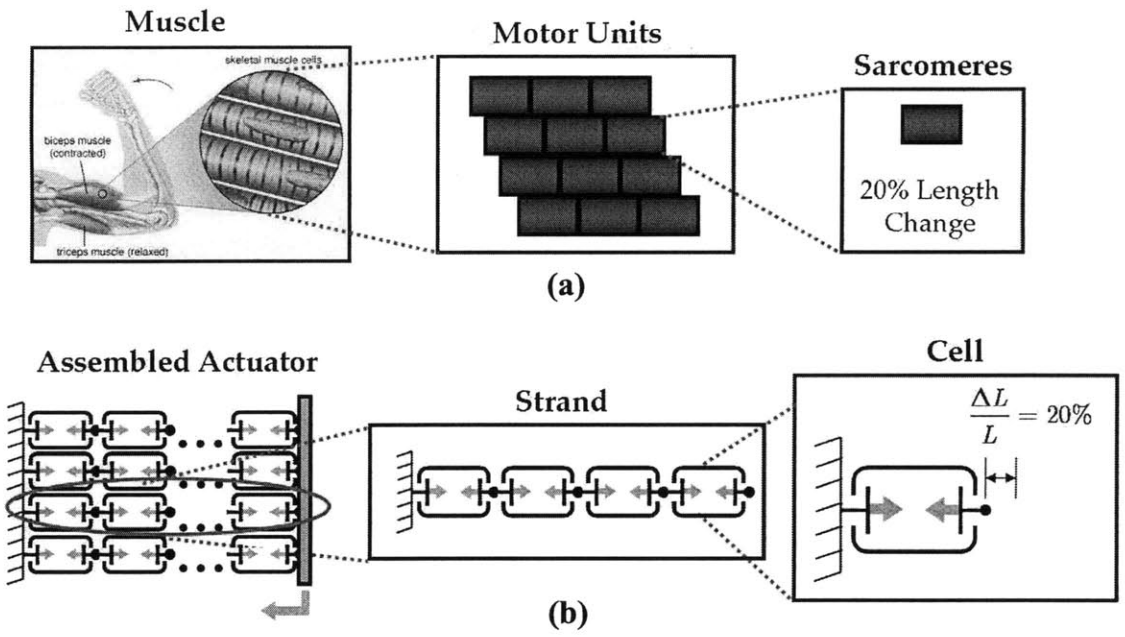

Figure 1-4: (a) Hierarchical structure of natural muscle and (b) its analog in the cellular actuator design paradigm of this thesis.

ditional actuators to biorobotic systems is that traditional actuators cannot readily tune their output stiffness or dynamic behavior. Although it is possible to modify these properties in a closed loop scenario, the bandwidth of such tuning is typically limited. Furthermore, standard motors do not have the inherent output stiffness that is required in biorobotic systems that interact with the environment. Thus, additional mechanical elements such as torsion springs are required to achieve output stiffness. In order to impart stiffness tunability, multiple actuators are often needed. For example, the designs in [24], [91], [106] and [111] all require two electromechanical actuators for a single degree-of-freedom: one motor allows for stiffness tunability and another for angular motion.

This thesis will produce a new artificial muscle actuator that integrates not only tunable stiffness but also tunable resonant frequencies into a single actuator design. Tunable resonance is a relatively unexplored area of actuators research and represents one of the key research objectives for this thesis. Resonance represents a condition that is highly favorable for increasing displacement at reduced energy costs in biorobotic systems undergoing periodic motion. Thus, this work aims to obtain tunable stiffness and tunable dynamic properties as inherent features of the actuator's construction.

Friction and Backdriveability: Most rotary motors used for biorobotic applications require gearing in order for the torque and speed characteristics of the motor to be matched with those of the load. The impedance mismatch between the motor and the load can commonly require large gear ratios. Thus, inertia and friction in the armature are reflected to the output shaft according to the square of the gear ratio.

This creates a high friction and non-backdriveable system. One unifying feature of biorobotic systems is that they interact with the surrounding environment. For example, a humanoid robot may interact with its environment by shaking the hand of a human user. This interaction requires that each joint within the robotic arm sustain backdrive conditions. Currently, high gear ratio motors make this interaction difficult and potentially hazardous to both the robotic hardware and the environment.

This thesis proposes an actuator technology that exhibits an output stiffness through which the actuator can be backdriven. Moreover, when the actuator is backdriven, it can be used as a power generator or an energy harvesting device. This objective, coupled with the previous aims, forms a complete set of desired outcomes addressed within this thesis.

1.4 Thesis Structure

This thesis is broken down into three main categories: design, extension, and application. The design phase of this thesis involves the ideation and realization of a cellular artificial muscle actuator based on strain amplified piezoelectric stacks. The extension phase of this thesis augments the capabilities of the base actuator design to include tunable stiffness and tunable resonance. An additional extension to include energy harvesting capability is also provided. In the final stage of this thesis, the newly developed actuator technology is applied to an underwater robotic system. Each of the three research phases are discussed in detail in the remaining chapters as shown in Fig. 1-5. Specific chapter descriptions are provided below.

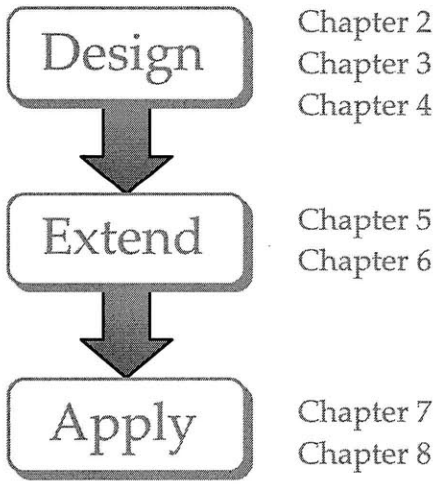

Figure 1-5: Categorical grouping of the thesis chapters.

Chapter 2
Chapter 2 provides an overview of actuator physics and its implications for the performance in key actuator metrics, which are also discussed in this chapter. The chapter then provides an overview of the piezoelectric material selection procedure for artificial muscle development. The physics of piezoelectric materials is discussed in detail

as a critical background for the remaining chapters.

Chapter 3
Chapter 3 begins with a discussion of the existing technology in strain amplification for piezoelectric stacks. These existing techniques provide the framework for the novel multilayer flexure amplification technique developed as a component of this thesis. An idealized kinematic model is used to illustrate the basic properties of multilayer systems while a pseudo-rigid body model provides the necessary degree of accuracy and simplicity needed to perform a scaling analysis of the piezoelectric cell design. The scaling analysis reveals that cellular architecture is the most effective way to utilize the performance of strain amplified piezoelectric stacks.

Chapter 4
This chapter addresses the major components of the design phase of this thesis. The chapter begins with a description of the unified flexure design procedure used to synthesize the cellular actuators. Material selection for the flexure design is discussed in detail, followed by a complete description of the solid mechanical model used for rapid assessment of flexure designs. The candidate flexure designs are then assessed based on a sensitivity analysis, which provides the basis for the final design revisions made using finite element modeling (FEM). The final portion of the chapter discusses the experimental techniques used to assess the blocking force and free displacement of the individual cell designs. The chapter concludes with additional analysis of the basic reliability properties of cellular systems as well as the power requirements for individual cells operating at frequencies away from resonance.

Chapter 5
This chapter marks the beginning of the design extension portion of the research shown in Fig. 1-5. Tunable stiffness cells are presented and the unique properties of the cell are then exploited using cellular assemblies. The particular features of interest are the resonant frequencies and mode shapes of the cellular assemblies. Models of the dynamic behavior reveal that stiffness and resonance can be tuned discretely and independently within a certain range. The upper and lower bounds of this tunability are established theoretically and proved rigorously. Both loaded and unloaded strands are considered and optimal activation selection criteria are provided. The remainder of the chapter describes the experimental validation of the theoretical concepts.

Chapter 6
Chapter 6 describes the second major extension of the actuator design, which is to provide a tunable resonance actuation and energy harvesting device. Modified tunable stiffness cells are introduced and used to create a system that can be used for actuation, sensing, and energy harvesting. This unification of features in a single package represents a major advantage over existing biorobotic systems that use separate components for each of these functions. This chapter also discusses the optimal actuation strategies that account for the bidirectional flow of energy between the electrical and mechanical domains of the cellular systems. The chapter concludes with a discussion of impedance matching as an additional optimization method for tunable energy harvesting systems. As in previous chapters, experiments illustrate the applicability and validity of theoretical concepts.

Chapter 7
This chapter applies the techniques and technology developed in the previous chapters to create an underwater biorobotic system. The advantages of piezoelectric technology are discussed in the context of underwater robotics with an emphasis on locomotion using periodic flapping of fin structures. In particular, the first portion of the chapter discusses the modifications of resonance that are attendant with underwater operation of flapping fins. The chapter describes the theoretical modeling of a custom designed carangiform swimming robot that utilizes the piezoelectric cellular actuators. The design paradigm presented in this chapter utilizes distributed actuators to achieve desired swimming kinematics. Both simulation and experiments are provided to illustrate methods of input synthesis for systems using distributed cellular actuators.

Chapter 8
Chapter 8 provides a summary of the major contributions of this work and discusses the directions for further technological development of piezoelectric cellular actuators.

Chapter 2

Background

This chapter provides an overview of key actuator metrics of performance and discusses how an actuator's underlying physics plays a critical role in determining such performance. The chapter then provides an overview of the piezoelectric material selection procedure for artificial muscle development. The physics of piezoelectric materials and stack actuators is also discussed in detail as a requisite background for the remaining chapters.

2.1 Actuator Physics

The goal of this section is to examine fundamental actuator physics and to introduce how the physics affect actuator performance metrics. Specific actuator physics will not be reviewed because many excellent references already exist (e.g. [40]). Fig. 2-1 shows the classification of actuators based on their dominant method of energy transduction. In this scheme, there are two main categories of actuators: field driven and diffusion driven. These two categories are particularly relevant when broadly considering an actuator's speed of response, maximum displacement, and maximum force or torque. Generally, field driven actuators outperform diffusion driven actuators in all of these categories. However, diffusion driven actuators are generally more physically pliable and flexible than are field driven actuators. The field versus diffusion generalization requires further classification into five primary sub-categories: electric, magnetic, pressure, thermal, and ionic.

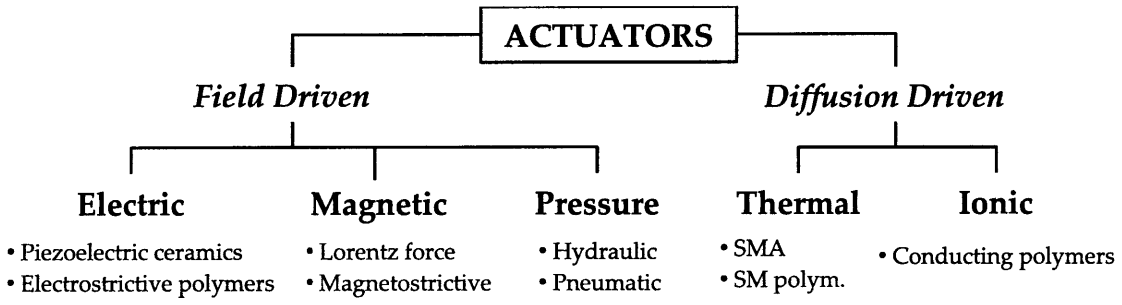

Figure 2-1: Actuator taxonomy based on governing physics.

In the case of field driven actuators, the three most commonly employed fields are electric, magnetic, and pressure. Examples of electric field driven actuators include piezoelectric ceramics and electrostrictive polymers. Perhaps the most quintessential actuator, however, is the Lorentz-force driven motor, which is an example of a magnetic field based actuator. Pressure driven actuators, such as hydraulic and pneumatic cylinders, are also commonly employed in many areas of robotics.

In diffusion driven actuators, two of the most commonly employed diffusion phenomenon include thermal diffusion and ionic diffusion. Shape memory alloys (SMAs), most commonly NiTi wires, are examples of thermal diffusion driven actuators and can provide large output forces at relatively small displacements. A common example of ionic diffusion actuators is polypyrrole conducting polymer actuators. This class of polymer actuators is still under extensive development and continues to improve in both stress and strain performance [114]. Overall, the nature of the actuator physics is crucial to determining the values of the performance metrics.

2.2 Actuator Performance Indices

This subsection defines a comprehensive collection of general actuator performance indices. The index values are largely determined by actuator physics discussed previously and may be used as a basis for actuator material selection. The following list of indices is an extension of the metrics provided in [73]. The metrics are grouped as quantitative metrics (those that can be quantified with a measured value), qualitative metrics (those that are not readily numerically quantified), and derived metrics (metrics that are functions of other metrics). In most metrics, the description is intentionally broad in order to encompass the definitions found in other sources (e.g. [54], [53], [72]). In the following list of metrics, the definitions are most applicable to linear actuators although the definitions may be readily adapted to rotary actuators as well.

Quantitative Metrics:

Stress: This performance index is generally defined as the maximum force generated by the actuator per unit area of the load bearing member.

Strain: A general definition of strain that applies to actuators is simply the active change in length of an actuator, $\Delta\ell$, divided by its relaxed length ℓ_0:

$$\epsilon \triangleq \frac{\Delta\ell}{\ell_0} \tag{2.1}$$

Bandwidth: An actuator's bandwidth is related to its ability to respond to a time-varying stimulus (e.g. an armature voltage). In this thesis, bandwidth will be defined according to Fig. 2-2, which is consistent with the standard definition in linear system frequency response. In Fig. 2-2, G_0 is static or DC gain and represents the ratio of actuator output for a constant input stimulus. The bandwidth is the frequency of the excitation input at which the actuator gain drops to 70.7% of the value of G_0.
This metric is extremely sensitive to loading conditions and must therefore be compared carefully among actuator materials and devices.

Output compliance: Output compliance is the inverse of stiffness (resisting force per unit displacement) as viewed from the output of an actuator.

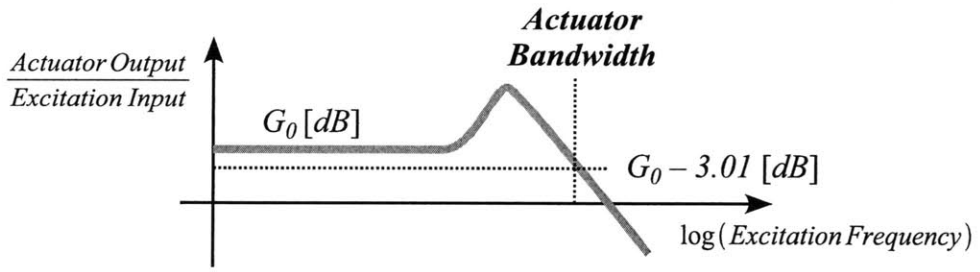

Figure 2-2: Graphical definition of actuator bandwidth.

Reliability: Reliability is most conservatively defined as mean time to failure ($MTTF$) of an actuator or actuator material under its most severe performance conditions (maximum stress, strain, operation frequency). If the reliability of the actuator versus time has been probabilistically defined as a continuous function $R(t)$, then $MTTF$ may be computed from

$$MTTF = \int_0^\infty R(t)dt. \tag{2.2}$$

Reliability may also be measured in cycle life under normal to severe loading. Note that reliability can be correlated with the component count required for the fully assembled actuator.

Linearity: Linear actuators are those for which for an increase or decrease in the input excitation amplitude results in a proportional increase or decrease in the actuator output amplitude in steady state. Linearity may be quantified as a percentage using

$$\%\text{Linearity} = \left(1 - \frac{\Delta_{max}}{R_{max}}\right) \times 100\% \tag{2.3}$$

where Δ_{max} is the maximum deviation from a best fit line and R_{max} is the maximum range of the device. The static linearity defined by (2.3) is often subject to environmental factors.

Efficiency: The ratio of mechanical work output to energy input during one complete cycle in cyclic operation. Note that this definition admits any variety of loading conditions, which can be a major confounding factor in comparing different actuator technologies. Furthermore, this definition does not account for the distinction between reactive and dissipative power, which also must be considered for overall system efficiency.

Electromechanical coupling: Proportion of input energy that is transformed into work, including external work done by the actuator and stored internal mechanical energy generated in the actuator itself. As with efficiency, this definition does not distinguish between reactive or dissipative characteristics and must therefore be used cautiously.

Displacement resolution: The displacement resolution is quantified by the smallest resolvable displacement of an actuator. As in sensor design, actuators may provide continuous or discrete outputs. An example of an actuator with a discrete output, and therefore a finite resolution, would be a conventional stepper motor.

Qualitative Metrics:

Controllability: Controllability is defined broadly as the ability to achieve desirable closed loop properties (e.g. large bandwidth) through the application of mathematically linear integro-differential (e.g. PID) control laws. Actuators having linear behavior generally exhibit greater controllability in this sense.

Mechanical pliability: Pliability is defined as an actuator's ability to conform to imposed structural curvature. For example, polymeric actuators often have high mechanical pliability.

Heating: An actuator's heating during normal operation may be a byproduct of parasitic power dissipation (e.g. a motor at low speed and high torque output) or may be a requirement for actuation (e.g. Joule heated SMA wire). Both levels of heating may be quantified as the maximum temperature observed at any point on the surface of the actuator in normal operation. However, this temperature depends heavily upon the boundary conditions of the actuator and is therefore considered only qualitatively.

Hysteresis: A non-hysteretic actuator is one whose output can follow changes in the input regardless of which direction the change is made. Although there are various way to quantify hysteresis, it is considered in this thesis insofar as its relative dominance in the actuator operating characteristics.

Scalability: Scalability is defined as a materials ability to maintain or improve its other performance metrics as the characteristic actuator length scales are changed.

Process Compatibility: Process compatibility broadly refers to the ease with which an actuator can be manufactured. This also includes the process of actuator assembly. Thus, actuators requiring extensive manual assembly would not be considered to have high processes compatibility.

Derived Metrics:

Strain rate: Strain rate is the percentage length change defined by (2.1) normalized by the time required to achieve this length change. Strain rate may be viewed as a metric derived from bandwidth and strain. As with bandwidth, this metric is highly dependent upon mechanical loading conditions. A standardized value may be obtained, for example, under zero load conditions.

Work Density: This may also be referred to as volumetric work or energy density. This metric is defined as the maximum work output in one cycle of operation normalized by the volume of the actuator material only. This definition excludes electrodes and power supplies although it does include transmissions in the volume calculation. Also, this metric is highly dependent upon loading conditions, but is typically taken as the maximum achievable value. This metric is derived from the stress, strain, and volume properties.

Specific Work: Specific work is the maximum work output in one cycle of operation normalized by the mass of the actuator material. As in the definition of work density, this definition excludes electrodes and power supplies although it does include transmissions in the mass calculation and assumes the most optimistic value possible. This metric is derived from the stress, strain, and mass properties.

Power Density: This metric may also be referred to as volumetric power or power density. This metric is defined as the maximum power output in one cycle of operation normalized by the volume of the actuator material only. This definition excludes electrodes and power supplies although it does include transmissions in the volume calculation. Also, this metric is highly dependent upon loading conditions, but is

typically taken as the maximum achievable value. This metric is derived from the stress, strain, bandwidth, and volume properties.
Specific Power: Specific power is the maximum power output in one cycle of operation normalized by the mass of the actuator material. As in the above definitions, this definition excludes electrodes and power supplies although it does include transmissions in the mass calculation and assumes the most optimistic value possible. This metric is derived from the stress, strain, bandwidth, and mass properties.

In all of the above performance metrics, there are several assumptions that can confound direct comparisons between actuators and actuator materials. First, the size of the required power supply, magnitude of applied excitation (e.g. voltages or pressures), and complexity of the drive hardware are all prominent confounding factors. For example, a McKibben pneumatic artificial muscle actuator has a very high stress and strain output, but requires an extremely cumbersome compressed air source and attendant tubing that obviates its candidacy for many mobile biorobotics applications. Another crucial, yet often overlooked, factor is the nature of the power storage and power flow within a material. In particular, actuators can exhibit inductive or capacitive energy storage or may be dominated by resistive effects. The nature of the power flow in the system must be addressed when considering the full system performance. The metrics above are also meant to include any transmission elements. For example motor-based actuators are examined with respect to the output of a particular motor-gearbox combination. By including transmission elements, a more meaningful comparison can be made between the state of the art in actuators systems rather than simply actuator materials alone. Other practical considerations include the time required to manufacture the actuator, although this depends upon technological developments within manufacturing that may not be correlated to a true bottleneck in the actuator technology. Cost is another factor that can often be misrepresented because it is driven by the economies of scale applied to the actuator manufacturing process and other more complex economic factors. All metrics must also be compared carefully due to the often ill-define nature of the imposed loading. Furthermore, in all cases, it is important to know the environmental conditions (temperature, humidity, vibration level, etc.) under which the specification was measured and is valid. With these caveats disclosed, it is insightful to apply the performance metrics to select and actuator material for artificial muscle development.

2.3 Actuator Material Selection

The primary goal of this work is to develop an artificial muscle material and therefore the scope of actuator material candidates is focused on linear displacement devices and smart materials. Fig. 2-3 shows a qualitative comparison of smart materials for linear actuation applications. The figure illustrates the major metrics discussed in Section 2.2. The figure plots the performance characteristics on a scale of 1 to 4 (with 1 being poor and 4 being excellent). Each metric is plotted on an oblique axis for selected candidate artificial muscle materials: shape memory alloys (SMA), thin film piezoelectric actuators (TF-PZT), conducting polymers (CP), and dielectric elastomers (DE) on oblique axes. The figure also includes skeletal muscle (SM) as a benchmark. In the figure, the greater the area enveloped by the actuator the higher

Table 2.1: Several performance metrics of biological skeletal muscle [54].

Performance Metric	Value	Units
Blocking Stress	300	kPa
Maximum Strain	20	%
Bandwidth	10	Hz
Strain Rate	50	$\%s^{-1}$
Work Density	8	kJ m^3
Power Density	52	kWm^3
Specific Power	50	Wkg^{-1}

its overall performance. Table 2.3 lists typical values of skeletal muscle for numerical reference [54].

All of the candidate materials in Fig. 2-3 have specific strengths and weaknesses. For example, shape memory alloys exhibit an extremely high output stress but perform poorly with regard to linearity, heating, bandwidth, and hysteresis performance metrics. Similarly, dielectric elastomers perform very well with regard to bandwidth and strain, but the current state of the art is highly sensitive to material membrane puncture [85]. The shaded region in Fig. 2-3 represents thin film piezoelectric materials. This shaded region illustrates that one of the main drawbacks to piezoelectric materials is very small inherent strain performance, which is on the order of 0.1%. Additional drawbacks include a low pliability (as the ceramic materials are very stiff), which is also manifested in the extremely high output stiffness of the piezoelectric stacks. The basic stack actuator is shown in Fig. 2-4 (a). The primary hypothesis of this thesis is that piezoelectric ceramics may be used for artificial muscles by overcoming the low performance metrics, particularly the low strain output relative to natural muscle.

The design developed in this thesis overcomes the small strain, low output compliance, and low mechanical pliability associated with piezoelectric materials by accepting a tradeoff in response speed, stress, reliability, and scalability performance. The tradeoff is accomplished by introducing a flexural transmission mechanism illustrated conceptually in Fig. 2-4 (b). The transmission is designed using compliant mechanisms, or flexures, in order to achieve much larger output strains at reduced levels of actuator stress. The basic transmission technique is introduced in the next chapter and a rigorous design procedure is then established in Chapter 4. Overall, using piezoelectric materials and flexural transmission mechanisms allows for a strain amplified PZT (SA-PZT) performance envelope that still exceeds that of the other candidate materials. This is denoted by the dashed line in Fig. 2-5. Although some effects of flexure based transmissions are known (e.g. increased strain and reduced stress), this thesis will also investigate the coupling between strain amplification and the optimum scale and architecture for the artificial muscle actuator. Specifically, this research shows that a subdivided, or cellular, architecture leads to many desirable actuator characteristics.

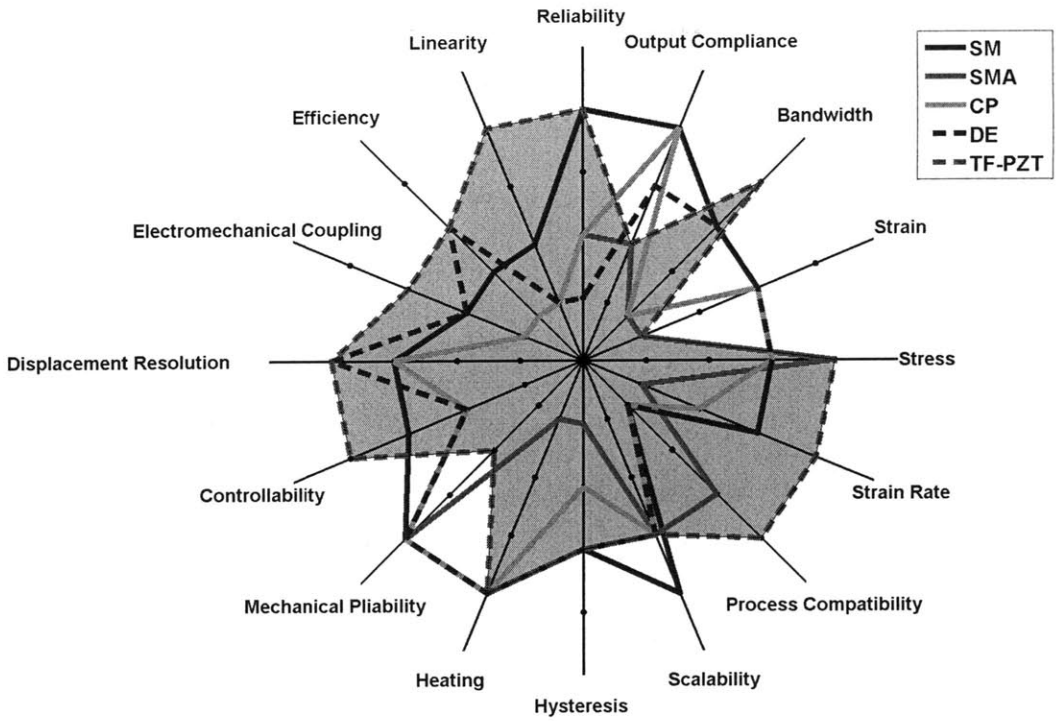

Figure 2-3: Qualitative comparison of several candidate actuator materials for artificial muscle actuators.

2.4 Piezoelectric Materials and Actuator Overview

Piezoelectric stack actuators are the base technology that is used throughout this thesis. Therefore, this subsection provides the relevant background on piezoelectric stack physics. In a conventional text on piezoelectric devices, tensor notation often obfuscates the practical equations required in engineering applications. On the other hand, in vendor application notes, the level of detail is often insufficient to perform rigorous engineering analysis. This section seeks to bridge the gap between a conventional text on piezoelectric devices and the application notes provided on most piezoelectric actuator vendor websites. A more detailed review of electrostatics and piezoelectric constitutive behavior is contained in Appendix A.

2.4.1 Piezoelectric Materials

Piezoelectric materials generate strain in response to applied electric fields and generate charge in response to applied stress. An understanding the nature of piezoelectricity is an important first step in the analysis of piezoelectric materials. This section describes the basic elements of piezoelectric material science and draws primarily from [102], [87], and [7].

Some crystals in which the centers of positive and negative charge do not coincide are said to be spontaneously polarized. When this property of a dielectric can be

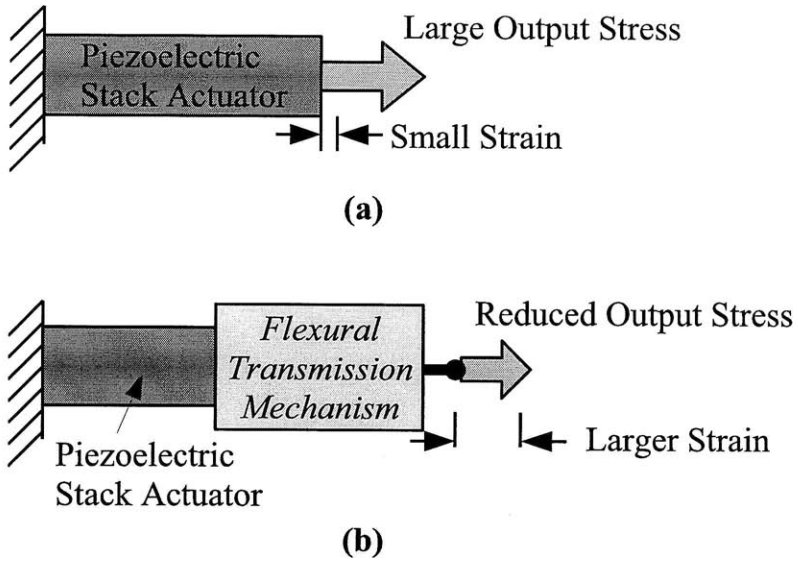

Figure 2-4: (a) Piezoelectric stack actuator inherent characteristics. (b) Piezoelectric actuator coupled with custom developed flexural amplification device.

modified by an electric field, the material is called ferroelectric. Crystals that do no posses a center of symmetry and have charges that appear on the surfaces when a stress is applied are piezoelectric. In short, some materials that are piezoelectric are also ferroelectric. On the atomic scale, groups of unit cells that have the same polarization orientation are called Weiss domains. After poling of a ferroelectric ceramic, the domains remain largely aligned.

One common piezoelectric material structure is the Perovskite structure pictured in Fig. 2-6. Lead Zirconate Titanate (PZT) has the Perovskite Structure and is the most widely used piezoelectric ceramic to date and has the structure shown in Figure 2-6. When this material is compressed along the vertical axis of the figure, dipoles are induced that point upwards along the vertical axis. The piezoelectric effect was first discovered by Pierre and Jacques Curie in 1880 while PZT was first discovered in the 1950s.

Piezoelectric materials exhibit a hysteresis between strain S and applied electric field E. If the electric field is raised beyond a critical value, the piezoelectric domains can begin switching and eventually the polarization direction can switch. This leads to the "butterfly" loop shown in Figure 2-7. Note that the hysteresis in typical operation results from the lossy nature of the piezoelectric media.

In solid state theory, the direct piezoelectric effect means that a piezoelectric material becomes polarized when strained. This effect is especially of interest for sensor design. The converse (also called the inverse) piezoelectric effect refers to the strain generated when a piezoelectric material is placed in an electric field. This effect leads to actuation capability, which is of primary interest for this thesis. Electrostriction refers to a second order effect in which strain is proportional to the square of the electric field. Thus, electrostriction is a second order property that is present in all

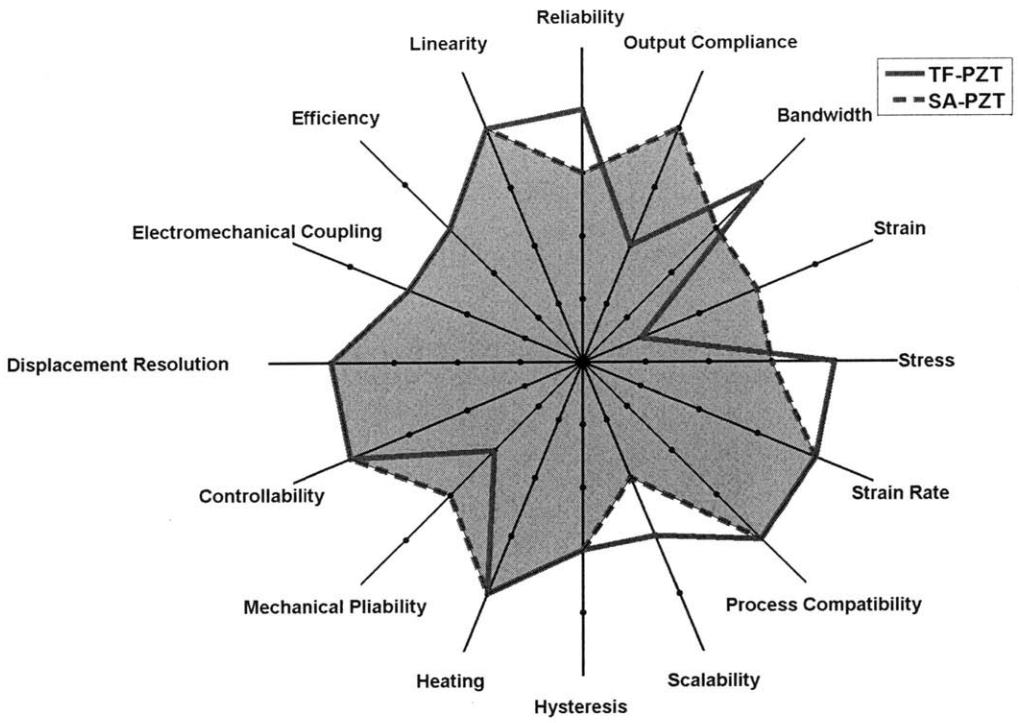

Figure 2-5: Qualitative comparison of piezoelectric materials and strain amplified piezoelectric materials.

materials when they are placed in an electric field.

Dielectrics can be defined as insulating materials. One class of dielectrics includes ionically bonded crystals. In such ionic crystals, when an electric field is applied, the positive charges are attracted to the negative terminal while the negative charges are attracted to the positive terminal. This is known as electric polarization, which can be quantified as the sum of electric dipoles per unit volume inside the dielectric. There are three kinds of polarization: electronic, ionic, and dipole reorientation. In electronic polarization, the electron clouds deform; in ionic polarization the bond lengths change; and in dipole reorientation, dipoles align with the electric field. This effect is shown for a parallel plate capacitor in Figure 2-8. The quantification of the charge accumulation is described in Appendix A.

2.4.2 Piezoelectric Stack Actuators

There are several different form factors for PZT actuators. One common form is a bimorph actuator that consists of two bonded piezoelectric elements that are activated differentially in order to achieve cantilever beam bending. These achieve large displacements but only small force outputs. Another type of actuator, the bending tube, is often used in scanning microscopes. Shear actuators are also used and utilize the d_{15} constant (see Appendix A for a discussion of the piezoelectric constants). Al-

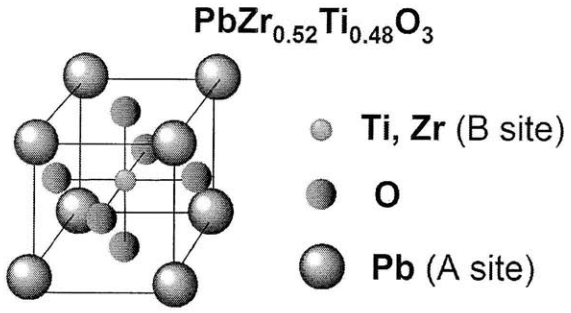

Figure 2-6: Perovskite crystal structure.

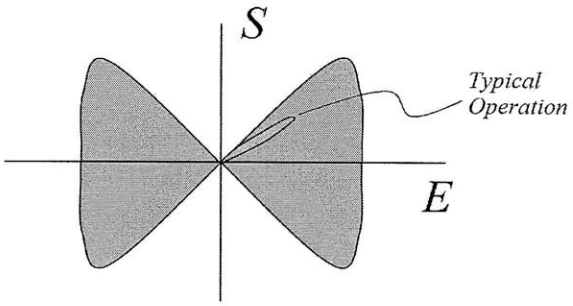

Figure 2-7: "Butterfly" loop of hysteresis behavior between strain and applied electric field at large applied electric fields. The smaller inset curve represents the typical operating regime in practical PZT-based devices.

though these foregoing form factors have important applications, this thesis utilizes stack actuators wherein the d_{33} constant of PZT is the source of the electromechanical coupling.

Piezoelectric stack actuators are most commonly constructed from several thin layers of PZT. A low voltage PZT actuator stack is typically constructed as a monolithic unit wherein the electrode material and ceramic are cofired in a single step. The resulting construction is shown in Fig. 2-9 (a). This following discussion will focus on rectangular cross section stacks although circular and annular geometries cross sections also common. The geometric parameters of a rectangular PZT stack are its length (L_{pzt}), height (h_{pzt}), width (w_{pzt}), and film thickness (t_{film}). The number of films in the stack is then $\frac{L_{pzt}}{t_{film}}$.

In response to an applied voltage of V_{pzt}, an electric field of strength $\frac{V_{pzt}}{t_{film}}$ is generated in each layer of the stack. If the ends of the stack actuator are unconstrained and the maximum voltage V_{pzt}^{max} is applied, then the free displacement (Δx_{pzt}^{free}) of the stack is generated:

$$\Delta x_{pzt}^{free} = N_{film} d_{33} V_{pzt}^{max}, \tag{2.4}$$

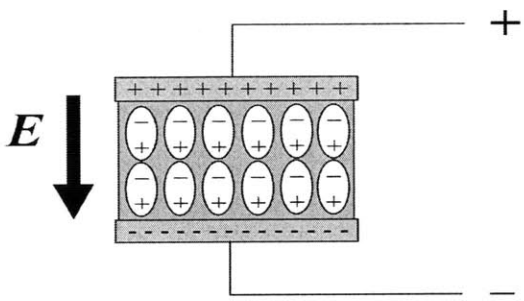

Figure 2-8: Charge accumulation on a capacitor.

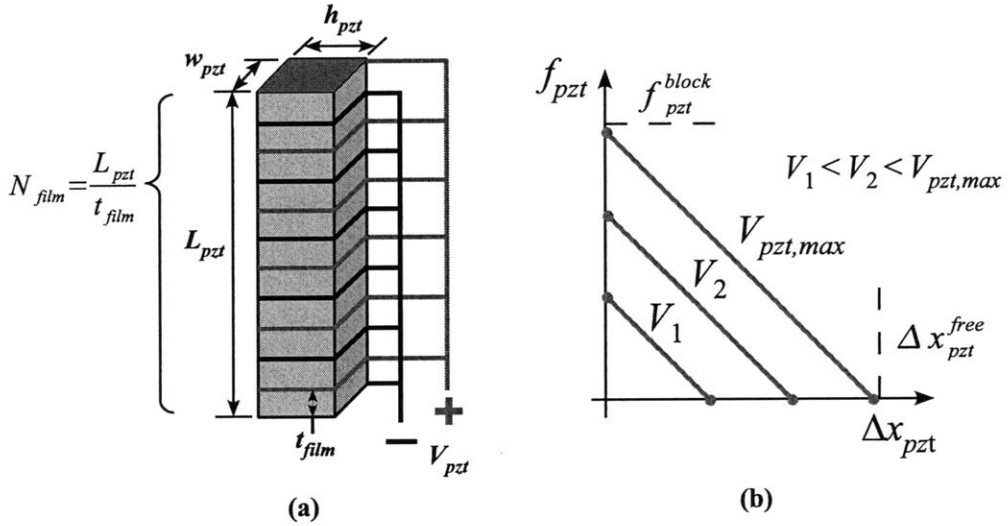

Figure 2-9: (a) Construction of a piezoelectric actuator stack (b) Linear model for actuator electromechanical behavior.

where d_{33} is the piezoelectric strain constant for electric fields and actuation along the axis of poling. Note that the maximum voltage is determined by the ability of the ceramic and electrodes to avoid dielectric breakdown. For low voltage PZT stacks, a maximum voltage of 150V is typical. If the ends of the stack are rigidly constrained at zero voltage and then the maximum voltage is applied again, the blocking force (f_{pzt}^{block}) is generated:

$$f_{pzt}^{block} = \frac{E_{pzt} h_{pzt} w_{pzt}}{L_{pzt}} N_{film} d_{33} V_{pzt}^{max}, \tag{2.5}$$

where E_{pzt} is the elastic modulus of the PZT material. Below internal resonant frequencies, the stack obeys the following linear relationship:

$$f_{pzt} = \frac{V_{pzt}}{V_{pzt}^{max}} \left(f_{pzt}^{block} - \frac{E_{pzt} h_{pzt} w_{pzt}}{L_{pzt}} \Delta x_{pzt} \right) \tag{2.6}$$

Fig. 2-9 (b) shows a graphical representation of the linear force displacement behavior of the PZT stacks.

For subsequent dimensionless analysis, notice from equations (2.4) and (2.5) that a stack's two key parameters are its length and aspect ratio α_{pzt}, which are defined respectively as L_{pzt} and

$$\alpha_{pzt} = \frac{L_{pzt}}{n_{pzt} h_{pzt} w_{pzt}}. \tag{2.7}$$

Here it is assumed that n_{pzt} stacks are arranged atop one another to form a total height of $n_{pzt}h_{pzt}$. For scaling purposes, the layer thickness t_{film} is introduced as the characteristic length scale. Using this characteristic length, the free displacement can be rewritten as

$$\Delta x_{pzt}^{free} = (d_{33}\mathcal{E}_{pzt,max}t_{film}) \cdot \bar{L}_{pzt} \tag{2.8}$$

where $\mathcal{E}_{pzt,max}$ is the maximum electrical field that the PZT can withstand before dielectric breakdown and $\bar{L}_{pzt} = \frac{L_{pzt}}{t_{film}} = N_{film}$, which is the number of layers within the stack. Similarly, the blocking force can be expressed as

$$f_{pzt}^{block} = \left(d_{33}\mathcal{E}_{pzt,max}t_{film}^2 E_{pzt}\right) \frac{\bar{L}_{pzt}}{\bar{\alpha}_{pzt}} \tag{2.9}$$

where $\bar{\alpha}_{pzt} = \frac{L_{film}t_{film}}{n_{pzt}h_{pzt}w_{pzt}}$. In both (2.8) and (2.9), the terms in parentheses are approximately constant for all low voltage stacks, which implies that $\bar{L}_{pzt}$ and $\bar{\alpha}_{pzt}$ are the critical geometric parameters that determine a PZT stack's force and displacement performance.

Chapter 3

Motion Amplified Piezoelectric Stacks and Cellular Architecture

This chapter examines the basic approach used to convert small piezoelectric stack motions into the larger motions required for artificial muscles. The pseudo-rigid body model developed in this chapter is particularly useful for establishing the scaling properties of the motion amplified piezoelectric actuator. The scaling analysis reveals that a subdivided architecture can yield the best overall performance with respect to actuator work output in an efficiently packed system. Cellular piezoelectric actuators are then analyzed with respect to their reliability and power requirements. The cellular architecture outlined in this chapter provides the foundation for the subsequent developments in this thesis.

3.1 Introduction

Over the last several decades, there have been numerous proposed designs for generating PZT displacements large enough to drive robotic and mechatronic systems. Some of the earliest examples include the first design by Toulis [2], and subsequent refinements by Newnham et al. [80] [33] [32], Haertling [44], Moskalik [78], and Uchino [102]. More recent research has produced many patented devices (e.g. [4], [1],[3]), commercially available devices [35] [43] [56], and designs tailored towards specific applications such as rotor blade active control [58] and MEMS scale devices [26]. A comprehensive summary of motion amplified piezoelectric technology is provided in [82].

Existing motion amplification designs can be classified into a) scissors motion or inching drives, b) bimetal-type bending, and c) flextensional mechanisms. Inching motion provides infinite stroke while bimetal-type mechanisms such as those in [94] [37] can also produce large displacement and strain. Such inching and bending actuators are applicable to various industrial applications when used as a single actuator unit; however, the reconfigurability of these actuator types is limited due to the difficulty in arbitrarily connecting a large number of actuator units in series or in parallel to increase the total stroke and force respectively. In contrast, flextensional mechanisms such as "Moonie" [80] [33], "Cymbal" [32], "Rainbow" [44], and others [58] are considered suitable for the reconfigurable cellular actuator design. Using these types

of flextensional devices, an individual actuator can be stacked in series to increase the total displacement. However, simple stacking increases the length of the overall mechanism but does not improve the strain in actuation direction, which is known to be only 2–3%. Thus, more amplification is needed.

This chapter presents a new approach to amplifying PZT displacement that can achieve approximately 20% effective strain from the inherent 0.1% strain of piezoelectric stack actuators. The key idea is hierarchical nested architecture. A large amplification gain on the order of 100 can be obtained with this method. This structure is fundamentally different from traditional layered structures, such as telescoping cylindrical units [82] or stacking multiple plates connected by actuator wires [6]. Unlike these traditional stacking mechanisms, where the gain g is proportional to the dimension of the lever or number of stacks, the amplification gain of the new mechanism increases exponentially as the number of layers increases. Suppose that strain is amplified g times at each layer of the hierarchical structure. For N_l layers of hierarchical mechanism, the resultant gain is given by g^{N_l}, the power of the number of layers. This nesting method allows for a large strain in a compact body, which is appropriate for artificial muscle actuators. Although this nesting approach is a straightforward extension of existing amplification devices, it leads to several unique properties that are discussed throughout this thesis. The following section provides a detailed description of the amplification mechanism.

3.2 Idealized Kinematic Model of Multilayer Amplification

Many applications in biorobotics require strain substantially larger than what is available from piezoelectric stack actuators. Chapter 2 illustrated that the maximal strain of a PZT stack actuator, given by $\frac{d_{33}V_{pzt}^{max}}{t_{film}}$, is typically 0.1%. Natural muscles, however, produce strains of approximately 20%. To amplify the inherent strain of piezoelectric stack actuators, the proposed design utilizes kinematic amplification devices shown in Fig. 3-1.

Fig. 3-1 shows the idealized kinematic behavior of two amplification mechanisms. These mechanisms consist of perfectly rigid beams and ideal revolute joints. The mechanisms in Fig. 3-1 (a) will be referred to as a non-inverting amplifier and the mechanism in Fig. 3-1 (b) as an inverting amplifier. Each mechanism converts a small input displacement, Δx_{in}, into a larger output motion Δx_{out} based on the angle θ_0 of the oblique beam elements. The basic device shown in the upper portion of the figure has been studied extensively and representative results include [33], [58], [70], and [79]. This chapter describes both the inverting and non-inverting schemes as well as the nesting combinations of these two elements. The non-inverting mechanism converts outward displacements into outward displacements while the inverting mechanism converts outward displacements into inward displacements. The instantaneous gain of these mechanisms is defined as

$$g = \frac{\Delta x_{out}}{\Delta x_{in}} = \pm \cot(\theta_0), \tag{3.1}$$

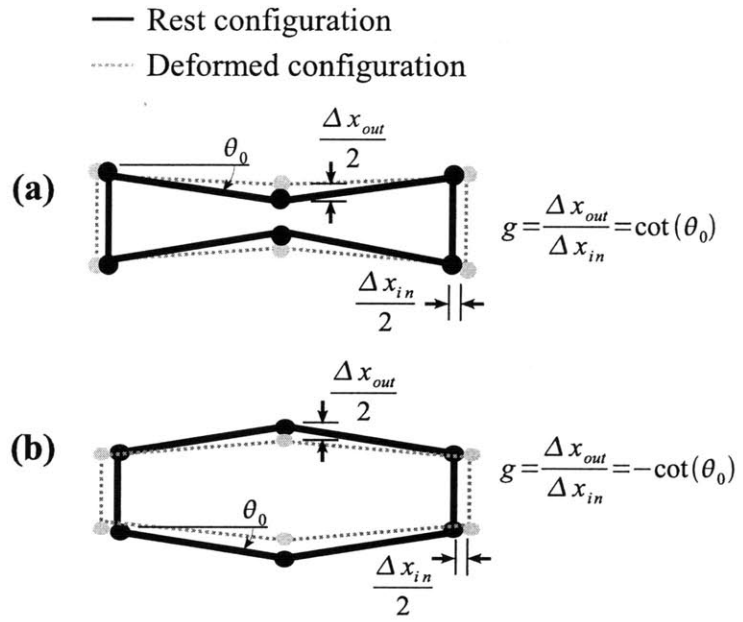

Figure 3-1: (a) Non-inverting kinematic amplifier (b) Inverting kinematic amplifier.

where g includes the sign. For amplification, the beam angle must reside in the range of $0 < \theta_0 < 45°$. The key tradeoff is between displacement amplification and force reduction. Because PZT has very high inherent force, but very small displacement, the amplification gain is typically chosen to be as high as possible such that the device still exhibits linear behavior. The largest value of g under those conditions is approximately 10, which corresponds to $\theta_0 = 5.71°$. For $g = 10$ the mean gain error over a $\pm 1°$ range is 10%. Although certain benefits can be realized by designing nonlinear amplifications mechanisms ([5]), such devices are outside the scope of the present discussion.

One of the fundamental design goals in this thesis is to create an actuator that can produce approximately 20% strain output under free conditions, thereby matching the strain performance of skeletal muscle. Thus, a substantial amplification mechanism is needed. Rather than design a single stage amplifier to achieve this output, an amplification using two layers of nested mechanisms is used. This method was first described in [103] and is illustrated in Fig. 3-2. Fig. 3-2 shows a generic combination of N_l layers of inverting and non-inverting amplifiers wherein the output of one layer is used as the input to the next. The cascading of these devices will ideally produce an overall free displacement that is the product of the individual layer gains:

$$\Delta x_{N_l}^{free} = \left(\prod_{i=1}^{N_l} g_i \right) \Delta x_{pzt}^{free} \tag{3.2}$$

where the input displacement has been taken as the piezoelectric stack free displacement Δx_{pzt}^{free}. The blocking force of the same arrangement is the reciprocal of the gain in (3.2) multiplied by the blocking force of the PZT f_{pzt}^{block}. Thus, using two layers provides a mechanism that increases the PZT free displacement by a factor of

approximately 100 and reduces the blocking force by the same factor. This is shown qualitatively in Fig. 3-3. As depicted in the figure, selecting two layers best meets the demands of artificial muscle design (20% strain at the maximum achievable force). Furthermore, it is desirable to minimize the number of layers in the overall amplifier design in order to minimize performance loss due to the flexure compliance. Thus, the design presented here uses $N_l = 2$.

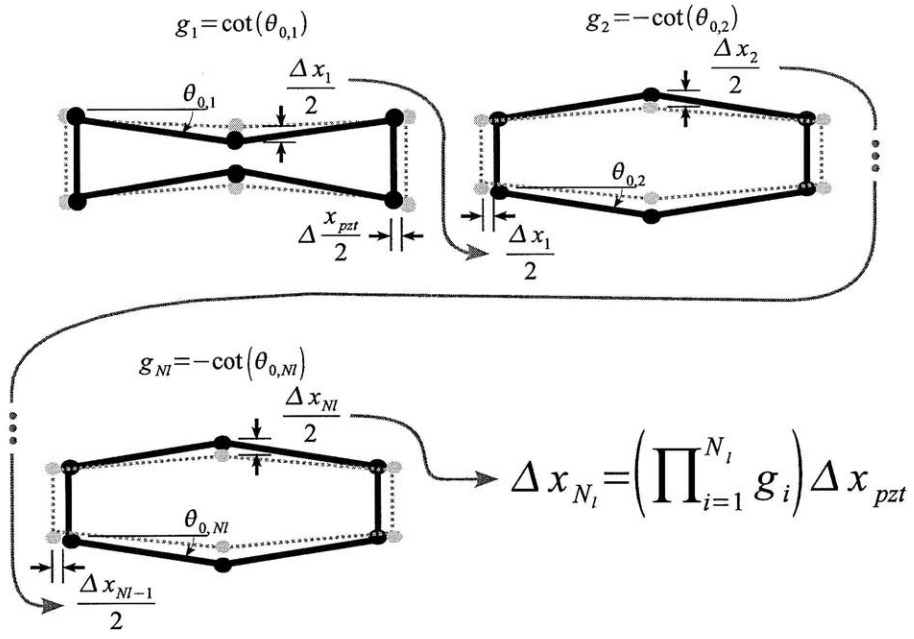

Figure 3-2: Kinematic principle of nested amplifiers.

3.3 Flexure Based Amplification

The idealized kinematic amplifiers described in 3.2 provide an upper bound on the performance of nested transmission systems. The ideal characteristics of the transmission mechanisms cannot be fully achieved due to structural compliance. Actual mechanisms will inevitably have some structural compliance, which may then degrade the aggregate force and displacement. Both the compliance of piezoelectric stack actuator as well as the compliance of the amplification structures must be taken into account in designing the nested strain amplification mechanism. Furthermore, the fabrication of free joints is difficult at small scales due to mechanical tolerance and play. For the first amplification stage in particular, the displacements are extremely small and thus the displacement created by the PZT is likely to diminish due to play within revolute joints. Therefore, as in [26] [35] [58], flexural pivots and flexible beams have been used for amplifying PZT displacement. Fig. 3-4 shows the components involved in a dual layer, flexure-based assembly. The most fundamental unit is the piezoelectric stack actuator. In the design shown in the figure, two stacks are used in parallel to meet the desired dimensions. The piezoelectric stacks are first assembled

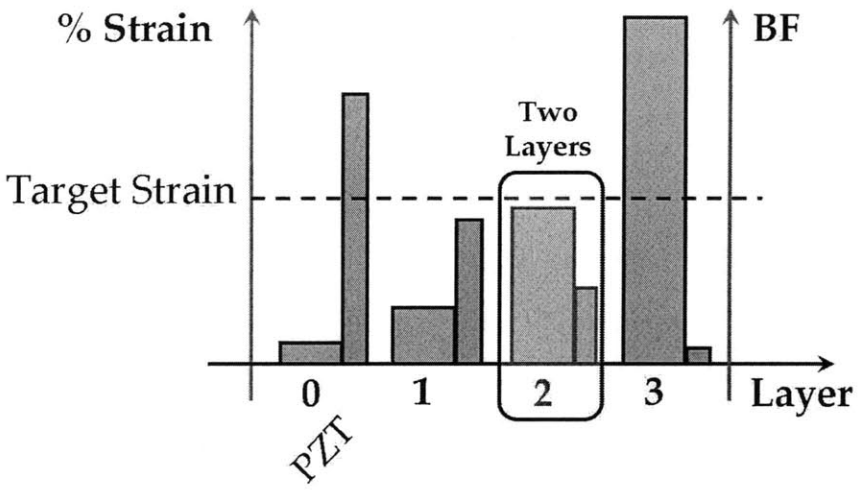

Figure 3-3: Graphical representation of maximum or blocking force (BF) and strain characteristics based on the as a function of layers in the motion amplifier.

into the first layer flexure (step (1) in the figure). The resulting unit is then placed within the second layer flexure (step (2) in the figure).

Fig. 3-5 shows the planar views of the assembled actuator subunit design. From the left portion of Fig. 3-5, observe that as a voltage is applied to the PZT stacks, the first layer flexure is pushed outward along the Y direction, which results in an outward amplified displacement in the Z direction provided that the undeformed beam angle θ_1 is small. The second layer flexure is then pushed outward in the Z direction by the first layer, which results in a further amplified displacement in the inward X direction when $\theta_2 \ll 1$. Therefore, a contraction force is generated along the X-axis output as the PZT stacks are activated, which is shown in the right portion of Fig. 3-5. This contractile double-layer flexure design provides motion along the X-axis and allows the connection of multiple units in series without buckling of the flexures.

A fully assembled two layer flexure system is shown in Fig. 3-6. Note that the system in the figure consists of two piezoelectric stacks ($n_{pzt} = 2$) in parallel providing input forces to the first layer mechanism. Although the equivalent design can be carried out using only a single stack, the limitations on commercially available stack dimensions require that two stacks be used to increase the blocking force of the base layer without sacrificing an increased length (and therefore reduced strain) along the output axis (X-axis in Fig. 3-5). The second layer inverting flexure is nested around the first layer and provides the desired tensile output motion as shown in the flexure realization of Fig. 3-5. The system exhibits small friction, natural axial compliance, and backdriveability. Furthermore, all of the beam elements are under tension when the PZT is activated. A detailed analysis of the design procedure for the flexure based mechanisms is provided in Chapter 4.

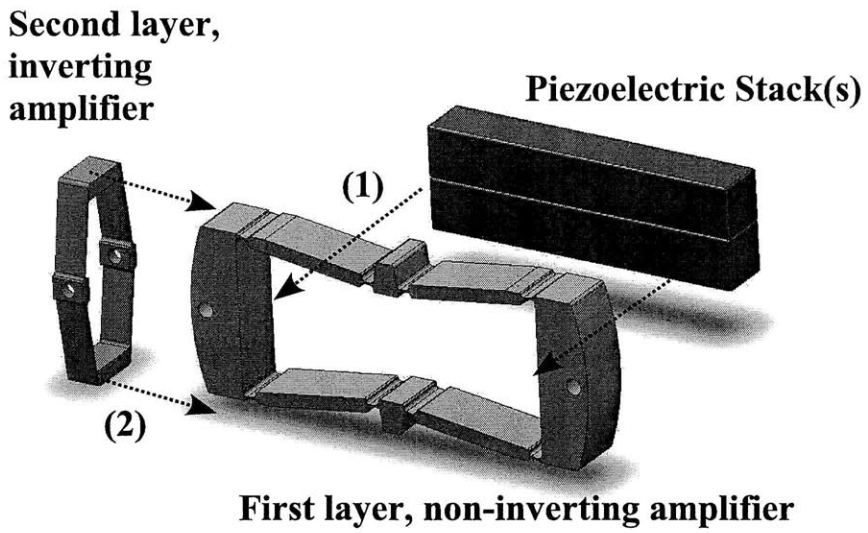

Figure 3-4: Flexure assembly process for a dual layer, flexure-based amplification design.

3.4 Pseudo-Rigid Body Model

The main goal in this section is to arrive at expressions for blocking force and free displacement of the fully assembled flexure system. These expressions provided the basis for assessing the effects of PZT stack size on actuator performance, which is examined in Section 3.5. To achieve this modeling objective, a pseudo-rigid body model of the flexure-based amplifiers is employed. This strategy of flexure modeling was first developed in [52], but is extended here to include nested flexures and a more systematic treatment of kinematic analysis and input-output stiffness transformations.

Although accurate solid mechanics analysis and finite element modeling are employed in the detailed design of Chapter 4, these modeling methods lead to complex equations that provide very little insight into the effects of changing the length scale of piezoelectric actuators. Thus, in order to describe the flexure system with sufficient accuracy to perform scaling analysis in the next section, the ideal kinematic model described in 3.2 is augmented to account for the compliant beams and torsional stiffness of the flexures. The modified kinematic model for two layers is shown in Fig. 3-7.

The two layer augmented kinematic model in Fig. 3-7 shows the model parameters for the first and second layer amplifiers. First, the layer 1 and layer 2 joint space parameters are defined as shown in the uppermost portion of Fig. 3-7. The stiffness parameters in the joint space consist of the corner torsional stiffness κ_{C1} and κ_{C2}, the apex torsional stiffness κ_{A1} and κ_{A2}, and the first layer strut stiffness κ_{S1}. The apex and corner stiffness elements represent the stiffness of flexure hinges. The strut stiffness accounts for the bending deformation of that member due to the large forces applied by the PZT stack(s). The rest configuration of the system occurs when all of the angular deviations $\theta_{b,1}$, $\theta_{s,1}$, and $\theta_{b,2}$ are zero. The equilibrium angles for the

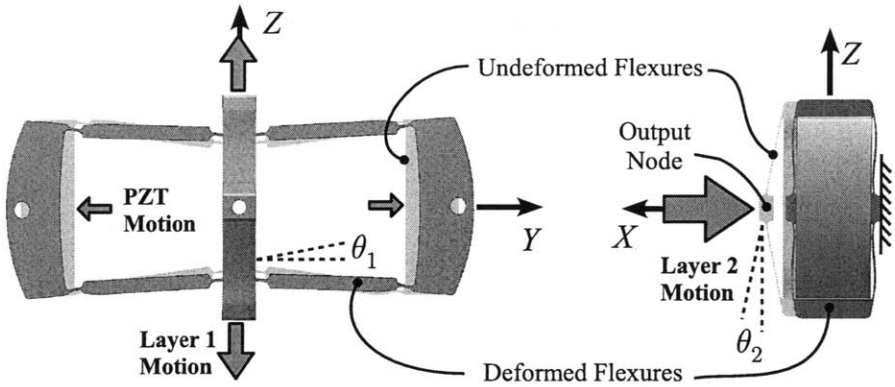

Figure 3-5: Working principle of nested flexure amplification mechanisms.

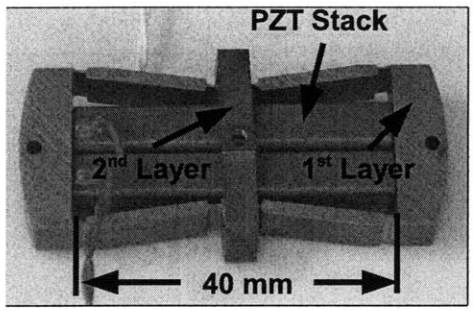

Figure 3-6: Fully assembled dual layer flexure system.

corresponding beams are $\theta_{0,1}$, 0, and $\theta_{0,2}$. The additional model parameters include the beam lengths h_{S1}, h_{S2}, $l_{0,1}$, and $l_{0,2}$, which are shown in the middle portion of Fig. 3-7. Based on the foregoing geometric parameters, the input and output displacements may be computed, which are then referred to as task space parameters. These parameters include Δx_{pzt}, Δx_1, and Δx_2.

Since a rigid connection between the first and second layer mechanisms is assumed, only two of the three joint space displacements ($\theta_{b,1}$, $\theta_{s,1}$, and $\theta_{b,2}$) are independent. This also implies that only two of the three task space parameters (Δx_{pzt}, Δx_1, and Δx_2) are independent. For model development, the joint space configuration is represented using $\theta_{b,1}$ and $\theta_{s,1}$. In this case, the linearized relationship between $\theta_{b,2}$ and $\theta_{b,1}$ is

$$\theta_{b,2} = \left(\frac{l_{0,1} \cos \theta_{0,1}}{l_{0,2} \sin \theta_{0,2}} \right) \theta_{b,1}. \tag{3.3}$$

If the task space parameters are then selected as Δx_{pzt} and Δx_2, the following linearized kinematic relationship is obtained:

$$\begin{pmatrix} \Delta x_{pzt} \\ \Delta x_2 \end{pmatrix} = \begin{pmatrix} h_{s1} & 2l_{0,1} \sin \theta_{0,1} \\ 0 & 2l_{0,1} \cot \theta_{0,2} \cos \theta_{0,1} \end{pmatrix} \begin{pmatrix} \theta_{s,1} \\ \theta_{b,1} \end{pmatrix}, \tag{3.4}$$

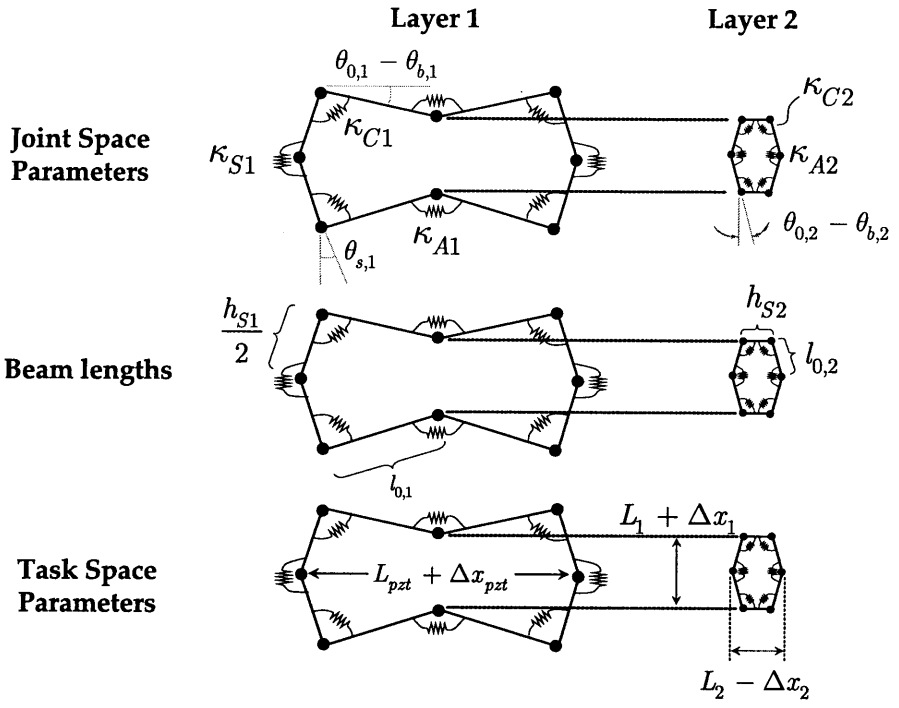

Figure 3-7: Augmented kinematic model for a two-layer flexure system.

where the coefficient matrix in (3.4) is defined as the Jacobian $\mathbf{J}_{\Theta \to X}$. Based on stored potential energy, the stiffness matrix in the joint space is also readily computed:

$$\mathbf{K}_\Theta = \begin{pmatrix} 8\kappa_{S1} + 4\kappa_{C1} & 4\kappa_{C1} \\ & 4\kappa_{C1} + 8\kappa_{A1} + \ldots \\ 4\kappa_{C1} & \left(\frac{l_{0,1}\cos\theta_{0,1}}{l_{0,2}\sin\theta_{0,2}}\right)^2 (4\kappa_{C2} + 8\kappa_{A2}) \end{pmatrix}. \tag{3.5}$$

In order to obtain expressions for the blocking force and free displacement of the flexure, the joint space stiffness matrix is transformed into the task space. This transformation uses the well known relation

$$\mathbf{K}_X = \mathbf{J}_{\Theta \to X}^{-T} \mathbf{K}_\Theta \mathbf{J}_{\Theta \to X}^{-1}. \tag{3.6}$$

In this transformation, kinematic dependence of the force transmission is ignored because sufficiently small deflections are assumed. Details of kinematic dependence can be included using an extra term in (3.6) as described by [19]. Considering the maximum voltage applied to a PZT stack, defining $k_{pzt,p} = \frac{E_{pzt} h_{pzt} w_{pzt}}{L_{pzt}}$, and denoting the entries of the task space stiffness matrix in (3.6) as k_{11}, k_{22}, and $k_{12} = k_{21}$ leads to the following expressions for blocking force and free displacement:

$$f_2^{block}(\mathbf{p}) = \left(\frac{k_{12}(\mathbf{p})}{k_{11}(\mathbf{p}) + k_{pzt,p}}\right) f_{pzt}^{block} \tag{3.7}$$

and

$$\Delta x_2^{free}(\mathbf{p}) = \left(\frac{-k_{12}(\mathbf{p})}{\det(\mathbf{K}) + k_{pzt,p} k_{22}(\mathbf{p})} \right) f_{pzt}^{block}, \tag{3.8}$$

where $\mathbf{p} \in \mathbb{R}^{15}$ is the parameter vector consisting of the PZT stack parameters, PZT geometry and arrangement, ideal amplification gains, and flexure stiffness values. The vector $\mathbf{p}$ may be more explicitly stated as

$$\begin{aligned} \mathbf{p} = \big[& \bar{\alpha}_{pzt},\ \bar{L}_{pzt},\ n_{pzt},\ \gamma,\ h_{s1},\ l_{0,1},\ h_{s2},\ l_{0,2}, \ldots \\ & \theta_{0,1},\ \theta_{0,2},\ \kappa_{C1},\ \kappa_{A1},\ \kappa_{S1},\ \kappa_{C2},\ \kappa_{A2} \big]^T \end{aligned} \tag{3.9}$$

where the first two elements are dimensionless parameters related to the piezoelectric stack characteristics defined in Section 2.4.2, γ is defined as

$$\gamma \triangleq \frac{h_{pzt}}{w_{pzt}}, \tag{3.10}$$

and the remaining parameters remain as previously defined.

3.5 Cell Scaling

The ultimate goal of the scaling analysis is to understand how changing the size of the PZT stack actuators will translate into an effect on the blocking force and free displacement as well as other derived performance metrics. Equations (3.7) and (3.8) provide the basis for assessing how best to scale the nested flexure actuator. In this section, the conventional Buckingham Pi theorem is applied to these equations in order to establish the number of parameters of an equivalent dimensionless model. The hypothetical dimensionless model implied by the Pi Theorem is then reduced to an even smaller dimensionless model by employing scaling assumptions that are consistent with good flexure design practices and practical manufacturing considerations. For the following analysis, the material design space is restricted to metallic materials because metals have many desirable characteristics for flexure fabrication and avoid stress relaxation and creep that is common in polymeric materials [51]. A thorough discussion of material selection is deferred to Chapter 4, while designs utilizing more advanced composites manufacturing are discussed in Chapter 8 as extensions of the present work.

3.5.1 Pi Theorem

The first step in the scaling analysis is to establishing the minimum number of dimensionless parameters used to fully describe the quantities of interest. In this analysis, the quantities of interest will be the blocking force and free displacement of a nested-flexure actuator unit. The fundamental tool in this analysis is the Buckingham Pi Theorem, a description of which can be found in most introductory texts on fluid mechanics (e.g. [117]).

The Pi Theorem first requires that both the blocking force and free displacement may be written compactly as scalar functions of the form

$$\Phi_{block}(\mathbf{p}) = 0 \tag{3.11}$$

and

$$\Phi_{free}(\mathbf{p}) = 0 \tag{3.12}$$

respectively. From (3.9), the number of dimensional parameters in $\mathbf{p}$ is 9. Thus, in (3.11) and (3.12), the number of dimensional parameters is 10 to account for the incorporation of the blocking force and free displacement respectively. Using the force (F), length (L), and time (T) unit system, (3.11) requires only force and length to fully characterize the dimensions of the parameters (i.e. time is not involved). Specifically, the torsional stiffness parameters are described with the units $\frac{N \cdot m}{rad}$ while the blocking force is described using N. Hence, F and L are the two required reference dimensions. The number of dimensionless parameters to describe the blocking force relation in (3.11) will be denoted by $N_{\Pi,block}$ and is computed as

$$\begin{aligned} N_{\Pi,block} &= 10 - 2 \\ &= 8. \end{aligned} \tag{3.13}$$

Similarly, (3.12) requires only force and length to fully characterize the dimensions of the parameters since time is still not involved. Again, the torsional stiffness parameters are described with the units $\frac{N \cdot m}{rad}$ while the free displacement is described using m. Hence, F and L are still the two required reference dimensions. The number of dimensionless parameters to describe the blocking force relation in (3.12) will then be denoted by $N_{\Pi,free}$ and computed as

$$\begin{aligned} N_{\Pi,free} &= 10 - 2 \\ &= 8. \end{aligned} \tag{3.14}$$

Since the models in (3.11) and (3.12) already contain 6 dimensionless parameters, the total number of dimensionless parameters required to describe the blocking force and free displacement is $N_{\Pi,block} + 6 = N_{\Pi,free} + 6 = 14$. The parameter space provided by the dimensionless model is still far too large to provide insightful scaling results. Thus, rather than utilize a 14 parameter dimensionless model, an analysis more akin to that provided in [61] and [28] is employed in the next subsection, wherein physical insight is used in place of the exhaustive enumeration method of establishing dimensionless groups that follows application of the Pi Theorem.

3.5.2 Scaling Assumptions

In this section, certain simplifying assumptions allow the model parameter space spanned by all possible $\mathbf{p} \in \mathbb{R}^{15}$ to be restricted to the positive plane $\mathbb{R}^{2+}$. The goal is then to utilize realistic design assumptions and manufacturing insight in order to yield a model that depends only upon the PZT dimensionless geometry defined by $\mathbf{p}' = [\bar{L}_{pzt} \quad \bar{\alpha}_{pzt}]^T \in \mathbb{R}^{2+}$. This reduced parameter vector then implies that the entire flexure design can be performed uniquely once a specific piezoelectric stack arrangement is selected.

The flexure design can be carried out uniquely if suitable assumptions are made. The first constraint is that the stack length must be consistent with the beam lengths and angles on the first layer:

$$2l_{0,1}\cos(\theta_{0,1}) = L_{pzt}. \tag{3.15}$$

The second constraint is that the first layer strut length should be consistent with the total height of the PZT stacks:

$$h_{S1} = n_{pzt}h_{pzt} + 2l_{0,1}\sin\theta_{0,1}. \tag{3.16}$$

Next, the first and second layers must have appropriate lengths to form a connection:

$$h_{S1} - 2l_{0,1}\sin\theta_{0,1} = 2l_{0,2}\cos\theta_{0,2}. \tag{3.17}$$

Finally, the strut height of the second layer mechanism (h_{S2})is set to be the width of the first layer flexure (w_1), which is then set to the width of the PZT stack:

$$h_{S2} = w_{pzt}. \tag{3.18}$$

The remaining assumptions are as follows:

- The number of stacks (n_{pzt}) acting as inputs to the first layer is fixed and the cross sectional aspect ratio $\gamma = \frac{h_{pzt}}{w_{pzt}}$ is approximately 1.
- The gains of each flexure layer are set to be g_0 so that $\theta_{0,1} = \theta_{0,2} = \text{arccot}(g_0)$.
- The apex and corner torsional stiffness will be set equal so that $\kappa_{C1} = \kappa_{A1}$ and $\kappa_{C2} = \kappa_{A2}$.
- The torsional stiffness parameters κ_{C1} and κ_{C2} are minimized while maximizing κ_{S1} using material selection and manufacturing constraints.

The final assumption in the above list is implemented using the general formula for torsional stiffness of a beam subjected to pure bending:

$$\kappa = \frac{E_{min/max}I_{min/max}}{L_{min/max}} \tag{3.19}$$

where E is the metallic flexure elastic modulus, I is the moment of inertia of the cross section, and L is the length of the bending zone under consideration. The subscript min/max is set such that the torsional stiffness parameter in question is minimized (apex and corner stiffness) or maximized (strut stiffness). In computing the maximum strut stiffness using (3.19), the assumed maximum strut thickness of the first layer is given by $t_{max,S1} = \frac{L_{pzt}}{3}$. Overall, this list of assumptions provides an optimistic or best-case set of the resulting metallic flexure designs. Furthermore, the assumptions may be relaxed if more explicit optimization is required.

With the foregoing assumptions, the blocking force and free displacement of the multilayered system given only the dimensionless stack parameters $\bar{L}_{pzt}$ and $\bar{\alpha}_{pzt}$, which is consistent with the original scaling analysis goal. Thus, the new design parameter vector is $\mathbf{p}' = [\bar{L}_{pzt} \;\; \bar{\alpha}_{pzt}]^T \in \mathbb{R}^{2+}$. The following subsection provides additional performance metrics that can be readily computed using this two parameter model.

3.5.3 Performance Metrics

The previously developed model is now used to compute the effects of PZT stack scale on several performance metrics. The primary performance metrics are the blocking force and free strain. The blocking force may be obtained directly from (3.7) while the free strain is computed using (3.8) and the output length:

$$\epsilon_2^{free} = \frac{\Delta x_2^{free}(\mathbf{p}')}{h_{S1} + 2l_{0,2}\sin\theta_{0,2}} \tag{3.20}$$

The corresponding dimensionless values normalize the blocking force and free strain by the maximum theoretical values given by the ideal kinematic model in 3.2:

$$\bar{f}_2^{block} = \frac{f_2^{block}(\mathbf{p}')}{f_{pzt}^{block}\prod_{i=1}^{2}\tan(\theta_{0,i})} \tag{3.21}$$

and

$$\bar{\epsilon}_2^{free} = \frac{\Delta x_2^{free}(\mathbf{p}')}{\Delta x_{pzt}^{free}\prod_{i=1}^{2}\cot(\theta_{0,i})} \tag{3.22}$$

To further understand the effects of the PZT stack scale parameters on the full system performance, the specific work output may be computed as

$$SW = \frac{\Delta x_2^{free}(\mathbf{p}')f_2^{block}(\mathbf{p}')}{w_{pzt}L_{pzt}n_{pzt}h_{pzt}\left(1 + \frac{l_{0,2}\sin(\theta_{0,1})}{n_{pzt}h_{pzt}} + \frac{l_{0,2}\sin(\theta_{0,2})}{L_{pzt}}\right)} \tag{3.23}$$

The dimensionless analog of this metric is given by the product of the dimensionless free strain, the dimensionless blocking force, and the packing efficiency (PE):

$$\overline{SW} = \bar{\epsilon}_2^{free}\bar{f}_2^{block} \cdot PE \tag{3.24}$$

where

$$PE = \frac{w_{pzt} L_{pzt} n_{pzt} h_{pzt} \left(1 + \frac{l_{0,2}\sin(\theta_{0,1})}{n_{pzt} h_{pzt}} + \frac{l_{0,2}\sin(\theta_{0,2})}{L_{pzt}}\right)}{h_{S1}(L_{pzt} + 2t_{S1,\max})(h_{S2} + 2l_{0,2}\sin(\theta_{0,2}))} \tag{3.25}$$

which is the ratio of the actual volume of the assembled system to the volume of a bounding box. A final performance metric is the capacitance of the piezoelectric stack, which can be computed from

$$C_{pzt} = N_{film}\left(\frac{k\epsilon_0 n_{pzt} h_{pzt} w_{pzt}}{t_{film}}\right) \tag{3.26}$$

where k is the relative dielectric permittivity for PZT and ϵ_0 is the permittivity of free space.

3.5.4 Numerical Results and Discussion

Table 3.1 shows the relevant parameters using in a numerical evaluation of the performance metrics discussed above. Note that the values for E_{min} and E_{max} represent the elastic moduli for metallic materials that can be made into flexures. Also, note that t_{min} is the minimum flexure thickness that can be achieved using wire electrical discharge machining (EDM) and $w_{2,min}$ is the minimum width of a flexure required to make connections between successive actuator cells.

Table 3.1: Numerical values used in the scaling analysis.

Parameter	Value	Units
$\theta_{0,1}$	8	deg
$\theta_{0,2}$	8	deg
E_{min}	70	GPa
E_{max}	207	GPa
E_{pzt}	35	GPa
d_{33}	150	$\frac{pm}{V}$
$V_{pzt,max}$	150	V
n_{pzt}	2	-
t_{min}	0.1	mm
$w_{2,min}$	3	mm
t_{film}	30	μm
k	1700	-
ϵ_0	8.85	$\frac{pF}{m}$

Fig. 3-8 shows the results of the scaling analysis. In each of the plots, the circular point shows the value on the predicted surface for the PZT stacks used in the design shown in Fig. 3-6, which has $\bar{L}_{pzt} = 1333$ and $\bar{\alpha}_{pzt} = 0.024$. Also shown on each plot is a square point indicating the maximum value of the surface on the domain

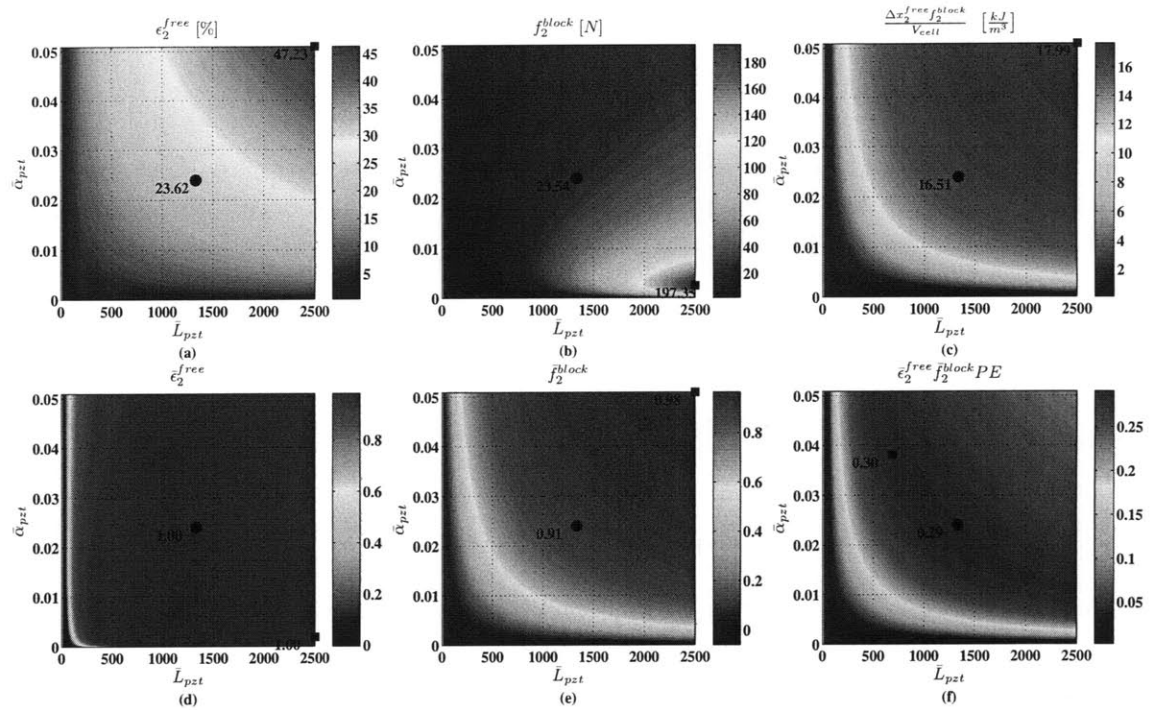

Figure 3-8: (a) Free strain performance (b) Blocking force performance (c) Work density performance (d) Free strain performance relative to ideal kinematic model (e) Blocking force performance relative to ideal kinematic model (f) Work output relative to ideal kinematic model having perfect packing efficiency.

considered: $\bar{L}_{pzt} \in (0, 2500)$ and $\bar{\alpha}_{pzt} \in (0, 0.05)$ This domain contains far exceeds the range of commercially available stacks.

Fig. 3-8 (a) shows the free strain performance. Note that the contours show a monotonic increase in strain as $\bar{L}_{pzt}$ and $\bar{\alpha}_{pzt}$ are simultaneously increased. This means that as the stacks get longer and their cross sectional area becomes small relative to the length, the free strain performance increases. The circular point on the surface indicates the predicted value for the cell design shown in Fig. 3-6. The actual measured strain for this design (described in Chapter 4) is 12% - 15%, which is lower than the predicted model because the model does not account for the additional output length that aries from the thickness of the tapped hole section on the second layer (Fig. 3-6).

Fig. 3-8 (b) shows the blocking force performance contours as functions of $\bar{L}_{pzt}$ and $\bar{\alpha}_{pzt}$. These contours show that the highest blocking force is possible when $\bar{\alpha}_{pzt} \approx 0.003$ and $\bar{L}_{pzt}$ (i.e. the number of individual layers in the stack) is made as large as possible. The predicted value of blocking force for the design in Fig. 3-6 is 23.54 N, which is very close to the measured value of 20 N for the design as described in Chapter 4.

Fig. 3-8 (c) shows the specific work performance contours as functions of $\bar{L}_{pzt}$ and $\bar{\alpha}_{pzt}$. These contours follow a similar pattern to those in Fig. 3-8 (a). That is, an increase in work density occurs when the stack aspect ratio is made large and the number of layers is increased. The predicted work density of the design in Fig. 3-6 is

16.51 $\frac{kJ}{m^3}$, which is an order of magnitude higher than skeletal muscle and compares favorably to the high work density of other artificial muscle materials [73].

Fig. 3-8 (d) shows the free strain output normalized by the upper bound on the performance imposed by the ideal kinematic model. A value of unity indicates that the upper bound on performance will be achieved with a design having the corresponding values of $\bar{L}_{pzt}$ and $\bar{\alpha}_{pzt}$. For all but only the shortest PZT stacks, the upper bound on performance can be achieved. The region near unity also implies that stacks in this range will lead to designs whose free strain performance is accurately predicted by the ideal kinematic model.

Fig. 3-8 (e) shows the blocking force output normalized by the upper bound on the performance imposed by the ideal kinematic model. As in (d), a value of unity indicates that the upper bound on performance will be achieved with a design having the corresponding values of $\bar{L}_{pzt}$ and $\bar{\alpha}_{pzt}$. Also, as in (d), the regions near unity imply that the ideal kinematic model is an accurate predictor of performance. For blocking force, the upper bound on blocking force performance can only be achieved when long stacks with a large aspect ratio are used. The design shown in Fig. 3-6 has a predicted normalized blocking force of 0.91. In other words, this design should achieve a blocking force that is within 9% of the maximum theoretical value.

The final plot, Fig. 3-8 (f), shows the contours of the metric described by (3.24). This metric is perhaps the most insightful since it represents the work output performance of a cell relative to the maximum theoretical upper bound imposed by the kinematic model and the maximum possible packing efficiency. In other words, if a cell could produce the maximum theoretical strain and free displacement such that it fit inside a box having the combined volume of the flexures and the PZT stacks, then this metric has a value of unity. Over the domain considered, there exists a crest of maximum performance that tapers off at high values of $\bar{L}_{pzt}$ and $\bar{\alpha}_{pzt}$. The maximum value is 0.3 and the present design achieves a predicted value of 0.29.

In each of the dimensionless plots (d) to (f), the regions of low performance involve stacks having fewer than 500 layers and aspect ratios smaller than 0.01. These regions are brought about because of the finite flexure stiffness and the manufacturing constraints. Specifically, the lower bound on flexure stiffness is determined by the minimum manufacturable thickness (where 0.1 mm is used for the EDM process) and the minimum elastic modulus (where 70 GPa is used for aluminum). If one relaxes the constraint on maximum strut thickness, and thereby removes the upper bound on κ_{S1}, the plot in (e) appears almost identical to the plot in (d) where the ideal kinematic performance can be achieved for nearly all values of $\bar{L}_{pzt}$ and $\bar{\alpha}_{pzt}$. Taken together, plots (d) and (e) indicate that the best designs are achieved when $\bar{L}_{pzt}$ and $\bar{\alpha}_{pzt}$ are made as large as possible. In (f), however, the performance loss due to imperfect packing is also accounted for. In this instance, the best designs occur in an interior region that achieves its maximum at $\bar{L}_{pzt} = 690$ and $\bar{\alpha}_{pzt} = 0.0381$. This point may be considered optimum the values listed in Table 3.1 and likely close to the optimum point for all metallic flexure designs. This point represents a cell that has a volume that is 15% of the present design's volume and achieves a slightly higher value of $\overline{SW}$.

If $\overline{SW}$ is the primary metric, then the scaling analysis may also be used to establish an optimum length scale for a given cross sectional area. For this purpose, the dimensionless aspect ratio may be rewritten using the stack cross sectional area A_{pzt}

as

$$\begin{aligned} \bar{\alpha}_{pzt} &= \frac{L_{pzt} t_{pzt}}{A_{pzt}} \\ &= \frac{\bar{L}_{pzt} t_{film}^2}{A_{pzt}} \end{aligned} \tag{3.27}$$

Therefore, in the $\bar{\alpha}_{pzt}$-$\bar{L}_{pzt}$ plane, a given cross sectional area defines a line passing through the origin. For example, the design shown in Fig. 3-6 uses stacks having a cross sectional area of 50 mm^2. The line is shown in Fig. 3-9. Operating along this line with the dimensionless length as a free parameter allows for constrained optimization. Note that the constrained optimum for the 50 mm^2 is very close to the actual flexure design.

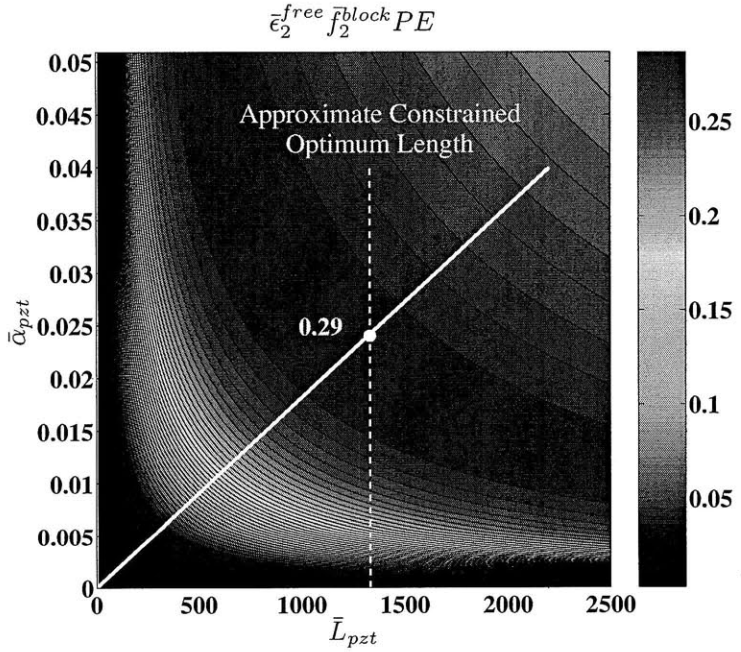

Figure 3-9: $\overline{SW}$ optimal scaling of the stack length for a given stack cross sectional area.

An additional scaling consideration is the effect of $\bar{L}_{pzt}$ and $\bar{\alpha}_{pzt}$ on the piezoelectric capacitance given in (3.26). The capacitance of a cell indirectly indicates its power requirements as discussed in Chapter 4. Thus, smaller cell capacitance is more desirable. Furthermore, higher drive amplifier bandwidth can be achieved for smaller values of the capacitance (see e.g. [101]). Fig. 3-10 shows the base 10 logarithm of the cell PZT capacitance versus the stack scaling parameters. The capacitance spans several orders of magnitude and has contours that grow increasingly dependent on aspect ratio as the number of stack layers increases. For the present design, $C_{pzt} \approx 33\mu F$ whereas for the optimum design from Fig. 3-8 (f) gives $5.5\mu F$.

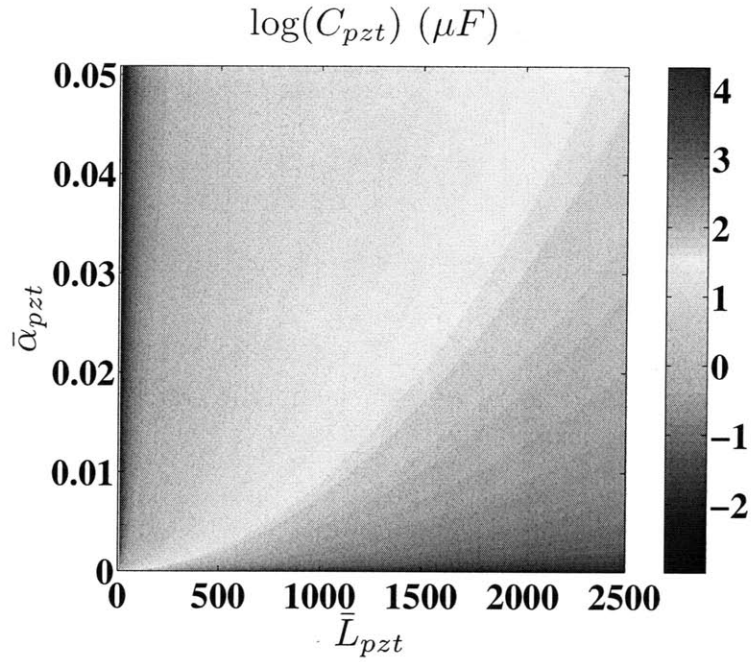

Figure 3-10: Base 10 logarithm of PZT capacitance vs. dimensionless aspect ratio of number of piezoelectric stack layers.

3.6 Cellular Architecture

The scaling analysis of the previous section indicates that there is an optimal size for motion amplified piezoelectric actuators. The best size for such actuator units is close to the size of the unit shown in Fig. 3-6. Thus, in order to create actuators that have a form factor similar to artificial muscles, a subdivided architecture consisting of many units is required. In the remainder of the thesis, these actuator subunits will be referred to as cells. The desired cellular architecture is depicted in Fig. 3-11. The cellular architecture can exhibit other advantages such as robustness to individual unit failures (for parallel assemblies), modularity and scalability to different force and displacement needs, and tunability of stiffness and dynamics (discussed in Chapter 5).

For cellular systems, combination of cells connected in series and in parallel can be described as a two dimensional array having force and displacement properties that are aggregate effects of all of the cells. A generic cellular assembly made up of N_p parallel strands of N cells is shown in Fig. 3-12. This assembly is subject to an external force F_{TOT} and is undergoing a contraction of Δx_{TOT}. For this system, each cell will be assumed to have the same rest length l_0 and therefore the overall free strain (i.e. strain under zero force conditions) of the assembly may be expressed as

$$\epsilon = \frac{\Delta x_{TOT}}{N l_0}, \tag{3.28}$$

where Δx_{TOT} is the total contraction displacement of the assembly as viewed from

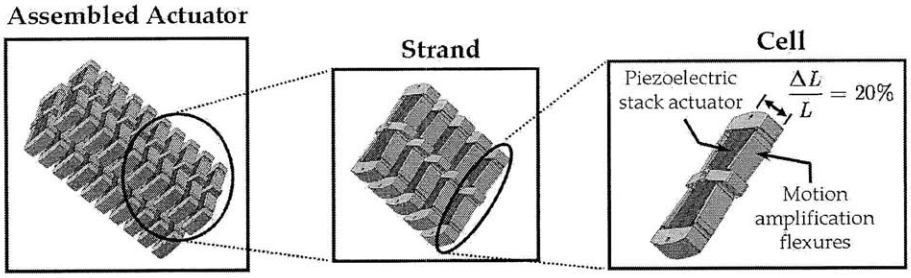

Figure 3-11: Cellular architecture of an artificial muscle system designed using motion amplified piezoelectric actuators.

the output. For identical cells each having a dual layer flexure structure with a free displacement of Δx_2^{free}, the strain simply becomes

$$\begin{aligned} \epsilon &= \frac{N\Delta x_2^{free}}{Nl_0} \\ &= \frac{\Delta x_2^{free}}{l_0}, \end{aligned} \tag{3.29}$$

which is the strain of a single cell. Hence, each cell must be designed to meet the desired strain performance for the artificial muscle assembly.

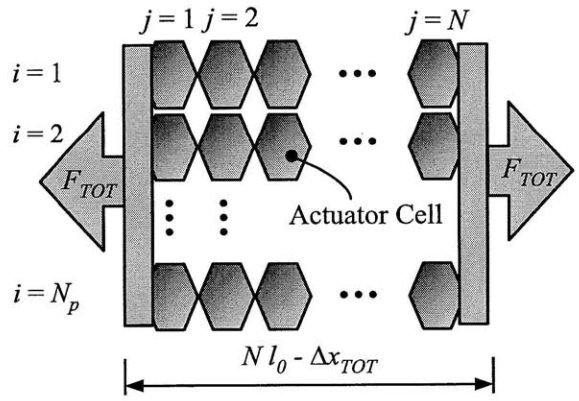

Figure 3-12: An array of cellular actuators with each cell contributing to the aggregate force and displacement.

Similarly, the maximum force of a cellular assembly may be determined based on the individual cell behaviors. For this analysis, the cell is modeled using the linear model shown in Fig. 2-9 and adjusted by the appropriate gains. For the dual layer flexure cell, the force versus displacement characteristic under maximum activation is shown in Fig. 3-13.

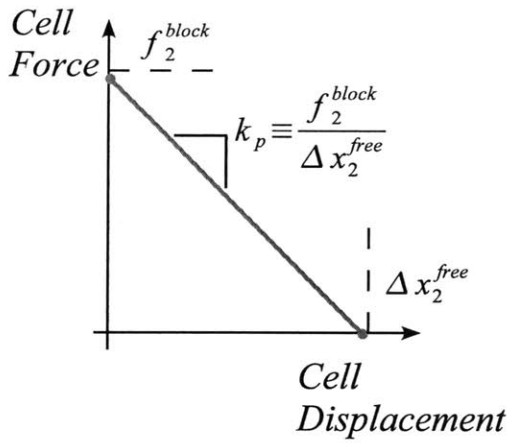

Figure 3-13: Force versus displacement characteristic for a dual layer flexure based cell at maximal activation.

The linear characteristic in Fig. 3-13 can be modeled using the static model shown in Fig. 3-14. Fig. 3-14 (a) shows the second, or output, layer of a single cell under an applied external force f_{ext}. The corresponding static model in Fig. 3-14 (b) consists of a pure force generator element in parallel with a spring defined to have the value

$$k_p \triangleq \frac{f_2^{block}}{\Delta x_2^{free}} \tag{3.30}$$

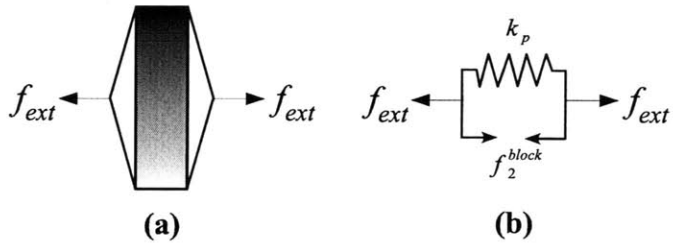

Figure 3-14: (a) Single cell subjected to an externally applied force along the second layer output. (b) Linear static model of cell behavior.

For most actuator assemblies considered in this thesis, a single strand of cells is used so that $N_p = 1$ in Fig. 3-12. Under this condition, consider a strand of $N = 2$ cells. If the ends of the strand are rigidly fixed and the cells are maximally activated, then the maximum total force generated (i.e. the blocking force) is given by

$$f_{strand}^{block} = \left(\frac{k_{p2}}{k_{p1} + k_{p2}}\right) f_2^{block,1} + \left(\frac{k_{p1}}{k_{p1} + k_{p2}}\right) f_2^{block,2} \tag{3.31}$$

where $f_2^{block,1}$ and $f_2^{block,2}$ are the individual cell blocking forces and k_{p1} and k_{p2} are the individual cell parallel stiffness elements. If the cells are identical, then (3.31)

shows that the blocking force generated at the output is equal to the blocking force of the individual cells. Overall, the cellular architecture leads to several interesting properties that are exploited throughout this work.

Chapter 4

Cell Design

This chapter addresses the major components of the design phase of this thesis. The chapter begins with a description of the unified flexure design procedure used to synthesize the cellular actuators. Material selection for the flexure design is discussed in detail, followed by a complete description of the solid mechanical model used for rapid assessment of flexure designs. The candidate flexure designs are then assessed based on a sensitivity analysis, which provides the basis for the final design revisions made using finite element modeling (FEM). The chapter also discusses the experimental techniques used to assess the blocking force and free displacement of the individual cell designs. The chapter concludes with additional analysis of the basic reliability properties of cellular systems as well as the power requirements for individual cells operating away from resonant frequencies.

4.1 A Unified Flexure Design Procedure for Static Performance

The cell design procedure is outlined in Figure 4-1. The goal of the design procedure is to create strain-amplified PZT cellular actuators that achieve functional requirements in terms of the static performance characteristics of maximum displacement and maximum force. Dynamic behavior of cells and the associated assemblies is addressed in subsequent chapters. The force and displacement of each cell are governed by the multiplicative nested flexure effect discussed in Chapter 3. Force and displacement characteristics represent the key tradeoff the static design. Too large of a force implies that the strain performance will be significantly lower than the target value of 20 %, while too small of a force limits the scope of the artificial muscle applications.

Each step of the design process in Fig. 4-1 is crucial to achieving the desired cell performance. Note that in this process, the first and second layers are designed together. The first step in the design process is to set maximum force f_2^{block} and displacement Δx_2^{max} requirements for an individual cell (see Figure 4-1). Based on these performance targets, commercially available PZT stacks may be selected using the simple kinematic models described in Section 3.2. These stacks are then used for the subsequent design steps. The first shaded block in the Fig. 4-1 represents a solid mechanics flexure model described in Section 4.3. Based on this analytical model, the stack selection can be revisited, which is denoted in the figure by the dashed feed-

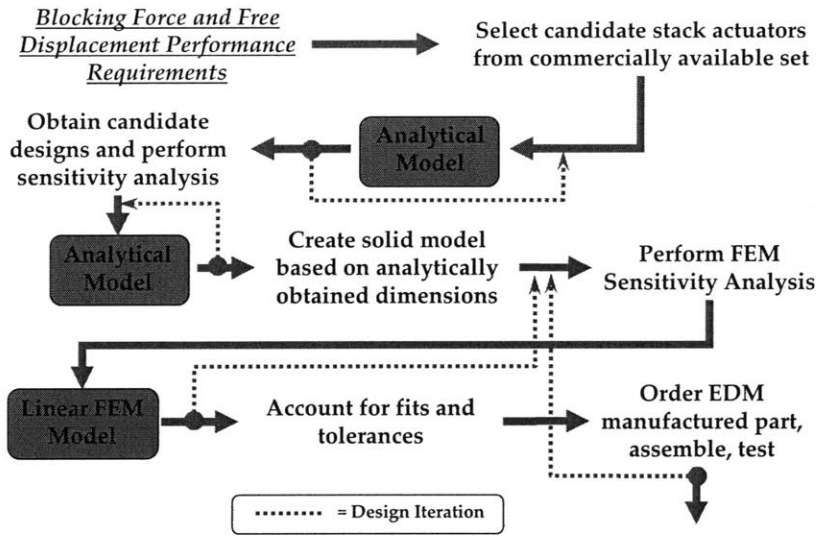

Figure 4-1: Design procedure for developing cellular PZT actuators.

back line. The output of the first design step is a set of candidate designs that can then be refined through a sensitivity analysis. The sensitivity analysis is discussed in Section 4.4. The sensitivity analysis also involves numerous iterations with the solid mechanical model. Following the sensitivity analysis, the dimensions of the flexure system are nominally set. Using these nominal dimensions as a starting point, a 3D solid model for the flexure is created in SolidWorks. The solid model is then used within the COSMOS linear FEM solver to assess the blocking force and free displacement performance of the cell (see Section 4.5). Furthermore, sensitivity analysis is performed again in order to make minor adjustments to the solid model. The final output of the FEM is a completed solid model that is modified slightly to account for the preload press fits and dimensional tolerances required for accommodating the piezoelectric stacks. Upon completing the final dimensioning, the flexures are then manufactured and assembled (see Section 4.6).

4.2 Flexure Material Selection

The first step in the design of flexure based mechanical amplifiers is material selection. This step is considered as a prerequisite for the design procedure in Fig. 4-1. The ideal kinematic model discussed in Section 3.2 sets an upper bound on amplification performance. For realistic amplifiers, perfectly rigid beams and ideal revolute joints cannot be achieved. Moreover, interfacing with the piezoelectric devices requires a strong, compression preloaded coupling between the PZT stack and the first layer amplifier (see Fig. 3-4). Material selection is crucial in order to approximate the ideal kinematic amplification devices while meeting the other pragmatic requirements (e.g. preload and manufactureability).

As a starting point for material selection, several material performance indices are considered. These performance indices and the associated rationale are provided in Table 4.1. Maximizing these indices will lead to the best performance for the

resulting flexures. In the table, E is Young's modulus, ρ is the material density, and σ_f is the failure strength (e.g. yield). All of the performance indices can be considered effectively using the material mapping shown in Fig. 4-2 [9].

Table 4.1: Material indices used in the selection of candidate flexure materials.

Performance Index to Maximize	**Importance in Flexure Design**
$\frac{E}{\rho}$	Meet stiffness specifications at minimum mass.
$\frac{\sqrt{\sigma_f}}{\rho}$	Avoid fracture in beam bending at minimum mass. The $\sqrt{\sigma_f}$ reflects that the width of the flexures is a pre-specified dimension.
$\frac{\sigma_f}{E}$	Achieve large strain in the flexure zone before yielding or fracture.

As noted in the Table 4.1, the width dimension (shown in Fig. 4-4 for both inverting and non-inverting mechanisms) is assumed to be fixed for the flexures. Flexure width for the first layer flexure is primarily dictated by PZT stack width and desired to maximize strain. The second layer flexure width is determined by the minimization of bending stiffness while maintaining a suitable width for inter-cell connections. These fixed widths lead to the $\sqrt{\sigma_f}$ term in the $\frac{\sqrt{\sigma_f}}{\rho}$ index [9]. The result of the $\sqrt{\sigma_f}$ term is to de-emphasize the failure strength.

Maximizing the first two performance indices in Table 4.1 is tantamount to operating in the far upper right corner of the material map in Fig. 4-2. This boxed corner of the material map contains materials that can meet both stiffness and strength constraints while minimizing mass. These classes of material include certain ceramics, carbon fiber reinforced polymers (CFRP), steels, and titanium, magnesium, and certain aluminum alloys. The third performance index, $\frac{\sigma_f}{E}$, indicates that suitable materials should also have a high yield strain. Thus, ceramic materials are readily eliminated from consideration. The remaining candidate materials include the previously mentioned metallic materials and composites. Although composite materials show particular promise for flexure design, these materials involve the most manufacturing complexity and have a high internal damping that is undesirable for high frequency applications. For the flexure designs in this thesis, metallic materials were selected. Among the materials, steel was selected for low cost and readily manufactured flexures. Composite materials are considered further in Chapter 8 as a possible extension of the present design. The properties of the steel chosen are listed in Table 4.2.

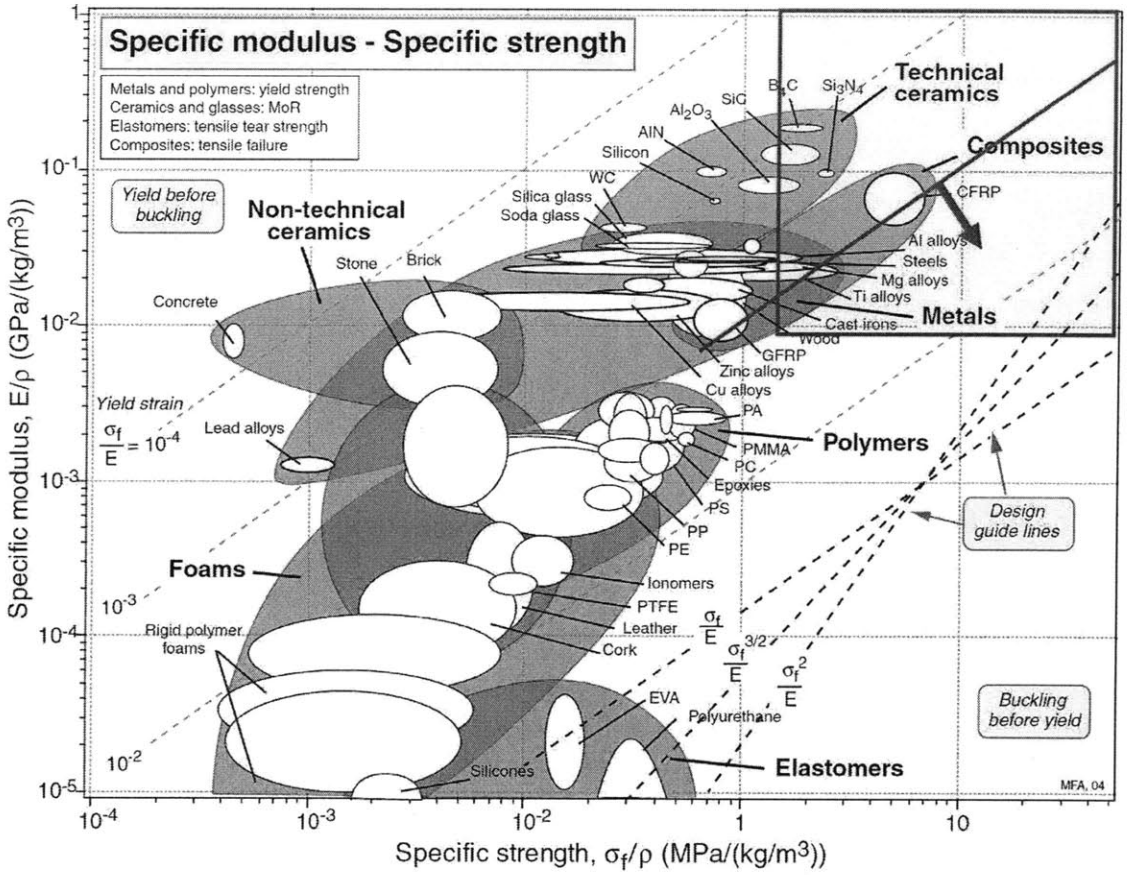

Figure 4-2: Material map showing specific modulus versus specific strength. Oblique contours represent lines of constant $\frac{\sigma_f}{E}$ [9].

4.3 Analytical Flexure Modeling

Several models of the amplification method are used within the design process of Fig. 4-1. The four major model types are listed in Fig. 4-3. Each of the models are be placed on a spectrum ranging from simplistic and approximate to complex and accurate. The simplest model is the idealized kinematic model discussed in Section 3.2. This model is used in order of magnitude analysis and basic stack selection. The next model is the augmented kinematic, or pseudo-rigid body, model discussed in Section 3.4. This model is well suited to scaling analysis and basic design calculations, but is difficult to use for synthesizing realistic flexure dimensions. The next model involves a complete strain energy analysis of the realistic flexure geometries. This model incorporates all of the dimensions that must be determined to synthesize both a first and second layer flexure. The advantage of this model is that it closely approximates realistic flexure behavior. However, this model does not account for the exact load distributions or additional features imposed on the flexures (e.g. fillets and chamfers). Thus, to obtain the most accurate prediction of performance, finite element modeling (FEM) is used, which is discussed in Section 4.5.

Table 4.2: Mechanical properties of 1010 cold drawn carbon steel [29].

Mechanical Property	**Value**	**Units**
Young's Modulus, E	205	GPa
Poisson's Ratio, ν	0.29	-
Yield Strength, σ_y	305	MPa
Ultimate Tensile Strength, σ_{UTS}	365	MPa

This remainder of this section focuses on the development of the strain energy, or solid mechanics, model used extensively throughout the design procedure. The assumptions of this model are that the flexures undergo small deflections, obey linear elasticity, experience plane stress, and are isotropic. Fig. 4-4 and Table 4.3 show the geometric parameters in both the first and second layers. Fig. 4-4 (a) shows the parameters that determine the geometry of a non-inverting flexure used as the first layer amplification device. Fig. 4-5 (a) shows that the piezoelectric stack force f_{pzt} applied outward along the horizontal input dimension, produces a corresponding amplified outward displacement Δx_1 along the vertical direction. Fig. 4-4 (b) shows the parameters that determine the geometry of an inverting flexure while Fig. 4-5 (b) shows that the first layer force f_1 applied along the second layer flexure's input produces a corresponding amplified contraction displacement Δx_2 in the vertical direction.

The first step in establishing the analytical flexure model is to formulate expressions for internal structure reactions and stress resultants (i.e. shear, bending moments, and normal forces) under the action of a force f_{pzt} applied at the input, a force f_1, and a force f_2 applied at the output as shown in Fig. 4-5. These external forces give rise to internal stress resultants that are shown explicitly in Fig. 4-6 for the first layer flexure. Fig. 4-6 (a) shows a one-quarter model of the mechanism that can be used to obtain all of the necessary stress resultants. Within this first layer model, f_{pzt} appears as an external force and an internal normal force. The force f_1 also appears as an external force and an internal normal force. The other internal forces for the quarter model include a moment within the strut mechanism M_s and a moment within the top section M_t. Fig. 4-6 also shows the three section cuts required to expose the stress resultants in the different portions of the flexure. Fig. 4-6 (b) shows the resultants for a hypothetical cut made in the vertical strut. These internal forces consist of a normal force $N(y)$, an internal moment $M(y)$, and a shear force $V(y)$, which are all functions of the coordinate y. Similarly, the hypothetical cuts made at sections (2) and (3) reveal normal, moment, and shear internal forces that are functions of x' and x respectively.

Having established the internal forces (i.e. stress resultants), the next step in obtaining the flexure model is to compute the strain energy that arises from these forces. The strain energy in the first flexure, U_1, is obtained from the sum of the shear, normal, and moment contributions:

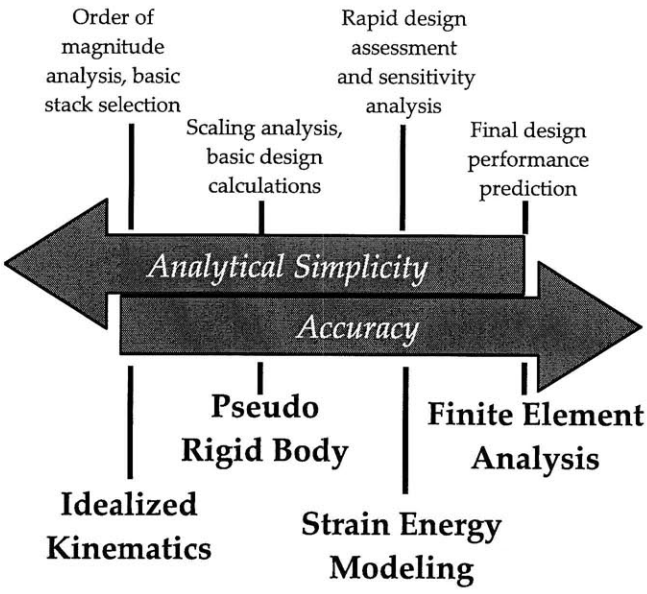

Figure 4-3: Accuracy versus tractability spectrum of the modeling techniques applied to strain amplification flexures.

$$U_1 = U_{1,V} + U_{1,N} + U_{1,M} \tag{4.1}$$

where $U_{1,V}$ is the shear contribution, $U_{1,N}$ is the normal contribution, and $U_{1,M}$ is the moment contribution. The total shear energy may be written by assuming a rectangular cross section through all of the members:

$$\begin{aligned} U_{1,V} = 4\Bigg(& \int_0^{\frac{h_s}{2}} \frac{3V(y)^2}{5Gwt_s} dy + \int_0^{l_{fc}} \frac{3V(x')^2}{5Gwt_{fc}} dx' + \int_{l_{fc}}^{l_o - l_{ft}} \frac{3V(x')^2}{5Gwt_b} dx' + \\ & \int_{l_o - l_{ft}}^{l_o} \frac{3V(x')^2}{5Gwt_{ft}} dx' + \int_0^{\frac{l_t}{2}} \frac{3V(x)^2}{5Gwt_t} dx \Bigg) \end{aligned} \tag{4.2}$$

where G is the shear modulus. Assuming a linearly elastic and isotropic material, the shear modulus can be written as

$$G = \frac{E}{2(1+\nu)}. \tag{4.3}$$

Similar to the shear, the normal and bending moment contributions are given by

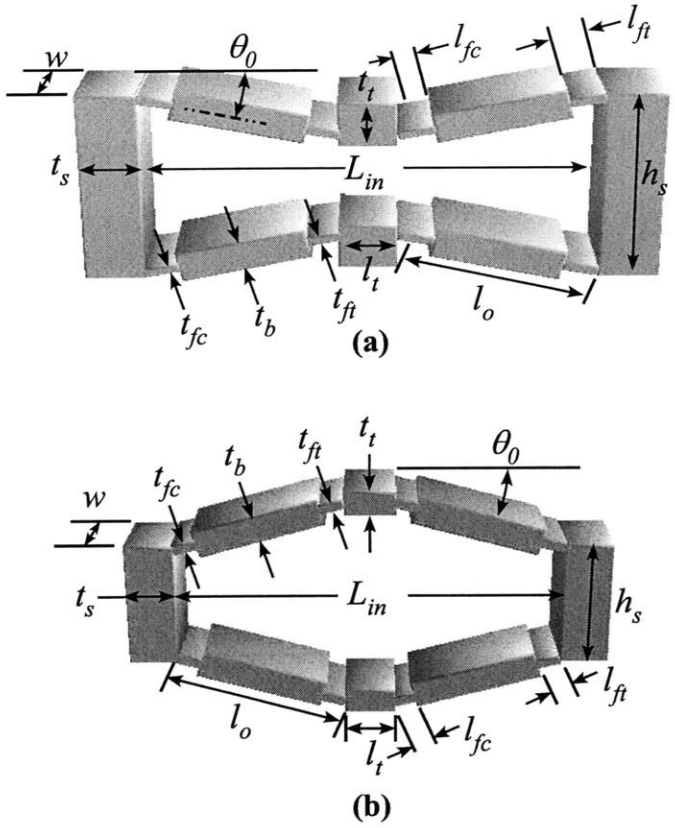

Figure 4-4: (a) Geometric parameters of a non-inverting flexure used for the first layer amplification. (b) Geometric parameters of an inverting flexure used for the second layer amplification.

$$U_{1,N} = 4\left(\int_0^{\frac{h_s}{2}} \frac{N(y)^2}{2Ewt_s}dy + \int_0^{l_{fc}} \frac{N(x')^2}{2Ewt_{fc}}dx' + \int_{l_{fc}}^{l_o-l_{ft}} \frac{N(x')^2}{2Ewt_b}dx' + \int_{l_o-l_{ft}}^{l_o} \frac{N(x')^2}{2Ewt_{ft}}dx' + \int_0^{\frac{l_t}{2}} \frac{N(x)^2}{2Ewt_t}dx\right) \tag{4.4}$$

and

$$U_{1,M} = 4\left(\int_0^{\frac{h_s}{2}} \frac{6M(y)^2}{Ewt_s^3}dy + \int_0^{l_{fc}} \frac{6M(x')^2}{Ewt_{fc}^3}dx' + \int_{l_{fc}}^{l_o-l_{ft}} \frac{6M(x')^2}{Ewt_b^3}dx' + \int_{l_o-l_{ft}}^{l_o} \frac{6M(x')^2}{Ewt_{ft}^3}dx' + \int_0^{\frac{l_t}{2}} \frac{6M(x)^2}{Ewt_t^3}dx\right). \tag{4.5}$$

The strain energy for the second layer U_2 can be computed analogously.

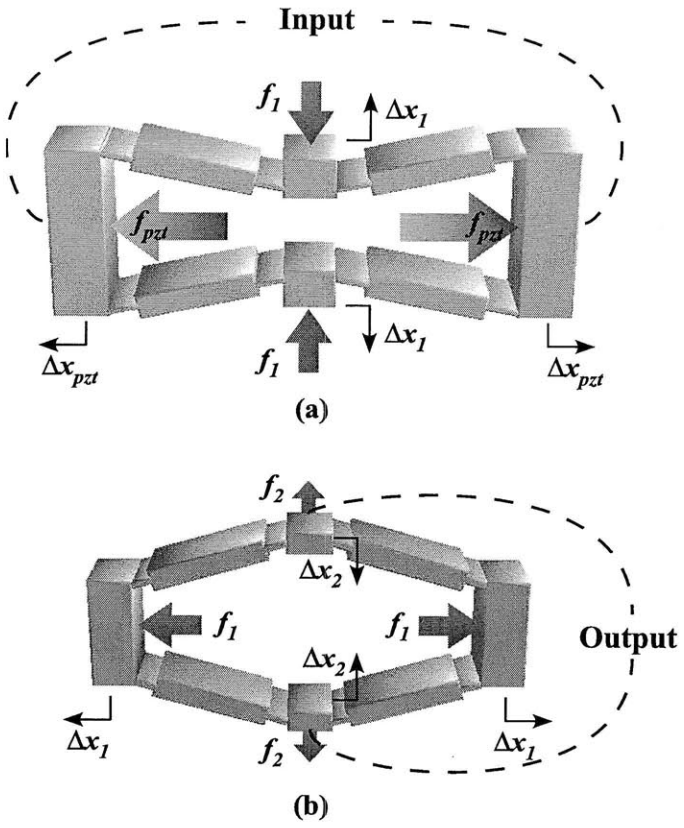

Figure 4-5: (a) External forces and displacements of a non-inverting flexure used for the first layer amplification. (b) External forces and displacement of an inverting flexure used for the second layer amplification.

To fully solve for the strain energy in an acceptable form, any unknown forces other than f_{pzt} and f_2 must be eliminated. For example, (4.2) through (4.5) involve the unknown internal moment M_b. This moment can be eliminated from the equations by applying Castigliano's second theorem [96]:

$$\frac{\partial U_1}{\partial M_b} = 0, \tag{4.6}$$

which states that there will be no angular deflection (although there will be linear deflection) where the moment occurs. Equation (4.6) can be used to eliminate M_b. Similarly, when examining the first and second layers as an assembled unit, the output of the first layer and the input of the second layer will have identical deflections, Δx_1, assuming a perfectly rigid point coupling. Thus, applying Castigliano's theorem yields

$$\begin{aligned} \Delta x_1 &= -\frac{\partial U_1}{\partial f_1} \\ &= \frac{\partial U_2}{\partial f_1}, \end{aligned} \tag{4.7}$$

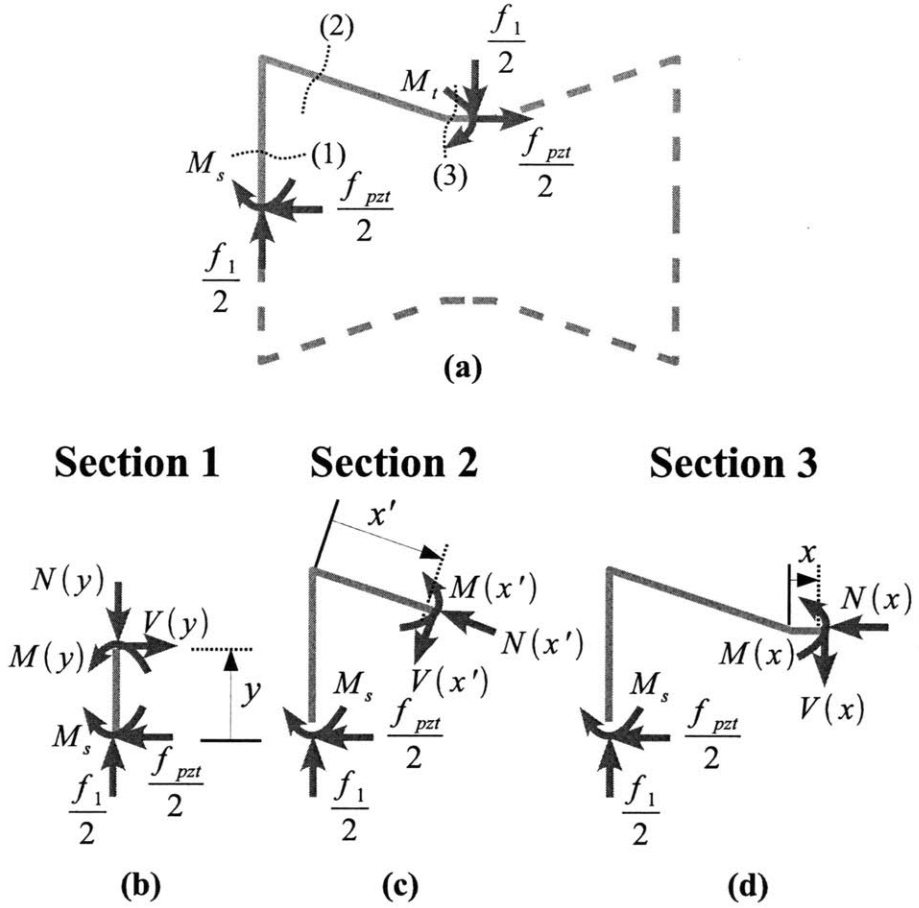

Figure 4-6: (a) Static quarter model of flexure mechanism showing three distinct sections for establishing internal forces. (b) Internal forces at section (1). (c) Internal forces at section (2). (d) Internal forces at section (3).

which allows the force f_1 to be eliminated from the strain energy expressions.

For compact subsequent formulation, the flexure design parameters enumerated in Table 4.3 for the first and second layer will be assembled into the vector $\mathbf{p}_f$. The total strain energy in the flexures, $U = U_1 + U_2$, may then be written as a general quadratic expression:

$$U = \frac{1}{2}\left(\chi_1(\mathbf{p_f}) f_{pzt}^2 + \chi_2(\mathbf{p_f}) f_2^2\right) + \chi_3(\mathbf{p_f}) f_{pzt} f_2. \tag{4.8}$$

where the functions χ_1, χ_2, and χ_3 are nonlinear algebraic functions of the flexure parameters. The above equation gives rise to a two port compliance model of the flexure: $\mathbf{x} = \mathbf{Cf}$, where $\mathbf{x}$ is vector of displacements at the input and output $[\Delta x_{pzt} \;\; \Delta x_2]^T$, $\mathbf{f}$ is the vector of forces at the input and output $[f_{pzt} \;\; f_2]^T$, and $\mathbf{C}$ is the compliance matrix

$$\mathbf{C} = \begin{pmatrix} \chi_1(\mathbf{p}_f) & \chi_3(\mathbf{p}_f) \\ \chi_3(\mathbf{p}_f) & \chi_2(\mathbf{p}_f) \end{pmatrix} \tag{4.9}$$

Additionally, neglecting hysteresis, the piezoelectric stacks obey the linear relationship

$$f_{pzt} = f_{pzt}^{block} - \left(\frac{f_{pzt}^{block}}{\Delta x_{pzt}^{free}} \right) \Delta x_{pzt}. \tag{4.10}$$

The remainder model derivation is similar to that found for the pseudo rigid body, or augmented kinematic model, found in Chapter 3. The stiffness matrix for the two port model is defined as $\mathbf{K} \triangleq \mathbf{C}^{-1}$ and, for convenience, the PZT parallel stiffness is defined as $k_{pzt,p} \triangleq \frac{f_{pzt}^{block}}{\Delta x_{pzt}^{free}}$. Now, using the usual notation for 2×2 matrix elements, the blocking force and free displacement expressions are found to be of the same form as (3.7) and (3.8):

$$f_2^{block}(\mathbf{p}_f) = \left(\frac{k_{12}(\mathbf{p}_f)}{k_{11}(\mathbf{p}_f) + k_{pzt,p}} \right) f_{pzt}^{block} \tag{4.11}$$

and

$$\Delta x_2^{free}(\mathbf{p}_f) = \left(\frac{-k_{12}(\mathbf{p}_f)}{\det(\mathbf{K}) + k_{pzt,p} k_{22}(\mathbf{p}_f)} \right) f_{pzt}^{block}. \tag{4.12}$$

Although (4.11) and (4.12) have the same functional form as discussed for the pseudo-rigid body model, the coefficients are much more algebraically complex and the model directly maps the true flexure design parameters $\mathbf{p}_f$ to the blocking force and free displacement. The closed form analytical expressions for blocking force and free displacement were obtained using the symbolic manipulation capabilities of Mathematica.

If it is required to find the specific operating point for the PZT stack(s), then the input stiffness of the assembled two layer mechanism can be computed at a given applied force f_2 at the cell output. The stack static equilibrium operating points for the two extreme cases of free displacement (zero force at the output) and blocked force are shown in Fig. 4-7. Fig. 4-7 illustrates that there will be a loss in free displacement performance due to parasitic stiffness k_{adm} acting in an admissible motion space. An example would be non-zero torsional stiffness of the flexure blades that deviates from pure revolute joints. On the other hand, there will be a deviation from ideal blocking force performance due to finite stiffness k_{con} acting in a constrained motion space. An example would be finite bending stiffness of the strut where the PZT stack force is applied. These performance deviations are clear justification for the foregoing detailed analytical model development. The corresponding parasitic stiffness values can be computed from

$$k_{adm} = \left. \frac{f_{pzt}}{\frac{\partial U}{\partial f_{pzt}}} \right|_{f_2=0} \tag{4.13}$$

and

$$k_{con} = \left. \frac{f_{pzt}}{\frac{\partial U}{\partial f_{pzt}}} \right|_{f_2 = f_2^{block}} . \tag{4.14}$$

Thus, the operating point in the force-displacement plane for free cell output conditions is

$$\left(\frac{f_{pzt}^{block}}{k_{adm} + k_{pzt,p}}, \frac{k_{adm}}{k_{adm} + k_{pzt,p}} f_{pzt}^{block} \right)$$

while the operating point for blocking force output conditions is

$$\left(\frac{f_{pzt}^{block}}{k_{con} + k_{pzt,p}}, \frac{k_{con}}{k_{con} + k_{pzt,p}} f_{pzt}^{block} \right)$$

As $k_{adm} \to 0$ and $k_{con} \to \infty$, these operating points move to their ideal extremes.

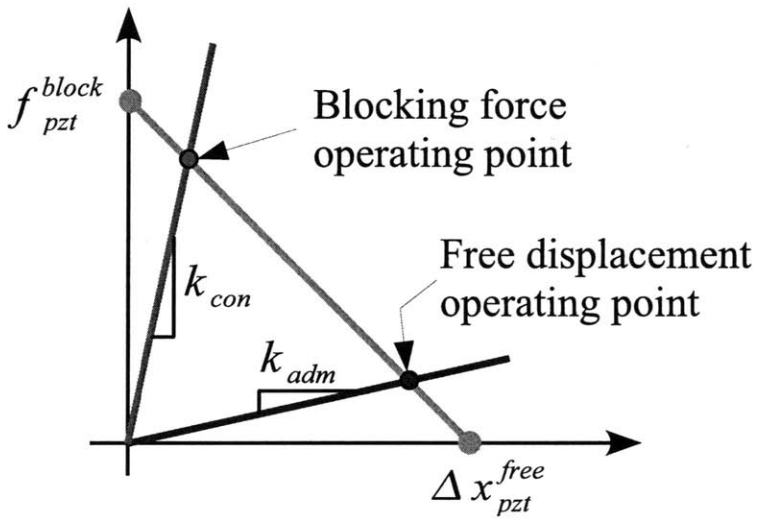

Figure 4-7: PZT stack operating points under different output boundary conditions.

Eq. (4.11) and (4.12) form the basis for the flexure design. In applying the model, a nominal set of flexure parameters $\mathbf{p}_{f,0}$ is selected based on previous approximate calculations with the ideal kinematic model and pseudo rigid body model as well as consideration of PZT stack geometry, mechanical assembly, and manufacturing constraints. Note that in the case of the second layer, the length l_0 is often insufficient to allow for $t_b > t_{fc}$ or $t_b > t_{ft}$ because the overall stiffness would be too high given the practical manufacturing constraints on the minimum flexure blade thicknesses. Thus, for the second layer flexures, $t_b = t_{fc} = t_{ft}$. Sensitivity analysis is then applied to tune the parameters appropriately to improve performance as much as possible.

4.4 Sensitivity Analysis

This section describes tuning of the nominal flexure parameters $\mathbf{p}_{f,0}$ using sensitivity analysis to achieve a second layer output strain that is as close as possible to 20% while maintaining a blocking force that is as large as possible. Although explicit optimization of a single performance metric is possible using the analytical model, sensitivity analysis is desirable because of the large number of parameters, complexity associated with the analytical expressions, numerous practical constraints on flexure parameters, and the desire to understand the design tradeoffs.

The sensitivity of blocking force (BF) and free displacement (FD) to a change in the i^{th} flexure parameter $p_{f,i}$ are readily obtained from the normalized partial derivatives

$$\phi_{i,BF} = \left(\frac{\partial f_2^{block}}{\partial p_{f,i}}\right)\left(\frac{p_{f,i}}{f_2^{block}}\right) \tag{4.15}$$

and

$$\phi_{i,FD} = \left(\frac{\partial \Delta x_2^{free}}{\partial p_{f,i}}\right)\left(\frac{p_{f,i}}{\Delta x_2^{free}}\right) \tag{4.16}$$

where $\phi_{i,BF}$ and $\phi_{i,FD}$ are the blocking force and free displacement sensitivity coefficients. In computing sensitivities, only the independent flexure parameters are considered. The dependent flexure parameters are the lengths l_0 and h_s for both the first and second layers. For the first layer,

$$l_o = \frac{L_{pzt} - l_t}{2\cos\theta_0} \tag{4.17}$$

and

$$h_s = n_{pzt}h_{pzt} + 2l_0\sin\theta_0 + c \tag{4.18}$$

where n_{pzt} is the number of PZT stacks used as an input to the first layer, h_{pzt} is the height of the stack within the plane of the first layer flexure, and c is a clearance between the stacks and the output of the first layer. Similarly, for the second layer, the constraints required that h_s be no less than the width w of the first layer flexure. Also, the oblique beam length of the second layer $l_{0,2}$ must satisfy:

$$l_{0,2} = \frac{h_{s,1} - 2l_{0,1}\sin\theta_{0,1} + 2t_{t,1} - l_{t,2}}{\cos\theta_{0,2}} \tag{4.19}$$

where the subscripted numbers indicate the associated layer for the parameter.

A typical plot from a sensitivity analysis is shown in Fig. 4-8. The top portion of Fig. 4-8 shows the ordered sensitivity coefficients for the free displacement of the assembled two layer cell. The first element of coefficient subscripts indicates the layer number to which the parameter belongs; the second part of each coefficient subscript is the parameter designation. The bottom portion of Fig. 4-8 shows the ordered sensitivity coefficients for the blocking force of the assembled two layer cell. For both blocking force and free displacement, the beam angles $\theta_{0,1}$ and $\theta_{0,2}$ have the most pro-

found effect on the performance. This illustrates that the idealized kinematic model is a meaningful starting point in predicting performance. Also, these beam angles have opposite effects on blocking force and free displacement. For a small increase in $\theta_{0,1}$ or $\theta_{0,2}$ from the nominal value, the free displacement will decrease, which is reflected in the negative value for the free displacement sensitivity coefficients. With regard to blocking force, a small increase in $\theta_{0,1}$ or $\theta_{0,2}$ from the nominal value leads to an increase in blocking force. This is also predicted by the idealized kinematic model. In addition to the beam angles, the other dominant parameters for this example include the thickness of the first layer strut, the width of the first layer, and the flexure blade thicknesses. The strut beam thickness t_s for the first layer is an example of a parameter that has a positive sensitivity coefficient for both free displacement and blocking force. Hence, when t_s increased for the first layer flexure, the performance will invariably improve. Through parameter adjustments such as these, the cell design refinement can be carried out quickly while satisfying manufacturing constraints, avoiding unrealistic geometries, and recognizing design tradeoffs.

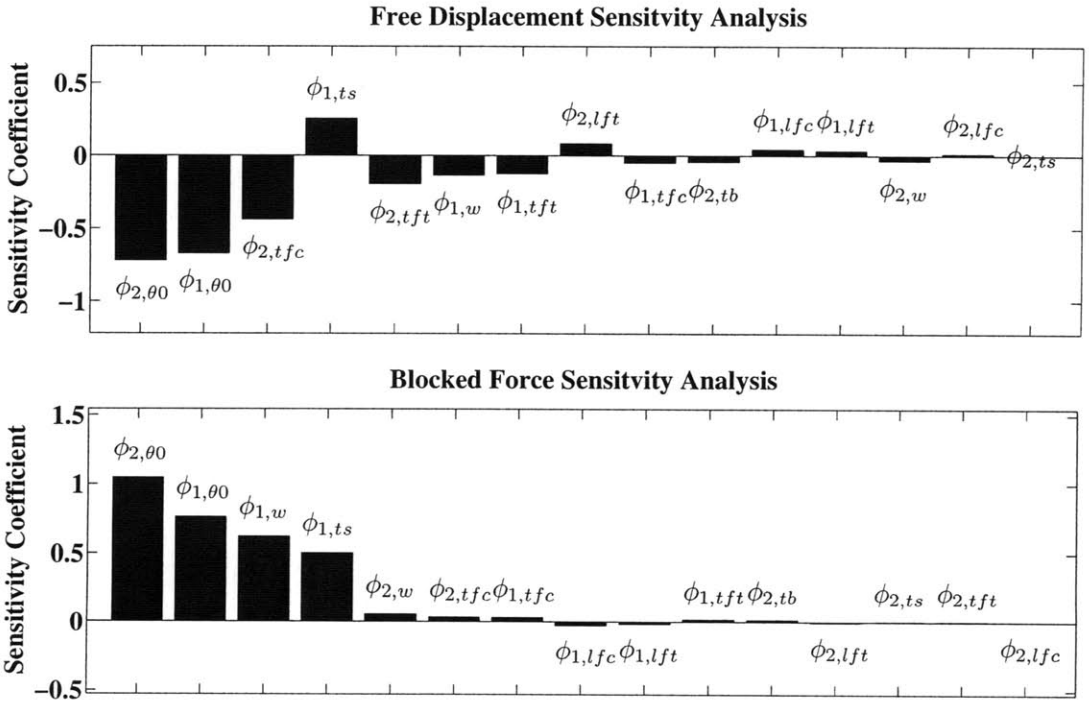

Figure 4-8: Representative sensitivity coefficient plot for free displacement (top) and blocking force (bottom).

4.5 Finite Element Analysis of Flexure Designs

This section provides a step-by-step methodology for analyzing the first and second layer cell assembly using a linear FEM analysis. The starting point for the analysis

is a solid model that has the geometry specified after several iterations of analytical model sensitivity analysis. All of the FEM computations are performed using the COSMOSWorks 2007.

Step 1: *Assign the appropriate material properties to the first and layer flexures.* For a majority of the flexures considered, the material of choice was plain carbon steel with the properties listed in Table 4.2.

Step 2: *Constrain the mechanism assembly and apply the appropriate boundary conditions.* Fig. 4-9 (a) shows the model setup. The specific setup shown in the figure represents a blocking force analysis wherein both ends of the second layer flexure output are spatially fixed. The two flexure layers are connected using a rigid coupling and the PZT force is applied along the inner surface of the first layer strut.

Step 3: *Create the finite element mesh.* A typical element mesh for the cell is shown in Fig. 4-9 (b). The FEM model was verified by checking solution convergence upon mesh size refinement.

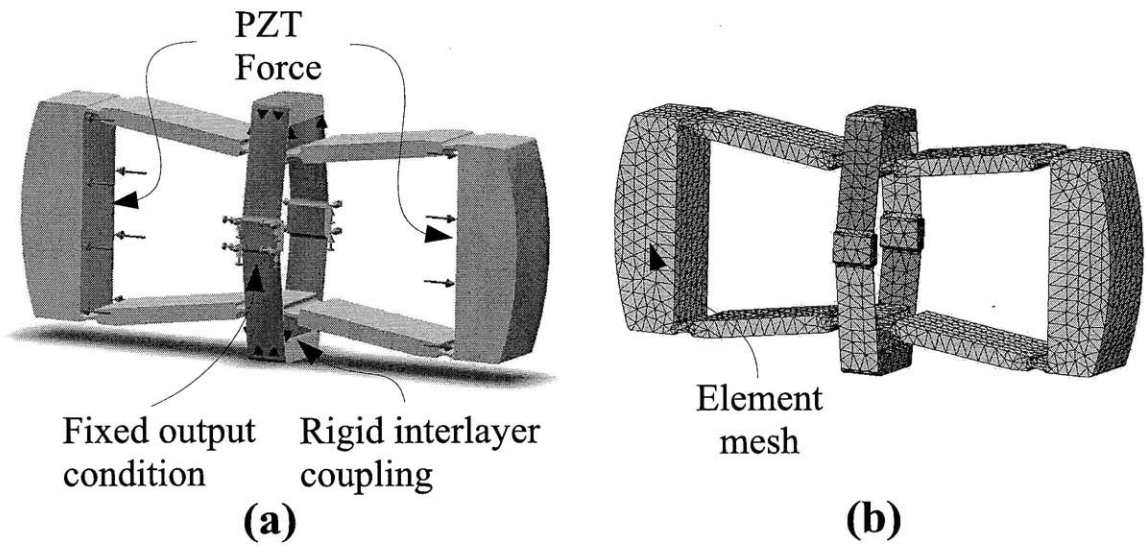

Figure 4-9: (a) Preliminary FEM model setup showing PZT force, boundary conditions, and interlayer coupling. (b) Meshed model for an assembled cell flexure system.

Step 4: *Apply a test load f_{test} and run an analysis to determine the input stiffness and PZT stack operating point.* The input stiffness under blocked conditions k_{con} or free conditions k_{adm} can be determined from the analysis by averaging the element node displacements at the center of the mechanism under the test load. This can be performed using the sensor function in COSMOS. The resulting input displacements measured at 6 sensors are shown in Fig. 4-10. These displacements can be averaged to obtain the overall input displacement Δx_{test} under the test load, which leads to an input stiffness estimate of

$$k_{in} = \frac{f_{test}}{\Delta x_{test}}, \tag{4.20}$$

where k_{in} represents k_{con} if the ends of the cell are blocked and it represents k_{adm} if the ends of the mechanism are free. The appropriate PZT stack input force consistent with the its operating characteristics is therefore

$$f_{pzt} = \frac{k_{in}}{k_{in} + k_{pzt,p}} f_{pzt}^{block}. \tag{4.21}$$

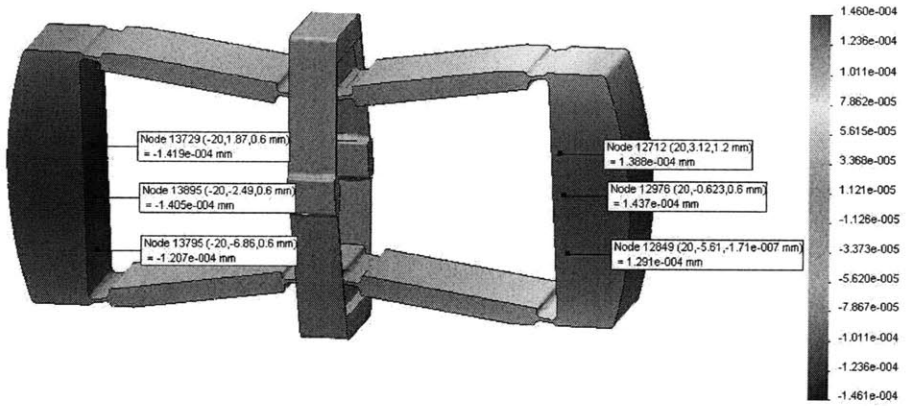

Figure 4-10: Test input displacements Δx_{test} at various locations where PZT stack test force f_{test} is applied.

Step 5: *Set the input force to be f_{pzt} as computed from Step 4.* The force in the model shown in Fig. 4-9 (a) is adjusted to be f_{pzt} computed from the previous step. The same mesh is then used for the subsequent analysis.

Step 6: *Run the model and record the results.* This final step will directly yield the blocking force or free displacement of the mechanism. In the case of a blocking force analysis, the result assessment is shown in Fig. 4-11. The results for a free displacement analysis are shown in Fig. 4-12. For the free displacement case, the cell displacement is concentrated in the second layer flexure while the first layer flexure is translating uniformly.

Step 7: *Assess the flexure stresses to check for yielding.* Based on a Von-Mises failure criterion for ductile materials, the safety factor is established throughout the flexures for both blocking force and free displacement conditions. A typical stress factor of safety distribution for a free displacement analysis is shown in Fig. 4-13. The free displacement end conditions represent a more severe state of stress and therefore is often the limiting case for design against yielding. As shown in Fig. 4-13, the safety factor is the lowest in the second layer flexure and can drop below unity slightly in a small localized region near the output of the mechanism. As discussed in Section 4.9, this location requires the most examination for both fatigue and static preload fractures.

Step 8: *Repeat steps 1 to 7 and re-assess parameter sensitivity.* Sensitivity analysis is performed using FEM to further refine the design. Each time a parameter is changed, steps 1 to 7 must be repeated. This process, although time consuming, is

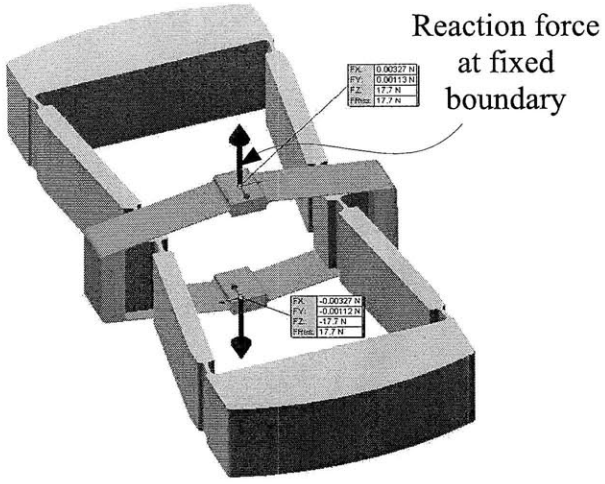

Figure 4-11: FEM blocking force results that show the generated reaction forces.

valuable in making final minor adjustments to the geometry that improve free displacement and blocking force performance. Upon completion, this step provides the final geometry required before assessing manufacturing and preload press fits for the PZT stacks.

4.6 Cell Manufacturing and Assembly

In the final stage of the design, the first layer flexure dimension L_{in} is adjusted so that an appropriate preload is applied to the stacks. The preload acts to reduce the effects of surface defects and provides a strong mechanical coupling between the PZT stacks and the flexure. Furthermore, a compressive preload stress up to approximately 25 MPa is also known to increase the effective coupling constant d_{33} for PZT materials [120]. To establish a compressive preload stress σ_{PL} in the stacks, the first layer flexure is designed to have an interference δ defined by

$$\delta \triangleq L_{pzt} - L_{in}. \tag{4.22}$$

This interference can be computed based on the open circuit stiffness of the piezoelectric stack $k_{pzt,oc}$ and the admissible motion space stiffness k_{adm} (i.e. the equivalent input stiffness under free output conditions for the cell):

$$\delta = \sigma_{PL} n_{pzt} h_{pzt} w_{pzt} \left(\frac{k_{adm} + k_{pzt,oc}}{k_{adm} k_{k_{in}}} \right) \tag{4.23}$$

The open circuit stiffness is a distinct quantity from the value $k_{pzt,p}$ because the value of $k_{pzt,p}$ is implicitly determined by the maximum voltage excitation applied to the stack. The interference δ is typically on the order of 100 μm, which is well within the

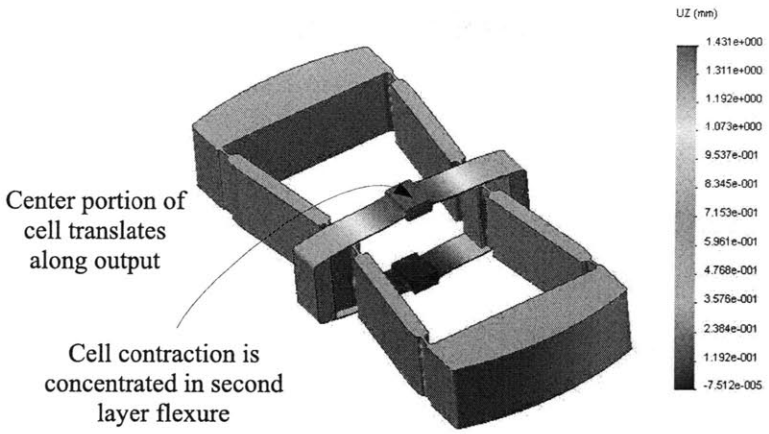

Figure 4-12: FEM free displacement results that show the generated reaction forces.

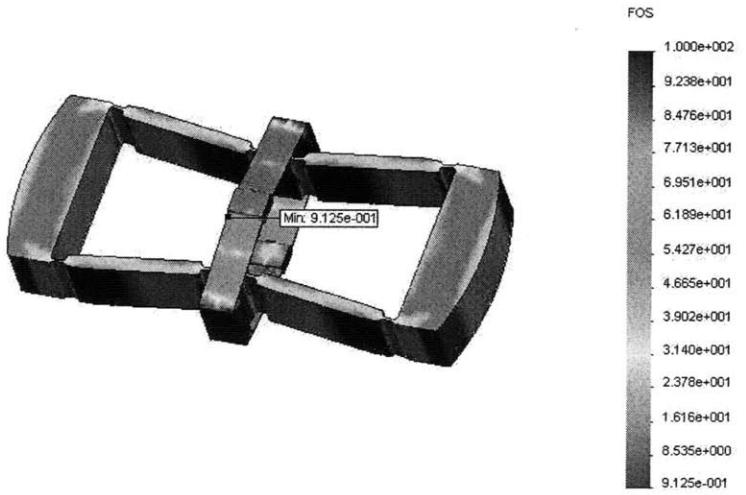

Figure 4-13: FEM factor of safety results for a typical free displacement analysis.

tolerances of the flexure manufacturing process. Hence, prior to manufacturing, the solid model first layer flexure dimension is adjusted to be $L_{in} = L_{pzt} - \delta$.

The primary manufacturing process for flexure fabrication is wire electrical discharge machining (EDM). A concise description of the process is available in [59]. This process was selected because it has high dimensional accuracy, produces a smooth surface finish, and avoids tapering of the thickness dimensions through the width that would be observed in water jet or laser cutting. Furthermore, EDM cutting does not load the material and therefore can produce flexures having feature thicknesses down to approximately 0.1 mm [59]. Once the first and second layer flexures have been machined, the cell assembly process is carried out as illustrated in Fig. 3-4. The next step in cell design is experimental performance validation.

4.7 Experimental Measurements of Static Performance

The final step in the design process is experimental validation of the cell designs. This section describes the associated experimental techniques for quantifying a cell's static metrics of free displacement, free strain, and blocking force. The experimental apparatus used for determining blocking force and free displacement is described followed by a discussion on the effects of cell preload.

The schematic representation of the experimental testing apparatus is shown in Fig. 4-14. The mechanical testing apparatus consists of a Mitutoyo micrometer-driven translational stage for imposing a desired displacement onto the cell. These displacements are constrained to provide only increases in the rest cell length so that no compressive forces are applied to the cell. The resulting imposed displacement is then measured manually using the micrometer and electronically using a Micro-Epsilon ILD-1401 laser displacement sensor. The imposed displacement also gives rise to a tensile force acting at the cell output points, which is then measured using a Transducer Techniques MLP-25 load cell. The load cell signal is the output voltage of a Wheatstone bridge, which is then conditioned using a custom designed instrumentation amplification circuit containing a 3rd order, 500 Hz cutoff, anti-aliasing, Butterworth low-pass filter. Although ideally rigid, the stage, load cell, and connection brackets form a finite parasitic stiffness that is lumped into the element k_{par}. The stiffness of the apparatus was estimated by connecting the load cell and the stage using a rigid metallic rod and measuring the resulting forces at various levels of displacement. The subsequent displacement measurements from the laser sensor Δx_{lds} were then modified using the load cell force signal f_{lc} to correct for the stiffness effect:

$$\Delta x'_{lds} = \Delta x_{lds} - \frac{f_{lc}}{k_{par}} \tag{4.24}$$

The final component of the apparatus shown in Fig. 4-14 is the piezoelectric amplifier. During the static evaluation tests, voltages were applied to the cell PZT stacks using a Cedrat CA-45 Amplifier. The signal data acquisition was performed at 1 kHz using the National Instruments PCI-6036E data acquisition card and a desktop PC running LabVIEW 8.

There are two separate experimental procedures required to obtain the static blocking force and free displacement. The procedure for obtaining blocking force was to apply the desired preload f_{pl} by adjusting the rigid stage and monitoring the load cell force output. Once the desired preload was set, the maximum voltage of $150V$ was then applied to the PZT stacks and the force rises to a peak force. The peak force from the load cell f_{max} was recorded and the estimate of blocking force $\hat{f}_{bf}$ at the preload level was then computed using

$$\hat{f}_{bf} = f_{max} - f_{pl}. \tag{4.25}$$

The experimental procedure for obtaining free displacement was to first set the desired preload as in the blocking force experiment. With the desired preload applied,

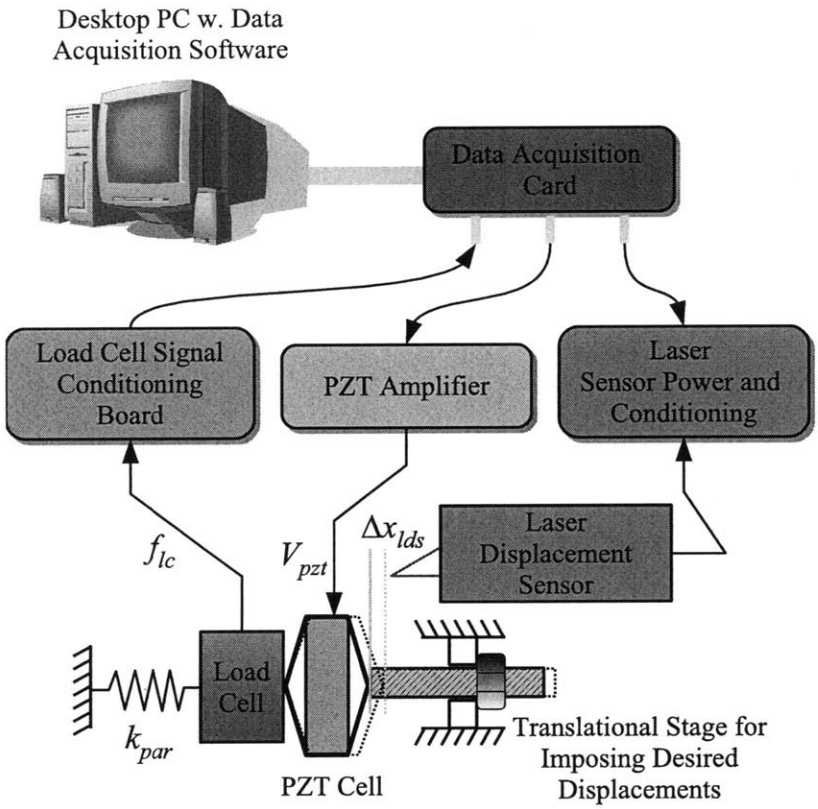

Figure 4-14: Schematic overview of test apparatus for assessing cell static performance.

the associated displacement was recorded as $\Delta x_{lds,1}$. The maximum voltage is then applied to the stacks, which causes the force to increase above the preload level. The displacement is adjusted until the force returns to the original preload level and the associated displacement is recorded as $\Delta x_{lds,2}$. The free displacement $\widehat{\Delta x}_{fd}$ is then estimated from

$$\widehat{\Delta x}_{fd} = |\Delta x_{lds,2} - \Delta x_{lds,1}| \,. \tag{4.26}$$

The primary effect of preload on the cell is to change the angle of the oblique beams as shown in Fig. 4-15. In practical applications, preload is required in order to avoid a serial connection of cells from going slack. A secondary effect of the cell preload is to provide a better mechanical coupling between the PZT stacks and the first layer. For increasing preload, the angle of the second layer flexure oblique beams also increases. This increased angle has the effect of decreasing free displacement and increasing blocking force over the modeling predictions. This effect is approximately linear of the range of preloads considered in the practical cell design. A schematic plot of free displacement versus preload is shown in Fig. 4-16 (a) with a plot of blocking force versus preload shown in Fig. 4-16 (b). The maximum preload applied to the cell, denoted by $f_{pl,max}$, is established based on maintaining a factor of safety of 2 with

respect to flexure yielding. The factor of safety is established using the static failure criterion discussed in Section 4.9. Data are gathered to estimate the curves shown in Fig. 4-16 (a) and (b). Each data set is fit with a line that may be extrapolated to zero preload. The median value of blocking force and free displacement from the linear fit is then taken as the final experimental cell blocking force f_2^{block} and cell free displacement Δx_2^{free}, respectively.

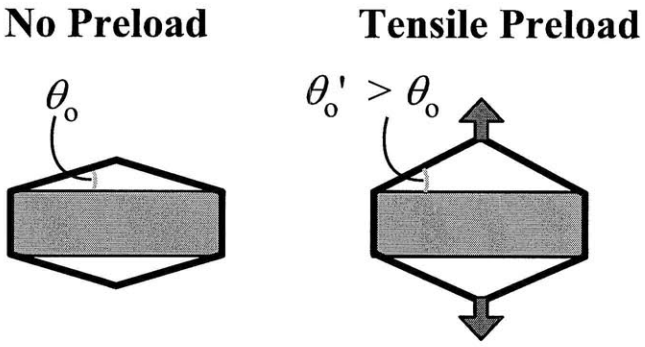

Figure 4-15: The effects of cell preload tension on oblique beam angle.

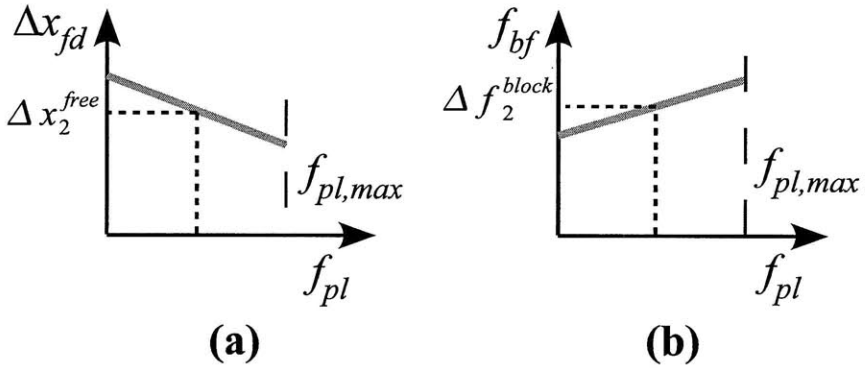

Figure 4-16: The effects of cell preload tension on blocking force and free displacement measurements.

The free displacement measurements can be used to estimate each cell's strain output under free end conditions. The strain is computed from (2.1), where ℓ_0 is taken as the resting distance between the output surfaces of the cell under zero preload. The following section provides the complete results for blocking force, free displacement, and strain for multiple cell prototypes.

4.8 Summary of Cell Designs

The procedure shown in Fig. 4-1 and described in the preceding sections was used to create multiple cell prototypes while the procedure in Fig. 4-14 was used to measure

their performance. The numbered prototypes are shown in Fig. 4-17 and are listed in order of increasing size. Each cell was designed to achieve a strain as close as possible to 20% while maintaining the largest possible blocking force for the chosen PZT stacks. The dimensioned drawings of each cell's flexure designs can be found in Appendix B. Table 4.4 lists the relevant performance and PZT stack information for each cell.

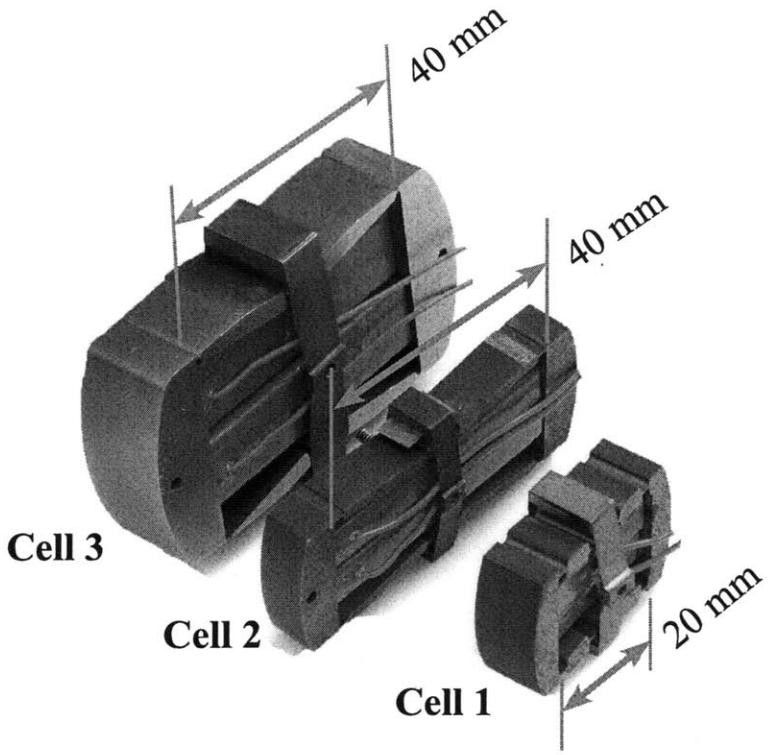

Figure 4-17: Three primary cell design prototypes listed in order of increasing size.

4.9 Failure Modes and Reliability Analysis

Reliability is a key quantitative metric of the an assembled actuator. As noted in Chapter 2, the reliability may be expressed as the integral of the reliability versus time, leading to the MTTF:

$$MTTF = \int_0^\infty R(t)dt. \tag{4.27}$$

which will be employed in this section to estimate mean failure times. This section will first examine individual cell static failure and then examine fatigue properties as they apply to the flexure based design. Using basic reliability theory, the mean failure times of both serial and antagonistic cellular assemblies is obtained. The following

discussion will focus primarily on a methodology for estimating mean failure times, but example numerical values will also be used.

4.9.1 Static Failure of a Single Cell

The cellular actuators are most often used with a tensile preload bias in order to eliminate slack in cell strands and to apply a preload to the piezoelectric stacks. Although useful in practical applications, the preload has the potential to cause fracture of the flexures as shown in Fig. 4-18. The figure shows a typical static failure of a single cell under tensile loading.

For a tensile load of f_{ext} applied to the cell having second layer beam angles of $\theta_{0,2}$, the maximum sustainable preload force (neglecting stress concentrations) is

$$f_{ext}^{max} = 2\sigma_y wt \sin\theta_{0,2} \tag{4.28}$$

where w is the width of the flexure, t is the flexure thickness, and σ_y is the yield strength of the flexure. As discussed in Chapter 4, the flexures are typically made from plain carbon steel having the approximate mechanical properties listed in Table 4.2. Using $\sigma_y = 305$ MPa, $t = 0.1$ mm, $w = 4$ mm, and $\theta_{0,2} = 8°$, the maximum preload force of a representative cell is approximately $f_{ext}^{max} = 34$ N. For a preload that greatly exceed the value computed from (4.28), static failure is extremely likely.

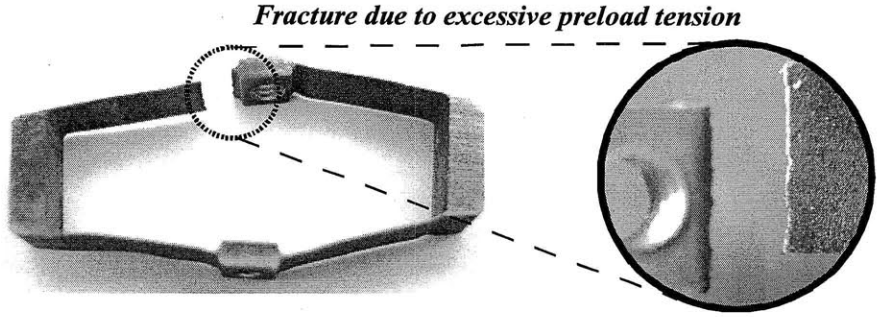

Figure 4-18: Fracture of the second layer flexure caused by excessive preload tension.

4.9.2 Fatigue Analysis

Another important factor in determining cellular assembly reliability is cell failure due to fatigue. In particular, the individual cell flexures are subject to cyclic stress that can lead to crack propagation and eventual failure of the second layer flexure. Although the first layer flexures are also subject to alternating stresses, these flexures involve larger beam thicknesses, leading to an extended fatigue life. Furthermore, all experimentally observed fatigue failures have occurred in the second layer flexure. In this subsection, simple probabilistic methods are applied to a fracture mechanics expression for crack propagation rate. The resulting expression for fatigue life provides a distribution of flexure lifetimes.

The assumed fatigue loading is shown in Fig. 4-19. Fig. 4-19 (a) shows the assumed sinusoidal nature of the loading. The applied force $f(t)$ has the form

$$f(t) = f_{ext} \sin(2\pi F_{cyc} t) \tag{4.29}$$

where f_{ext} is the amplitude of the applied force and F_{cyc} is the frequency of the loading in Hertz. Fig. 4-19 (b) shows the isolated flexure element that is subjected to the highest cyclic stress. This region of the flexure is also the site of all observed flexure failures. For model development, the cyclic stress amplitude is denoted by $\Delta\sigma$. The instantaneous crack length within the flexure is denoted by a where its initial value is a_i and final value is a_f. The final length of the crack is the length at which complete fracture occurs. This length will be given by

$$a_f = \min\left(t, \ \frac{1}{\pi}\left(\frac{K_{Ic}}{F\Delta\sigma_{max}}\right)^2\right) \tag{4.30}$$

where K_{Ic} is the critical plane strain fracture toughness of the flexure material, F is a geometric parameter that is near unity, and $\Delta\sigma_{max}$ is the maximum stress observed at the crack tip [34]. For all of the flexure designs considered in this thesis, the expression in (4.30) evaluates to the flexure thickness t.

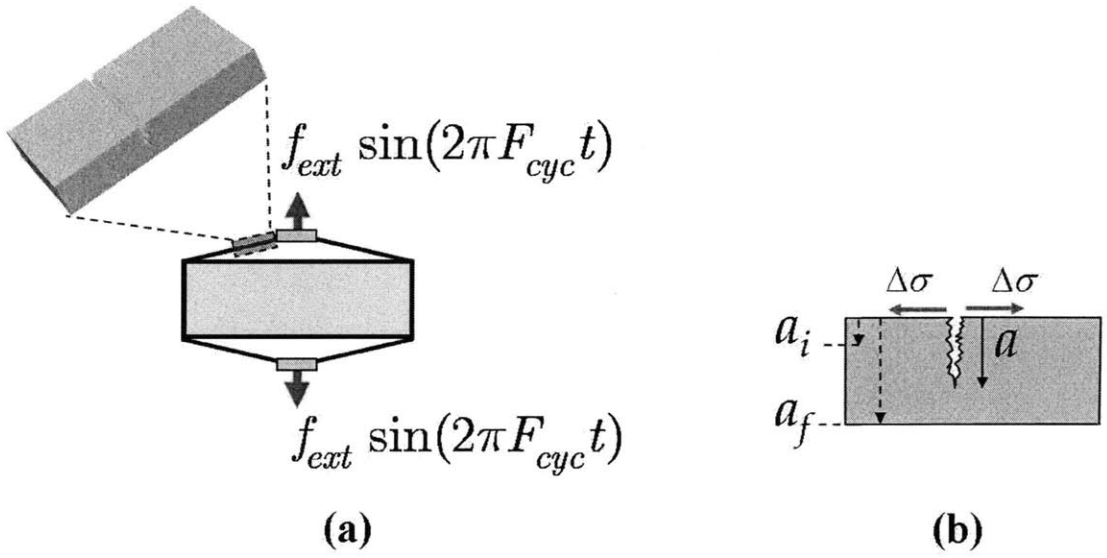

Figure 4-19: (a) Fatigue crack location for cells under cyclic loading, (b) Schematic of crack length and stress

To obtain a probabilistic model, the stress amplitude $\Delta\sigma$ is assumed to be constant over the flexure lifetime although stochastic in nature. For constant stress amplitude, the fatigue life may be obtained from the integration of the Paris Power Law [34]:

$$N_f = \frac{1}{\Delta\sigma^m}\left[\frac{a_f^{1-\frac{m}{2}} - a_i^{1-\frac{m}{2}}}{C(F\Delta\sigma\sqrt{\pi})^m\left(1-\frac{m}{2}\right)}\right] = \frac{C_F}{\Delta\sigma^m} \tag{4.31}$$

where m and C are empirically determined constants from the Paris Power Law and all other terms remain as previously defined. Apart from $\Delta\sigma$ all of the other parameters are assumed to be known and therefore lumped into the constant C_F.

An estimate of fatigue lifetime $\hat{T}_{life}$ is then given by

$$\hat{T}_{life} = \frac{\hat{N}_f}{\hat{F}_{cyc}} \tag{4.32}$$

where $\hat{N}_f$ is the estimate of the number of cycles to failure obtained from (4.31) and $\hat{F}_{cyc}$ is the frequency of operation, which is also stochastic in nature. Thus, $\hat{T}_{life}$ is a random variable whose distribution $\tau(t_{life})$ depends upon the distributions for N_f and F_{cyc}, which are denoted by $\nu(n_f)$ and $\phi(f_{cyc})$ respectively. Moreover, the distribution of N_f depends upon the distribution of stress amplitudes, which will be denoted by $s(\Delta\sigma)$. An *a priori* knowledge of the $s(\Delta\sigma)$ and $\phi(f_{cyc})$ distributions is assumed.

To determine the distribution $\nu(n_f)$, the following random variable transformation is used:

$$\nu(n_f) = s\left(\left(\frac{n_f}{C_F}\right)^m\right)\left|\frac{m}{C_F}\left(\frac{n_f}{C_F}\right)^{(m-1)}\right|. \tag{4.33}$$

Once $\nu(n_f)$ is obtain, the expression for the lifetime distribution is obtained from the following multivariate random variable transformation:

$$\begin{aligned}\tau(t_{life}) &= \int_0^\infty \nu(\xi)\phi\left(\frac{\xi}{t_{life}}\right)\det\begin{pmatrix}\frac{\partial n_f}{\partial t_{life}} & \frac{\partial n_f}{\partial \xi}\\ \frac{\partial f_{cyc}}{\partial t_{life}} & \frac{\partial f_{cyc}}{\partial \xi}\end{pmatrix}d\xi \\ &= \int_0^\infty \nu(\xi)\phi\left(\frac{\xi}{t_{life}}\right)\left(\frac{\xi}{t_{life}^2}\right)d\xi\end{aligned} \tag{4.34}$$

where ξ is a dummy variable of integration and $\nu(\cdot)$ and $\phi(\cdot)$ are assumed to have support on $[0,\infty)$.

For numerical evaluation, Weibull distributions are used for both $s(\Delta\sigma)$ and $\phi(f_{cyc})$. In particular, mean and standard deviations of the stress and frequency are set and the corresponding Weibull distribution parameters are then obtained using the appropriate inverse function in Matlab. Using nominal values for steel [34], the distributions shown in Fig. 4-20 were obtained. Fig. 4-20 (a) and (b) show the assumed stress and frequency distributions, while (c) and (d) show the resulting distributions for the number of cycles to failure and the overall lifetime in days. For this example, the mean lifetime, or MTTF, for the continuously operating cell is 33.6

days with a standard deviation of 14.4 days.

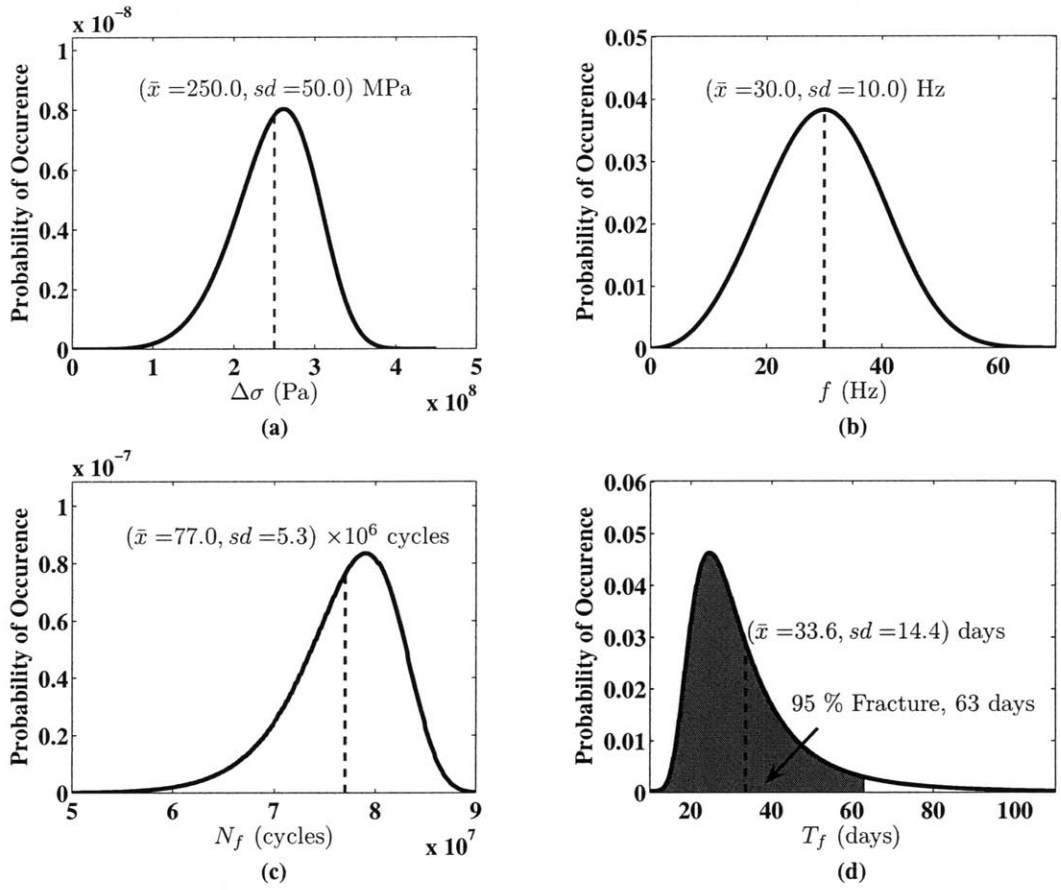

Figure 4-20: (a) Distribution of stress amplitudes applied at flexure crack sites, (b) Distribution of frequencies of cyclic loading, (c) Resulting distribution of the number of cycles to failure, (d) Resulting distribution of the lifetime.

4.9.3 Reliability and System MTTF

Based on the preceding analysis, there are two primary failure modes for an individual cell: static preload failures and fatigue failures. These two failure modes are linearly superposed to create the overall cell reliability map shown in Fig. 4-21. The two independent variable axes in Fig. 4-21 are the dimensionless ratios of cyclic operation time to mean cell failure time $\frac{t}{T_{f,mean}}$ and preload to maximum preload $\frac{f_{ext}}{f_{ext}^{max}}$. The third axis is the reliability expressed as a percentage. If the cell has not been used ($t = 0$) and the applied preload is zero ($f_{ext} = 0$), then the baseline reliability is taken to be r_0. In Fig. 4-21, a value of $r_0 = 90\%$ is used. Similarly, if the maximum preload is reached so that $\frac{f_{ext}}{f_{ext}^{max}} = 1$ or the mean cycle life is reached so that $\frac{t}{T_{f,mean}}$, then the reliability of the cell is assumed to be 0% and a failure would be imminent. Fig. 4-21 also shows an example cross-section slice for a constant preload ratio of 0.2.

For a constant preload, the reliability is then constant for $\frac{t}{T_{f,mean}} < 0.2$ and begins to decline linearly until fracture occurs from fatigue. Thus, the reliability of a single cell $r(t)$ is assumed to be the time function

$$r(t) = \begin{cases} r_0\left(1 - \frac{f_{ext}}{f_{ext}^{max}}\right) & \frac{t}{T_{f,mean}} < \frac{f_{ext}}{f_{ext}^{max}} \\ r_0\left(1 - \frac{t_{op}}{T_{f,mean}}\right) & \frac{t}{T_{f,mean}} \geq \frac{f_{ext}}{f_{ext}^{max}} \end{cases} \tag{4.35}$$

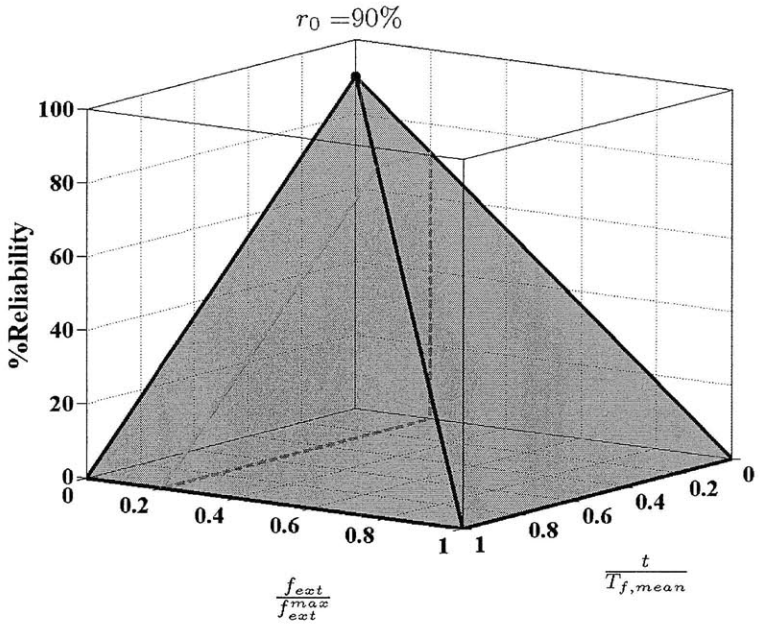

Figure 4-21: Model of a reliability surface for a single cell subject to preload and cyclic loading.

The analysis for single cells may now be extended to systems involving connections of multiple cells. Two particular connection topologies will be considered: series and antagonistic. These two topologies are shown in Fig. 4-22 (a) and (b) respectively. In the case of serially connected cells, a failure occurs when one of the N serially connected cells fractures. For the antagonistic connection in (b), failure occurs when one cell from each of the strands fractures. From reliability theory [30], the overall reliability $R_{tot}(t)$ for the serial connection of N identical cells can be obtained from

$$R_{tot}(t) = r(t)^N \tag{4.36}$$

while the reliability versus time for the antagonistic connection is given by

$$R_{tot}(t) = 1 - \left(1 - r(t)^N\right)^2. \tag{4.37}$$

Plots of the overall system reliability versus time for (4.36) and (4.37) are provided in Fig. 4-23(a) and (b) respectively. Values of N ranging from 1 to 5 are considered

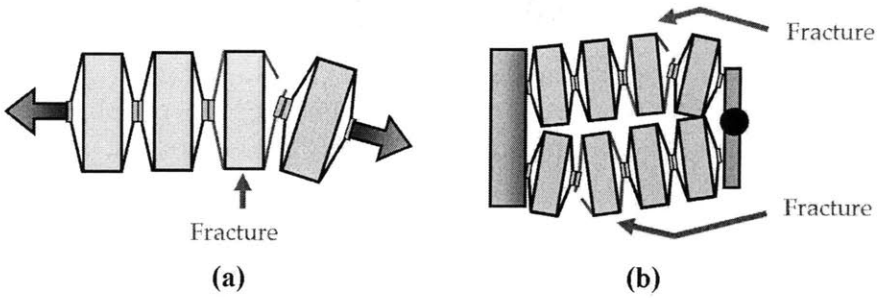

Figure 4-22: Reliability surface for a single cell subject to preload and cyclic loading.

at a preload level of 20%. These plots also indicate the MTTF as computed from (4.27). For the computation of MTTF, the single cell mean failure time at zero preload was taken to be $T_{f,mean} = 33.6$ days as computed in the example calculations of Section 4.9.2. In Fig. 4-23 (a), the serial connection has a reliability characteristic that reduces drastically for even two cells in series. With $N = 5$, the reliability of the system, even for short times, can be below 20%. By contrast, the antagonistic system reliability with $N = 2$ cells (i.e. four total active cells) has a higher reliability than the single preloaded cell in (a). Furthermore, as illustrated by the curve for $N = 1$, the reliability of antagonistic connections does not fall off as sharply as the case of serial connections. In general, to improve the reliability of the overall system, parallel or antagonistic arrangements are highly beneficial.

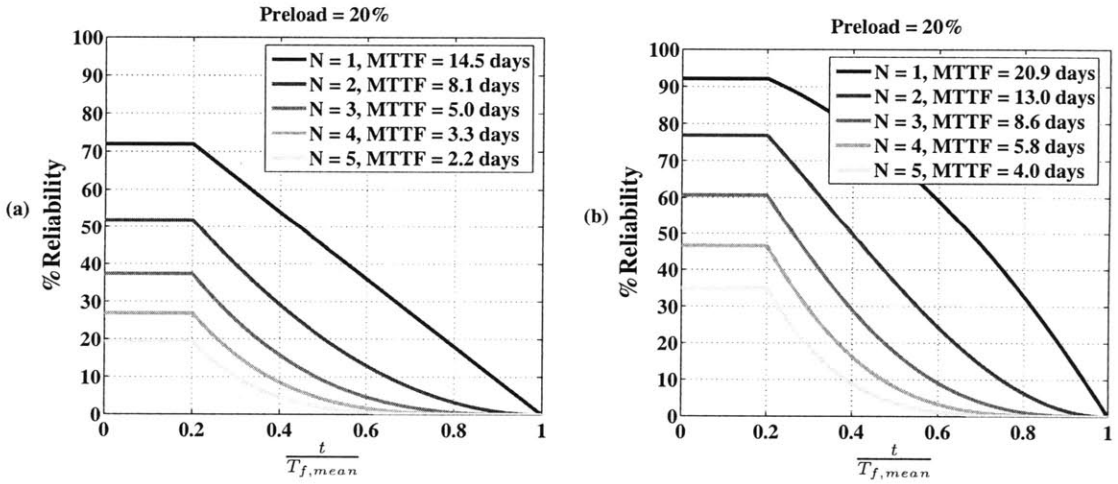

Figure 4-23: (a) Reliability versus time for a serial connection having $1 \leq N \leq 5$ (b) Reliability versus time for an antagonistic connection with each strand having $1 \leq N \leq 5$.

4.10 Non-Resonant Power Analysis

Basic power analysis is often needed in evaluating the amplifier requirements for a given cell connection topology. Although electromechanical coupling exists in the piezoelectric actuator, this coupling is most clearly manifested at system resonant frequencies. Below mechanical and electromechanical resonant frequencies, piezoelectric stack actuators can be modeled as a purely capacitive elements [7]. The electrical port behavior may include reflected stiffness from the mechanical domain, but is typically dominated by the piezoelectric capacitance. Although a more detailed electromechanical power analysis will be provided in Chapter 6, a basic analysis assuming purely capacitive behavior is provided here.

For a reactive element, such as a capacitor, subject to sinusoidal voltages, the apparent power S is equal to the reactive power Q and is given by the product of the RMS current into the element and RMS voltage across the element:

$$Q = V_{rms} I_{rms}. \tag{4.38}$$

The root mean square of a general sinusoid $y(t) = y_{max} \sin(\omega t)$ is computed from the integral

$$y_{rms} = \sqrt{\frac{1}{T_2 - T_1} \int_{T_1}^{T_2} (y_{max} \sin(\omega t))^2 dt} \tag{4.39}$$

where $T_2 - T_1$ is taken to be an integer number of periods, ω is the angular frequency of the signal and y_{max} is its amplitude. For a sine wave voltage input into a capacitance, both the RMS voltage and RMS current simplify to their maximum amplitudes divided by a factor of $\sqrt{2}$. The current into a capacitor with capacitance C may be more explicitly computed from the voltage amplitude divided by the capacitive impedance magnitude:

$$\begin{aligned} I_{max} &= \frac{V_{max}}{\frac{1}{C\omega}} \\ &= V_{max} C \omega \end{aligned} \tag{4.40}$$

Thus, applying (4.38) and (4.39), the reactive and apparent power into a capacitive element subject to a voltage $V_{max} \sin(\omega t)$ is

$$Q = \frac{1}{2} V_{max}^2 C \omega \tag{4.41}$$

or, replacing ω with $2\pi f$,

$$Q = \pi V_{max}^2 C f. \tag{4.42}$$

For most applications in this thesis, a serial strand of N cells is used with each cell wired electrically in parallel and driven with a single amplifier. If the capacitance of a single cell is denoted by C_{pzt}, then the equivalent capacitance is NC_{pzt}. If all of

the power transferred to the capacitance is returned to ground after each cycle, then for a sine wave voltage excitation, the required amplifier power is

$$P = N\pi V_{max}^2 C_{pzt} f. \tag{4.43}$$

Table 4.3: Flexure geometric parameter definitions.

Parameter	Definition
t_s	Thickness of the flexure input strut
t_t	Thickness of the top flexure output
t_{fc}	Thickness of the corner flexure blade
t_{ft}	Thickness of the top flexure blade
t_b	Thickness of the oblique beam
w	Width of the flexure
L_{in}	Length along the flexure input
h_s	Height of the flexure input strut
l_t	Length of the top flexure output
l_o	Length of the oblique beam
l_{fc}	Length of the corner flexure blade
l_{ft}	Length of the top flexure blade
θ_0	Oblique beam angle with respect to horizontal axis

Table 4.4: Summary of cell design specifications and performance.

Parameter	**Cell 1**	**Cell 2**	**Cell 3**
NEC Tokin PZT Stack Model	0505D20	0505D44H40	1010D44H40
Number of stacks, n_{pzt}	2	2	2
Width of stacks, w_{pzt} $[mm]$	5	5	10
Height of stacks, h_{pzt} $[mm]$	5	5	10
Length of stacks, L_{pzt} $[mm]$	20	40	40
Free disp. of stacks, Δx_{pzt}^{free} $[\mu m]$	21	42	42
Blocking force of single stack, f_{pzt}^{block} $[N]$	850	850	3500
Blocking force at $f_{pl} = 0$ $[N]$	7.09	10.70	23.46
Blocking force at $f_{pl} = \frac{f_{pl,max}}{2}$, f_2^{block} $[N]$	7.71	17.93	30.26
Blocking force at $f_{pl} = f_{pl,max}$ $[N]$	8.32	25.15	37.07
R^2 for linear fit $(n = 5)$	0.90	0.98	1.0
Free disp. at $f_{pl} = 0$ $[mm]$	0.57	1.33	1.81
Free disp. at $f_{pl} = \frac{f_{pl,max}}{2}$, Δx_2^{free} $[mm]$	0.45	1.09	1.44
Free disp. at $f_{pl} = f_{pl,max}$ $[mm]$	0.34	0.85	1.07
R^2 for linear fit $(n = 5)$	0.97	0.98	0.98
Maximum preload, $f_{pl,max}$ $[N]$	15	25	40
Output length, ℓ_0 $[mm]$	10.3	11.3	18.1
Free strain at $f_{pl} = 0$ $[\%]$	6	12	10

Chapter 5

Tunable Stiffness and Resonance in Cellular Assemblies

The previous chapters have focused on piezoelectric technology and design of individual cellular units. This chapter marks the transition into extended performance of the design as a result of cellular assemblies. Cellular assemblies can exhibit several interesting behaviors such as increased force through parallel connections, increased displacement through serial connections. Beyond this, however, is the ability to introduce additional design elements to each cell that enable the cellular actuators to exhibit tunable stiffness and tunable resonant frequencies.

In this chapter, tunable stiffness cells are introduced and their properties are then exploited using cellular assemblies. The particular assembly features of interest are the structural resonant frequencies. Models of the dynamic behavior reveal that stiffness and resonance can be tuned discretely and independently within a certain range. The upper and lower bounds of this tunability are established theoretically and proved rigorously. Both loaded and unloaded strands are considered and optimal activation selection criteria are provided. The remainder of the chapter describes the experimental validation of the theoretical concepts.

5.1 Introduction

Variable stiffness actuators have the capability to meet the increased demand for safety, robust locomotion, and dynamic manipulation. In robots interacting with humans, variable stiffness actuators allow maximum forces to be held to acceptable levels [91]. In mobile robots, joint compliance absorbs impulsive forces from the ground and allows a vehicle to better negotiate with rough terrain. Actuator compliance is also essential in manipulating objects in unstructured environments, where the properties of the manipulated object are not known *a priori*. Although feedback control is one way of varying task space stiffness [50], the bandwidth of the control loop is usually insufficient for rapid and highly dynamic physical interaction. Therefore, it is desirable to have variable mechanical compliance inherent in the actuator's physical construction.

Several groups have investigated both constant stiffness and variable stiffness actuators. In the early work on the elastic hand ([47],[48]), elastic elements were inserted

in an actuator drive train for stable grasping and dexterous manipulation. The seminal work of Pratt [86] demonstrated the advantages of constant series elasticity to increase shock tolerance, reduce reflected inertia, and improve force control. These concepts are still employed in current systems such as advanced protheses that utilize both series and parallel elasticity to enhance force bandwidth [10]. Although constant stiffness in a drive train is beneficial, additional advantages are obtained when the stiffness is allowed to vary. A majority of the work in variable stiffness actuators has been directed at developing new variable stiffness rotary joints. For example, in [24], the stiffness of a joint is varied by changing the overlapping area of two permanent magnets. In [91], a combined spring and belt drive system achieves variable stiffness. Contemporary designs using similar ideas were proposed by [106] and [10]. A theme among these actuator designs is the requirement of two actuators for a single degree-of-freedom. Moreover, the designs all employ standard electromechanical actuators: one actuator allows for stiffness tunability and another for angular motion.

Apart from variable stiffness actuators is the use of resonance in robotics. Resonance is a condition exhibited by linear (and weakly nonlinear) systems and is a manifestation of maximal potential and maximal kinetic energy oscillating 180° out of phase. For multi degree-of-freedom systems, this condition can occur at multiple frequencies. The frequencies where resonance occurs depend upon the distribution of mass and stiffness within the oscillatory system. In robotics, resonance has been recognized as an important phenomenon that can be used to increase power transmission to a load, reduce the effort of actuators, and achieve a large amplitude motion for cyclic tasks such as running (e.g. [88], [55]), flapping (e.g. [57],[115]), or fin-based swimming (e.g. [105]).

Variable stiffness and resonance can be intimately connected because the ability to vary actuator stiffness provides the ability to tune a robotic system's resonant frequencies. Indeed, some recent work has simulated tunable stiffness as a means for tuning resonant-like frequencies in multi-DOF manipulators [104]. Other work in actuator design has considered the constant resonant frequencies in certain material systems such as piezoelectric beam actuators [71] and electrostrictive polymers [63]. Because of the great importance of both variable stiffness and tunable resonance, there exists a need for an actuator that can provide both functions.

This chapter presents the design, analysis, and testing of a new linear artificial muscle actuator that incorporates both variable stiffness and tunable resonant frequencies by using a modular, cellular architecture. Artificial muscle actuator design is considered because of its importance to many areas of biorobotics that require smooth, natural motions that cannot be achieved with either linear or rotary electromechanical actuators. The basic principle of the actuator design is to connect a plurality of actuator cells in series or parallel (as in natural muscle) and then control stiffness and resonance by turning units ON to increase compliance and OFF to reduce compliance. The distribution of stiff versus compliant units within the actuator also determines the mass distribution and thereby allows the resonance properties to be tuned. The cellular architecture discussed in this chapter has been successfully applied by the authors' group (e.g. [60], [83]), and is extended here to include variable stiffness and resonance.

The early conference publications on this work ([93],[92]) had initial theoretical results and only limited experimental validation. This chapter presents the complete

theoretical analysis on tunable resonant frequencies, new experiments using an improved prototype, and new results from the application of the actuator to a single degree-of-freedom leg.

This chapter first presents the conceptual design and method for varying stiffness in a cellular actuator based on discrete, piezoelectric (PZT) actuator units. In the following section, the effect of distributed mass in the actuator is then taken into account, which leads to tunable resonant frequencies. The properties and ranges for tuning resonant frequencies are rigorously established using an idealized analytical model. For experimental comparison and design, the idealized model is extended to include realistic parasitic effects such as damping. Finally, the actuator is tested experimentally.

5.2 Variable Stiffness Cell Design

Fig. 5-1 shows a modification to the design in Fig. 3-5 to achieve variable stiffness. This prototype was designed using Cell 2 as discussed in Section 4.8 because this cell performs better than Cells 1 and 3 with respect to $\overline{SW}$ metric discussed in 3.5.3. Outside the second layer flexure is a rigid structure that limits the stroke of the output displacement in the Y direction (see Fig. 3-5). When the PZT is not activated, the output node of the second layer flexure rests on the stroke limiting beam. The output node movement is also limited when an excessive tensile force acts on the output node. As the applied PZT voltage increases, the output node is pulled inward and is detached from the stroke limiting beam.

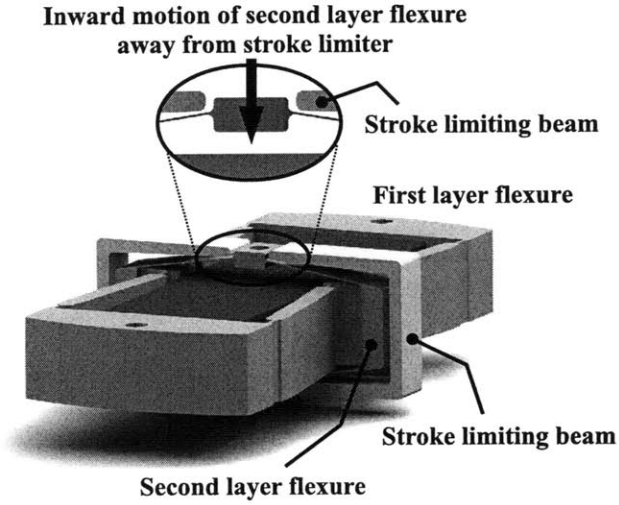

Figure 5-1: Design of a variable stiffness PZT-based cell. The system consists of two strain amplification layers. The second layer flexure incorporates a stroke limiting beam.

Fig. 5-2 shows the displacement versus compliance characteristics for a single cell and corresponding schematic representations of a cell at various points along the operating curve. In the schematic representations (a), (b), and (c), the outermost thin

lines indicate the stroke limiter, while the vertical thick line represents the output node of the flexure. The schematics show all of the stiffness within the cell lumped into a single element with a constant value k. Similarly, all of the mass of a cell is lumped into a single mass element m and damping effects are neglected to simplify the initial analysis.

As the PZT-induced force f_p increases, inward displacement also increases and the thick vertical line detaches from the limiter. For the ideal cell, the equivalent compliance seen at the output node is $1/k$. The nonlinearity in the actual compliance curve occurs because of the geometric nonlinearity of the flexure that becomes more pronounced as the cell contracts. The nonlinearity is often negligible during typical operation of the PZT-based system.

Note that it is also possible to design the stroke limiting system so that the stroke is limited only after the maximum contraction is achieved. This would provide a compliance characteristic that drops to zero upon achieving maximum contraction. Such a cell would be actively OFF and passively ON rather than actively ON and passively OFF. This chapter only consider cells that are actively ON and passively OFF. However, passively OFF cells will be examined in the next chapter.

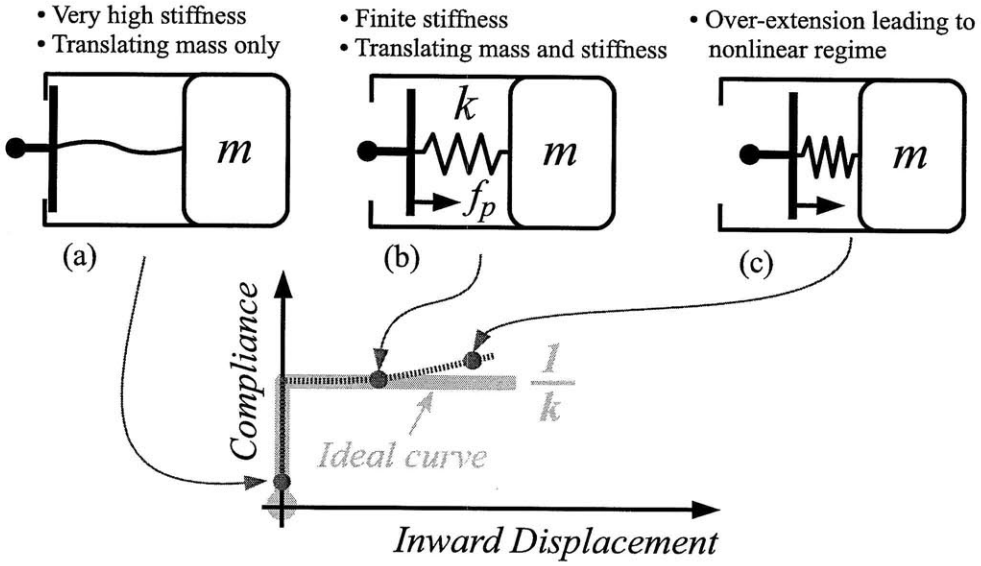

Figure 5-2: Compliance versus displacement characteristics and schematic representations for a variable stiffness, PZT-actuated cell. (a) Cell in the OFF state. (b) Cell in the ON state and linear regime. (c) Cell in the ON state and nonlinear regime.

5.3 Variable Stiffness Cellular Assemblies

The above cellular units can be connected in series, parallel, or antagonistic configurations, creating diverse stiffness characteristics as a collective sum. The most fundamental VSCA is a serial connection of N units. This arrangement is referred to as a strand. For simplicity, assume that the stiffness of an OFF state unit is infinitely large, while stiffness in the ON state is a constant k. If n units are ON and the others are OFF, then the resultant stiffness of an N-unit strand reduces to

$$k_S = \frac{k}{n} \quad 1 \leq n \leq N. \tag{5.1}$$

Next, consider a parallel arrangement of strands. As shown in Fig. 5-3 (a), N_p strands of N serially connected units may be arranged in parallel. If the i^{th} strand of serially connected units has stiffness $k_{S,i}$, the resultant stiffness of the entire system is given by

$$k_P = \sum_{i=1}^{N_p} k_{S,i}. \tag{5.2}$$

To accommodate the stiffness to a desired value, one can determine the number of parallel strands, N_p, and the number of ON units n_i in each strand of serial units.

The N_p strands can be divided into two sets of strands to form an agonist-antagonist arrangement as shown in Fig. 5-3 (b). Both the agonist and antagonist strands contribute to an output stiffness as a direct sum: $k_{out} = k_{P,ag} + k_{P,an}$. The antagonistic arrangement allows for varying stiffness independent of position, as in the case of natural skeletal muscles [49]. However, unlike skeletal muscles, the stiffness seen at the output of a VSCA will decrease as more cells are activated. Therefore, the limitation of the VSCA technique is that large displacements and large stiffness cannot be obtained simultaneously because many units must be in the ON (compliant) state to accommodate large displacements.

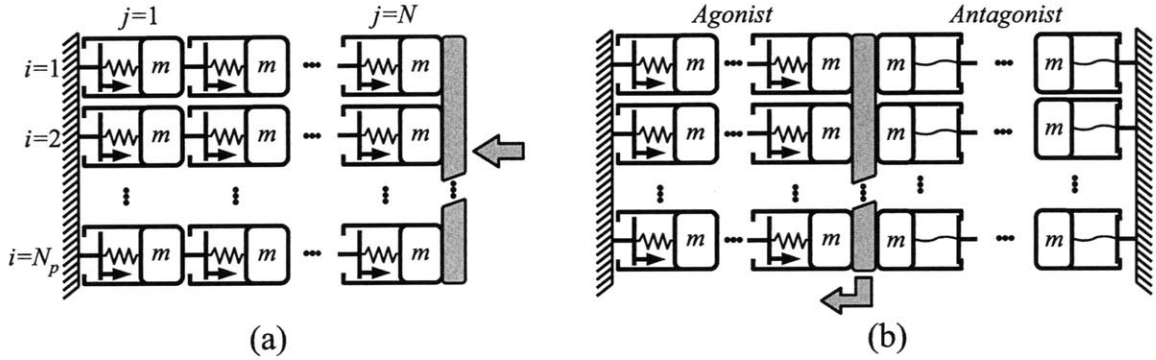

Figure 5-3: (a) Parallel arrangement of cellular units. Note that one end of the actuator is shown connected to ground only for clarity, but myriad other boundary conditions are possible. (b) Antagonistic pairing of actuator strands.

5.4 Tunable Resonance of Serial Strands

As demonstrated for varying stiffness, the resonant frequencies of a collection of cellular units can also be varied by exploiting the cellular architecture. The key behavior is that turning on a specific number of units to achieve a desired static stiffness still allows for numerous ON-OFF unit combinations, each of which exhibits different vibration modes with different resonant frequencies. Although the total number of

ON state units remains the same, the resonant frequencies may vary significantly depending upon the location of the ON units within the actuator.

To illustrate the basic concept, recall the simplified dynamic model shown in Fig. 5-2. Consider three of these units connected serially. Suppose that two out of the three units are turned ON so that the static stiffness of the serial connection is $k_S = k/2$. There are three unique ways of selecting two units to turn ON and they are shown in the upper portion of Fig. 5-4. Depending upon which two units are ON, the assembly dynamic behavior is different while the static behavior is the same.

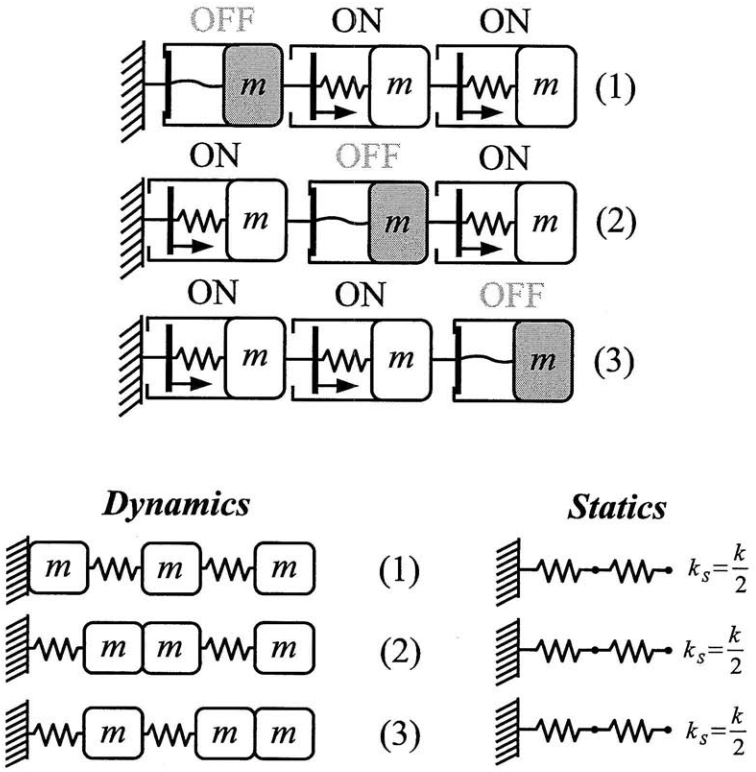

Figure 5-4: Comparison of static and dynamic behavior for all possible ON-OFF distributions for three serially connected units having two units activated.

Since all of the actuator configurations in Fig. 5-4 have two degrees of freedom, each configuration has two distinct vibration modes with distinct resonant frequencies. Table 5.1 shows the normalized resonant frequencies for each of the three ON-OFF states having $n = 2$. The second mode of configuration (1), OFF-ON-ON, provides the highest resonant frequency overall ($1.62\sqrt{k/m}$), while the lowest resonant frequency ($0.47\sqrt{k/m}$) occurs for the first mode of the ON-ON-OFF configuration. In each case, the OFF unit mass creates a different dynamic system and thereby changes the resonant frequencies.

Since all three cases have the same static stiffness k_S but different resonance properties, this example demonstrates that actuator stiffness and resonant frequencies can be changed independently. Although the resonant frequencies do not vary continuously, multiple choices are available for different task requirements and, as the

Table 5.1: First and second natural frequencies of each of the three configurations.

Configuration	$\frac{\omega_1}{\sqrt{k/m}}$	$\frac{\omega_2}{\sqrt{k/m}}$
1) OFF-ON-ON	0.62	1.62
2) ON-OFF-ON	0.54	1.31
3) ON-ON-OFF	0.47	1.51

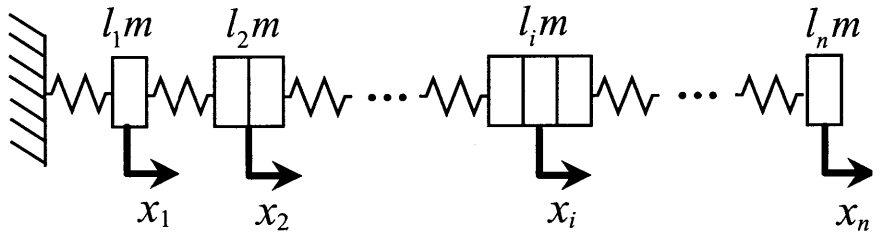

Figure 5-5: Idealized dynamic model for an N-unit strand of cells having n units activated.

number of cellular units increases, the number of possible stiffness levels and resonant frequencies also increases. The next subsection establishes the model for determining resonant frequency bounds of N serially connected units.

5.5 Theoretical Resonance Tuning Limits

5.5.1 Basic Model of Serial Connection Dynamics

Consider a single serially connected strand of N cellular units. Suppose that n units are in ON state so that n springs are detached from the stroke limiters. This creates an n degree-of-freedom system with each degree-of-freedom corresponding to a single lumped mass that moves independently along a single axis. This means that $(N-n)$ OFF-state units are rigidly connected to other units as illustrated in Fig 5-5. Let x_i be the position of the i^{th} combined masses and $\mathbf{x}$ be a vector collectively representing the n lumped mass displacements: $\mathbf{x} = [x_1, x_2, \ldots, x_n]^T$.

The i^{th} lumped mass consists of l_i cellular units with total mass of $l_i m$ with $l_i \in \mathbb{N}$. From Fig. 5-5, the equations of unforced motion are obtained as

$$l_i m\ddot{x}_i = -2kx_i + kx_{i-1} + kx_{i+1}, \quad 2 \leq i \leq n-1, \tag{5.3}$$

and for $i = 1$ and $i = n$,

$$l_1 m\ddot{x}_1 = -2kx_1 + kx_2, \quad l_n m\ddot{x}_n = -kx_n + kx_{n-1}. \tag{5.4}$$

These equations can be arranged into vector-matrix form:

$$\mathbf{M}\ddot{\mathbf{x}} + \mathbf{K}\mathbf{x} = \mathbf{0}, \tag{5.5}$$

where $\mathbf{M} = m \cdot diag(l_1, l_2, \ldots, l_n) \triangleq m\mathbf{L}$ and

$$\begin{aligned} \mathbf{K} &= k \begin{pmatrix} 2 & -1 & & 0 \\ -1 & 2 & \ddots & \\ & \ddots & 2 & -1 \\ 0 & & -1 & 1 \end{pmatrix} \\ &\triangleq k \cdot \mathbf{S}. \end{aligned} \tag{5.6}$$

One important assumption of the model is that the longitudinal vibrations in a strand are the dominant dynamic behavior for the actuator. This assumption will be addressed in the practical system through an application of preload tension as discussed in Section 5.9.

5.5.2 Maximum and Minimum Resonant Frequencies for a Specified Static Stiffness

The model developed in the previous subsection can now be utilized to determine how widely the resonant frequencies can be tuned while satisfying the static stiffness requirement, i.e. a specified number of ON units n. For the model in (5.5), the squared resonant frequencies of the n degree-of-freedom mass-spring system are given by the eigenvalues of matrix product $\mathbf{M}^{-1}\mathbf{K}$:

$$\omega_i^2 = \lambda_i(\mathbf{M}^{-1}\mathbf{K}) = \frac{k}{m}\lambda_i(\mathbf{L}^{-1}\mathbf{S}), \quad 1 \leq i \leq n. \tag{5.7}$$

The n eigenvalues of the matrix are ordered from the minimum to the maximum and written as

$$\lambda_{\min}(\mathbf{M}^{-1}\mathbf{K}) \leq \lambda_2(\mathbf{M}^{-1}\mathbf{K}) \leq \cdots \leq \lambda_{\max}(\mathbf{M}^{-1}\mathbf{K}). \tag{5.8}$$

For a fixed number of ON-state units n, the stiffness matrix, $\mathbf{K}$, remains the same regardless of the arrangement of ON-OFF units. The mass matrix, $\mathbf{M}$, on the other hand, varies depending on the ON-OFF arrangement within the strand. Therefore, the above $\lambda_{min}(\lambda_{max})$ can be further decreased (increased) by changing the ON-OFF unit configurations and thereby changing the mass matrix.

Given a specific static stiffness k_S, which will uniquely determine n, consider the set of all mass matrices associated with the possible distributions of N cells into n clusters of masses:

$$\mathfrak{M}_n = \left\{ \mathbf{M} = m \cdot diag(l_1, \ldots, l_n) \Big| \sum_{i=1}^{n} l_i = N - p, \right.$$
$$\left. p = 0, \ldots, N-n;\ l_i \in \mathbb{N} \right\},\quad n = 1, 2, \ldots, N. \tag{5.9}$$

The number of possible arrangements of n ON units within a strand is equivalent to the cardinality of $\mathfrak{M}_n$ and is $\binom{N}{n}$.

If the first p units are turned OFF, then they become fixed to the base structure and do not participate in the dynamics. With p units OFF at the base, the total number of ON units is then $(N-p)$ where p can take on values $1, 2, \ldots, (N-n)$. Thus, the subset of $\mathfrak{M}_n$ defined by $p = 0$ in (5.9) is the set of all possible mass matrices assuming that the first unit in the strand is in the ON state so that all cell masses are participating dynamically.

Let $\sigma_{\min}(n)$ be the minimum of the positive square root of $\lambda_{\min}(\mathbf{M}^{-1}\mathbf{K})$ with respect to all $\mathbf{M} \in \mathfrak{M}_n$:

$$\sigma^2_{\min}(n) = \min_{\mathbf{M} \in \mathfrak{M}_n} \lambda_{\min}(\mathbf{M}^{-1}\mathbf{K}). \tag{5.10}$$

$\sigma_{\min}(n)$ provides the lowest resonant frequency among all the ON-OFF unit distributions having n ON-state units.

Recall that minimum eigenvalue of $\mathbf{M}^{-1}\mathbf{K}$ is given by the minimum of the Rayleigh quotient:

$$\lambda_{\min}(\mathbf{M}^{-1}\mathbf{K}) = \min_{\mathbf{x} \in \mathbb{R}^n} \frac{\mathbf{x}^T\mathbf{K}\mathbf{x}}{\mathbf{x}^T\mathbf{M}\mathbf{x}}. \tag{5.11}$$

Similarly, the highest resonant frequency is given by

$$\begin{aligned} \sigma^2_{\max}(n) &= \max_{\mathbf{M} \in \mathfrak{M}_n} \lambda_{\max}(\mathbf{M}^{-1}\mathbf{K}) \\ &= \max_{\mathbf{M} \in \mathfrak{M}_n} \left(\max_{\mathbf{x} \in \mathbb{R}^n} \frac{\mathbf{x}^T\mathbf{K}\mathbf{x}}{\mathbf{x}^T\mathbf{M}\mathbf{x}} \right). \end{aligned} \tag{5.12}$$

Using (5.12), one can prove the following proposition concerning the highest resonant frequency $\sigma_{\max}(n)$ and the ON-OFF unit distribution that provides $\sigma_{\max}(n)$.

Proposition 1:
Let $\mathbf{M} = m\mathbf{L}$ *and* $\mathbf{K} = k\mathbf{S}$ *be, respectively, the* $n \times n$ *mass and stiffness matrices of* N *serially-connected cellular units among which* n *units are active (turned ON). The highest resonant frequency occurs when the first* $N - n$ *units are turned OFF. This maximum frequency is given by*

$$\sigma_{\max}(n) = \sqrt{\frac{k}{m}\lambda_{\max}(\mathbf{S})}. \tag{5.13}$$

Proof:
Since $\mathbf{x}^T\mathbf{M}\mathbf{x} \geq m\mathbf{x}^T\mathbf{I}\mathbf{x}\ \forall \mathbf{M} \in \mathfrak{M}_n$ and $\forall \mathbf{x} \in \mathbb{R}^n$

$$\begin{aligned}\lambda_{\max}(\mathbf{M}^{-1}\mathbf{K}) &= \max_{\mathbf{x}\in\mathbb{R}^n} \frac{\mathbf{x}^T\mathbf{K}\mathbf{x}}{\mathbf{x}^T\mathbf{M}\mathbf{x}} \\ &\leq \max_{\mathbf{x}\in\mathbb{R}^n} \frac{k\mathbf{x}^T\mathbf{S}\mathbf{x}}{m\,\mathbf{x}^T\mathbf{I}\mathbf{x}} \\ &= \frac{k}{m}\lambda_{\max}(\mathbf{S}).\end{aligned}$$

Therefore,

$$\arg\max_{\mathbf{M}\in\,\mathfrak{M}_n} \lambda_{\max}(\mathbf{M}^{-1}\mathbf{K}) = diag(m, m, \ldots, m).$$

Hence, the arrangement where the first $(N-n)$ units are turned OFF (i.e. $p = (N-n)$ in (5.9)) yields $\sigma_{\max}(n)$. ■

To address the lowest possible resonant frequency configuration, first consider the following two lemmas:

Lemma 1:

The fundamental mode of a fix-free vibrating system as shown in Fig. 5-5 has nodal displacements that satisfy $0 \leq x_1 \leq x_2 \leq \ldots \leq x_n$.

Lemma 2:

Consider the scalar function defined by

$$J(l_1, l_2, \ldots, l_n) \triangleq \mathbf{x}^T diag(l_1, l_2, \ldots, l_n)\mathbf{x}, \tag{5.14}$$

where the l_i *satisfy the conditions in (5.9) and the vector* $\mathbf{x}$ *has elements that are monotonically increasing*

$$0 \leq x_1 \leq x_2 \leq \ldots \leq x_n. \tag{5.15}$$

The scalar function J *is maximized when* $l_1 = 1, l_2 = 1, \ldots, l_{n-1} = 1, l_n = N-n+1$.

A proof of Lemma 1 can be found in [42] while a proof of Lemma 2 is given in the appendix; both may be used in the following proposition for $\sigma_{\min}(n)$.

Proposition 2:

The arrangement having all the inactive units placed at the unconstrained end of the serial connection gives the lowest un-damped resonant frequency $\sigma_{\min}(n)$.

Proof:

By Lemma 1, the first mode shape can be considered positive and monotonically increasing. Therefore,

$$\begin{aligned}\min_{\mathbf{M}\in\mathfrak{M}_n} \frac{k\mathbf{x}^T\mathbf{S}\mathbf{x}}{\mathbf{x}^T\mathbf{M}\mathbf{x}} &= \min_{\substack{\mathbf{M}\in\mathfrak{M}_n \\ 0\leq x_1\leq\cdots\leq x_n}} \frac{k\mathbf{x}^T\mathbf{S}\mathbf{x}}{\mathbf{x}^T\mathbf{M}\mathbf{x}} \\ &= \min_{0\leq x_1\leq\cdots\leq x_n} \frac{k\mathbf{x}^T\mathbf{S}\mathbf{x}}{\mathbf{x}^T\mathbf{M}_0\mathbf{x}},\end{aligned}$$

where $\mathbf{M}_0 \triangleq m \cdot diag(1, 1, \ldots, N-n+1)$ by Lemma 2. This represents the case where all of the inactive units are placed at the unconstrained end. ■

In many practical situations, the first (i.e. fundamental) mode is the most readily excited. Therefore, to establish a range for the fundamental frequency tunability, the highest value for the first resonant frequency will be given the notation $\sigma_{\text{max,first}}(n)$ and defined as

$$\begin{aligned} \sigma^2_{\text{max,first}}(n) &= \max_{\mathbf{M}\in\mathfrak{M}_n} \lambda_{\min}(\mathbf{M}^{-1}\mathbf{K}) \\ &= \max_{\mathbf{M}\in\mathfrak{M}_n} \left(\min_{\mathbf{x}\in\mathbb{R}^n} \frac{\mathbf{x}^T\mathbf{K}\mathbf{x}}{\mathbf{x}^T\mathbf{M}\mathbf{x}} \right). \end{aligned} \tag{5.16}$$

Corollary to Proposition 2:
The arrangement having the first $(N-n)$ units turned OFF gives the highest possible value for the first un-damped resonant frequency $\sigma_{\text{max,first}}(n)$.

Proof:
The proof follows from the proof of Proposition 1 since $\forall \mathbf{M} \in \mathfrak{M}_n$ and $\forall \mathbf{x} \in \mathbb{R}^n$, $\mathbf{x}^T\mathbf{M}\mathbf{x} \geq m\mathbf{x}^T\mathbf{I}\mathbf{x}$. Hence,

$$\begin{aligned} \lambda_{\min}(\mathbf{M}^{-1}\mathbf{K}) &= \min_{\mathbf{x}\in\mathbb{R}^n} \frac{\mathbf{x}^T\mathbf{K}\mathbf{x}}{\mathbf{x}^T\mathbf{M}\mathbf{x}} \\ &\leq \min_{\mathbf{x}\in\mathbb{R}^n} \frac{k\mathbf{x}^T\mathbf{S}\mathbf{x}}{m\,\mathbf{x}^T\mathbf{I}\mathbf{x}} \\ &= \frac{k}{m}\lambda_{\min}(\mathbf{S}). \end{aligned}$$

Therefore, the same configuration as Proposition 1 gives the highest resonant frequency of the first mode. ■

5.5.3 Global Maximum and Minimum Resonant Frequencies

The above analysis provides the highest and lowest resonant frequencies for a fixed n, i.e. a given static stiffness. If instead the synthesis objective is to achieve the highest or the lowest resonant frequency regardless of the static stiffness, then the highest and lowest bounds can be further extended by considering all possible values of n varying from 1 to N.

The global minimum $\Sigma_{\min}(N)$ is then defined with an additional minimization over n:

$$\begin{aligned} \Sigma^2_{\min}(N) &= \min_{1\leq n\leq N} \left\{ \min_{\mathbf{M}\in\mathfrak{M}_n} \left\{ \lambda_{\min}(\mathbf{M}^{-1}\mathbf{K}) \right\} \right\} \\ &= \min_{1\leq n\leq N} \left\{ \sigma^2_{\min}(n) \right\}. \end{aligned} \tag{5.17}$$

A similar expression is obtained for the global maximum $\Sigma_{\max}(N)$. For the maximum, the following definition and lemma are required.

Definition:
For the eigenvalue problem

$$\mathbf{K}\mathbf{x} = \lambda\mathbf{M}\mathbf{x} \tag{5.18}$$

with $\mathbf{M}, \mathbf{K} \in \mathbb{R}^{N\times N}$, the associated r^{th} reduced eigenvalue problem is

$$\mathbf{K}^{(r)}\mathbf{x}^{(r)} = \lambda^{(r)}\mathbf{M}^{(r)}\mathbf{x}^{(r)},\ r = 0,\ 1,\ \ldots,\ N-1, \tag{5.19}$$

where $\mathbf{M}^{(r)}$ and $\mathbf{K}^{(r)}$ are obtained by deleting the first r rows and first r columns in $\mathbf{M}$ and $\mathbf{K}$ respectively.

Lemma 3:
The eigenvalues of the r^{th} reduced eigenvalue problem $\lambda_i^{(r)}$, $i = 1,\ 2,\ \ldots,\ (N-r)$ and the eigenvalues of the $(r+1)^{st}$ reduced eigenvalue problem $\lambda_j^{(r+1)}$, $j = 1,\ 2,\ \ldots,\ (N-r-1)$ satisfy the following relation

$$\begin{aligned}\lambda_1^{(r)} \le \lambda_1^{(r+1)} \le \lambda_2^{(r)} \le \lambda_2^{(r+1)} \le \ldots \\ \le \lambda_{N-r-1}^{(r)} \le \lambda_{N-r-1}^{(r+1)} \le \lambda_{N-r}^{(r)}.\end{aligned} \tag{5.20}$$

Lemma 3 can be proved using the technique found in [13], while a proof for the more general case of Jacobi matrices can be found in [41]. Now the following proposition may be proved.

Proposition 3:
A serial strand of N units takes the globally maximum resonant frequency $\Sigma_{\max}(N)$ at a configuration where all the N units are turned ON.

Proof:
From Proposition 1, the maximum resonant frequency for a given n, $\sigma_{\max}(n)$, occurs when the first $(N-n)$ units are turned OFF, i.e. fixed to the base structure. The associated mass matrix is given by deleting the first $(N-n)$ rows and the first $(N-n)$ columns of the $N \times N$ identity matrix multiplied by m: $m\mathbf{I}_N$. The stiffness matrix is similarly obtained by deleting the first $(N-n)$ rows and the first $(N-n)$ columns of the $N \times N$ stiffness matrix given in (5.6). Therefore, the global maximum of the resonant frequency can be found by comparing the largest eigenvalues of all the reduced eigenvalue problems in (5.19) with $r = 1,\ 2,\ \ldots,\ N-1$.

Setting $r = N-1$ in Lemma 3 gives $\lambda_1^{(N-1)} \le \lambda_2^{(N-2)}$. Repeatedly applying Lemma 3 for $r = N-2,\ N-3,\ \ldots,\ 1$ yields

$$\lambda_1^{(N-1)} \le \lambda_2^{(N-2)} \le \ldots \le \lambda_{N-1}^{(1)} \le \lambda_N^{(0)}. \tag{5.21}$$

The final eigenvalue in (5.21), $\lambda_N^{(0)}$, is the maximum eigenvalue of $\mathbf{M}^{-1}\mathbf{K}$ for the original $N \times N$ matrices $\mathbf{K} = k\mathbf{S}$ and $\mathbf{M} = m\mathbf{I}_N$. Therefore,

$$\begin{aligned}
\Sigma^2_{max}(N) &= \lambda_{\max}\left[(m\mathbf{I}_N)^{-1}\mathbf{K}\right] \\
&= \frac{k}{m}\lambda_{\max}(\mathbf{S}) \\
&= \lambda_N^{(0)} \\
&\geq \lambda_{N-r}^{(r)}, \quad r = 1, 2, \ldots, N
\end{aligned} \tag{5.22}$$

which concludes the proof. ■

Corollary to Proposition 3:

As N increases, the globally maximum resonant frequency of an N unit strand increases monotonically:

$$\Sigma_{\max}(N) \leq \Sigma_{\max}(N+1). \tag{5.23}$$

Proof:

Considering $\mathbf{M}$ and $\mathbf{K}$ of sufficiently large dimension and applying Lemma 3 immediately proves the corollary. ■

To obtain the global minimum $\Sigma_{\min}(N)$, recall Proposition 2. The lowest resonant frequency for a given n occurs when the last $(N-n)$ units are turned OFF, i.e. creating a lumped mass of $m(N-n+1)$ at the free end. Therefore, the question is how many units must be lumped together at the free end to minimize the resonant frequency. This can be solved by comparing the lowest eigenvalue of a strand with $(N-n)$ OFF units at the free end to the case with $(N-n-1)$ OFF units. This situation is depicted in Fig. 5-6.

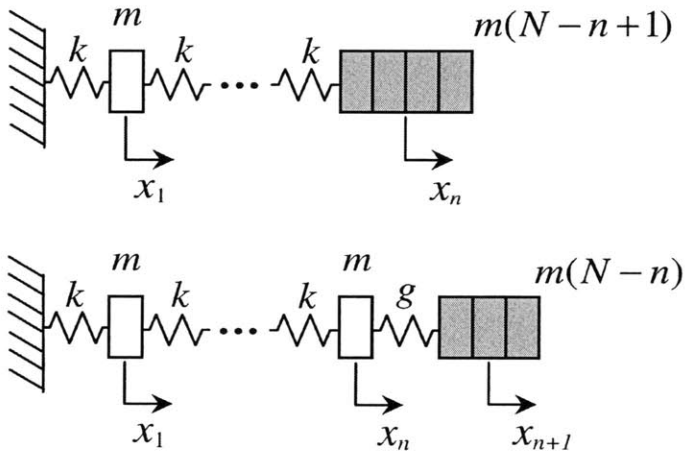

Figure 5-6: Comparison of the minimum resonant frequency for the case with n units ON (top) and with $(n+1)$ units ON (bottom).

The lower portion of Fig. 5-6 shows the case with $(n+1)$ units ON with a stiffness of g connecting the n^{th} and the $(n+1)^{th}$ unit. The stiffness of g is assumed to have a

lower bound value of k so that $k \leq g < \infty$. As $g \to \infty$, the vibrating system behaves as if n units are ON and as $g \to k$, the vibrating system behaves as if $n+1$ units are ON. Using this definition of the stiffness g, it can be shown that $\sigma_{\min}(n) \geq \sigma_{\min}(n+1)$, which leads to the following proposition.

Proposition 4:

A serial strand of N units takes the global minimum resonant frequency $\Sigma_{\min}(N)$ at a configuration where all the N units are turned ON.

Proof:

For the $(n+1)^{th}$ order system, define the mass matrix $\mathbf{M} = m \cdot diag(1,\ 1,\ \ldots,\ 1,\ N-n)$ and define the stiffness matrix $\mathbf{K}'$ as

$$\mathbf{K}' = \left(\begin{array}{ccc:cc} 2k & -k & & & 0 \\ -k & \ddots & \ddots & & \\ & \ddots & 2k & -k & \\ \hdashline & & -k & k+g & -g \\ 0 & & & -g & g \end{array}\right). \tag{5.24}$$

The quadratic form $\mathbf{x}^T\mathbf{K}'\mathbf{x}$ can be written as two separate scalar functions:

$$\mathbf{x}^T\mathbf{K}'\mathbf{x} = \Phi(x_1,\ x_2,\ \ldots,\ x_n, k) + g(x_{n+1} - x_n)^2. \tag{5.25}$$

where $\Phi(x_1,\ x_2,\ \ldots,\ x_n, k)$ is a positive function for any non-zero x_i with $i = 1,\ 2,\ \ldots,\ n$. Note that g is factored out in the second scalar function. Hence, $\forall \mathbf{x} \in \mathbb{R}^{n+1}$

$$\begin{aligned} \frac{\mathbf{x}^T\mathbf{K}'\mathbf{x}}{\mathbf{x}^T\mathbf{M}\mathbf{x}} &= \frac{\Phi(x_1,\ x_2,\ \ldots,\ x_n, k) + g(x_{n+1} - x_n)^2}{\mathbf{x}^T\mathbf{M}\mathbf{x}} \\ &\geq \frac{\Phi(x_1,\ x_2,\ \ldots,\ x_n, k) + k(x_{n+1} - x_n)^2}{\mathbf{x}^T\mathbf{M}\mathbf{x}} \\ &= \frac{\mathbf{x}^T\mathbf{K}\mathbf{x}}{\mathbf{x}^T\mathbf{M}\mathbf{x}}. \end{aligned} \tag{5.26}$$

Now let $\mathbf{x}^*$ denote the fundamental mode shape for the system having a stiffness matrix $\mathbf{K}'$. Then, using (5.26) and the properties of the Rayleigh quotient, it follows that

$$\begin{aligned} \lambda_{\min}(\mathbf{M}^{-1}\mathbf{K}') &= \frac{\mathbf{x}^{*T}\mathbf{K}'\mathbf{x}^*}{\mathbf{x}^{*T}\mathbf{M}\mathbf{x}^*} \\ &\geq \frac{\mathbf{x}^{*T}\mathbf{K}\mathbf{x}^*}{\mathbf{x}^{*T}\mathbf{M}\mathbf{x}^*} \\ &\geq \min_{\mathbf{x}\in\mathbb{R}^{n+1}} \frac{\mathbf{x}^T\mathbf{K}\mathbf{x}}{\mathbf{x}^T\mathbf{M}\mathbf{x}} \\ &= \lambda_{\min}(\mathbf{M}^{-1}\mathbf{K}). \end{aligned} \tag{5.27}$$

The above inequality shows that the case having only n units ON will have a

higher fundamental frequency than the case with $n+1$ units ON because the case having only n units ON is a special case of the system with the stiffness matrix $\mathbf{K}'$ when $g \to \infty$. Therefore, $\sigma_{\min}(n) \geq \sigma_{\min}(n+1)$ for $n = 1, ..., N-1$, from which it immediately follows that

$$\sigma_{\min}(1) \geq \sigma_{\min}(2) \geq \ldots \geq \sigma_{\min}(N) = \Sigma_{\min}(N). \tag{5.28}$$

This result shows that turning all units ON leads to the global minimum resonant frequency. ■

A numerical illustration of Propositions 1 to 4 is offered in Fig. 5-7 for $N = 5$. Fig. 5-7 shows the locations of all possible resonant frequencies as triangles. The maximum and minimum bounds indicated by the uppermost and lowermost solid lines are the resonant frequencies based on the configurations in Proposition 1 and 2, respectively. That is, the uppermost points on the solid lines are achieved by placing all OFF units next to the base structure while the lowermost points are achieved by placing all OFF units at the free end. Note that as n increases toward the maximum value of $N = 5$, the upper and lower resonant frequency bounds monotonically approach the limits specified by Propositions 3 and 4 where all units are ON. As n increases, the reduction in the absolute slope of the overall upper and lower resonance bounds implies that including more than $N \approx 5$ units in a strand does not significantly improve the range of attainable resonant frequencies although it would increase the static stiffness tuning range.

The darker region in Fig. 5-7 indicates the tunable range of the first resonance only. This region's upper bound is dictated by the Corollary to Proposition 2. As in Proposition 1, the configurations for highest first resonance have all OFF units placed at the base. The general trend of this first mode region is a downward and narrowing behavior.

A further note regarding the theoretical resonance tunability is that there is a gap between the first mode and higher modes for $n \geq 2$. For a given n, this spacing creates a band of frequencies over which no resonance can occur. However, if all values of n are considered, the overall modal density is fairly uniform between the global limits $\Sigma_{\min}(N)$ and $\Sigma_{\max}(N)$.

5.5.4 Maximal Tuning for Long Strands

The previous propositions establish the conditions under which maximum and minimum resonant frequencies are achieved for finite N. In this section, the case where $N \to \infty$ is considered to establish the maximal tunability using the proposed actuation method. Given an N, Propositions 3 and 4 indicate that $\Sigma_{min}(N)$ and $\Sigma_{max}(N)$ are given by $\sqrt{\frac{k}{m}}$ multiplied by the positive square root of the maximum and minimum eigenvalues of $\mathbf{S} \in \mathbb{R}^{N \times N}$ having the form defined in (5.6).

Lemma 4:
The eigenvalues λ_i $(i = 1, 2, \ldots, N)$ *of* $\mathbf{S} \in \mathbb{R}^{N \times N}$ *are given by*

$$\lambda_i = 4 \sin^2 \left(\frac{(2i-1)\pi}{2(2N-1)} \right). \tag{5.29}$$

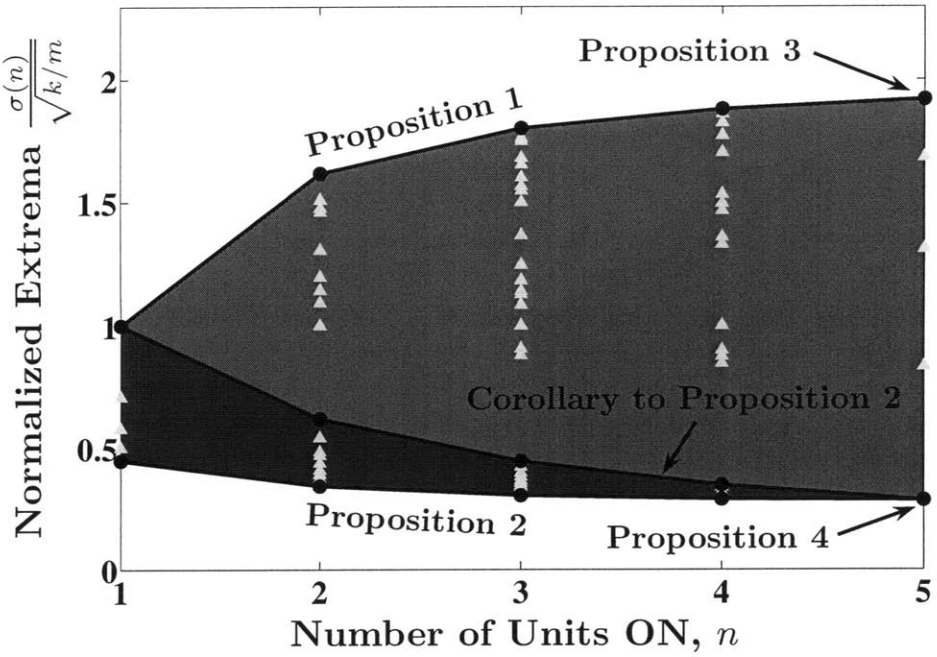

Figure 5-7: An illustration of the theoretical propositions for $N = 5$. All possible resonant frequencies are shown as well as numerical bounds on the minimum and maximum achievable resonant frequencies for $N = 5$.

Proof:
The proof follows from [42] and is adapted here. Notice that the standard eigenvalue problem for $\mathbf{S}$ can be written as a difference equation:

$$-x_{j-1} + (2 - \lambda)x_j - x_{j+1} = 0 \quad (j = 1,\ 2,\ \ldots, N). \tag{5.30}$$

This difference equation has the general solution

$$x_j = A\cos(j\theta) + B\sin(j\theta). \tag{5.31}$$

Substituting the general solution into the difference equation (5.30) implies (after a great deal of trigonometric simplification) that

$$2\cos\theta = 2 - \lambda. \tag{5.32}$$

The end conditions for this difference equation are

$$x_0 = 0 \tag{5.33}$$

and

$$x_{N+1} - x_N = 0, \tag{5.34}$$

which reflect the fix-free nature of the system. Applying the end conditions implies that

$$A = 0 \tag{5.35}$$

and

$$\sin\left((N+1)\theta\right) = \sin\left(N\theta\right), \tag{5.36}$$

which holds when

$$\theta_i = \frac{(2i-1)\pi}{2N+1}, \quad (i = 1,\ 2,\ \ldots, N). \tag{5.37}$$

Substitution of (5.37) into (5.32) provides the desired expression for the eigenvalues:

$$\begin{aligned} \lambda_i &= 2 - 2\cos\theta_i \\ &= 4\sin^2\left(\frac{(2i-1)\pi}{2(2N-1)}\right) \quad (i = 1,\ 2,\ \ldots, N). \end{aligned} \tag{5.38}$$

■

Thus, as described in [42], the eigenvalues for $\mathbf{S}$ can be written in closed form:

$$\lambda_i(\mathbf{S}) = 4\sin^2\left(\frac{(2i-1)\pi}{2(2N+1)}\right) \quad i = 1, 2, \ldots, N. \tag{5.39}$$

Therefore, the following two propositions bound $\Sigma_{max}(N)$ and $\Sigma_{min}(N)$ for all N.

Proposition 5:

The maximum un-damped resonant frequency $\Sigma_{\max}(N)$ has a least upper bound of $2\sqrt{\frac{k}{m}}$.

Proof:

Applying (5.39) with $i = N$, yields

$$\Sigma_{\max}(N) = 2\sqrt{\frac{k}{m}}\sin\left(\frac{1-\frac{1}{2N}}{2+\frac{1}{N}}\pi\right). \tag{5.40}$$

Letting $N \to \infty$ gives an upper bound of $2\sqrt{\frac{k}{m}}$. ■

Proposition 6:

The minimum un-damped resonant frequency $\Sigma_{\min}(N)$ has a greatest lower bound of 0.

Proof:

Applying (5.39) with $i = 1$, yields

$$\Sigma_{\min}(N) = 2\sqrt{\frac{k}{m}}\sin\left(\frac{1}{2(2N+1)}\pi\right). \tag{5.41}$$

Letting $N \to \infty$ gives a lower bound of 0. ■

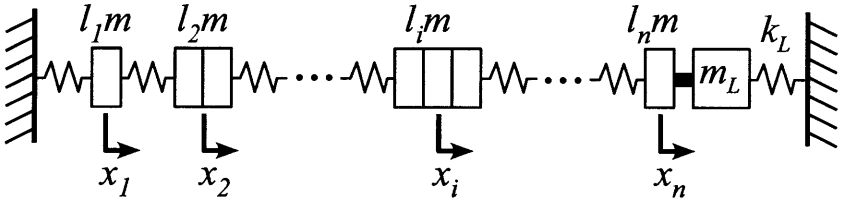

Figure 5-8: Idealized dynamic model for an N-unit strand of cells rigidly connected to a spring-mass load and having n units activated.

5.6 Loading Effects

While the system shown in Fig. 5-5 possesses fixed-free boundary conditions, practical applications entail a load end condition. A simple extension of the model in Fig. 5-5 is provided in Fig. 5-8, which shows the addition of a mass and spring load connected rigidly to the n^{th} node. The load mass and stiffness will dictate the following dimensionless ratios:

$$\gamma_m \triangleq \frac{m_L}{m}, \tag{5.42}$$

and

$$\gamma_k \triangleq \frac{k_L}{k}. \tag{5.43}$$

As $\gamma_m \rightarrow 0$ and $\gamma_k \rightarrow 0$, the system in Fig. 5-8 approaches the system of Fig. 5-5 and the theoretical conclusions of the previous sections apply directly. In this section, the effects of the load ratios on the static and dynamic tuning properties are considered.

The static behavior of a loaded cell strand can be classified by the tunability of the output stiffness, which will be defined as

$$\begin{aligned} \%\text{Static Tunability} &= \left(\frac{\max(c_S) - \min(c_S)}{\min(c_S)}\right) \times 100 \\ &= \left(\frac{N-1}{1+\gamma_k N}\right) \times 100, \end{aligned} \tag{5.44}$$

where c_S is the equivalent compliance as viewed by forces applied at the n^{th} node. A plot of the static tunability as a function of N and γ_k is shown in Fig. 5-9. Beyond $\gamma_k \approx 1.5$, the tunability drops below 50% even for the larger N values. In general, the static tunability is reduced greatly if the load stiffness exceeds approximately $0.5k$, where the curvature of the tunability curves nears its maximum.

The dynamic behavior of a strand of cells is characterized by the ability to tune resonant frequencies. The new dynamic model is the same as described previously but with $\mathbf{M} = m \cdot diag(l_1, l_2, \ldots, l_n + \gamma_m)$ and the (n,n) entry of $\mathbf{K}$ given by $k(1+\gamma_k)$. In practical applications, the first (i.e. fundamental) mode is the most readily excited. Therefore, the tunability of the dynamic system's fundamental frequency will be defined as

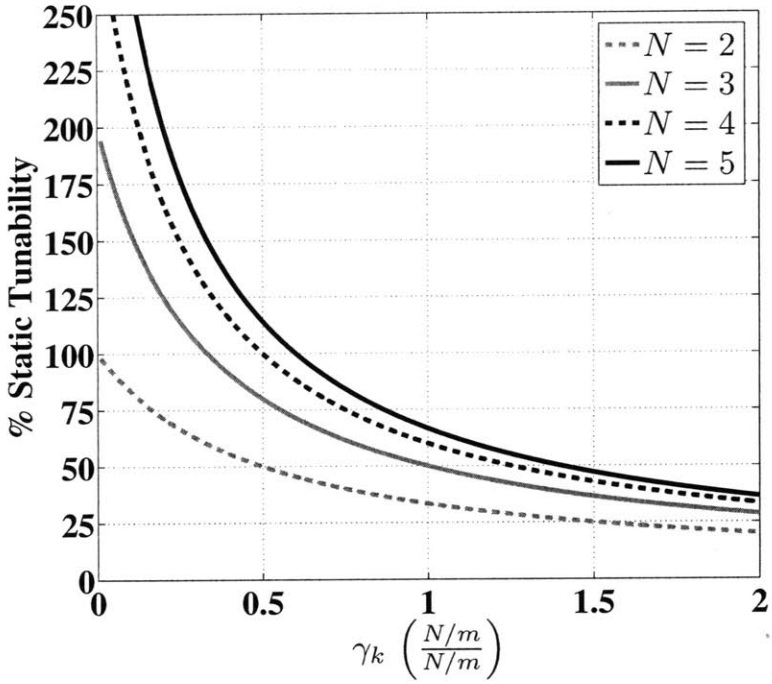

Figure 5-9: Illustration of static tunability as a function of the load stiffness ratios for $N = 2$, $N = 3$, $N = 4$, and $N = 5$.

$$\%\text{Dynamic Tunability} = \left(\frac{\sigma_{\max,\text{first}}(1) - \Sigma_{\min}}{\Sigma_{\min}}\right) \times 100. \tag{5.45}$$

A plot of (5.45) is provided in Fig. 5-10 for $N = 2$ to $N = 5$. Fig. 5-10 shows that the tunability decreases as γ_m and γ_k increase. However, for low values of γ_k, increasing γ_m has a very weak effect on tunability. Likewise, for low γ_m, the tunability is only a weak function of γ_k. The dynamic tunability also increases as N is increases. Overall, the frequency spacing between possible fundamental modes decreases as the stiffness and mass of the load increase or as N decreases.

Based on numerical evaluation, the propositions described previously remain valid except under the condition when $N = 2$ and $\gamma_k = \gamma_m + 1$. In this case, the configuration having $n = 1$ unit ON with the first unit remaining OFF (i.e. grounded) and the case having $n = N = 2$ (i.e. all units ON) both achieve a minimum fundamental frequency of $\Sigma_{\min} = \sqrt{\frac{k}{m}}$. Overall, the loading effects illustrate that this cellular tuning method is most effective when N is large and the actuator is scaled such that γ_k and γ_m remain within the high tunability regions of Fig. 5-10.

5.7 Activation Selection

For a strand of cells, $\Omega(n, N)$ will denote the set of achievable resonant frequencies at a given static compliance level (i.e. a given number of ON units n). The total set of all possible resonant frequencies $\Omega_T(N)$ is therefore

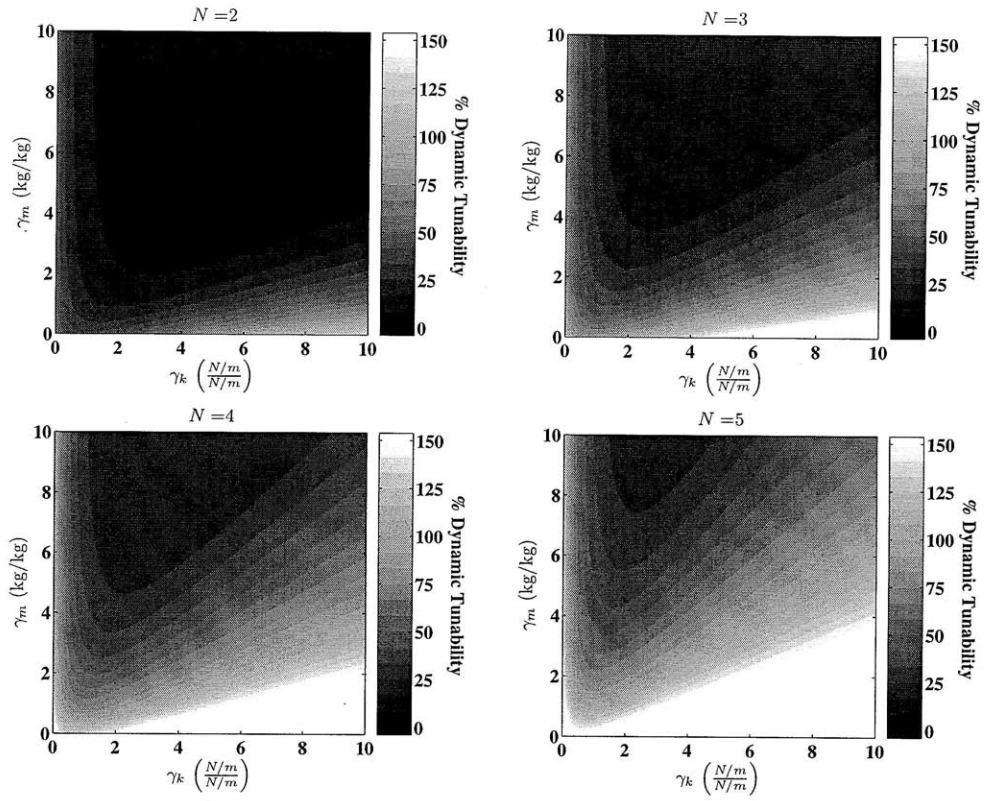

Figure 5-10: Illustration of fundamental frequency tunability as a function of the load stiffness and mass ratios for $N = 2$, $N = 3$, $N = 4$, and $N = 5$.

$$\Omega_T(N) = \bigcup_{n=1}^{N} \Omega(n, N). \tag{5.46}$$

For a robot to undergo periodic motion at a desired frequency, the cells are first activated so that the activation vector, $\boldsymbol{\alpha}$, corresponds to the element of $\Omega_T(N)$ closest to the desired frequency. The ON cells are then excited using a sinusoidal voltage at the desired frequency. From a basic combinatoric analysis, the cardinality of $\Omega_T(N)$ grows as $N2^{N-1}$ and this provides a remarkable ability to tune resonant frequencies over a large, albeit discrete, range.

5.8 Experimental Validation

The analysis in the previous part of the chapter provides useful insight into the mechanism of variable resonant frequencies and the associated tunable range under idealized conditions. This section will consider a specific implementation of the VSCA and extend the previous analysis to account for parasitic dynamics including additional mass, damping, and compliance of the stroke limiter for the PZT-based cell design.

5.8.1 Single Cell Dynamic Model

A detailed lumped parameter model for the specific PZT-based VSCA cell is shown in Fig. 5-11 for the i^{th} cell in a strand. This model is a necessary extension of the idealized model because it includes the parasitic effects of stroke limiter mass, stroke limiter stiffness, and flexure damping that are present in the implemented system. Moreover, the new detailed model allows for a straightforward translation from the actual cell construction to the lumped parameter representation. The stroke limiter mass is lumped in to the element m while the finite stroke limiter stiffness is given by K. The flexure stiffness is spatially divided into two springs of equal value $2k$ on each side of the large suspended mass M. The stiffness $2k$ does vary slightly with displacement, but this variation is assumed to be small for the purpose of model development. The damping effects of the flexures are assumed to be viscous in nature and modeled using a dashpot with a constant value of b. The damping of the flexures, as well as any damping in the load, will shift the resonant frequencies away from their undamped counterparts. However, this shift is small provided that b is relatively small. The PZT-generated force at the output of the second layer is now denoted by $f_{p,i}$.

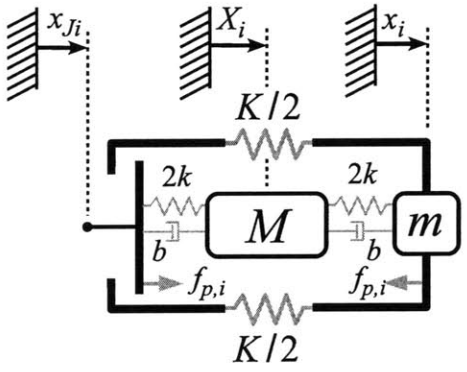

Figure 5-11: Single cell model that includes the parasitic effects of the mass m and stiffness K in the stroke limiting beam as well as flexure damping b.

Each cell requires three generalized coordinates to describe its configuration with respect to an inertial reference frame. The first coordinate, x_i, determines the position of the stroke limiter mass. The second coordinate, X_i, determines the position of the second layer unit suspended mass. The third coordinate, x_{Ji}, determines the location of the output node junction. Note that if another cell is connected to the output node, then $x_{Ji} = x_{i-1}$.

5.8.2 Assembled System Behavior

Consider an arbitrary strand of cells having length N as shown in Fig. 5-12. The strand is connected to a load mass, m_L, which is further connected to ground through a parallel arrangement of a spring and dashpot having values of k_L and b_L. The arrangement depicted in Fig. 5-12 represents the usage of the actuator described in Section 5.9.

Within the actuator, each cellular unit behaves according to the lumped model in Fig. 5-11. For the low frequency or static behavior, mass and damping in the dynamic model may be neglected yielding a series compliance of

$$c_S(n, N) = \frac{n}{k} + \frac{(N-n)}{K+k}, \tag{5.47}$$

where the first term is consistent with the idealized model in (5.1) and the second term accounts for the finite stiffness of the stroke limiting beams.

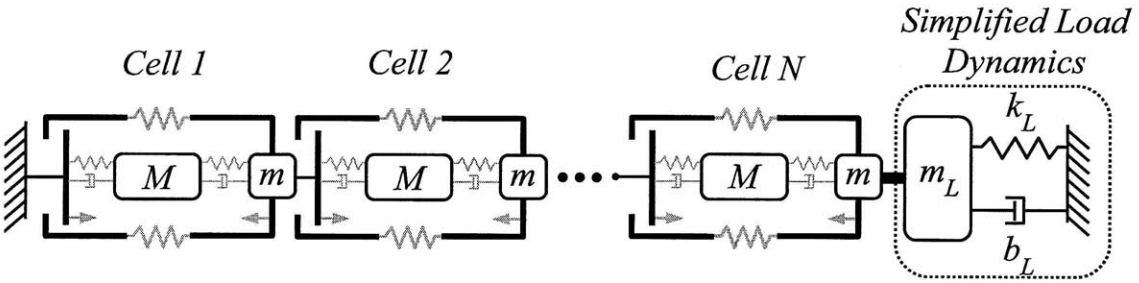

Figure 5-12: Model of an assembled strand of PZT-driven cellular units connected to a general spring-mass-damper load.

If the effects of mass and damping are included, then the dynamic model for a serial chain of units, as well as the dynamic models presented in [93] and [92], can be written in the standard vibratory form as

$$\mathbf{M}\ddot{\mathbf{q}} + \mathbf{B}\dot{\mathbf{q}} + \mathbf{K}(t)\mathbf{q} = \mathbf{Q}(t). \tag{5.48}$$

The vector $\mathbf{q}$ contains the generalized coordinates of the strand while the vector $\mathbf{Q}(t)$ contains the piezoelectrically generated forces, $f_{p,i}(t)$, acting within each cell. For simplicity, these forces are taken as the voltage applied to the cell $V_{pzt,i}$, scaled by an constant electromechanical transduction factor κ.

The parameters of the physical system used in the theoretical model are given in Table 5.2. The stiffness parameters were taken from finite element simulation while the transduction constant κ was obtained from the DC response of the assembled system described in Section 5.9. As is standard practice in vibration models, the damping b was used as a free parameter. Therefore, the damping constant b was tuned to match the experimentally observed resonant peak amplitudes.

5.8.3 Cell Switching Conditions

One important requirement for the implementation of the PZT-based VSCA system is that the combination of load and driving conditions allow the cells to turn ON or OFF without making inadvertent state transitions. The condition for turning a cell ON may be stated in terms of the applied voltage as

$$V_{min} \leq V_{pzt} \leq V_{max}, \tag{5.49}$$

Table 5.2: Model parameters

Parameter	Value	Units
k	16.2	$\frac{N}{mm}$
K	80.1	$\frac{N}{mm}$
b	0.62	$\frac{N \cdot s}{mm}$
m	2.5	g
M	26.0	g
κ	15×10^{-3}	$\frac{C}{m}$
m_L	21.9	g
k_L	0.23	$\frac{N}{mm}$
b_L	$\approx b = 0.62$	$\frac{N \cdot s}{mm}$

where V_{max} is the maximum voltage as specified by the material manufacturer and V_{min} is taken as the maximum value of the time-varying voltage $V_{switch}(t)$ where switching from ON to OFF first occurs:

$$V_{min} = \max_{0 \leq t \leq T} V_{switch}(t). \tag{5.50}$$

Note from (5.50) that the minimum voltage is selected for a given usage duration T. Note also that $V_{switch}(t)$ arises from the time varying forces at the cell-cell connection points. The minimum ON voltage is reduced when the transduction constant κ is increased or the overall preload tension in the strand is decreased.

5.9 Experimental Results

5.9.1 Static Stiffness Tunability

To demonstrate that the static tunability obeys (5.47), the stiffness of a serial chain having $N = 5$ was measured using the experimental apparatus shown in Fig. 5-13. With $N = 5$, there are $2^5 = 32$ possible arrangements of ON-OFF units. As shown in Fig. 5-13, the serial chain was connected to a voice coil actuator and preload tension springs. Units were turned ON or OFF by applying voltages of 150 V and 0 V respectively. Voltages were generated using a Cedrat CA-45 amplifier. The ON-OFF switching was performed with a manual switchboard. With the voice coil actuator, a 1 N peak-peak sinusoidal force was applied at 0.5 Hz about the preload force of 8 N. In general, some preload force is necessary to ensure that the units remain OFF when they receive a zero voltage input and that non-longitudinal vibration modes remain at high frequencies. Forces were measured using a Transducer Techniques load cell while strand displacements were measured using a MicroEpsilon laser displacement sensor. All measured signals were sampled at 1 kHz with a National Instruments data

acquisition board.

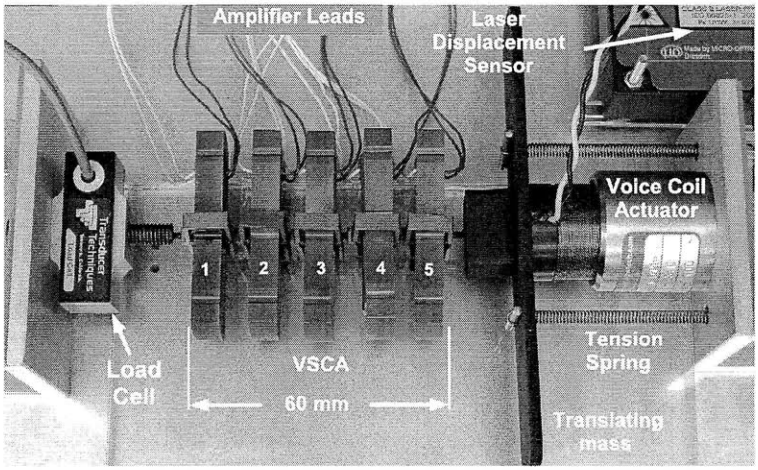

Figure 5-13: Experimental apparatus for measuring static and dynamic properties of a 5-cell system.

The results for the static experiment are shown in Fig. 5-14. For each n there were $\binom{N}{n}$ measured data points. Each compliance data point was generated from a least squares fit to the force versus displacement data. According to (5.47), the equivalent series compliance is constant for a fixed value of n. However, in the real system, there are variations in the series compliance for a given n due to individual cell differences. The mean and standard deviations of the measured data were computed for each value of n. In Fig. 5-14, the mean is indicated by a circle while the vertical bars represent one standard deviation about the mean. The solid staircase line is the predicted compliance based on (5.47). The main cell-cell difference occurs in the slight dimensional variation of the second layer flexure angle, which can have a notable influence on the stiffness k. Other causes of stiffness variation are the slight geometric nonlinearity of the flexure and the variation in ON versus OFF stiffness of the PZT stacks. Despite these sources of variation, the model and the data agree well over the entire range of ON-OFF cases and both illustrate the large tunable range for static compliance. For the experimentally considered case of $N = 5$, the compliance tunability computed from (5.44) is over 350%.

5.9.2 Resonant Frequency Tunability

This experimental section reinforces and illustrates the theoretical concepts developed in this chapter. Frequency response tests were conducted for a VSCA with $N = 3$. The case with $N = 3$ units provides $2^3 - 1 = 7$ possible cases that can be clearly illustrated on frequency response plots. The experimental apparatus is the same as that shown in Fig. 5-13 only oriented so that gravity is acting along the strand.

A chirp voltage input was used to obtain the frequency response characteristics of the actuator. The chirp signal ranged from 5 Hz to 150 Hz and contained a DC offset of 145 V to assure that the conditions in (5.49) were satisfied. The peak-to-peak voltage amplitude was 10 V.

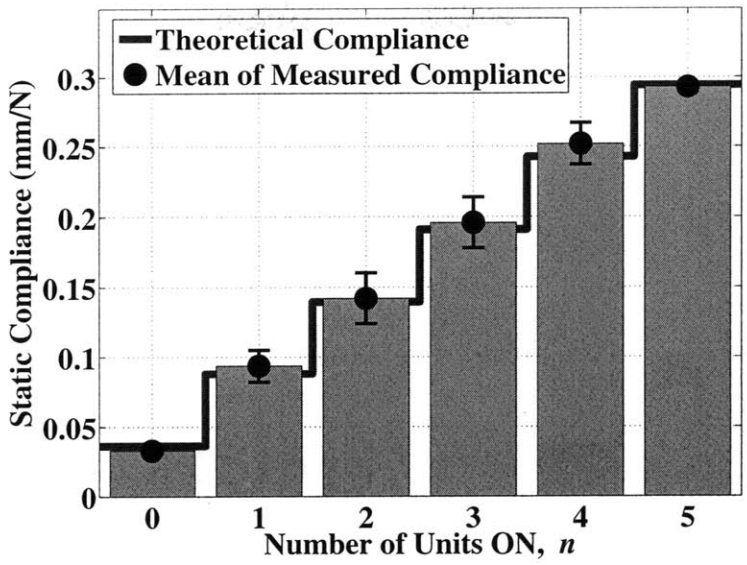

Figure 5-14: Experimentally measured compliance compared to the predicted values based on theoretical stiffness.

The theoretical model and experimental model are compared in Fig. 5-15 for all of the 7 possible cases. Each case is given a binary number where the most significant bit denotes the unit connected to ground and the least significant bit denotes the unit connected to the load. The gain in the frequency response is normalized with respect to the DC displacement. Therefore, the vertical axes in Fig. 5-15 represent the frequency dependent amplification of displacement. The average measured amplification at the fundamental resonance was 17.8 with a standard deviation of 4.4. When comparing the fundamental frequency location between the model and the experimental results, the coefficient of determination is very high ($R^2 = 0.993$) for the entire tuning range of nearly 38 Hz.

For the loaded strand, the load mass and stiffness ratios can be computed from the parameters in Table 5.2 as $\gamma_m = 21.9/26.0 = 0.84$ and $\gamma_k = 0.23/16.2 = 0.014$. From Fig. 5-10 for the case with $N = 3$, the tunability as predicted by the idealized model is over 100%. Furthermore, as indicated by theoretical propositions, the lowest fundamental frequency ($\Sigma_{\text{min}} = 37.5$ Hz) was obtained in the [1 1 1] case while the highest fundamental resonant frequency ($\sigma_{\text{max,first}}(1) = 75.2$ Hz) was obtained was in the [0 0 1] case. Computing the dynamic tunability from (5.45) yields a value of over 100%, which agrees well with the idealized model.

5.9.3 Resonant Frequency Tunability for a Single DOF Leg

An extension of the previous experiment is the application of the VSCA to a single degree of freedom leg shown in Fig 5-16. The leg is driven by a serial strand VSCA with $N = 5$. Although the leg shape does not affect the experimental tunability outcome for free rotation, the leg shape was chosen as an example of a locomotion subsystem for use in a reduced scale humanoid robot. The actuator is opposed an-

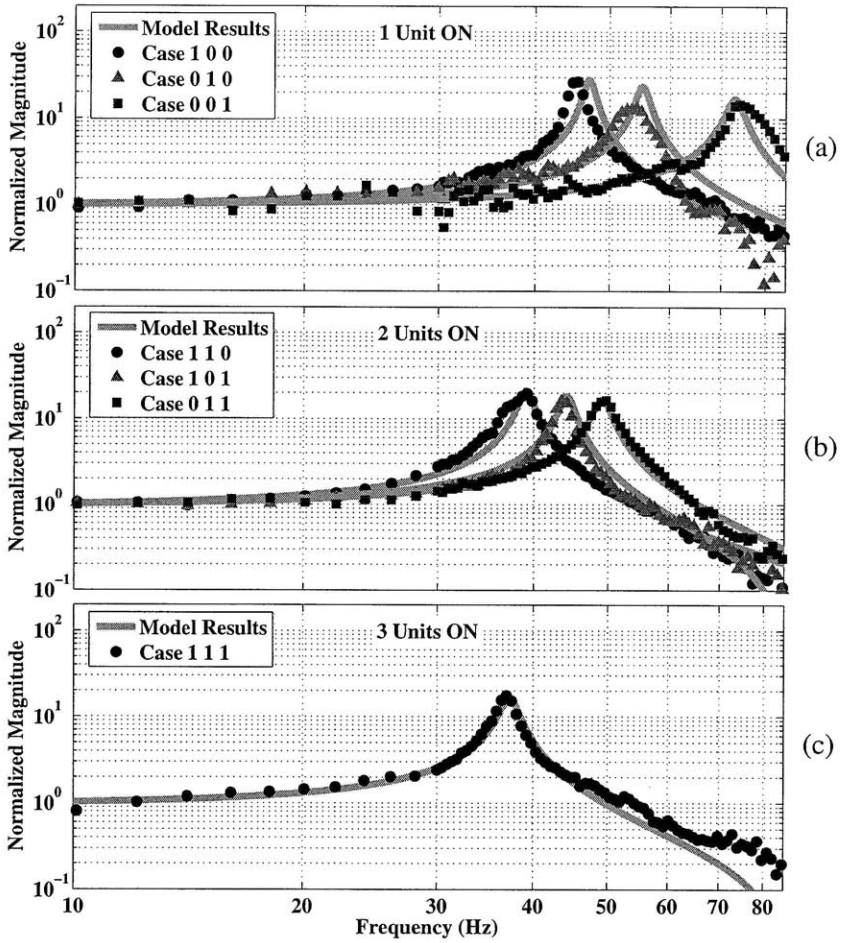

Figure 5-15: Experimental results demonstrating the variable resonance concept for three serially connected cells.(a) Cases with one unit ON. (b) Cases with two units ON. (c) All three units ON.

tagonistically by a passive linear spring because an antagonist actuator pair requires displacement biasing away from the stroke limiters, which is beyond the scope of the present work. The rightmost portion of Fig. 5-16 also shows the switchboard used to turn cells ON or OFF according to the particular case under consideration. The linearized model of this system is still given by (5.48). The equivalent load mass and stiffness are now given by

$$m_{L,eq} = \frac{I_{leg}}{l_g^2} \tag{5.51}$$

and

$$k_{L,eq} = k_a \cos\beta \left(\frac{l_a}{l_g}\right)^2, \tag{5.52}$$

where I_{leg} is the mass moment of inertia of the leg about the joint axis, l_g is the

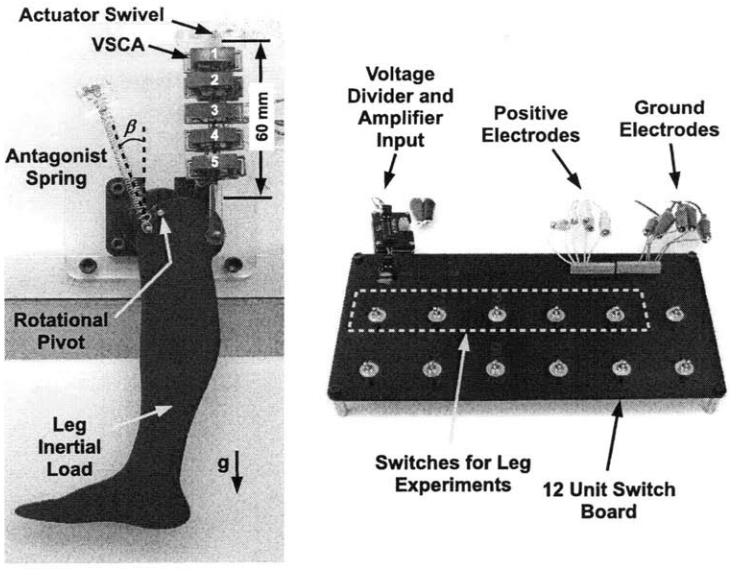

Figure 5-16: Single DOF leg and actuator switchboard used for dynamic experiments.

moment arm of the agonist actuator, k_a is the stiffness of the antagonist spring, β is the angle of the antagonist spring with respect to the vertical (Fig. 5-16), and l_a is the moment arm of the antagonist spring. The computed values are $m_{L,eq} = 0.089\ kg$ and $k_{L,eq} = 5.2\ \frac{N}{m}$.

The experimentally identified and model predicted fundamental frequencies are plotted together in Fig. 5-17 for 29 of the 31 possible ON-OFF combinations. The cases of [0 0 0 1 1] and [0 0 1 1 1] are not included in the plot because of errors introduced from improper alignment of the stroke limiting beam on cells 4 and 5. All of the dynamic results were obtained using the same voltage driving conditions applied previously. The angular displacement of the leg was measured using a rotational potentiometer connected to the joint shaft.

The maximum experimental tunability range is 9.33 Hz or, using (5.45), 125%. This agrees well with the tunability prediction in Fig. 5-10 for the idealized model of a loaded strand having $N = 5$ and $\gamma_m = 89/26 = 3.4$ and $\gamma_k = 0.0052/16.2 = 3 \times 10^{-4}$. Also, as expected from Proposition 2 and its Corollary, the lowest fundamental frequency (7.48 Hz) occurs when the activation is [1 1 1 1 1] (all units ON) and the highest fundamental frequency (16.81 Hz) occurs when the activation is [0 0 0 0 1] (all units grounded except the unit adjacent to the load). The data in Fig. 5-17 show an even spread about the unity slope line and yield $R^2 = 0.89$, which indicates that the model agrees well with the physical system behavior for the numerous configurations associated with $N = 5$. In all cases, the dynamic amplification was approximately 5. The large dynamic amplification of rotational angle for small applied voltages again illustrates a major advantage of the resonance system.

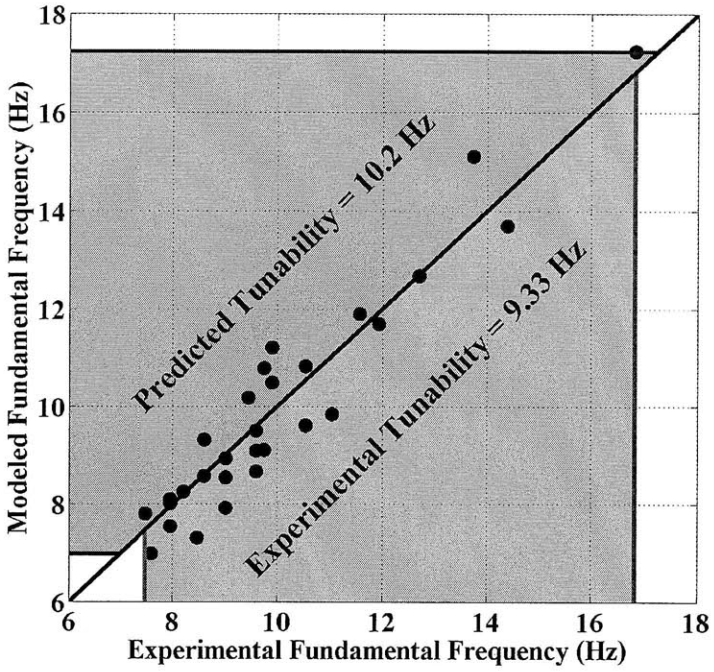

Figure 5-17: Comparison of the model-predicted fundamental resonant frequencies and experimentally obtained fundamental resonant frequencies for the single degree-of-freedom leg system.

5.9.4 Discussion

The experimental results presented in this section illustrate three key features of the VSCA approach.

1. The VSCA approach allows for a wide tunability of both the static stiffness and the first resonant peak in an assembled system. For the experimental system having only $N = 3$ units, the tunability exceeds 100% and for the leg system with $N = 5$ the tunability is approximately 125%. The tunability is also increased as N becomes larger and as higher modes are excited.

2. The results show the high degree of dynamic displacement amplification ($\geq$ 5) when there is low damping in the system. Hence, the pre-existing large static amplification produced by the nested flexures is augmented in the VSCA approach such that resonant peaks occur over a wide range of frequencies useful for robotic locomotion and manipulation.

3. The experimental results and the model prediction are in close agreement for nearly all cases tested. The small model residuals, especially near resonance, validate linearity assumptions and demonstrate a sound model for the dominant energy storage and dissipation modes in the driven system.

Chapter 6

Combined Energy Harvesting and Actuation

The second major extension of the actuator design is to develop a system that is capable of harvesting energy from the environment while maintaining the previously established tunable resonance behavior. The design of the previous chapter is modified to have a normally compliant stiffness characteristic. These revised cells can then used to create a system that can be used for actuation, sensing, and energy harvesting. This unification of features in a single package represents a major advantage over existing biorobotic systems that use separate components for each of these functions. This chapter also discusses the optimal actuation strategies that account for the bidirectional flow of energy between the electrical and mechanical domains of the cellular systems. The chapter concludes with a discussion of impedance matching as an additional optimization method for tunable energy harvesting systems. As in previous chapters, experiments illustrate the theoretical concepts. Overall, the content presented here provides a foundation for applying the cellular piezoelectric technology to systems involving both actuation and energy harvesting.

6.1 Introduction

Traditional electromechanical actuators are rarely used for energy harvesting applications. One of the key drawbacks of motor-based actuators, for example, is that large gear ratios are often needed in order to match the force-speed characteristics of the motor to that of the load. These large gear ratios lead to reduced efficiency of the motor to recover energy either from the environment or the robot's own kinetic and potential energy.

This chapter presents a modular device that is capable of achieving energy harvesting and actuation in a unified package. Specifically, the subsequent sections will examine the design of a cellular, piezoelectric device that produces linear motion commensurate with natural muscle and also has the capability to effectively harvest energy from the environment. These two separate modalities of the device emerge from cellular architecture and revised cell design.

As shown in Chapter 5, cellular architecture provides unique functionality and versatility that a single bulk actuator system cannot provide. For example, cellular

architecture is beneficial for PZT stack actuators because the stacks cannot be scaled arbitrarily; only certain aspect ratios are manufacturable and robust to buckling or electrode failure. Another more general advantage of a cellular architecture is that the cellular devices can be scaled to meet the demands of many different robotic systems. For example, a robot requiring a large force actuator can be accommodated by using several cellular units in parallel. Finally, similar to muscle, a cellular architecture can simplify control by using local controllers that only need to switch a cell between an ON or OFF state [22], while the collective behavior of the parallel and serial cellular assembly is smooth and widely tunable.

One of the salient features of the cellular PZT device is that it exhibits mechanical resonance. Mechanical resonance can be very useful for producing large amplitude periodic motions such as flapping [115], [57], running [88], [55], hopping [106], or swimming behavior [105] in bio-robotic systems. As in the design of Chapter 5, the proposed design modification not only exhibits the benefits of resonance but also allows the cellular device to tune its resonance to match the frequency of an imposed periodic forcing, which maximizes the energy harvested by the device.

This work extends the previous results in three main ways. First, a revised design of the variable stiffness mechanism is presented. Second, the additional functionality of energy harvesting is introduced. Third, the entire device is applied to a variable resonance fin that can achieve both actuation and energy harvesting.

Variable stiffness actuators have been developed by several groups (e.g. [55], [106], and [24]). However, a challenge in this development is to produce a large (i.e. >10) ratio of maximum stiffness to minimum stiffness. With a minor change to the PZT cell, a very large stiffness tuning ratio (i.e. >100) is obtained and the multi-cell architecture allows the device stiffness to be adjusted to various levels.

6.2 Modified Cell Design

The existing design for tunable stiffness and tunable resonance is not suitable for energy harvesting applications. To harvest energy by backdriving a cell, the cell must be away from any stroke limiting device. In the case of the design from Chapter 5, a non-zero voltage (i.e. an activation) is required to move the second layer flexure output away from the stroke limiter as shown in Fig. 5-1. That is, the previous cell design was normally stiff (nS). It is therefore desirable to have a normally compliant (nC) cell that has a passive state away from any hard stop or stroke limiter. The required design modification is to move the hard stop mechanism to the inside of the second layer flexure. Fig. 6-1 shows a schematic interpretation of the design change. In order to achieve a high stiffness with the nC design, the full voltage must be applied to the PZT stacks in order to contact the stroke limiter and hold the second layer flexure in place. Because PZT is a capacitive device, holding the cell against the hard stop (i.e. holding the cell OFF) requires no power. This nC cell enables tunable stiffness and tunable resonance in a single package.

A more detailed consideration of the nC design implementation and operation is shown in Fig. 6-2. Fig 6-2 (a) shows how the stroke limiting beam is introduced to create the compliance nonlinearity shown in Fig. 6-2 (b). When the second layer flexures are not in contact with the stroke limiting beam, the cell is considered to be

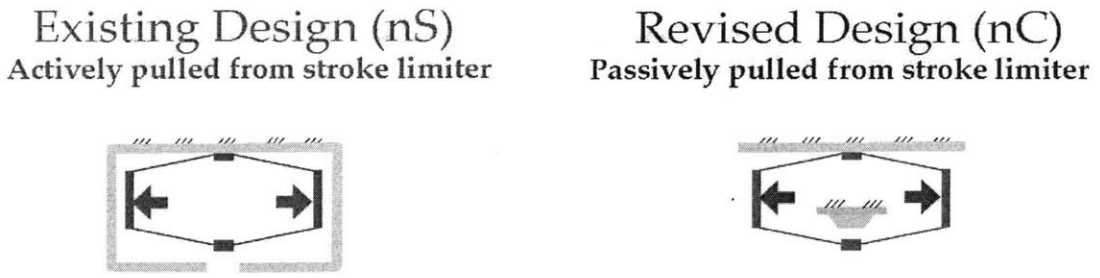

Figure 6-1: Existing normally stiff (nS) design compared to a normally compliant design (nC).

in its ON state and the equivalent compliance, c, of the flexures is $c = 1/k$, where k is the equivalent stiffness of the flexures as viewed from the output node. As voltage is applied to the PZT within the cell, the second layer flexure pulls in toward the stroke limiter. When the stroke limiter is reached at an inward contraction distance of x_{max} and additional voltage is applied, the compliance of the second layer flexures becomes very low (ideally zero) and the cell is then in its OFF state. The additional voltage is necessary to hold the flexure against the stroke limiter in the presence of tensile forces acting on the cell in the OFF state. Due to the capacitive nature of piezoelectric actuators, holding the device in the OFF state requires no current and therefore no power. Using this stroke limiting technique, each cell may readily toggle between a high compliance ON state and a low compliance OFF state. An image of a cell prototype is shown in Fig. 6-3. In the prototype, the inward hardstop is made from plain carbon steel identical to the flexure material. As in Chapter 5, the prototype was designed using Cell 2 from Section 4.8 because this cell performs better than Cells 1 and 3 with respect to $\overline{SW}$ metric discussed in Section 3.5.3.

In Fig. 6-2(b), notice that the main deviation of a real cell from the ideal case arises from the finite compliance of the stroke limiting beam. Nevertheless, the ratio of the highest stiffness to the lowest is very large due to the hard surface contact nonlinearity. When cells are arranged in series or in parallel, the static stiffness of the assembly can be tuned from very rigid to very compliant in small increments.

6.3 Bidirectional Driving Capability of PZT-Based Cells

For the purposes of energy harvesting and actuation, the electromechanical coupling becomes a central concern. Several models exist to describe both the direct and converse piezoelectric effects [90]. A two-port model illustrating the PZT electromechanical transduction through an ideal flexure amplifier system (no flexure stiffness or inertia) is shown in Fig. 6-4 (a). The figure shows that the electrical domain behavior for PZT is characterized by a capacitance C while the mechanical domain is characterized by an inherent mechanical stiffness k_{pzt}. The voltage-to-force coupling constant between the domains is denoted by and the coupling between the second

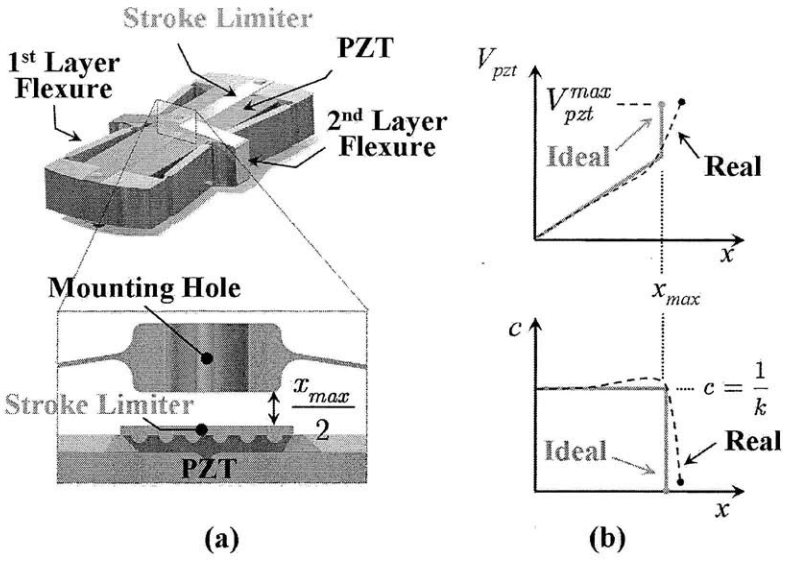

Figure 6-2: (a) Modified cell design for achieving normally compliant characteristics with an internal stroke limiter. (b) Cell compliance characteristics as a function of applied voltage.

layer and the first layer is a lever with a displacement amplification ratio $Gf \gg 1$.

Fig. 6-4(a) shows the converse effect of PZT when the device is used as an actuator. For this case, a PZT voltage V_{pzt} is applied and the large displacement gain, G_f, is used to amplify the PZT motion. For the harvesting case shown in Fig. 6-4 (b), the high gain is again used advantageously because forces applied at the second layer are transmitted back to the PZT stack through the same gain G_f. The generated PZT voltage is then applied across the harvesting impedance Z_h.

The principal advantages of the dual layer flexure energy harvesting approach are 1) compared to electromechanical actuators with large gear reducers, the frictional loss in the flexures is negligibly small and 2) the large amplification gain from the double-layer flexure cell, $G_f = g_1 g_2 > 100$, generates a high voltage, which is a critical requirement for effective energy harvesting. In [38], a single layer amplification stage is used with a gain of approximately 10. The design proposed here significantly extends this gain while maintaining the advantages of a flexure-based system.

6.4 Actuation Driving Frequency Modification for Power Optimization

In many cases, modeling the electrical behavior of piezoelectric stacks as a pure capacitance will lead to erroneous results, particularly if the PZT system is operating near a lightly damped resonance. This was first stated explicitly in [67], although the resulting analysis did not provide convenient closed form expressions based on lumped parameter models. The goal of this section is to provide a lumped model interpretation of PZT electromechanical behavior.

As introduced in the previous section, the bidirectional nature of the electrome-

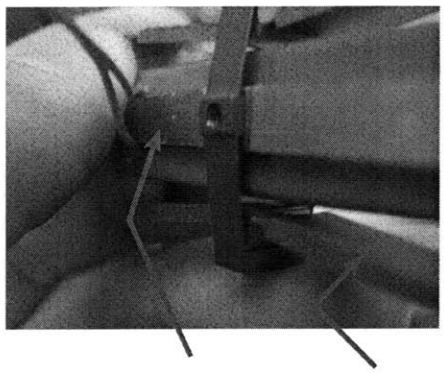

Figure 6-3: Prototype of modified cell design for achieving normally compliant characteristics with an internal stroke limiter.

chanical coupling in PZT is the foundation of its usefulness in energy harvesting applications. Thus, the power analysis from Section 4.10 must now be extended to include the bidirectional nature of the piezoelectric stack and cell system. This analysis will focus on actuation of a single stack coupled to a mass-damper load. This analysis provides the simplest representation of the resonance-antiresonance behavior that must be considered in selecting a driving frequency that is optimal with respect to achieving large displacements at small currents. In particular, the goal of this section is to find the frequency at which the displacement is amplified yet the current required from the piezoelectric amplifier is a minimum for a given applied voltage.

For the analysis, the simplest model of a piezoelectric stack is shown in Fig. 6-5. Fig. 6-5 (a) shows the bond graph interpretation of piezoelectric transduction. This model represents an unloaded piezoelectric stack operating away from its resonant frequencies in a static regime. In both the electrical and mechanical domains, the piezoelectric behavior is capacitive. The electrical domain contains a common effort, or 0, junction while the mechanical domain contains a common flow, or 1, junction. Connected to these junctions are the electrical PZT capacitance C_{pzt} and the internal PZT stiffness k_{pzt}. Connecting the mechanical and electrical domains is a transformer element indicated by TF whose coupling constant is β. The bond graph model is displayed as an equivalent circuit in Fig. 6-5 (b). The equivalent circuit building block for piezoelectric transduction will be the foundation for considering a loaded PZT stack.

The simplest, yet sufficiently general, model for dynamic excitation of a piezoelectric stack is a viscously damped mass acting in the mechanical domain. The schematic representation of this is shown in Fig. 6-6 (a). In this representation, the piezoelectric stack is driven by a voltage source $V_s(t)$. The force applied to the mass M_m is given by βV_{pzt}, where V_{pzt} will be equal to the applied source voltage $V_s(t)$. The viscous damping coefficient will be denoted by B_m. For consistent notation, the stiffness k_{pzt} in the mechanical domain will be denoted by K_m. Fig. 6-6 shows an equivalent circuit model representation of this electromechanical system. In making the transition to the purely electrical representation, the mass is replaced with an inductance, the damping with a resistance, and the stiffness with a capacitance whose value is $\frac{1}{K_m}$.

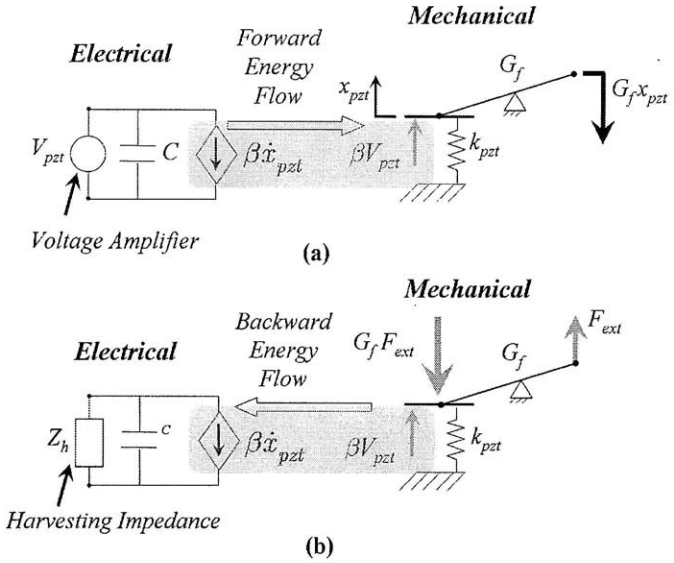

Figure 6-4: (a) PZT converse effect where an applied voltage source is used to produce flexure displacements. (b) PZT direct effect where applied forces are used to generate a potential difference across an impedance. In both figures, the arrows indicate the primary direction of energy flow.

Fig. 6-6 (c) shows the circuit model after reflecting all of the mechanical elements into the electrical branch of the circuit. The simplified circuit has three currents: the source current i_s, the current in the PZT capacitance i_1, and the current transmitted to the mechanical elements i_2. These currents provide the foundation for a complete AC power analysis of the loaded PZT stack.

The currents in the circuit in Fig. 6-6 (c) can be analyzed using a standard impedance analysis. The resulting equations will indicate the frequency dependence of the current magnitudes. The following transfer functions capture the current behavior:

$$\frac{I_1(s)}{V_s(s)} = C_{pzt}s \tag{6.1}$$

$$\frac{I_2(s)}{V_s(s)} = G_2\frac{s}{s^2 + 2\zeta_m\omega_m s + \omega_m^2} \tag{6.2}$$

$$\begin{aligned}\frac{I_s(s)}{V_s(s)} &= A(s) \\ &= C_{pzt}\frac{s(s^2 + 2\zeta_{em}\omega_{em}s + \omega_{em}^2)}{s^2 + 2\zeta_m\omega_m s + \omega_m^2}\end{aligned} \tag{6.3}$$

where $A(s)$ is the equivalent admittance, $G_2 = \frac{\beta^2}{M_m}$, $\omega_m = \sqrt{\frac{K_m}{M_m}}$, $\zeta_m = \frac{B_m}{2\sqrt{K_m M_m}}$, $\omega_{em} = \left(\sqrt{1 + \frac{\beta^2}{C_{pzt}K_m}}\right)\omega_m$, and $\zeta_{em} = \frac{1}{2\omega_{em}}\left(\frac{B_m}{M_m}\right)$. The mechanical displacement

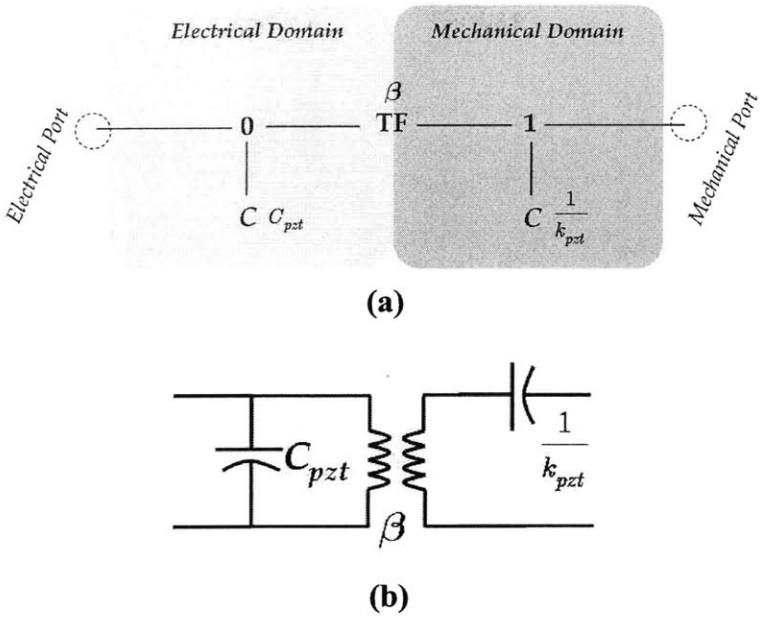

Figure 6-5: (a) Bond graph representation of piezoelectric transduction. (b) Equivalent circuit model of piezoelectric transduction.

transfer function can be obtained by integrating the expression for i_2. Thus, from (6.2),

$$\begin{aligned} H(s) &= \frac{X(s)}{V_s(s)} \\ &= \left(\frac{\beta}{K_m}\right) \frac{\omega_m^2}{s^2 + 2\zeta_m \omega_m s + \omega_m^2}. \end{aligned} \tag{6.4}$$

To assess the best driving frequency for a given voltage amplitude, the frequency dependent magnitudes of the transfer functions in (6.3) and (6.4) are of interest. The salient feature of the admittance transfer function (6.3) is that there exists a pair of complex poles and zeros. The natural frequency of the zeros is at a frequency higher than that of the poles because $\omega_m > \omega_{em}$ for all $\beta > 0$ and all finite C_{pzt} and K_m. Unlike $A(s)$, however, the mechanical response transfer function $H(s)$ has only the pair of complex poles. A resulting magnitude frequency response plot of admittance and mechanical displacement is shown in Fig. 6-7 for small B_m. Fig. 6-7 shows that the mechanical resonant peak at ω_m coincides with the peak in overall system admittance $|A(j\omega)|$. Hence, at the resonant peak, the maximum current is required. At zero damping, the current becomes infinite. Proceeding higher in frequency, the admittance of the system becomes minimized when $\omega \approx \omega_{em}$. Referring to Fig. 6-6(c), ω_{em} is the frequency at which there is an internal resonance between the piezoelectric capacitance, the piezoelectric stiffness, and the mass or inductance. As viewed by the voltage source, this is an antiresonance and the required current to sustain this condition is therefore very low. The ratio of the mechanical gain at ω_{em} to the DC

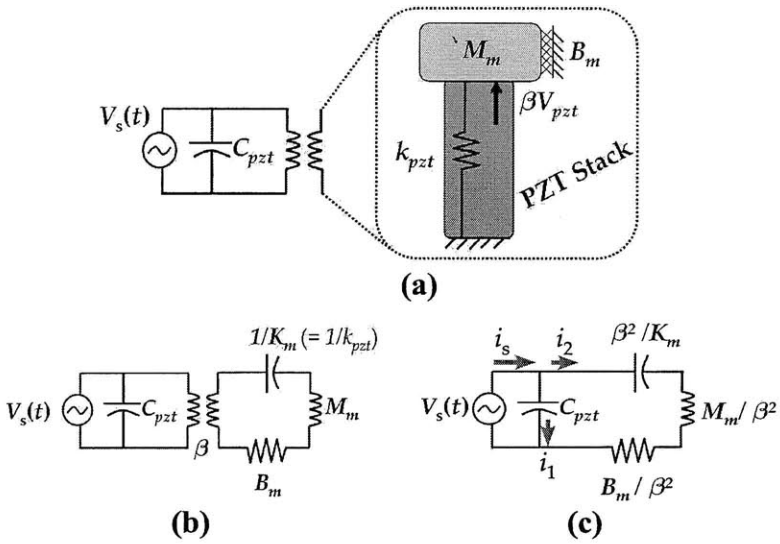

Figure 6-6: (a) Electromechanical model of PZT stack loaded with a mass and damping. (b) Equivalent electrical model showing the electrical domain and mechanical domain on opposite sides of a transformer element. (c) Equivalent electrical model with all elements reflected to the electrical domain side of the transformer.

mechanical gain is given by $\frac{K_m C_{pzt}}{\beta^2}$. If this value is greater than unity, there will still be dynamic displacement amplification at $\omega = \omega_{em}$. The overall goal in driving the piezoelectric stacks is to achieve the largest displacement at the minimum current. Equivalently, the goal is to maximize the value of

$$\begin{aligned} \frac{X(s)}{I_s(s)} &= \frac{\frac{X(s)}{V_s(s)}}{\frac{I_s(s)}{V_s(s)}} \\ &= \frac{H(s)}{A(s)} \\ &= \left(\frac{\beta}{K_m C_{pzt}}\right) \frac{\omega_m^2}{s(s^2 + 2\zeta_{em}\omega_{em}s + \omega_{em}^2)} \end{aligned} \tag{6.5}$$

Eq. (6.5) shows that for dynamic operation, the largest displacement at smallest current will occur when

$$\omega = \omega_{em}\sqrt{1 - 2\zeta_{em}^2}. \tag{6.6}$$

The foregoing antiresonance subtlety of piezoelectric power analysis is often omitted from analysis in the literature, yet is crucial to biorobotics applications.

If the goal of actuation is maximize the power delivered to the damping element B_m, then the appropriate metric is the power factor. The power factor is a concept from AC circuit power analysis that is defined as the cosine of the angle between the current and the voltage. For a completely reactive system (i.e. a pure capacitance or

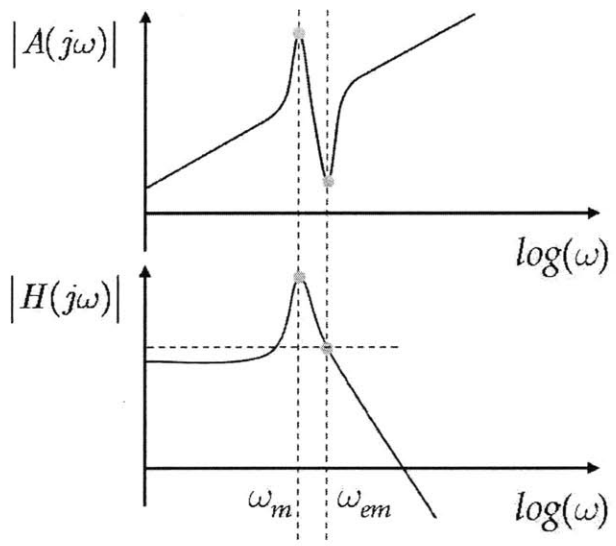

Figure 6-7: Admittance response (top) and mechanical response (bottom) of the loaded PZT stack.

pure inductance), the power factor is zero because the current and voltage in these systems is 90° out of phase. In a purely resistive load, the current and the voltage are exactly in phase so the power factor becomes unity. For systems of mixed character, the power factor will be frequency dependent. The power factor η_{PF} may equivalently be expressed in terms of the angle of the complex impedance:

$$\eta_{PF} = \cos\left(\angle Z_{eq}(j\omega)\right). \tag{6.7}$$

$Z_{eq}(s)$ is the inverse of $A(s)$ as defined in (6.3). A representative plot of the impedance and power factor for the system considered in this section is shown in Fig. 6-8. This figure shows that the power factor will approach unity near both ω_m and ω_{em}. Therefore, considering maximum power delivery at minimum current, the damped antiresonance frequency in (6.6) should always be used.

6.5 Tunable Resonance for Energy Harvesting

Piezoelectric devices have been studied extensively as a means for harvesting energy from mechanical excitation sources (e.g. walking, bridge vibrations, etc.). Sodono et al. [98] provide a concise overview of existing designs, where they point out that resonance is a key operating requirement for optimizing the power output of a harvesting device. Therefore, harvesting energy across a band of frequencies requires tunable resonance. As a result, some tunable resonance designs have been recently proposed. For example, Challa et al. [18] utilize a magnetically imposed stiffness to tune the resonant frequencies of a cantilever while a similar effect is achieved in [65] using a compressive axial preload on a vibrating piezoelectric bimorph. Purely electrical methods for achieving tunable resonance have also been explored [112]. Al-

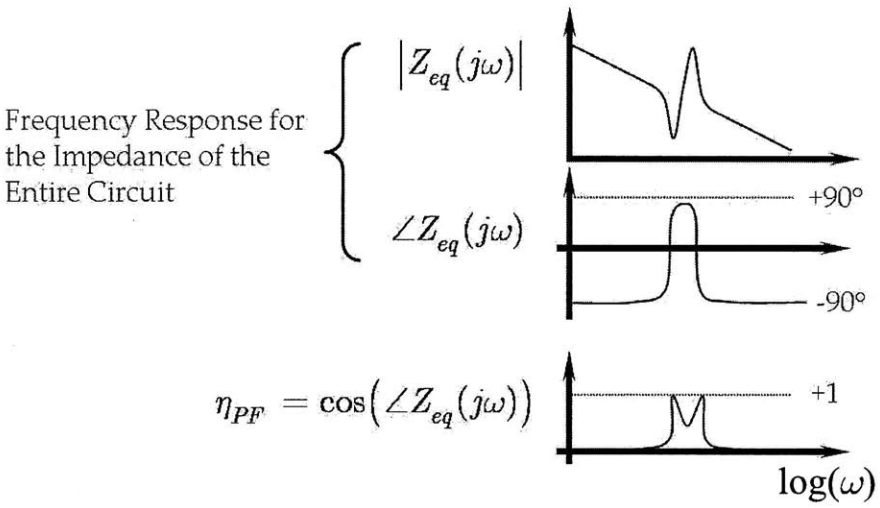

Figure 6-8: Impedance and power factor versus frequency for the loaded PZT cell.

though existing designs are effective for their intended purpose, they operate only as harvesters, require an additional actuator and drive circuitry, and are tunable only within a narrow band of the structure's inherent fundamental resonant frequency. The approach that is described in this section overcomes these difficulties using the piezoelectric cellular architecture.

6.5.1 Two Cell Example

A simple two-cell connection for variable resonance energy harvesting is shown in Fig. 6-9(a). The corresponding schematic model is shown in Fig. 6-9(b). For simplicity, it is assumed that energy is harvested across a purely resistive impedance $Z_h = R_h$. Using the PZT electromechanical transduction constant β, the electrical resistance may be reflected into the mechanical domain as the dashpot element b shown in Fig. 6-9(b). The resulting constant is $b = \beta^2 R_h$. As before, the mass m represents the combined flexure and PZT mass, while the stiffness k now accounts for the reflected PZT capacitance as well as the flexure stiffness.

The dynamic equations governing the vibration of the structure include a damping matrix that also depends upon the activation of the strand:

$$\mathbf{M}(\boldsymbol{\alpha})\ddot{\mathbf{x}} + \mathbf{B}(\boldsymbol{\alpha})\dot{\mathbf{x}} + \mathbf{K}\mathbf{x} = \mathbf{0}. \tag{6.8}$$

Given full state knowledge of the system in (6.8), the internal damper displacements x_{bi} can be computed. Then, for a given serial configuration with n ON units, the instantaneous power harvested in the dashpot elements is given by summing the power from all ON units:

$$P = \sum_{i=1}^{n} b\dot{x}_{bi}^2 \tag{6.9}$$

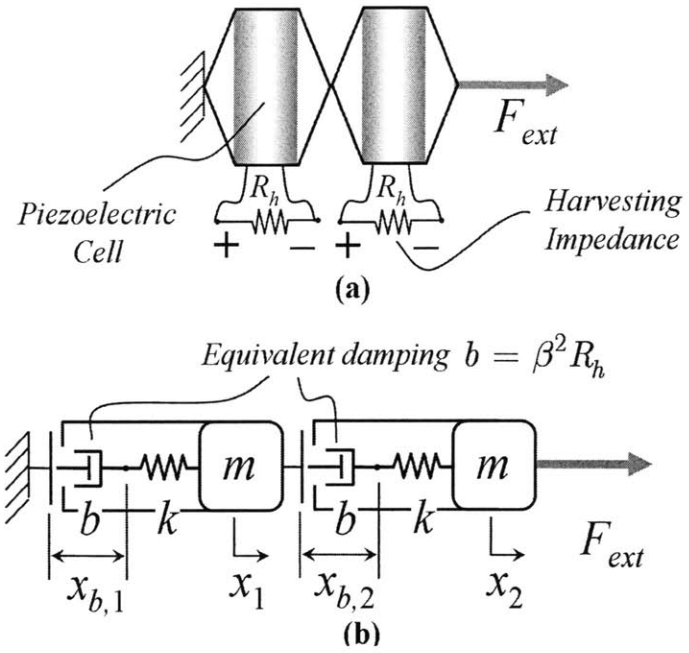

Figure 6-9: (a) Two cells connected in series with harvesting resistances across the PZT electrodes. (b) Schematic model of the two cell harvesting system in (a).

Fig. 6-10 shows a plot of the harvested power computed from (6.9) versus frequency and activation for the two cell example. The vertical power axis is scaled by the peak power, $P_{max}(N)$, over all possible configurations while the horizontal frequency axis is scaled by the single cell resonant frequency $\sqrt{\frac{k}{m}}$. In Fig. 6-10, each ON-OFF activation of the cells provides different resonance characteristics. The undamped normalized resonant frequencies for a two-cell system are 0.62, 0.71, 1.0, and 1.62. Provided that the damping introduced by the harvesting resistance is not too large, the resonant peaks remain close to their undamped counterparts. The vertical bands in Fig. 6-10 that surround each peak indicate where the power drops to half of its maximum value for each resonance. If these four distinct ranges are taken to be the effective harvesting frequency bands, then with only two cells the system is expected to harvest energy over a 300% larger spectrum than would be possible with a single, fixed-resonance harvesting device.

Fig. 6-10 also illustrates a more counter-intuitive aspect of the variable resonance harvesting mode of the device. Specifically, considering a single frequency sinusoid, it is possible to provide the most power to the resistance in the case where only the second cell is ON ($\boldsymbol{\alpha} = [0\ 1]^T$) and not the case with both cells ON ($\boldsymbol{\alpha} = [1\ 1]^T$), which indicates the importance of modeling for selecting a cellular activation.

6.5.2 Activation and Impedance Optimization

In general, the imposed forcing $F_{ext}(t)$ on a PZT-based harvester will not be a sinusoid of a single frequency, but rather it will have power distributed across a band of frequencies. In this instance, the magnitude of the frequency spectrum of $F_{ext}(t)$

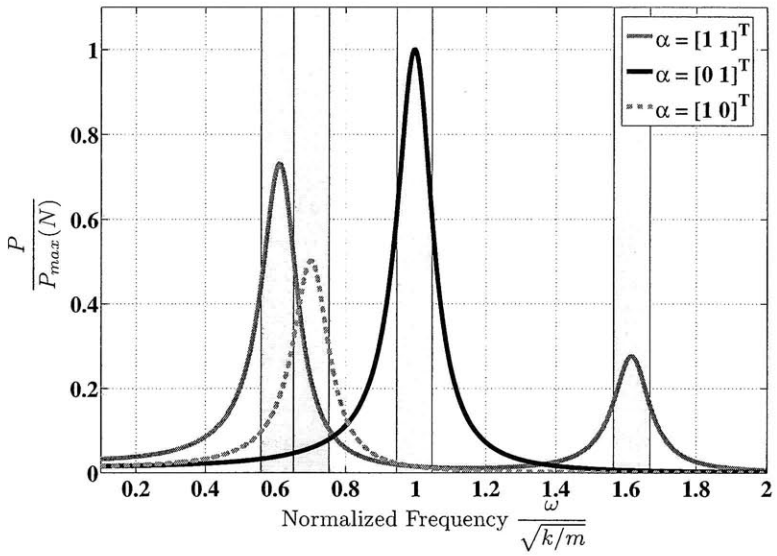

Figure 6-10: Harvested power for various configurations of a two cell strand.

is denoted by $|F_{ext}(j\omega)|$ and the transfer function from the applied force to relative velocity of the i^{th} dashpot (i.e. reflected electrical resistance) element is denoted as $H_i(s) = \frac{V_{rel,i}(s)}{F_{ext}(s)}$. These transfer functions will be dependent upon the activation $\boldsymbol{\alpha}$. Under these conditions, the optimal activation is computed from

$$\boldsymbol{\alpha}^* = \underset{\boldsymbol{\alpha} \in V_N}{\arg\max} \left(\sum_{i=1}^{n} \int_0^{\infty} |H_i(\boldsymbol{\alpha}, j\omega)|^2 \, |F_{ext}(j\omega)| \, d\omega \right) \tag{6.10}$$

where the vector $\boldsymbol{\alpha}$ belongs to the set $V_{n,N}$, which is the set of binary vectors having N components, n of which are 1 and $(N-n)$ of which are 0. Note that $V_{n,N} \subset V_N$, which is the set of all binary vectors having N components. Eq. (6.10) assures that the maximum total power is harvested by the assembly considering all possible activations in V_N. This optimization search space is quite large and illustrates a major advantage of the cellular approach over existing designs with limited mechanical tunability.

An additional technique to further optimize energy harvesting performance involves electrical impedance matching. The preceding analysis has assumed a simple resistive harvesting impedance as shown in Fig. 6-11 (a). As discussed in Section 6.4, the impedance seen at PZT's electrical terminals has a mixed reactive and resistive nature. At low frequencies the terminal impedance is primarily capacitive, near resonance the impedance becomes primarily resistive (damping dominated), and at high frequencies the impedance is mass or inductance dominated. Thus, optimal power transfer to the harvesting impedance requires that the harvesting impedance be adjusted to match both the real and imaginary components of PZT's inherent impedance. The matched impedance scheme is shown in Fig. 6-11 (b), where the PZT has been represented as a Thévenin equivalent circuit. In this scheme, the harvesting impedance $Z_h(j\omega)$ is at all times tuned to match the equivalent output impedance $Z_{eq}(j\omega)$ such that

$$Z_h(j\omega) = \overline{Z_{eq}(j\omega)} \tag{6.11}$$

where $\overline{Z_{eq}(j\omega)}$ denotes the complex conjugate of the cell output impedance. For this technique to be effective, however, the method of tuning the electrical impedance must incur less power cost than the power gain associated with the impedance matching. Moreover, for online optimization, the criterion in (6.10) should be extended to include (6.11). Although the concept of impedance matching has been used in structural damping literature (e.g. [75]) and single resonance energy harvesting devices (e.g. [89]), the optimal impedance matching for tunable resonant frequencies is a subject for further investigation.

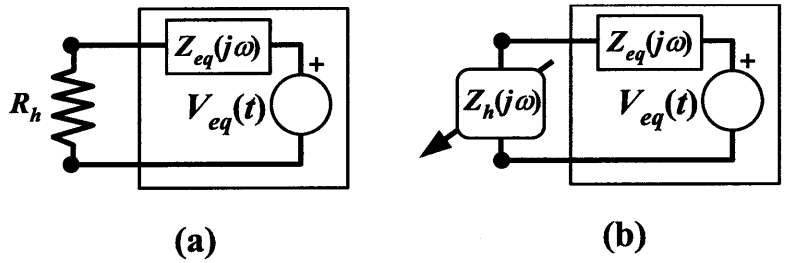

Figure 6-11: (a) Thévenin equivalent circuit for harvesting cell connected to a purely resistive harvesting impedance. (b) Thévenin equivalent circuit for harvesting cell connected to a tunable, complex harvesting impedance.

6.6 Experimental Results

There are three key elements required for tunable resonance actuation and energy harvesting: 1) a functioning nC cell, 2) an understanding of a cell's electromechanical coupling, and 3) the demonstrable ability to tune resonance using an assembly of nC cells. This section addresses these three elements and thereby provides the foundation for tunable resonance energy harvesting. A preliminary demonstration of tunable resonance energy harvesting applied to an underwater fin system is then presented in the final subsection.

6.6.1 Tunable Stiffness in Normally Compliant Cell

The experimental apparatus for measuring the properties of the nC cell is shown in Fig. 6-12. The nC cell is mounted in a vertical test stand and connected to a load cell and hanging preload mass. The preload mass is adjusted using calibrated laboratory weights to provide a constant preload tensile force on the cell. At different levels of preload, the voltage is applied to the PZT cells through the electrodes indicated in the figure. The deflection of the second layer output Δx_2 versus applied voltage V_{pzt} is shown in Fig. 6-13. Fig. 6-13 shows that the device deflects linearly until the internal hard stop is reached. At the point of contact, the deflection is thereafter restricted by the stiffness of the hard stop. This reduction is slope is as predicted

from the schematic curve in Fig. 6-2 (b). Three levels of preload are considered for the prototype cell: 3.7 N, 9.8 N, and 16 N. Fig. 6-13 also illustrates the hysteresis of the piezoelectric stack. For energy harvesting applications, this hysteresis has no major deleterious effect. However, if precise positioning is needed in actuation mode, then feed-forward hysteresis compensation may be indicated [27].

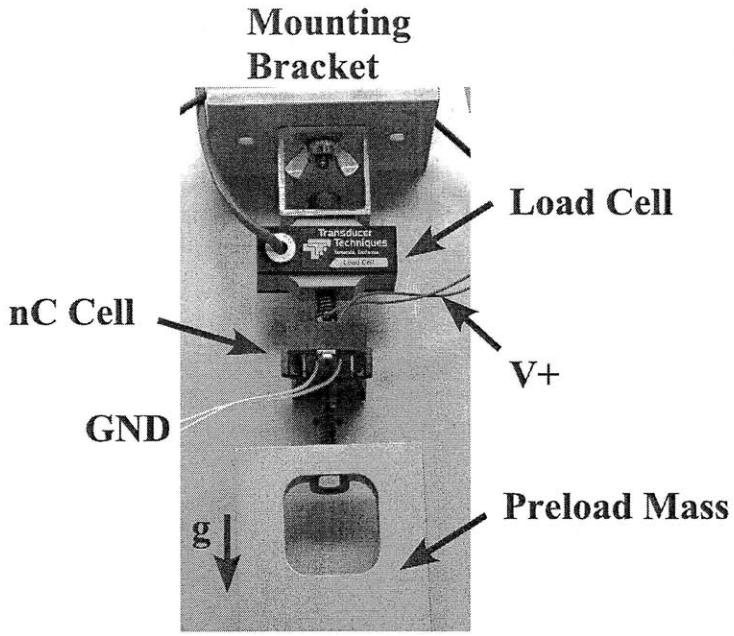

Figure 6-12: Experimental apparatus for testing the stiffness characteristics of an nC cell.

6.6.2 Electromechanical Coupling

The theoretical discussion of electromechanical coupling in Section 6.4 was demonstrated experimentally under fixed-free conditions for a single cell. Using an experimental apparatus in Fig. 6-12 with no attached mass, a chirp swept sine input was applied to the PZT stacks. The current provided by the amplifier was measured using the voltage difference across a series 1Ω resistor. The voltage applied to the PZT was measured using the output of a voltage divider connected to the National Instruments data acquisition board discussed in Section 4.7. The displacement of the second layer flexure output was measured using the Micro-Epsilon ILD-1401 laser displacement sensor described in Section 4.7. The acquired signals were used in the Matlab System Identification Toolbox to estimate the transfer function magnitudes for (6.3) and (6.4). The estimation method is a frequency-dependent windowing based on the Blackman-Tukey algorithm. The resulting admittance and mechanical response transfer function gains are shown in Fig. 6-14. Note that this plot exhibits the same qualitative behavior as the system described by (6.3) and (6.4) shown in Fig. 6-7. A detailed examination of the experimental admittance and mechanical gain near the first resonance is shown in Fig. 6-15. The resonant peak is located

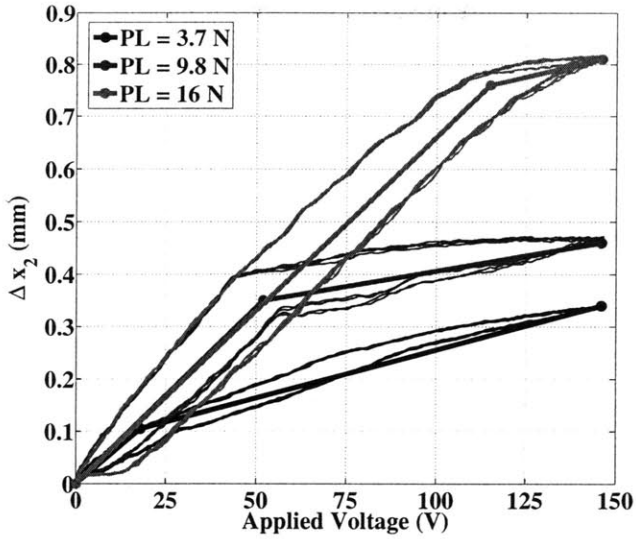

Figure 6-13: Displacement versus voltage of a nC cell under various levels of preload tension.

at 36.9 Hz while the antiresonance is located at 38.0 Hz. The detailed plot shows that for a 25% reduction in the current at the antiresonance, there is an associated 33% reduction in the displacement amplitude. Despite the reduction in displacement amplitude, the system is still operating under a condition of dynamic amplification. Specifically, the gain of the mechanical system still exceeds that of the DC value by a factor of approximately 10. Thus, for energy savings, this frequency may be preferred over the actual mechanical resonant frequency.

6.6.3 Tunable Resonance in Normally Compliant Cell

The nC cell should exhibit the same resonance tunability as the nS system described in Section 5.9.2. The previously described apparatus for measuring tunable resonant frequencies was modified slightly to allow for inactive cells (cells against their stroke limiter) to be connected to a high voltage rail. The modified apparatus is shown schematically in Fig. 6-16. As shown in the figure, there are three nC cells placed in series and connected to the same spring-mass loading described in Section 5.9.2. The PZT stacks of the ON cells were connected in parallel to the PZT amplifier via a custom design switchboard. The PZT amplifier was then driven using an Agilent 33220A function generator. For each ON-OFF combination, a 10 V sinusoidal chirp from 5 Hz to 150 Hz was applied. The inactive cells were connected to a 150 V voltage rail to cause them to contract against their hard stop or stroke limiter. The displacement of the load mass $x_L(t)$ was measuring using the laser displacement sensor and the applied voltage $V_{pzt}(t)$ was measured using the output of a voltage divider circuit.

The results of the experiment are shown in Fig. 6-17. The figure also includes the best fit model from Section 5.8.2. The tunable resonant frequencies follow the behavior predicted by the analysis in Chapter 5. However, the resonant peaks for the

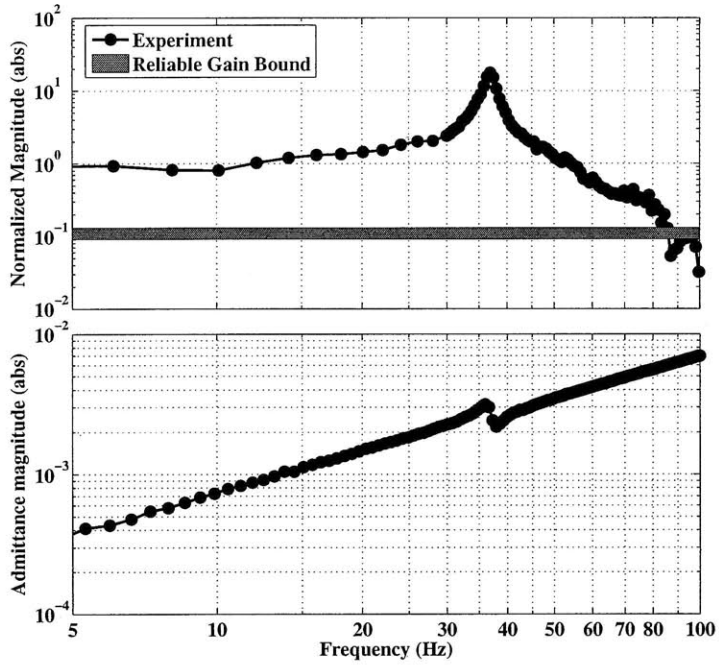

Figure 6-14: Experimentally measured admittance and mechanical displacement gain for a fixed-free nC cell.

nC system are shifted to a higher frequencies. This shift is likely the result of specific cell-differences and differences in the applied preload. Recall that the preload can effect the beam angles and therefore contribute to an increasing kinematic stiffness at the output.

6.6.4 Tunable Resonance in an Underwater Flapping Fin

There are many sources of energy in aquatic environments, some of which include ocean currents, wavy stream currents, and unsteady flow around objects. The proposed PZT system may be used to harvest energy from any such flows.

The experimental apparatus for an underwater fin system is shown in Fig. 6-18. The figure shows the fin supported by a gantry arm that is free to rotate inside of a circular water tank. The fin itself is a NACA 0012 airfoil with a chord length of 150 mm and span of 76 mm. This fin is a reduced-scale version of the fin used in similar underwater experiments [14]. The fin is attached to a drive shaft, which extends out of the water to the actuator mounting frame on the end of the gantry arm shown in the inset of Fig. 6-18 and as a top view in Fig. 6-19. The actuators reside out of the water to alleviate the need for an underwater encapsulating structure. For the energy harvesting experiments, a drive motor was coupled the center shaft of the gantry arm in Fig. 6-18 and sinusoidal voltages were applied to the motor (0 to 24V) at frequencies ranging from 0.2 Hz to 3 Hz. The gantry arm drove the fin forward resulting in fin deflection due to drag forces caused by the relative velocity of the fin and the water. The fin deflection results in reaction forces borne by the actuators and

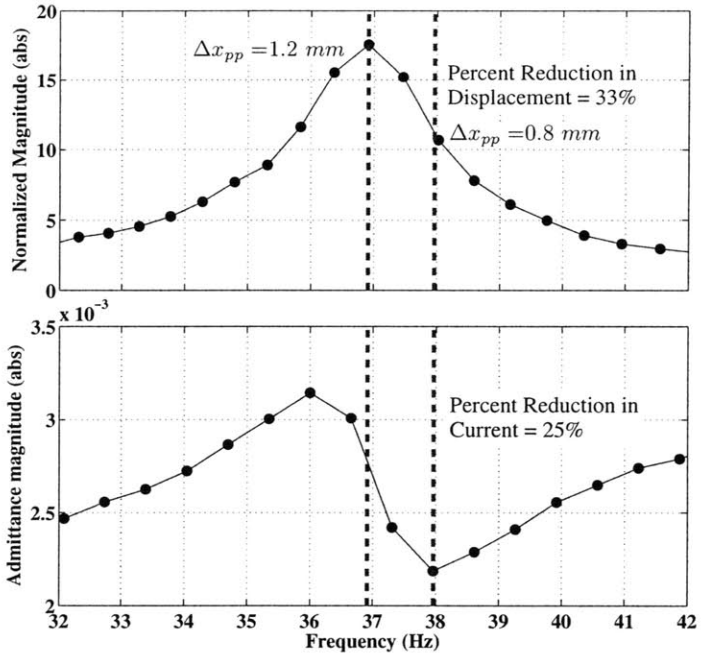

Figure 6-15: Measured admittance and mechanical displacement gain for a fixed-free nC cell showing the detail near the first mechanical resonance.

voltages generated at the PZT stacks. These voltages were then applied to purely resistive harvesting impedances.

A 23.4 $k\Omega$ resistor was placed across each of the cells and the output power across the resistance at cell 4 (see Fig. 6-19) was acquired using a cRIO system (National Instruments). The resistance value was based on modulus matching the piezoelectric electrical capacitive impedance using

$$R_h = \frac{1}{2\pi f_{ave} C} \tag{6.12}$$

where f_{ave} is the average frequency for the experiment (taken as 3 Hz), and C is the electrical capacitance of the stack (measured using an impedance analyzer to be 9 μF). Such modulus matching is consistent with much of the piezoelectric energy harvesting literature (e.g. [18], [65], [112]), but is known to be sub-optimal because it does not account for reactive power effects. This was discussed previously in Section 6.5.2 and has recently been noted in the literature [15], [89].

The results of a representative harvesting experiment are shown in Fig. 6-20. The top portion of the figure shows a time profile of the velocity imposed upon the fin using the motor-driven gantry arm. The two experiments yielded nearly identical velocity profiles. The power spectra of the fin velocity data reveal that the dominant frequency components reside at 1.25 Hz and 8.75 Hz.

The lower portion of Fig. 6-20 shows the resulting instantaneous power at the harvesting resistance as well as its integral (total energy) for the experiment. In

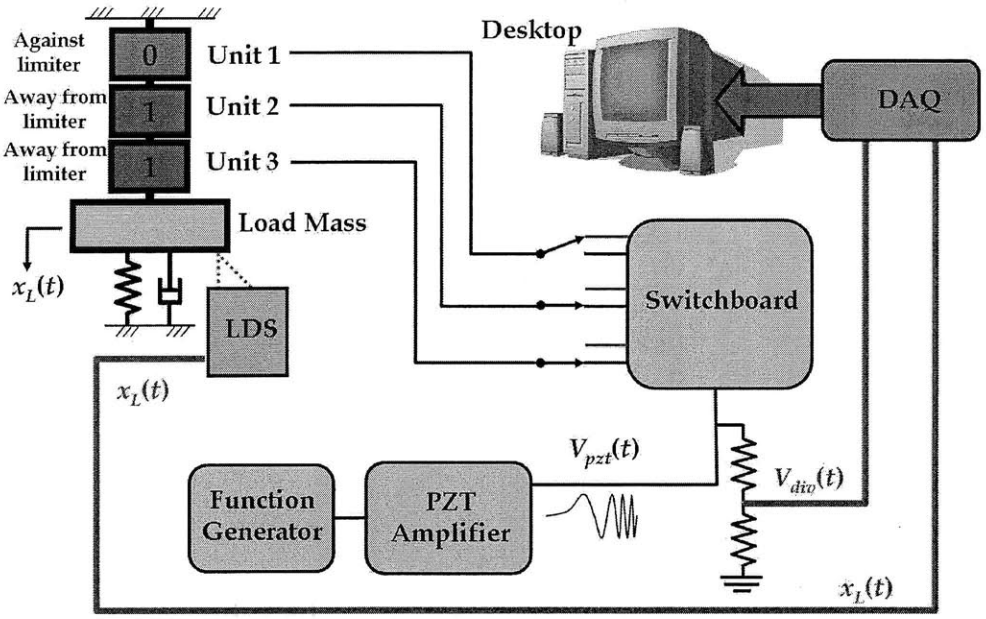

Figure 6-16: Schematic of experimental apparatus for determining nC cell resonance characteristics.

the case with all units ON, the instantaneous power was appreciably lower than the case with the first two units grounded because the all-ON case is not excited as effectively by the higher frequency component of the imposed velocity. Hence, as in the example of described in Section 6.5.1, turning OFF units leads to a higher resonance that is more effective for the given forcing condition. For this particular example, the total energy for $[0011]^T$ (0.2 mJ) is 25% greater than that of the all ON case $[1111]^T$ (0.16 mJ) over the 5 s duration. However, if one assumes that all cells harvest an identical amount of energy, then the all ON case is still preferable because the all ON case would yield 0.64 mJ whereas the two OFF case would only yield 0.40 mJ. This example highlights the importance of the activation selection criteria given in (6.10). Overall, the results throughout this chapter illustrate that the combined cellular actuator and energy-harvesting device performs two ubiquitous functions in a single package.

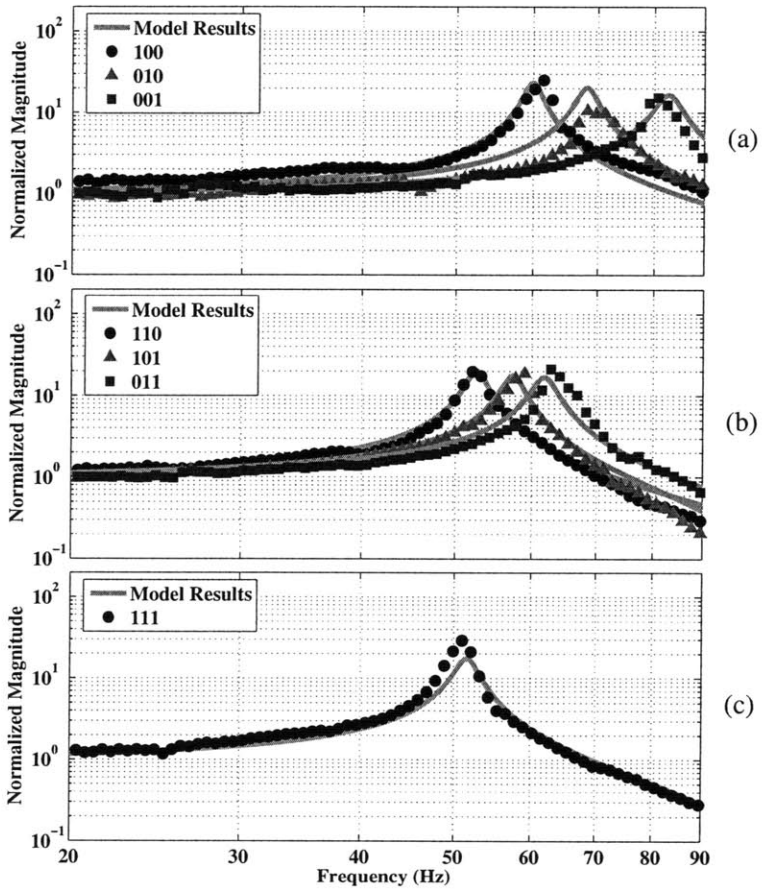

Figure 6-17: Experimental results demonstrating the variable resonance concept for three nC serially connected cells.(a) Cases with one unit ON. (b) Cases with two units ON. (c) All three units ON.

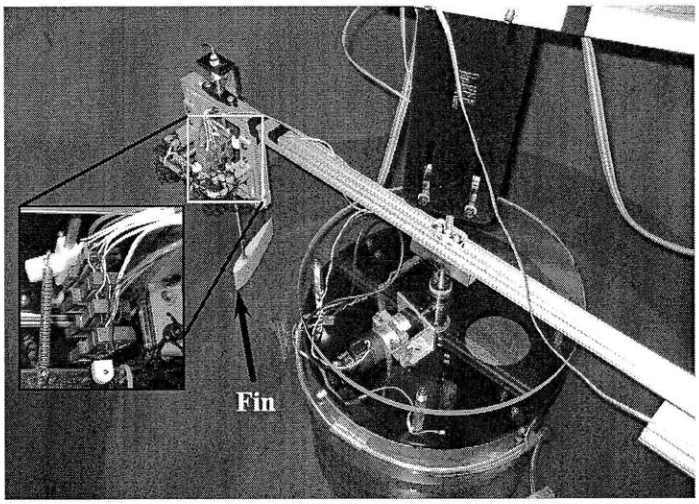

Figure 6-18: Experimental apparatus for an underwater flapping fin system. The motor attached to the center shaft is used for the harvesting experiment.

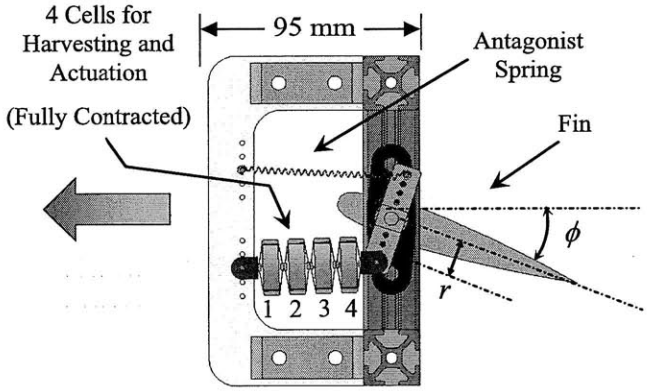

Figure 6-19: Top view of rigid fin system.

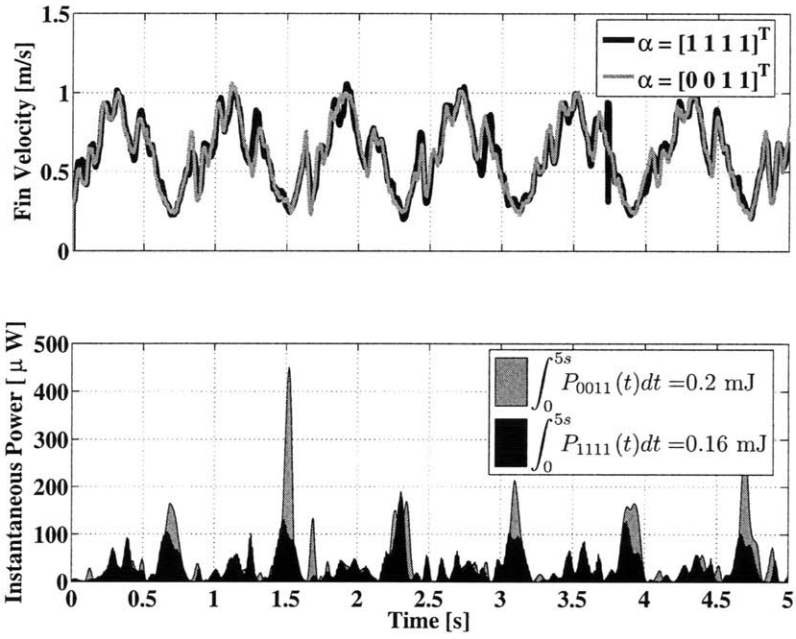

Figure 6-20: Plot of the imposed fin velocity and instantaneous power across the fourth cell's harvesting resistor for two representative 5 s experiments, one having an activation of $[1111]^T$ and the other having $[0011]^T$.

Chapter 7

Application to an Underwater Robot

The previous chapters have described the key characteristics of a new cellular, piezoelectric, artificial muscle actuator. Starting with different cell designs allows the cellular assembly to exhibit tunable static and dynamic characteristics as well as energy harvesting capability. Due to its inherent mass and output stiffness, this cellular actuator technology is particularly well suited to applications where periodic motion is the desired dominant behavior for a robot. Furthermore, the actuator cells can be distributed throughout a robotic kinematic structure to provide a nearly continuous force or moment distribution. It is this distributed architecture that is highlighted in this chapter.

The advantages of piezoelectric technology are discussed in the context of underwater robotics with an emphasis on locomotion using periodic flapping of fin structures. The design paradigm presented in this chapter involves utilizing distributed actuators to achieve desired swimming kinematics. Specifically, the actuators will be used to approximate the spatiotemporal moment distribution required to locomote using traveling waves. The first portion of the chapter discusses the modifications of resonance that are attendant with underwater operation of flapping fins. To achieve the desired swimming kinematics, a theoretical model of a custom designed carangiform swimming robot is developed. Both simulation and experiments are provided to illustrate methods of input synthesis for systems using distributed, cellular actuators.

7.1 Introduction

Researchers at the Office of Naval Research (ONR) describe three recent research trends in underwater bio-robotics: 1) neuroscience-based control, 2) biologically-inspired high-lift unsteady hydrodynamics, and 3) artificial muscle technology [11]. Research in neuroscience based control is revealing new ways to actuate control surfaces while research in biological hydrodynamics is directed toward understanding and recreating the hydrodynamics of live animals. One of the foremost contributions in this area has been the development of the RoboTuna [100]. Hydrodynamics research continues to reveal insight into harnessing biological hydrodynamics in biorobotic systems [99]. The final trend, artificial muscle design, has seen limited practical inte-

gration into underwater bio-robotic systems and presents a large design opportunity.

PZT-based actuators are particularly well suited to underwater tasks because PZT can operate at large depths underwater, produce high oscillatory frequencies for fin-based propulsion, operate at low current anti-resonance frequencies, exhibit inherent energy harvesting capability, and provide silent propulsion. These features are illustrated in Fig. 7-1 as they pertain to fish robots. In a fish, for example, there is an approximate correlation of body natural frequencies with locomotion frequencies [8], which makes the resonance-based actuator concept extremely appealing. Recent underwater bio-inspired robots are achieving impressive performance (e.g. [105] and [74]), but these systems use traditional motor-based actuation schemes that are not ideally suited to the periodic nature of biological systems. Therefore, the robotic design presented in this chapter uses a continuous and flexible fish body actuated by numerous actuator cells distributed along a portion of the body length.

The proposed design in this chapter is meant to serve primarily as a case study in applying the previously developed cellular actuators. However, certain novel aspects of the distributed actuator design emerge and provide the basis for further research. The proposed paradigm of the design is to combine biologically inspired fish geometry with a muscle-like distribution of actuators along a backbone structure. This design approach is unique because existing fish robot designs utilize motors located at discrete point along a flexible structure (e.g. [105], [118]) or along a multi-link mechanism ([100], [77],) although some designs utilizing conducting ionic polymer metal composites ([84],[116]), shape memory alloys ([21]), and piezoelectric unimorph cantilevers ([81]) have emerged in the literature. A commercialized fish based on artificial muscles is also available from the Eamex Corporation in Japan. The design presented here will also examine the coupled dynamics of the flexible fish body and the actuators to synthesize open-loop PZT driving voltages for achieving desired swimming kinematics. The resulting voltages will be applied in both numerical and experimental models to illustrate the tradeoff between swimming velocity and actuator power requirements. This is a contrast to most input synthesis schemes that involve producing neural driving schemes (e.g. [64], [119]). Finally, the present design will incorporate the sensing and energy harvesting features of the cells discussed in Chapter 6. An overview of the proposed design paradigm is illustrated in Fig. 7-2.

7.2 Modifications of Resonance Underwater

The first step in applying the cellular actuators to an underwater robot is to assess the feasibility of utilizing resonance in an underwater environment. Fig. 7-3 shows the construction of a single degree of freedom rigid fin test apparatus for this purpose. The test apparatus is to determine if the effects of added mass and drag on a simple flapping fin will prevent mechanical resonance from occurring. The initial test setup consisted of a 90 mm $\times$ 40 mm tapered fin that is mounted on a rigid stainless steel shaft. The fin is placed inside of 45 $cm \times 30$ $cm \times 30$ cm water tank and the shaft was supported on bearings mounted to an aluminum frame outside the tank. The shaft was then driven using two antagonistically arranged actuators (also located outside the tank and secured to the rigid frame).

An experiment was conducted for the case where one side of the fin is actuated

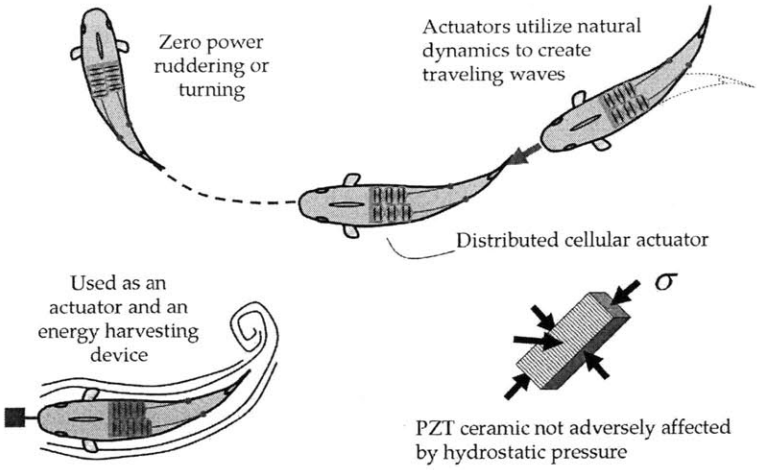

Figure 7-1: Key facets of the cellular actuator robotic fish.

with 4 cells and the other is connected to a tension spring to provide preload and a angular restoring torque. Using standard system identification techniques described in previous chapters, a frequency response of the fin in water was obtained. The magnitude and phase responses of the fin vibration in air and water is shown are Fig. 7-4. The vibration magnitude in air exhibits a large resonant peak (7 times the DC gain) at 20 Hz while the vibration in water reduces the resonant peak to 8.5 Hz and the normalized peak magnitude to 2. The results suggest that a resonant peak is indeed achievable in an underwater environment and the behavior for a rigid fin can be well approximated by a linear second order model. Therefore, added mass and drag for an appropriate fin design fin do not prevent resonance from occurring and a resonance based approach to actuation can still be valuable.

7.3 Underwater Robot Mechanical Design and Manufacturing

This section describes the design of a biorobotic fish used for operations in water and based on a trout body geometry. The trout belong to a class of swimmers known as carangiform swimming fish [110], [95], [25]. Carangiform swimmers have been one of the primary focal points of fish robotics literature because they are some of the fastest and most efficient swimmers [95]. Within this class of fish, trout are also known to be generalist cruisers and rely on long periods of periodic fin motion. Thus, a trout designed to utilize the piezoelectric cell's stiffness and mass characteristics will exhibit resonant frequencies and large tail beat amplitudes in the range of frequencies desired for swimming.

The proposed design is shown in Fig. 7-5. For simplicity, the fish will not be free swimming and will instead be supported on a low friction gantry system. This allows the initial design focus to be on actuation rather than electronics design, pitch

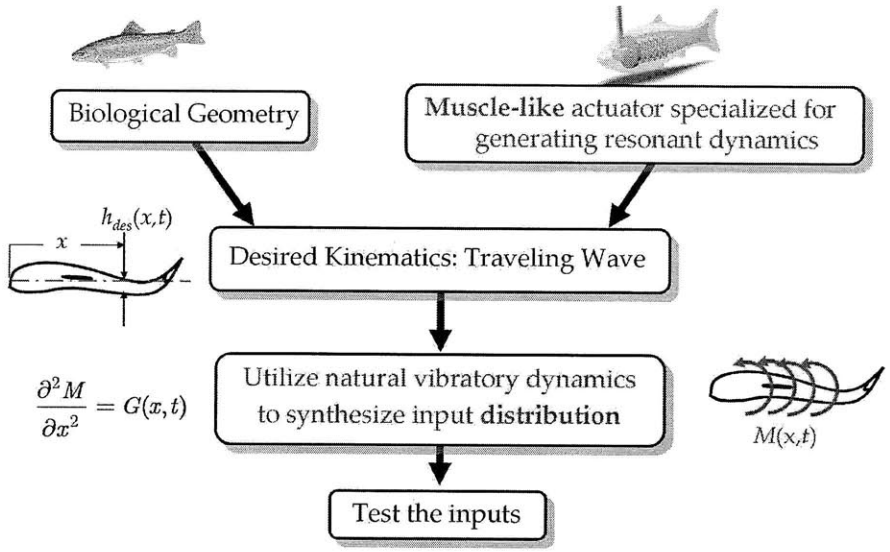

Figure 7-2: Design paradigm for the cellular actuator robotic fish.

stability, and neutral buoyancy. Ten of the actuator cells (Cell 2 in Table 4.4) are installed in pairs on opposite sides of a flexible acrylic backbone structure. The ten cells reside in the anterior section of the fish and transmit moments primarily in this region of the backbone structure. Although, it is possible to extend the design to include more cells, most biological fish generate a majority of their thrust using the anterior muscles [107]. The first actuator pair is secured to the actuator baseplate and an acrylic rib while subsequent actuators are secured between two adjacent ribs. After applying a preload tension to all of the actuators, each rib is secured in place. The cells, backbone, and baseplate constitute the actuation module shown in Fig. 7-6 (a) to (c). Fig. 7-6 (c) shows the actuators sealed within a polyethylene bag in order to prevent silicone from flowing into the actuator flexures and impeding their motion. The completed actuation module is then attached to the gantry connector block, which holds the baseplate and routes the PZT electrode wires up through the aluminum gantry rod. The entire assembly is then placed within a custom designed mold and cast in Silicone Rubber (Ecoflex 0010, Smooth-On, Inc.).

The overall manufacturing process for the fish robot is shown in Fig. 7-7. The two major steps in the process are the actuator module assembly discussed previously and mold machining. The molds cavities were fabricated within machineable wax blocks. The geometry of the mold was designed to include the appropriate sprue and vents for the required silicone casting operation. All CNC machining was performed using a 0.25 inch ball end mill on an EZTrak Lathe (Bridgeport).

Fig. 7-8 shows a completed fish prototype. Fig. 7-8 (a) shows a model of the fish after the casting operation while Fig. 7-8 (b) shows the physical prototype. In Fig. 7-8, note that the tail section is covered by an additional polyethylene shrink wrap to avoid any possible leaks into the actuator cavity. The total length L of the fish body is 345 mm and the gantry rod is placed at 70 mm down the length of the body. The length of the actively flapping body and caudal fin section is therefore

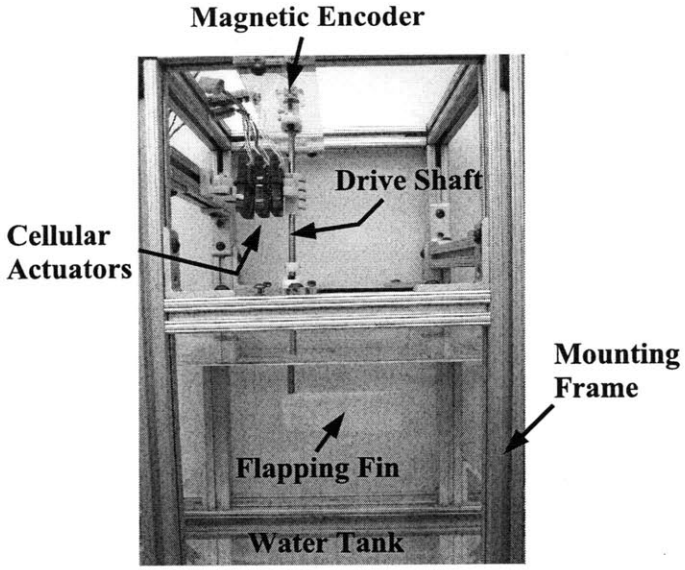

Figure 7-3: Flapping fin system used to assess the modification of resonance underwater.

$L_{fin} = 345\ mm - 70\ mm = 275\ mm$. As discussed in Section 7.5.1, the fish centerline overlays in the desired swimming kinematics has the minimal amplitude envelope in the region of $\frac{x}{L} = 0.2$. Thus, it is not expected that the gantry rod appreciably hinders the desired motion of the fin beyond this connection point. However, the rod does prevent head motion, which can play a role in the formation of vortices and the wake structure as found for a similar compliant fish robot [36].

The final component of the fish robot system is a drive amplifier for independently driving each of the actuator cells. The amplifier is shown in Fig. 7-9. This amplifier design is necessary in order to apply the synthesized voltage inputs to the actual system. The primary design challenge in creating the amplifier is accounting for the instability that results from a coupling of the amplifier output impedance and the PZT stack capacitance. A detailed description of the design is provided in Appendix C.

7.4 Theoretical Modeling of Body Vibratory Dynamics

7.4.1 Continuous Model

The fish body during steady swimming is first modeled as a continuous structure using Euler-Bernoulli beam theory [109] and Lighthill's elongated body theory [69]. This is consistent with much of the existing literature [20],[105]. The assumptions associated with the Euler-Bernoulli theory are that the dominant dynamic effects in the structure are due to translating mass kinetic energy and bending deformation potential energy. Further assumptions include sufficient slenderness, sufficiently small

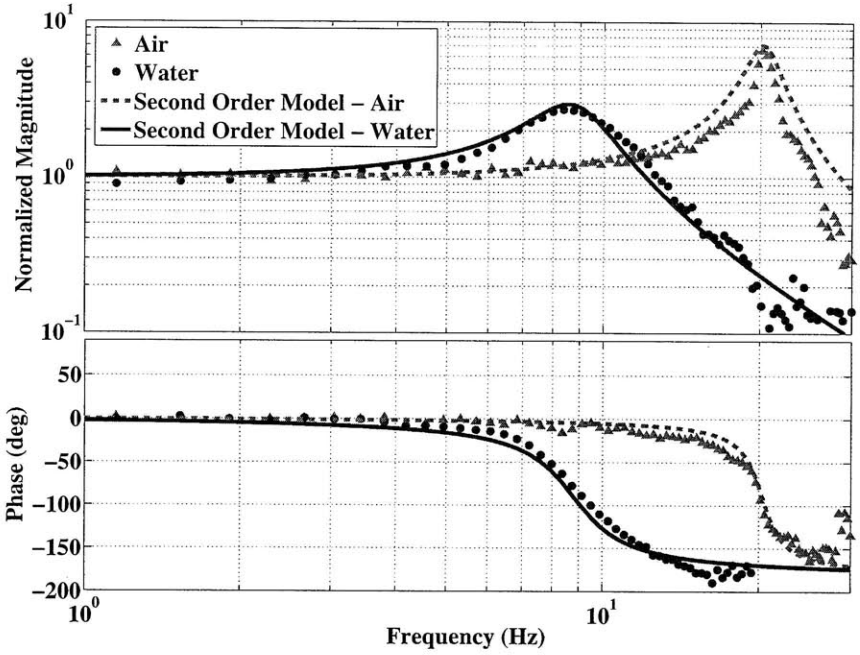

Figure 7-4: Comparison of frequency response resonance characteristics for a flapping fin in air and water.

beam deflections and deflection slope. A schematic representation of the cantilever beam and the lateral deflection $h(x,t)$ are shown in Fig. 7-10 (a). The assumptions of Lighthill's theory include body symmetry, small surface slopes, zero cross sectional area at both ends, small lateral perturbation velocity small in comparison to forward velocity, and inviscid flow. The inviscid assumption allows the model to omit any effects of drag on the skin of the fish because typical fish swimming speeds produce high Reynolds numbers [95].

The first goal of the analysis is to incorporate the effects of the actuator mass and stiffness into equivalent structural properties or effects on the beam. The effects of the actuator stiffness are shown in Fig. 7-10 (b). In this representation, each actuator is modeled as a linear stiffness element having a stiffness k. This stiffness acts between first rib and the base and between subsequent adjacent ribs. The actuator line of action is at a distance a from the backbone and assumed to be parallel to the neutral axis of bending. If each inter-rib section is approximated as having a constant curvature taken as the average value over that section, then the passively induced moments $M_{k,i}$ acting at the i^{th} rib attachment can be computed from

$$M_{k,i} = 2ka^2 \left(\int_{(i-1)l_{sep}}^{il_{sep}} \frac{\partial^2 h}{\partial x^2} dx - \int_{l_{sep}}^{(i+1)l_{sep}} \frac{\partial^2 h}{\partial x^2} dx \right) \delta(x - il_{sep}) \quad i = 1,\ 2,\ \ldots,\ N-1 \tag{7.1}$$

where $\frac{\partial^2 h}{\partial x^2}$ approximates the local curvature of the fin, N is the number of actuators

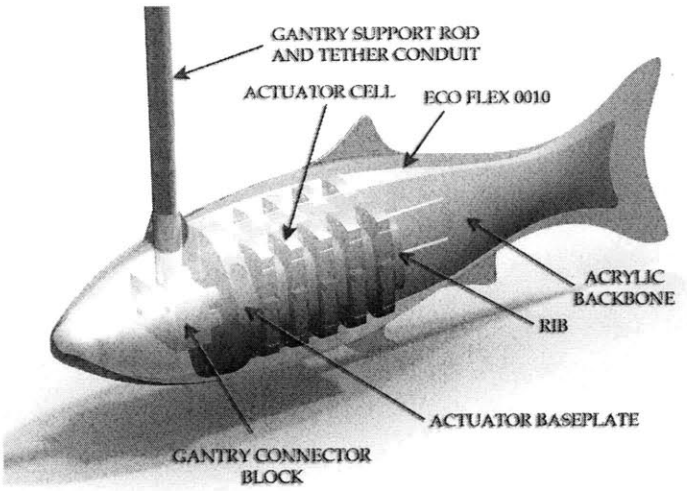

Figure 7-5: Proposed design for a robotic fish driven by cellular PZT actuators.

on a single side of the fin, $\delta(\cdot)$ is the Dirac delta function, and l_{sep} is the rib separation distance. Note that when $i = N$,

$$M_{k,N} = 2ka^2 \left(\int_{(N-1)l_{sep}}^{Nl_{sep}} \frac{\partial^2 h}{\partial x^2} dx \right) \delta(x - Nl_{sep}). \tag{7.2}$$

Thus, the total effect of the actuator passive stiffness is captured by the moment distribution function

$$M_k(x,t) = 2ka^2 \sum_{i=1}^{N} M_{k,i} \delta(x - il_{sep}). \tag{7.3}$$

The mass of the actuators is assumed to act as translational mass the discrete locations where the ribs attach as shown in Fig 7-10 (c). Mathematically, the mass acting at the i^{th} rib can be captured as a linear mass density given by

$$\lambda_{m,i}(x) = 2m\delta(x - il_{sep}) \quad i = 1,\ 2,\ \ldots,\ N \tag{7.4}$$

where m is the mass of a single cell. Therefore, the linear mass density function for all of the actuators is given by

$$\lambda_m(x) = 2m \sum_{i=1}^{N} \delta(x - il_{sep}). \tag{7.5}$$

The actuator induced linear forces must also be accounted for in the model. The pairing of actuator induced forces is grouped in terms of agonist forces $f_{g,i}$ and antagonist forces $f_{a,i}$. At the i^{th} rib, activation of the actuators give rise to a force couple that exerts a total moment on the backbone of

$$M_{a,i} = a(f_{gi} - f_{gi+1}) + a(f_{ai+1} - f_{ai}) \tag{7.6}$$

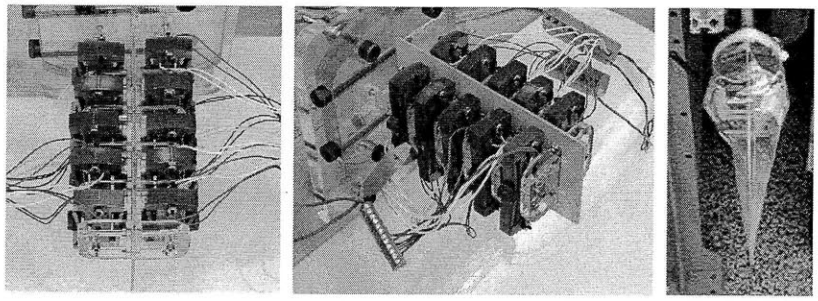

(a) (b) (c)

Figure 7-6: (a) Top view of actuation module on truncated backbone. (b) Side view of actuation model on truncated backbone. (c) Top view of fully sealed actuation module on gantry rod.

If the forces acting within these moments are assumed to be approximately proportional to the applied voltage at the respective PZT stacks (see Section 5.8.2), then

$$M_{a,i} = a\phi_1(V_{gi} - V_{gi+1}) + a\phi_1(V_{ai+1} - V_{ai}) \tag{7.7}$$

where V indicates the voltage applied to the PZT within the cell having the given subscript designation and ϕ_1 is the proportionality constant. The constant ϕ_1 is given by the approximation

$$\phi_1 \approx \frac{f_2^{block}}{V_{max}} \tag{7.8}$$

where the numerator is the cell blocking force and the denominator is the maximum voltage as previously defined. Eq. (7.7) can now be rearranged to the form

$$\begin{aligned} M_{a,i} &= a\phi_1(V_{gi} - V_{ai}) - a\phi_1(V_{gi+1} - V_{ai+1}) \\ &= a\phi_1 V_{diff,i} - a\phi_1 V_{diff,i+1} \end{aligned} \tag{7.9}$$

where $V_{diff,i}$ represents the voltage difference between the i^{th} corresponding agonist and the antagonist cells. Note that when $i = N$,

$$M_{a,N} = a\phi_1 V_{diff,N} \tag{7.10}$$

The actuator induced moments distribution is then given by

$$M_a(x,t) = \sum_{i=1}^{N} M_{a,i}\delta(x - il_{sep}). \tag{7.11}$$

One additional consideration for the beam dynamics is the effects of polymer

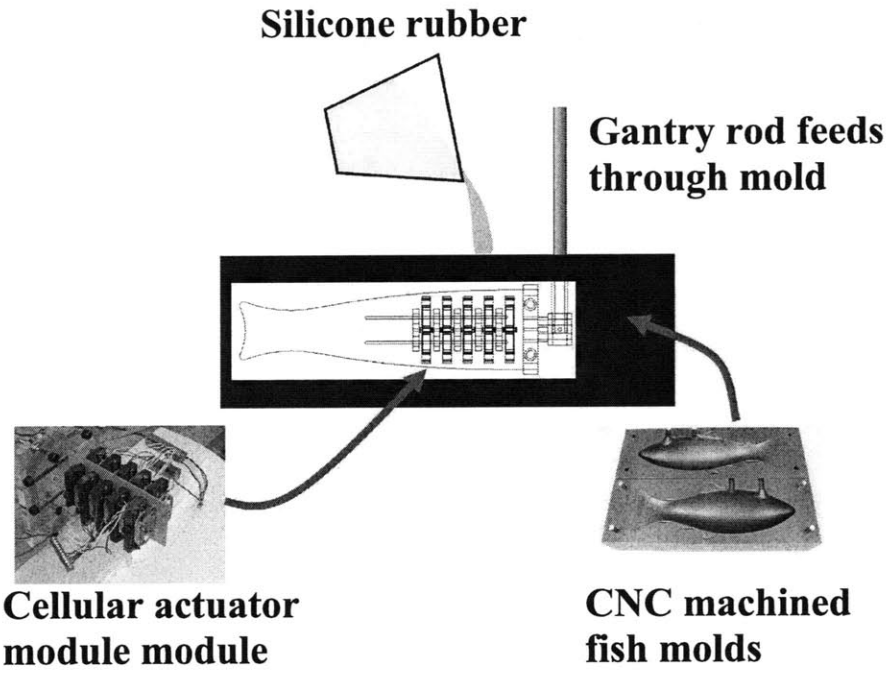

Figure 7-7: Manufacturing procedure for creating the robotic fish prototype.

viscosity. This can play a crucial role in creating the desired traveling wave kinematics discussed in Section 7.5.1 [105]. The simplest linear model for the viscous dissipation moment is given by

$$M_v(x,t) = \mu I_{fb}(x)\frac{\partial}{\partial t}\frac{\partial^2 h}{\partial x^2} \tag{7.12}$$

where μ is the polymer viscous damping coefficient [20] and [105] and $I_{fb}(x)$ is the cross sectional moment of inertia of the fish body.

The preceding relations can now be assembled into the governing equation for beam vibration:

$$\begin{aligned}\frac{\partial^2 M_a(x,t)}{\partial x^2} &= \frac{\partial^2}{\partial x^2}\left(EI_{eq}(x)\frac{\partial^2 h}{\partial x^2} + \mu I_{fb}(x)\frac{\partial}{\partial t}\frac{\partial^2 h}{\partial x^2} + M_k(x,t)\right) + \\ &\left(\rho_{fb}A_{fb}(x) + \rho_{cs}A_{cs}(x) + \lambda_m(x)\right)\frac{\partial^2 h}{\partial t^2} + L_y\end{aligned} \tag{7.13}$$

where L_y is the lateral force induced from the momentum change of the water surrounding the fin computed using Lighthill's elongated body theory [69]. The lateral force can be derived by considering an infinitesimal slice of the fish body moving forward at a velocity U as shown in Fig. 7-11. The material derivative of the lateral momentum at the slice and the assumption that the vorticity occurs at contracting points along the body will yield:

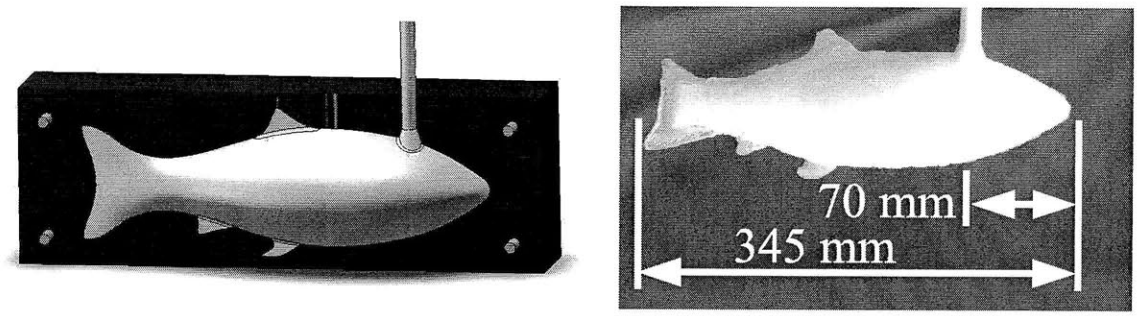

(a) **(b)**

Figure 7-8: (a) Fish robot in mold cavity following molding. (b) Final fish robot showing the total length and the length to the gantry rod.

$$L_y = \lambda_{am}(x)\left(\frac{\partial^2 h}{\partial t^2} + 2U\frac{\partial}{\partial t}\frac{\partial h}{\partial x} + U^2\frac{\partial^2 h}{\partial x^2}\right). \tag{7.14}$$

In (7.14), the term $\lambda_{am}(x)$ represents the equivalent added or apparent mass for the surrounding water, which may be approximated as

$$\lambda_{am}(x) \approx \frac{1}{4}\beta\pi s(x)^2\rho_w \tag{7.15}$$

where β is a geometric factor close to unity, $s(x)$ is the body depth at x, and ρ_w is the density of water [69].

The remaining terms in (7.13) must also be defined. First, the total equivalent flexural rigidity is computed from

$$EI_{eq}(x) = E_{fb}I_{fb}(x) + E_{cs}I_{cs}(x). \tag{7.16}$$

where the fb subscript denotes the parameters for the fish body and cs denotes the center support or backbone. Second, the density of the fish body ρ_{fb} and the density of the acrylic center support (backbone) ρ_{cs} are assumed to be constant throughout their respective material volumes. Thus, the equivalent linear density $\lambda_{eq}(x)$ of the fish beam model is given by

$$\lambda_{eq}(x) = \rho_{fb}A_{fb}(x) + \rho_{cs}A_{cs}(x) + \lambda_m(x). \tag{7.17}$$

The position dependence flexural rigidity and mass density along the fin are shown together in Fig. 7-12 for the parameter values in Table 7.1. Any of the required geometric parameters were obtained directly from the solid model. The top portion of the figure shows the flexural rigidity as a function of the normalized length $\bar{x} \triangleq \frac{x}{L_{fin}}$. The total flexural rigidity is dominated by the bending stiffness of the fish body with relatively little contribution from the center support (backbone) structure. Because

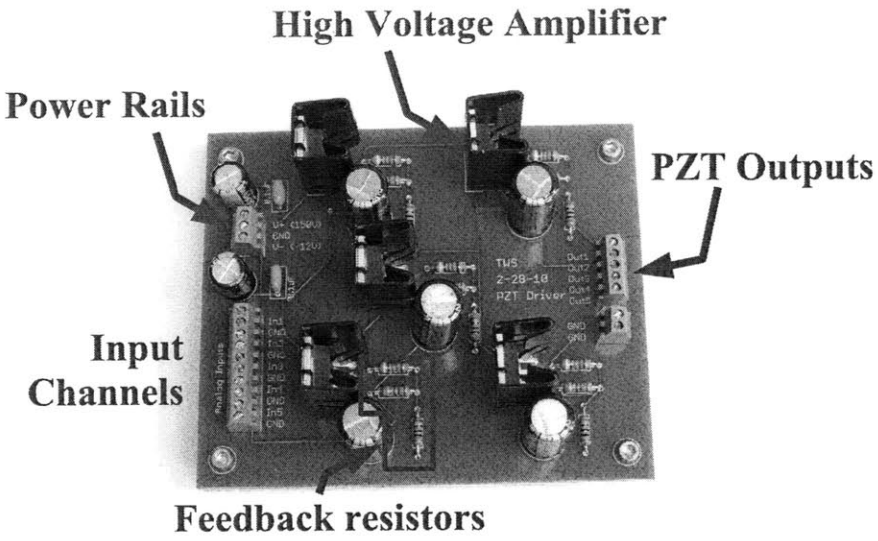

Figure 7-9: Custom designed amplifier board for applying arbitrary high voltage waveforms to PZT stacks.

of the sealing method for the actuation module, the silicone does not flow into the gaps between the ribs. This creates the large jump in bending stiffness near $\bar{x} = 0.3$ which represents the location of the final rib. The lower portion of Fig. 7-12 shows the equivalent mass density $\lambda_{eq}(x)$ along the length of the fin. The mass density is dominated primarily by the water added mass and the fish body mass. The mass density of the fish body also has the discontinuous jump associated with the sealed actuator section. Within $\lambda_{eq}(x)$, the actuators contribute the localized delta functions at each rib attachment point. As in the flexural rigidity, the center support structure has a negligible contribution.

Table 7.1: Parameter values for fish robot materials.

Parameter	Value	Units	References
E_{fb}	97.84	kPa	[113]
E_{cs}	2.75	GPa	
ρ_w	1.00	$\frac{g}{cm^3}$	
ρ_{fb}	1.08	$\frac{g}{cm^3}$	[113]
ρ_{cs}	1.20	$\frac{g}{cm^3}$	
m	26.0	g	
μ	92.3	$\frac{N \cdot s}{m^2}$	[113]
k	16.2	$\frac{N}{mm}$	

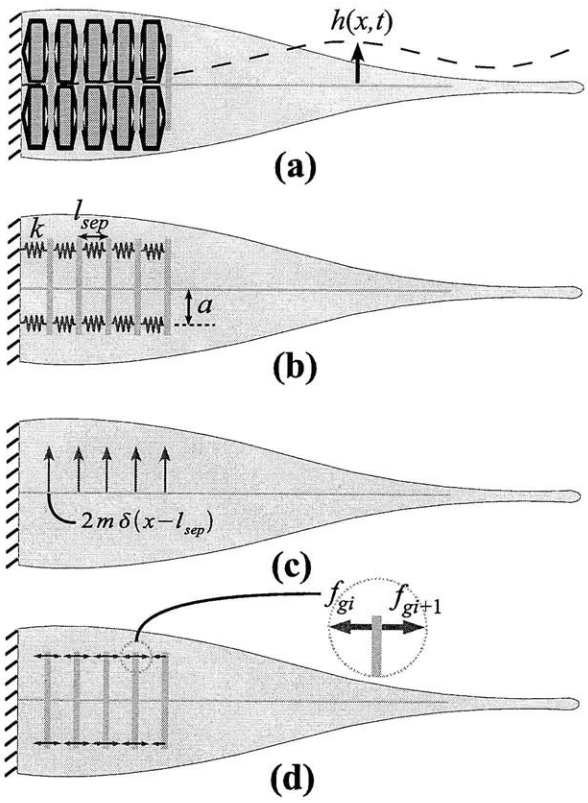

Figure 7-10: (a) Physical system showing beam centerline deflection. (b) Actuator stiffness effects. (c) Actuator mass effects. (d) Actuator forces for moment to voltage mapping.

7.4.2 Discrete Model

The continuous beam model presented in the previous section is useful for determining the exact vibration response of the beam structure and can also be used to determine a continuous actuator moment distribution $M_a(x,t)$. However, for the purposes of numerical simulation and for analytically tractable methods of vibration analysis, a discrete model of the beam vibration will be described in this section. This model is also advantageous for directly accounting for the discrete nature of the actuators and for subsequent studies in control using reduced order models.

The discrete beam model is shown in Fig. 7-13. The model consists of n rigid links of length l. The i^{th} link is connected to the $(i-1)^{th}$ link with a torsional spring κ_i. The horizontal deflection of each link is assumed to be small and therefore the generalized coordinates of the discrete beam are the center of mass vertical displacements h_i, where the center of mass of the i^{th} link is located a distance l_{Ci} from the i^{th} joint. Thus, for small displacements, another suitable set of generalized coordinates is the angular deflection of each link θ_i with respect to the beam centerline reference. The linearized change of coordinates between vertical deflections and joint rotations is then given by

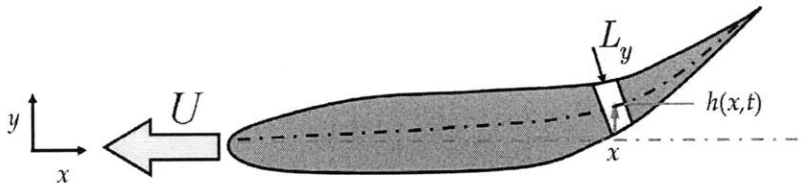

Figure 7-11: Lateral force acting on an infinitesimal slice of the fish body moving forward at a velocity U.

$$\begin{aligned} \mathbf{h} &= l \begin{pmatrix} \frac{l_{C1}}{l} & 0 & 0 & \dots & 0 \\ 1 & \frac{l_{C2}}{l} & 0 & \dots & 0 \\ & & \ddots & & \\ 1 & 1 & \dots & 1 & \frac{l_{Cn}}{l} \end{pmatrix} \boldsymbol{\theta} \\ &\triangleq \mathbf{S}\boldsymbol{\theta} \end{aligned} \tag{7.18}$$

where $\mathbf{h} = [h_1 \quad h_2 \quad \dots \quad h_n]^T$ and $\boldsymbol{\theta} = [\theta_1 \quad \theta_2 \quad \dots \quad \theta_n]^T$. Applied at each joint within the beam are the reaction forces f_i. These reaction forces affect both the linear momentum and angular momentum of each segment. Unlike the continuous beam model, the present model can readily account for rotational inertia. The i^{th} link is assumed to have a rotational inertia J_i in addition to the translational mass m_i.

The next major component of the discrete model is the attachment of the actuators to the appropriate individual beam segments. As in the continuous model, each actuator is modeled as a lumped mass m rigidly connected to a rib and a stiffness k connected between the ribs at a distance a from the backbone centerline. The specific segments where the actuators are attached will be determined by the discretization length l. These segments will be denoted by the letter p and a number in the subscript. For example, θ_{p1} denotes the first actuator attachment segment and not the first overall segment. The deflection of a passive stiffness k for an actuator is then approximated using $a(\theta_{pj+1} - \theta_{pj})$ where $j = 1, \ 2, \dots \ N$. For simplicity, the ribs will be assumed to travel through the center of mass of the nearest link. To each actuator mass, an actively generated force is applied as defined in the continuous model. Recall that the resulting moments depend only on the voltage differences $V_{diff,i}$ between the i^{th} agonist cell and antagonist cell PZT voltages.

From the Newton-Euler equations of motion, the model of the discrete beam can now be written compactly as

$$\mathbf{M}_{sys}\ddot{\mathbf{h}} + \mathbf{B}_{sys}\dot{\mathbf{h}} + \mathbf{K}_{sys}\mathbf{h} = \mathbf{Q}\mathbf{V}_{diff} \tag{7.19}$$

where $\mathbf{V}_{diff} = [V_{diff,1} \quad V_{diff,2} \quad \dots \quad V_{diff,N}]^T$, $\mathbf{Q}$ is the input distribution matrix, $\mathbf{M}_{sys}$ is the assembled system mass matrix, $\mathbf{K}_{sys}$ is the system stiffness matrix, and $\mathbf{B}_{sys}$ is the damping matrix. The mass matrix in (7.19) may be written more explicitly as

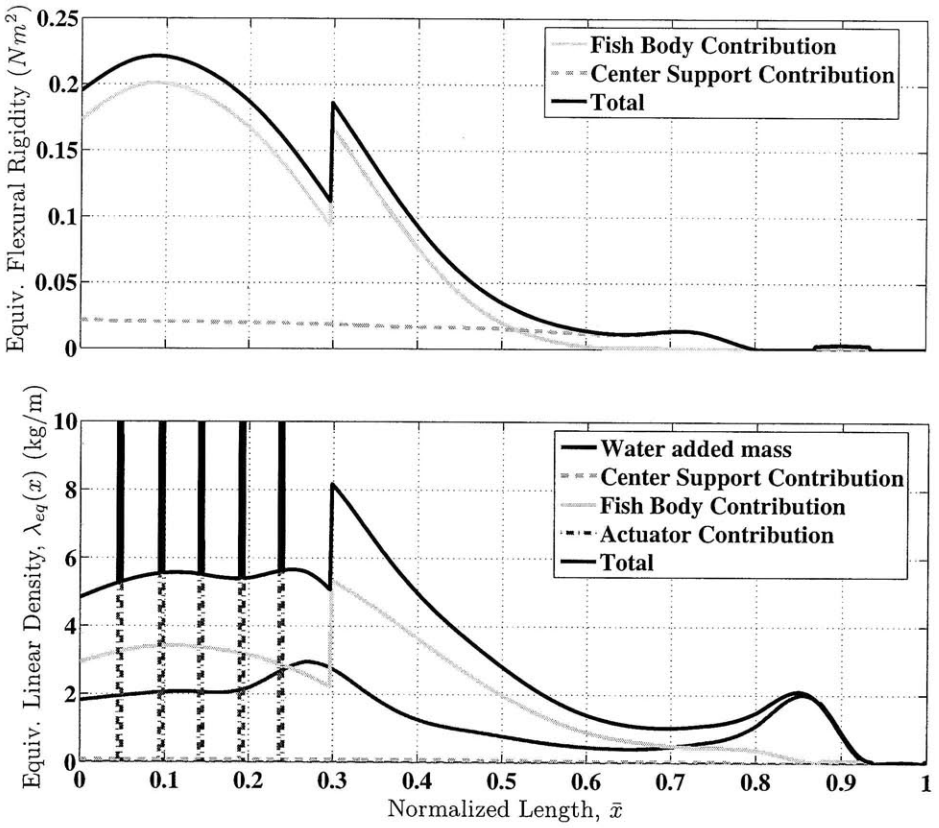

Figure 7-12: Distribution of flexural rigidity and mass density along the length of the freely vibrating fish body.

$$\mathbf{M}_{sys} = \mathbf{S}^{-T}(\mathbf{J}_R + \mathbf{J}_A)\mathbf{S}^{-1} - \mathbf{S}^{-T}\mathbf{L}_F\mathbf{D}^{-1}(\mathbf{M}_T + \mathbf{M}_A) \tag{7.20}$$

where $\mathbf{J}_R$ is the rotational inertia matrix for the lumped segments:

$$\mathbf{J}_R = \begin{pmatrix} J_1 & & & \\ & J_1 & & \\ & & \ddots & \\ & & & J_n \end{pmatrix}, \tag{7.21}$$

$\mathbf{J}_A$ is the rotational inertia due to the actuators acting only at the p_j segments:

$$\mathbf{J}_A = \begin{pmatrix} \ddots & & & & \\ & 2ma^2 & & & \\ & & \ddots & & \\ & & & 2ma^2 & \\ & & & & \ddots \end{pmatrix}, \tag{7.22}$$

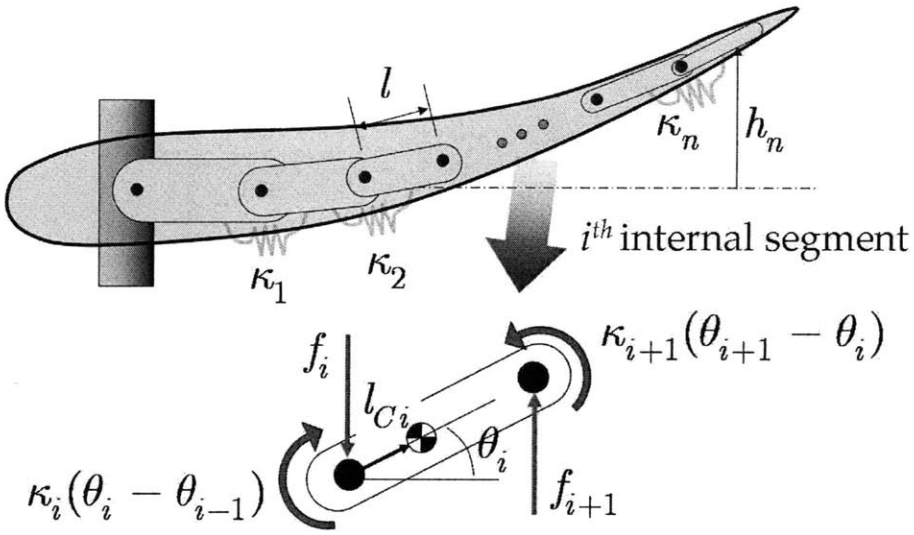

Figure 7-13: Lumped parameter definitions for the discrete beam model of the fish body.

$\mathbf{L}_F$ is the matrix representing the moment arms of the internal revolute joint reactions:

$$\mathbf{L}_F = \begin{pmatrix} l_{C1} & l - l_{C1} & & & \\ & l_{C2} & l - l_{C2} & & \\ & & \ddots & \ddots & \\ & & & & l - l_{Cn-1} \\ & & & & l_{Cn} \end{pmatrix}, \tag{7.23}$$

$\mathbf{D}$ is the difference matrix arising from the linear momentum equation:

$$\mathbf{D} = \begin{pmatrix} -1 & 1 & & & \\ & -1 & 1 & & \\ & & \ddots & \ddots & \\ & & & & 1 \\ & & & & -1 \end{pmatrix}, \tag{7.24}$$

$\mathbf{M}_T$ is the translational mass of each beam segment:

$$\mathbf{M}_T = \begin{pmatrix} m_1 & & & \\ & m_1 & & \\ & & \ddots & \\ & & & m_n \end{pmatrix}, \tag{7.25}$$

and $\mathbf{M}_A$ is the translational inertia of the actuators acting only at the p_j segments:

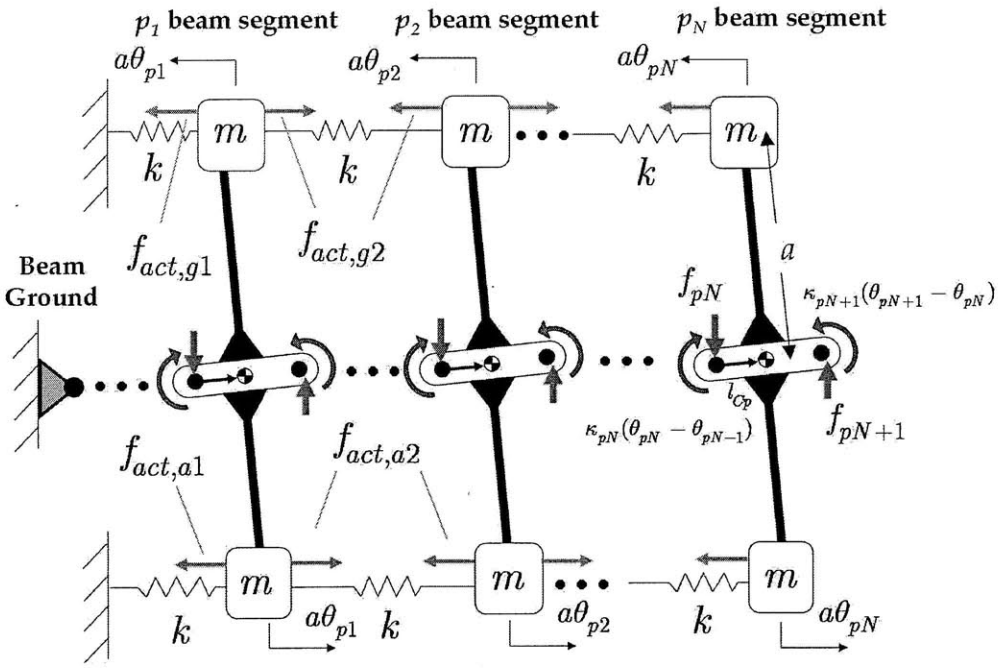

Figure 7-14: Definitions associated with the actuator attachment points in the discrete beam model.

$$\mathbf{M}_A = \begin{pmatrix} \ddots & & & & \\ & 2m & & & \\ & & \ddots & & \\ & & & 2m & \\ & & & & \ddots \end{pmatrix}. \tag{7.26}$$

Similarly, the stiffness matrix in (7.19) may be written more explicitly as

$$\mathbf{K}_{sys} = \mathbf{S}^{-T}\mathbf{K}_R\mathbf{S}^{-1} + 2ka^2\mathbf{S}^{-T}\mathbf{T}\mathbf{S}^{-1} \tag{7.27}$$

where $\mathbf{K}_R$ is the tri-diagonal Toeplitz second difference matrix:

$$\mathbf{K}_R = \begin{pmatrix} \kappa_1 + \kappa_2 & & & & & \\ -\kappa_2 & \kappa_2 + \kappa_3 & -\kappa_3 & & & \\ & \ddots & \ddots & \ddots & & \\ & & & & & -\kappa_n \\ & & & & -\kappa_n & \kappa_n \end{pmatrix} \tag{7.28}$$

and $\mathbf{T}$ is the matrix used to establish the equivalent torsional stiffness of the actuator passive stiffness:

$$\mathbf{T} = \begin{pmatrix} 2 & & -1 & & \\ & \ddots 0 \ddots & & \ddots 0 \ddots & \\ -1 & & 2 & & -1 \\ & \ddots 0 \ddots & & \ddots 0 \ddots & \\ & & -1 & & 1 \end{pmatrix}. \tag{7.29}$$

Note that in $\mathbf{T}$, the entries are placed at the appropriate p_j rows and columns. The damping matrix in (7.19) can be written using a central difference scheme applied to (7.12):

$$\mathbf{B}_{sys} = \begin{pmatrix} \beta_1 + \beta_2 & & & & \\ -\beta_2 & \beta_2 + \beta_3 & -\beta_3 & & \\ & \ddots & \ddots & \ddots & \\ & & & & -\beta_n \\ & & & -\beta_n & \beta_n \end{pmatrix} \tag{7.30}$$

Finally, the matrix $\mathbf{Q}$ is given explicitly by

$$\mathbf{Q} = a\phi_1 \mathbf{S}^{-T} \mathbf{A} \tag{7.31}$$

where $\mathbf{A}$ is the $n \times N$ matrix with staggered elements at the p_j rows:

$$\mathbf{A} = \begin{pmatrix} 1 & -1 & & & \\ & 1 & -1 & & \\ & & & \cdots & \\ & & & & 1 \end{pmatrix}. \tag{7.32}$$

From this model structure, the values of the lumped parameters must be assigned based on the continuous beam parameter distributions discussed previously. The appropriate integrals are listed below.

$$l_{Ci} = \frac{\int_{(i-1)l}^{il} x\lambda_{eq}(x)dx}{\int_{(i-1)l}^{il} \lambda_{eq}(x)dx} - l(i-1) \tag{7.33}$$

$$\kappa_i = \frac{1}{\int_{(i-1)l}^{il} \frac{1}{EI_{eq}(x)} dx} \tag{7.34}$$

$$\beta_i = \frac{\mu}{l^3} \int_{(i-1)l}^{il} I_{fb}(x)dx \tag{7.35}$$

$$m_i = \int_{(i-1)l}^{il} \lambda_{eq}(x)dx \tag{7.36}$$

$$J_{Ci} \approx \frac{1}{4}m_i b_i^2 + \frac{1}{12}m_i l^2 \tag{7.37}$$

In (7.37), each segment of the fish body is approximated using elliptical cylinders having a minor axis of b_i which is the appropriate average of the continuous function $b(x)$ representing the half width of the fish body as taken directly from the solid model:

$$b_i = \frac{1}{l}\int_{(i-1)l}^{il} b(x)dx. \tag{7.38}$$

In subsequent analysis, it will at times be convenient to approximate the damping matrix in (7.30) using Rayleigh, or proportional, damping:

$$\mathbf{B}_{sys} \approx c_1\mathbf{K}_{sys} + c_2\mathbf{M}_{sys} \tag{7.39}$$

where c_1 and c_2 are computed based on a knowledge of two modal damping ratios. The damping ratios are typically for the first two modes (ζ_1 and ζ_2) and can be computed by solving

$$c_2 + c_1\omega_i^2 = 2\omega_i\zeta_i \quad i = 1,\ 2 \tag{7.40}$$

simultaneously with ω_i as the natural frequency of the i^{th} mode of the undamped system [13]. This approximation will work quite well for systems with damping in the tridiagonal form in (7.30). The convenience of this approximation is that the resulting mode shapes of the damped system are identical to the undamped system and the damping matrix is diagonalized by the mode shapes (eigenvectors) from the associated generalized eigenvalue problem:

$$\mathbf{K}\boldsymbol{\phi}_i = \omega_i^2\mathbf{M}\boldsymbol{\phi}_i \quad i = 1,\ 2, \ldots,\ n. \tag{7.41}$$

7.5 Creating Traveling Waves in Flexible Structures

A majority of biological fish species generate thrust by using distributed muscles to bend their body into a backward-traveling propulsive wave. Although other swimming mechanisms exist, the traveling wave propulsion is very dominant behavior in carangiform swimmers such as trout [110], [95], [25]. The primary goal of this chapter is to recreate, as closely as possible, the backwards propagating wave to generate thrust with the biorobotic fish. The cellular actuators are a new and enabling technology that can be used approximate the localized effects of muscle within the fish and can utilize structural resonant frequencies to increase tail beat amplitude.

This section aims to describe the methods by which desired swimming kinematics can be approximated in the robot by synthesizing the appropriate PZT voltage inputs. The methods applied in this section may all be termed inverse dynamics. In the subsequent analysis, a desired kinematic behavior (e.g. fin position, velocity, and acceleration) is specified and inserted into the governing dynamic equation(s) to obtain constraints on the forces or moments required to produce such kinematics. The forces and moments can then be mapped to the required PZT voltage inputs. The voltage solutions do not specify a unique voltage to each cell and therefore allow for power optimization between cell pairs, which is another tremendous advantage of applying the distributed cellular architecture.

This approach can be viewed as a logical compliment to that of Valdivia and Youcef-Toumi [105] who used the desired swimming kinematics to synthesize material property distributions and geometry. Their approach solved an infinite dimensional inverse problem of obtaining parameter distributions that could be excited using a single actuator. In their design implementation, the material parameters were approximated discretely [105] [113]. By contrast, the present approach uses the known material property distributions of a pre-specified design to solve for the infinite dimensional (i.e. distributed) actuator inputs. These inputs are then approximated in the prototype using discrete cellular actuators.

The remainder of this section examines desired kinematics and various related input synthesis methods. The desired kinematics of carangiform swimmers are examined to develop a closed form expression for the spatiotemporal lateral fin deflection for the specific robot design. Subsequent analysis will yield three methods of solving the inverse dynamics for input synthesis: 1)Integrating the continuous model directly, 2) Employing a discrete modal decomposition, and 3) Applying a heuristic method. The first method is viewed as the most dynamically accurate approach to constructing the required actuator inputs and it uses all of the available information about the system. The remaining methods, however, have advantages of simplicity and real-time implementation capability and allow for established vibration results (e.g. modal controllability) to be applied effectively. Although several other methods exist, and indeed variations on the present methods also exist, it will be valuable to explore these particular methods of input synthesis to guide future bio-robotic designs using PZT cellular artificial muscle actuators.

7.5.1 Desired Kinematics

Fish kinematics has been investigated and well characterized by many researchers in both biology and engineering. For the particular carangiform swimmer considered here, the desired kinematics may be expressed in the functional form:

$$h_{tw}(x,t) = (\eta_0 + \eta_1 x + \eta_2 x^2)\sin(\kappa x - 2\pi f t) \tag{7.42}$$

where the term in parentheses that pre-multiplies the sine wave is the quadratic amplitude envelope used by many investigators (e.g. [12], [105], [118]). Within the sine argument, the constant κ is referred to as the wave number for the traveling wave computed using $\kappa = \frac{2\pi}{\lambda}$ with λ representing the wave length; f is the body wave frequency.

Based on a survey of existing literature, Valdivia showed that the constants in the quadratic envelope may be approximated for carangiform swimmers as follows [113]:

$$\kappa \approx \frac{7}{L} \tag{7.43}$$

$$\eta_0 \approx 0.004 f L \tag{7.44}$$

$$\eta_1 \approx -0.02 f \tag{7.45}$$

and

$$\eta_2 \approx \frac{0.04 f}{L} \tag{7.46}$$

Note that the expression in (7.43) provides a value of the wave number that is in good agreement with the values described in [110] for trout of length L. In most cases, approximately one wavelength resides on the body at any given time since (7.43) can be equivalently expressed as $\lambda = 0.9L$.

Using $L = 345$ mm and $f = 3$ Hz, an example of the desired traveling wave kinematics is shown in Fig. 7-15 at several times throughout a single oscillation period of length T. The corresponding amplitude envelope for the fish centerline is shown in Fig. 7-16. Both of these plots indicate that most of the motion in carangiform swimmers is concentrated in the caudal fin, which provides a sound basis for anchoring the fish to the gantry as described in Section 7.3. In subsequent calculations, the kinematic behavior anterior of the gantry attachment point will be ignored and only the posterior motion will be considered across the length L_{fin}.

These desired kinematics serve as the basis for synthesizing actuator inputs. However, it will also be useful to note that biological carangiform swimmers have forward velocities U that can be approximated using [108]:

$$U \approx 0.628 L \cdot f. \tag{7.47}$$

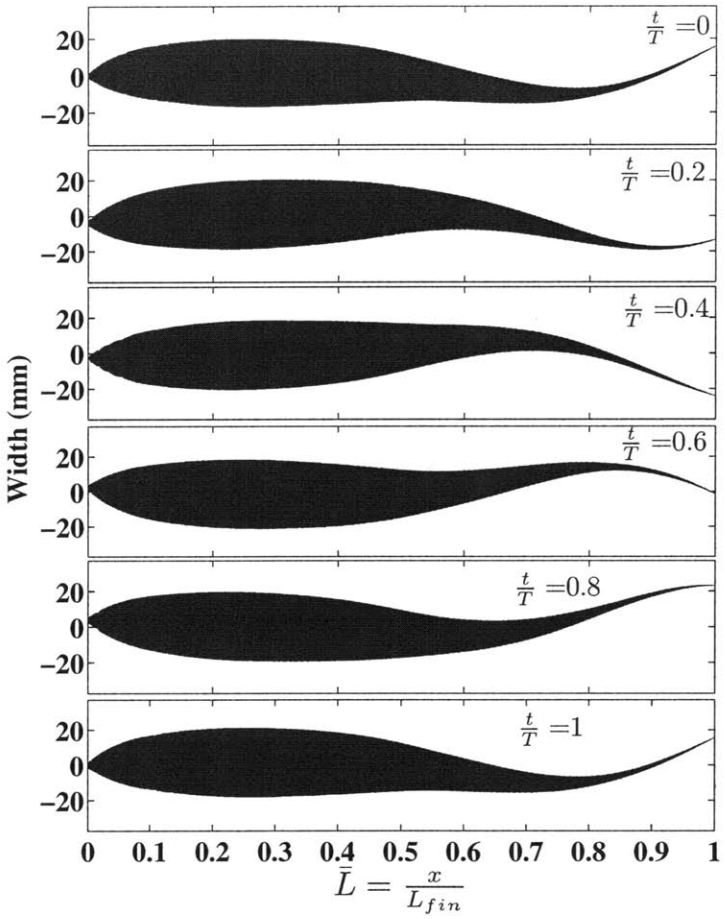

Figure 7-15: Desired kinematics for carangiform swimming fish at a 3 Hz tail beat frequency.

The above expression will be particularly useful when considering the effects of lateral forces in (7.13).

7.5.2 Direct Method

The direct method of PZT voltage synthesis computes actuator inputs based on the governing equation for the motion in (7.13) and an approximate mapping back to actuator voltages. For a forward solution, this equation will admit traveling waves of the form $h(x,t) = \Re(H(x)e^{j\omega t})$. Moreover, closed form solutions for a simplified expression of (7.13) can also be stated in terms of Green's functions [113]. For computing the required moment distribution, the beam dynamics in (7.13) may be written as

$$\frac{\partial^2 M_a(x,t)}{\partial x^2} = G_{tw}(x,t) \tag{7.48}$$

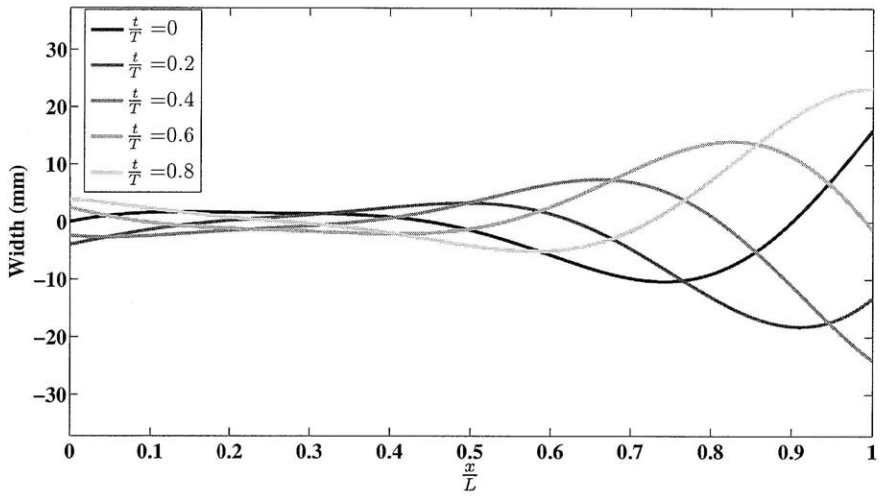

Figure 7-16: Superimposed centerline deflections of the fish body at various values through a single period of motion.

where the right hand side of the above expression represents the entire right hand side of (7.13) evaluated with $h(x,t) = h_{tw}(x,t)$ given by (7.42). Hence, (7.48) represents a simple PDE that may be directly integrated to find admissible continuous actuator moment distributions $M_a(x,t)$. Performing the integration yields:

$$M_a(x,t) = \iint G_{tw}(x,t)dxdx + G_0(t)x + G_1(t) \tag{7.49}$$

where $G_0(t)$ and $G_1(t)$ are arbitrary time functions. In practical designs the actuator moment and its first spatial derivative at the tail tip would necessarily be zero, which could be enforced by solving for the second and third terms on the right hand side of (7.49). However, because the actuators are only in the anterior section of the fish, these terms will be taken as zero for simplicity. An example of an admissible moment distribution is shown schematically in Fig 7-17 (a). This moment distribution is spatially sampled at the actuator points as shown in (b). This step is required order to reflect that the actuators only apply moments as described by (7.11). As the number of actuators N increases along the length, a higher fidelity reconstruction of the moment distribution will be achieved.

A numerical example of the required moment distribution for $f = 3Hz$ and $L = 345$ mm is shown in Fig. 7-18. In the figure, the surface topology shows a rearward 'bending' of the moments in time at lengths near the gantry attachment point (shown as a length of 0 in this plot). This bent shape represents a temporal phase lag of the applied moments near the base and a simultaneous application of moments further down the tail. Any particular cross section at a fixed length x will be found to oscillate as a sine wave at $f = 3Hz$.

As shown in Fig. 7-10 (d), the forces applied at each rib are assumed to be parallel to the neutral axis of bending. Therefore, using (7.9) and (7.10), yields a unique linear

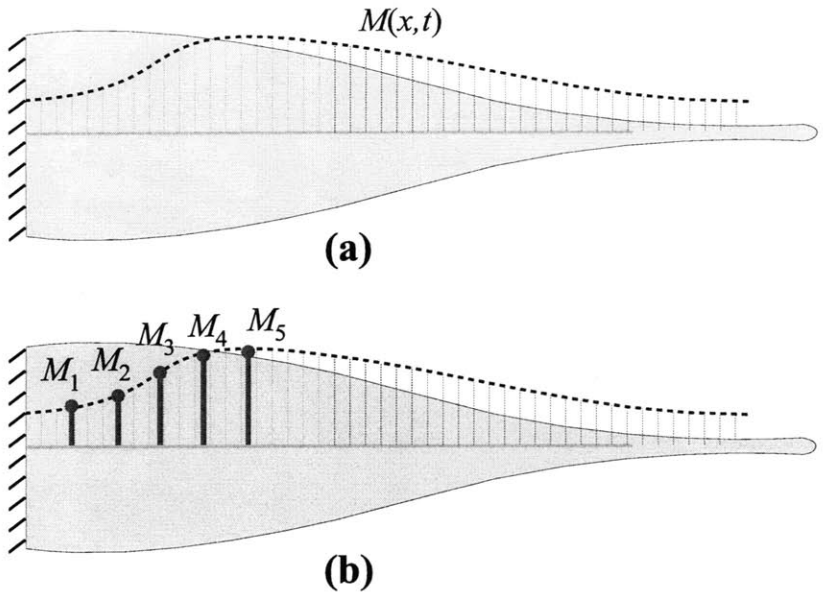

Figure 7-17: (a) Distributed moment that must satisfy governing partial differential equation. (b) Spatially sampled moment used to estimate actuator voltages.

mapping from voltage differences to moments:

$$\begin{pmatrix} M_a(l_{sep},t) \\ M_a(2l_{sep},t) \\ \vdots \\ M_a(Nl_{sep},t) \end{pmatrix} = a\phi_1 \begin{pmatrix} 1 & -1 & & \\ & 1 & -1 & \\ & & \ddots & \\ & & & 1 \end{pmatrix} \begin{pmatrix} V_{diff,1} \\ V_{diff,2} \\ \vdots \\ V_{diff,N} \end{pmatrix}. \tag{7.50}$$

The inverse map is therefore

$$\begin{pmatrix} V_{diff,1} \\ V_{diff,2} \\ \vdots \\ V_{diff,N} \end{pmatrix} = \frac{1}{a\phi_1} \begin{pmatrix} 1 & 1 & \cdots & 1 \\ & 1 & \cdots & 1 \\ & & \ddots & \\ & & & 1 \end{pmatrix} \begin{pmatrix} M_a(l_{sep},t) \\ M_a(2l_{sep},t) \\ \vdots \\ M_a(Nl_{sep},t) \end{pmatrix}. \tag{7.51}$$

Now that the required PZT voltage differences are specified, there are two remaining steps in the synthesis procedure: 1) assure that the voltages are within a range reasonable for application to the PZT and 2) derive a power-optimal method for selecting the agonist and antagonist voltages within the desired difference. Step 1 is achieved by first identifying the maximum voltage during steady state as

$$V_{diff,max} = \max_{\substack{t_{ss} \le t \le (t_{ss}+T) \\ 1 \le i \le N}} V_{diff,i}(t) \tag{7.52}$$

where t_{ss} is the time required for the system to reach steady state given the synthesized inputs and $T = \frac{1}{f}$ is the oscillation period. The new scaled voltages are then given by

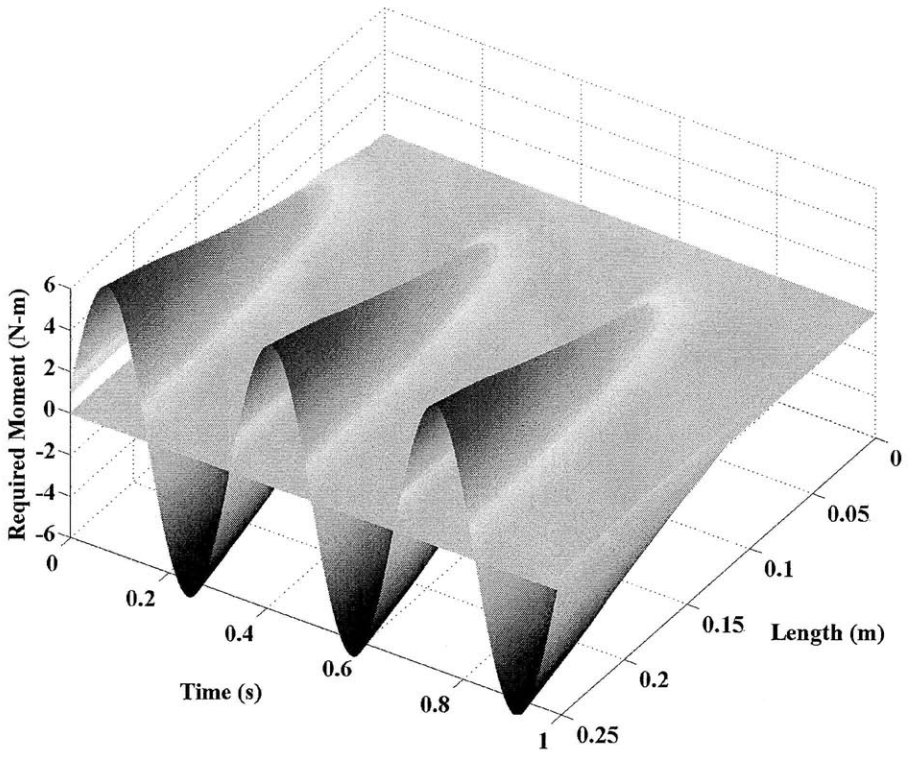

Figure 7-18: Spatio-temporal moment distribution within the fish that satisfies the required beam vibration equation. The surface shown is for a 3 Hz tail beat frequency.

$$\widetilde{V}_{diff,i} = \left(\frac{V_{diff,i}}{V_{diff,max}} \right) V_{pzt}^{max}. \tag{7.53}$$

Note that the nonlinear terms in (7.13) are typically very weak (e.g. U is typically small so that $L_y \approx \lambda_{am}(x)\frac{\partial^2 h}{\partial t^2}$, which makes the governing PDE linear). Therefore, the system response before and after input scaling will look identical in morphology because linear dynamical systems obey the well known scaling property. For the results discussed in Section 7.6, the ratio $\frac{V_{diff,max}}{V_{pzt}^{max}}$ is typically no greater than 1.5. Therefore, the synthesized voltages at the frequencies considered are typically no more than 50% higher than what the PZT manufacturer suggests for V_{pzt}^{max} and the moment requirements for the desired traveling waves are well matched to the PZT actuators.

The final step for completing the voltage synthesis is to select a specific agonist and antagonist voltage for each actuator pair:

$$\widetilde{V}_{diff,i} = V_{g,i} - V_{a,i} \quad i = 1, \ , 2, \ldots, \ N. \tag{7.54}$$

This freedom of choice in voltage selection allows for the optimization of power, which is an advantage inherent in the antagonistic cellular architecture. For the i^{th} actuator pair, the power supplied to the actuator will be proportional to $V_{g,i}^2 + V_{a,i}^2$. Hence, power optimization is the constrained minimization of the paraboloid

$$P = V_g^2 + V_a^2 \tag{7.55}$$

subject to the constraint that the voltage difference is the desired difference $V_{diff,des}$ given by

$$V_{diff,des} = V_g - V_a \iff V_g = V_{diff,des} + V_a. \tag{7.56}$$

A graphical interpretation of this optimization is shown in Fig. 7-19 wherein the constraint (7.56) appears as straight lines. First, note that the PZT cannot withstand negative voltages (see Appendix A for a discussion). This limits the solutions to those in the first quadrant where $V_g \in [0, V_{pzt}^{max}]$ and $V_a \in [0, V_{pzt}^{max}]$. Therefore, Fig. 7-19 shows that smallest voltages that satisfy the constraint will always be

$$V_g = \begin{cases} V_{diff,des} & V_{diff,des} \geq 0 \\ 0 & V_{diff,des} < 0 \end{cases} \tag{7.57}$$

and

$$V_a = \begin{cases} 0 & V_{diff,des} \geq 0 \\ V_{diff,des} & V_{diff,des} < 0 \end{cases} \tag{7.58}$$

The above voltage selection criterion is then applied to the voltage difference for each actuator pair in order to minimize power and meet the desired voltage difference constraint.

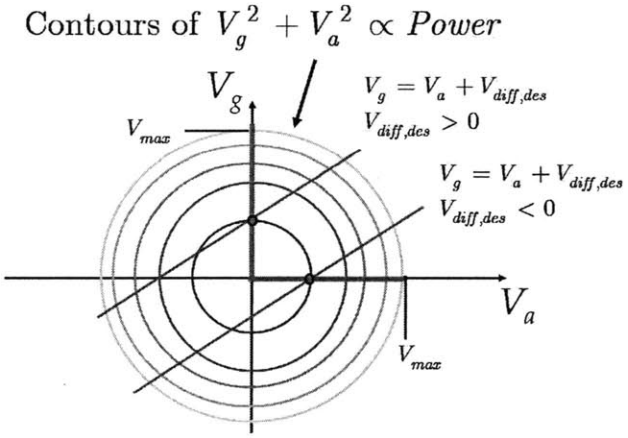

Figure 7-19: Selection of optimal agonist and antagonist voltages to minimize power.

Based on the previously defined desired kinematics and material parameters, the synthesized voltages for 3 Hz are shown in Fig. 7-20. The bottom portion of the

figure shows the voltage differences for each actuator pair. The voltages are phased temporally and scaled in amplitude with respect to one another. Actuator pairs 1 and 2 closest to the baseplate (see Fig.7-5) are contracting almost simultaneously while the remaining actuators receive phase delayed and reduced amplitude signals. The upper portion of the figure shows how these voltages are split according to the optimality conditions in (7.57) and (7.58). The synthesized voltages may be compactly parameterized by defining the following amplitude scale ratio $\alpha_{r,i}$ and phase delay parameters $\delta_{d,i}$:

$$\alpha_{r,i} \triangleq \frac{\max(V_{diff,i})}{V_{pzt}^{max}} \quad i = 1,\ 2, \ldots,\ N \tag{7.59}$$

and

$$\delta_{d,i} = 2\pi f(t_{peak,i} - t_{peak,i-1}) \quad i = 2, \ldots,\ N \tag{7.60}$$

where $t_{peak,i}$ is the time at which the i^{th} actuator pair voltage difference reaches its maximum within a given period. The values of these parameters for the continuous synthesis method are shown in Table 7.2.

Table 7.2: Voltage parameters for continuous model input synthesis method

Amplitude Scale Parameter $\alpha_{r,i}$	**Phase Delay Parameter** $\delta_{d,i}$ (rad)
1.00	-
0.98	0.023
0.90	0.047
0.72	0.094
0.42	0.165

7.5.3 Modal Method

The continuous model applied to synthesize voltages assures that the exact dynamics of the structure are considered. However, there is no convenient means to establish how the natural vibration characteristics of the beam are superposed in order to obtain the response of the fin. Because of computational simplicity and conditions of overall power consumption, there may be a desire to approximate the solution to the inverse dynamics using a superposition of only the most controllable and most prevalent vibration modes leading to the desired kinematics. Toward this end, the discrete beam model will be employed as it captures the dynamics in a form convenient for modal analysis. It will also allow for an investigation of model order on the performance of the inverse dynamics algorithm. This will have particularly important implications in online implementations.

Taken alone, the natural modes of vibration are not suitable to create the desired kinematics because the natural mode shapes appear in the system as standing waves.

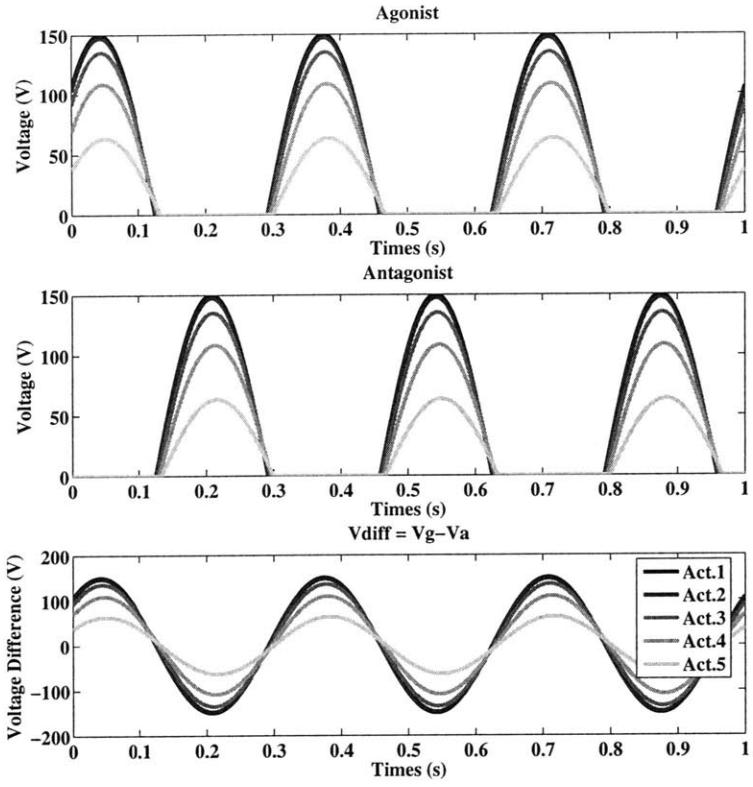

Figure 7-20: Synthesized voltage waveforms for continuous beam model at 3 Hz tail beat frequency.

However, [39] recently proposed a new methodology for input synthesis to create traveling waves that is based on well established modal superposition techniques. This method is applied and extended here to solve the inverse dynamics problem in the vibrating fin structure.

The goal of the modal method is to select this moment function as a weighted superposition of the natural modes of vibration. First, suppose that the right hand side of (7.19) is replaced with a time-varying moment vector $\mathbf{M}_a(t)$ that may be chosen arbitrarily. Next, proportional damping will be assumed so that the mode shapes in the system are real valued and will diagonalize $\mathbf{B}_{sys}$ in (7.19). The undamped eigenvalue problem for the discrete system is

$$\mathbf{K}\boldsymbol{\phi}_i = \omega_i^2 \mathbf{M}\boldsymbol{\phi}_i \quad i = 1,\ 2, \ldots,\ n. \tag{7.61}$$

where ω_i is the natural frequency of the i^{th} vibration mode and $\boldsymbol{\phi}_i$ is associated mode shape. These frequencies and mode shapes will be assembled into the matrices

$$\Phi = [\boldsymbol{\phi}_1\ \ \boldsymbol{\phi}_2\ \ \ldots\ \ \boldsymbol{\phi}_n] \tag{7.62}$$

and

$$\Lambda = \begin{pmatrix} \omega_1^2 & & 0 \\ & \ddots & \\ 0 & & \omega_n^2 \end{pmatrix}. \tag{7.63}$$

The desired traveling wave may be expressed in the discrete vibrating beam by sampling the continuous kinematics function in (7.42):

$$h_{tw,i}(t) = h_{tw}(x,t)\,|_{x_i = il} \qquad i = 1,\ 2, \ldots,\ n. \tag{7.64}$$

The desired traveling wave vector can be written as a superposition of the mode shapes:

$$\mathbf{h}_{tw}(t) = \Phi \eta_{tw}(t) \tag{7.65}$$

where $\eta_{tw}(t)$ is the vector of modal coordinates that achieve this decomposition. Therefore,

$$\eta_{tw}(t) = \Phi^{-1}\mathbf{h}_{tw}(t) = [(\Phi^T \mathbf{M}_{sys}\Phi)^{-1}\Phi \mathbf{M}_{sys}]\mathbf{h}_{tw}(t) \tag{7.66}$$

The moments can also be decomposed as a superposition of the natural modes premultiplied by the system mass matrix $\mathbf{M}_{sys}$. The primary reason for this premultiplication will be convenience. Thus, for another vector of coordinates $\alpha(t)$,

$$\mathbf{M}_a(t) = \mathbf{M}_{sys}\Phi\alpha(t). \tag{7.67}$$

Given the proportional damping assumption of (7.39), the dynamic equations may be written as the uncoupled system

$$\Phi^T \mathbf{M}_{sys}\Phi\ddot{\eta} + \Phi^T(c_1\mathbf{K}_{sys} + c_2\mathbf{M}_{sys})\Phi\dot{\eta} + \Phi^T\mathbf{K}_{sys}\Phi\eta = \Phi^T\mathbf{M}_a(t). \tag{7.68}$$

Substituting (7.67) into the above equation and letting $\eta = \eta_{tw}$ yields the required vector $\alpha(t)$ for creating the desired traveling wave:

$$\alpha(t) = \ddot{\eta}_{tw} + (\Phi^T\mathbf{M}_{sys}\Phi)^{-1}\Phi^T(c_1\mathbf{K}_{sys} + c_2\mathbf{M}_{sys})\Phi\dot{\eta}_{tw} + \Lambda\eta_{tw} \tag{7.69}$$

Therefore, using $\ddot{\eta}_{tw} = -(2\pi f)^2\eta_{tw} = -\omega^2\eta_{tw}$ and using (7.66) for η_{tw}, yields

$$\mathbf{M}_a(t) = \mathbf{G}_p\mathbf{h}_{tw}(t) + \mathbf{G}_v\dot{\mathbf{h}}_{tw}(t) \tag{7.70}$$

where $\mathbf{G}_p$ is the position gain matrix

$$\mathbf{G}_p = \mathbf{M}_{sys}\Phi(\Lambda - \mathbf{I}\omega^2)(\Phi^T\mathbf{M}_{sys}\Phi)^{-1}\Phi\mathbf{M}_{sys} \tag{7.71}$$

and $\mathbf{G}_v$ is the velocity gain matrix

$$\mathbf{G}_v = \mathbf{M}_{sys}\Phi(c_1\Lambda - c_2\mathbf{I})(\Phi^T\mathbf{M}_{sys}\Phi)^{-1}\Phi\mathbf{M}_{sys}, \tag{7.72}$$

which completes the method for input synthesis using modal superposition. Note that the position gain matrices will depend upon how closely the desired flapping frequency ω matches any of the existing natural frequencies in the matrix Λ while the velocity gain matrix will depend upon the proportional damping coefficients.

There are two practical considerations required for applying the foregoing input synthesis method. The first is that not all modes are controllable given the system's actuator input distribution. Second, the system order needs to be considered in order to accurately estimate the resonant frequencies and mode shapes.

To address the modal controllability, the measure proposed by [46] is used. The controllability of the i^{th} mode shape from the j^{th} input is given geometrically by the cosine of the angle between the input vector $\mathbf{q}_j$ which is the j^{th} column of $\mathbf{Q}$ in (7.19) and the mode shape $\boldsymbol{\phi}_i$. The result is taken as the controllability coefficient c_{ij}.

$$c_{ij} \triangleq \cos(\theta_{ij}) = \frac{|\varphi_i^T\mathbf{q}_j|}{||\varphi_i|| \cdot ||\mathbf{q}_j||} \tag{7.73}$$

The overall controllability of the i^{th} mode is denoted by χ_i and taken as the norm across all N inputs

$$\chi_i = \sqrt{c_{i1}^2 + c_{i2}^2 + \ldots + c_{iN}^2}. \tag{7.74}$$

Once the most controllable modes have been selected from the entire set, then the inverse dynamics may be approximated by replacing Λ and Φ with $\overline{\Lambda}$ and $\overline{\Phi}$ where $\overline{\Lambda} \in \mathbb{R}^{r\times r}$ for the natural frequencies of the r most controllable modes and $\overline{\Phi} \in \mathbb{R}^{n\times r}$ contains the mode shapes of the r most controllable modes.

Fig. 7-21 shows the mode contribution and controllability of the first 12 modes for a system having $n = 20$. The mode contribution coefficient is established by taking the absolute value of the associated modal coordinate computed using (7.66) and the mode controllability coefficient is computed using (7.74). For both cases, the coefficients were normalized to have a maximum value of unity. The plot shows that the first modes contribute the most information to the traveling wave kinematics. Furthermore, the controllability of the first modes is low because the portion of the fish body closest to the gantry does not deflect appreciably in these modes and yet the actuators exert all of their influence in that region. This is represented in Fig. 7-22 for the first four mode shapes. In Fig. 7-22, the arrows next to each mode shape indicate the relative orthogonality between the input direction and the mode shape. In situations of complete orthogonality, controllability of that mode shape is lost completely. It is important to note that although the first mode shapes have only small controllability, the actuators can still readily channel energy into these modes leading to increased amplitude near the associated resonant frequencies. The fundamental resonance for the discrete system is approximately $f = 1.7$ Hz. Because the traveling wave decomposition does not possess information beyond approximately mode 7, this is taken as the value of r for the truncated formulation. Although it is possible to take $r = N$ in order to create a discrete approximation to the continuous

model inverse dynamics, this is not practically feasible when numerical conditioning is considered.

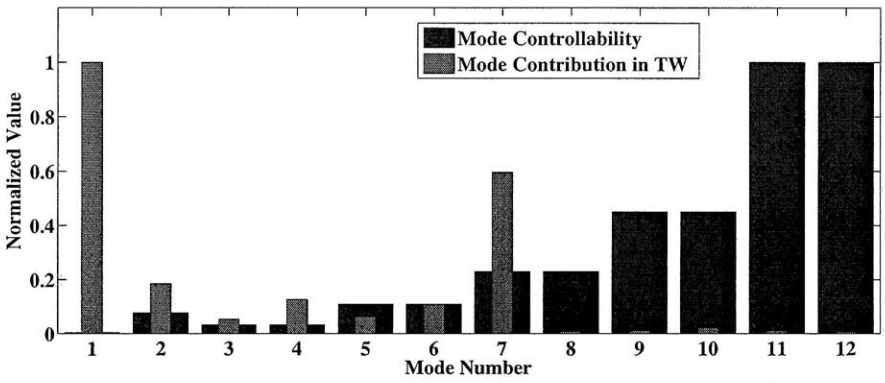

Figure 7-21: Modal decomposition of traveling wave and mode controllability based on input directions.

The numerical conditioning of a discrete system resonant frequency (i.e. eigenvalue) may be computed in terms of the condition number of the eigenvalue. This condition number is typically computed as the angle between the left and the right eigenvectors in the eigenvalue problem shown in (7.61). The condition numbers for the first several eigenvalues using different discretization lengths $l = \frac{L}{n}$ are considered in Fig. 7-23. As shown, if the mesh length l becomes too large, then the numerical conditioning becomes poor. However, this is not viewed negatively because lower order models can suitably capture the natural frequency locations, particularly at lower frequencies. Thus, to maintain good numerical conditions with as much accuracy as possible a value of $n = 20$ was used in all of the subsequent simulations.

The modal method described here provides the required moment vector $\mathbf{M}_a(t) = [M_{a,1}(t), \quad M_{a,2}(t), \ldots, \quad M_{a,n}(t)]^T$ using (7.70). The final step is to then map the moments to the corresponding PZT voltages. Eq. (7.51) is for mapping a sampled continuous moment distribution to a set of actuator inputs. However, in the case of the discrete model, the same idea is employed, but the mapping is modified to the expression in the right hand side of (7.19). Thus, the voltages and moments are related according to

$$\mathbf{M}_a(t) = \mathbf{Q}\mathbf{V}_{diff}(t) \tag{7.75}$$

which has no unique inverse because $\mathbf{Q} \in \mathbb{R}^{n \times N}$. As in the continuous model, increasing the number of actuators N yields a higher fidelity match between the voltage induced moments and the desired moments from the inverse dynamics. The closest solution in a least squares sense is

$$\mathbf{V}_{diff}(t) = \left(\mathbf{Q}^T\mathbf{Q}\right)^{-1}\mathbf{Q}^T\mathbf{M}_a(t). \tag{7.76}$$

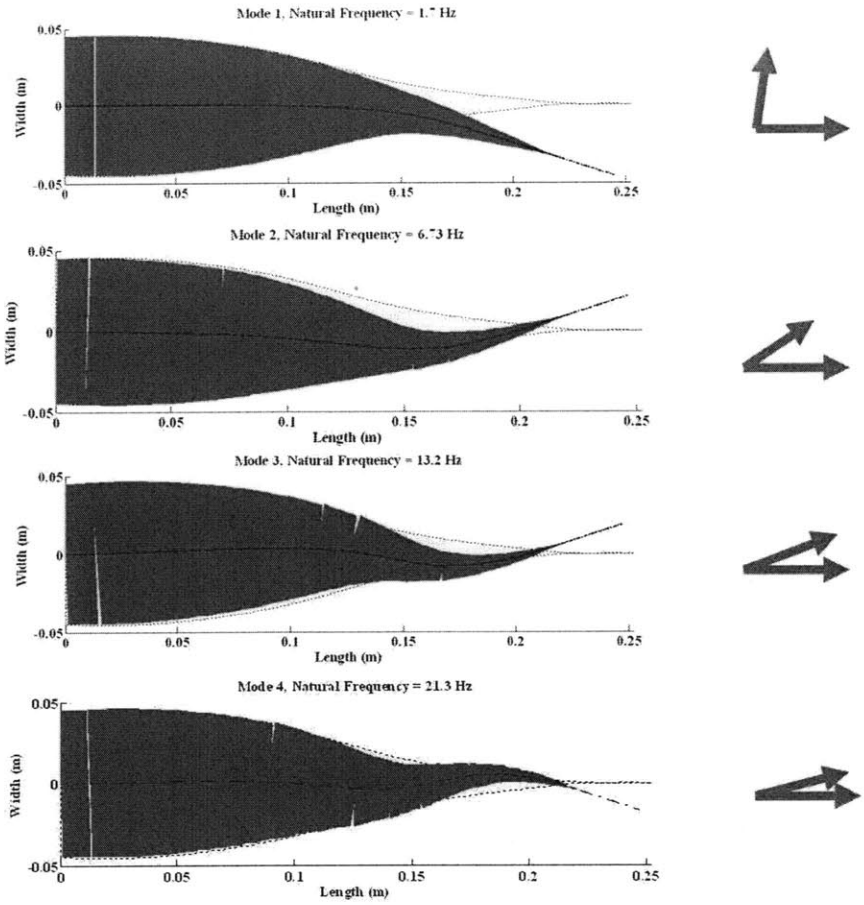

Figure 7-22: First four mode shapes of the fin based on the discrete beam model. To the right of each mode shape is a conceptual representation of the overall mode controllability; perpendicular arrows indicates low controllability.

which has been used to generate the voltages shown in Fig. 7-24 for $f = 3Hz$. In the figure, the same optimization techniques described in the continuous formulation were used. The modal scaling and phase parameters for this are shown in Table 7.3

7.5.4 Heuristic Method

As a final method for approaching the input synthesis, a heuristic technique is used. The technique assumes that the i^{th} actuator pair should be maximally activated in phase with the local lateral deflection $h_{tw}(il_{sep}, t)$ computed at the location corresponding to the actuator attachment. The resulting voltages are shown in Fig. 7-25 and the associated parametrization is listed in Table 7.4.

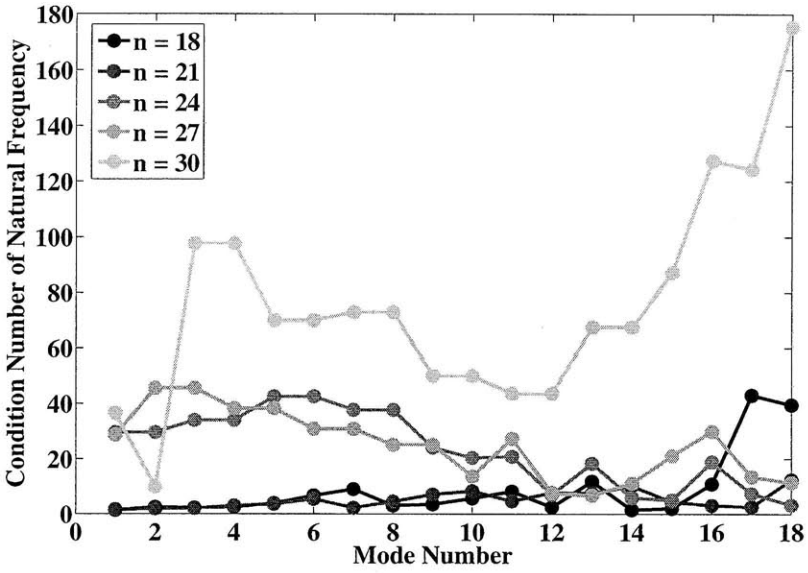

Figure 7-23: Eigenvalue condition numbers for different discretization levels.

7.6 Forward Simulation Results

This section provides the simulation results for the proposed synthesis methods. For each method, the fin response was obtained by forward simulating (i.e. numerically integrating) the discrete beam model in (7.19) with $n = 20$ and $\mathbf{V}_{diff}$ determined by one of the synthesis methods. Note that at this level of discretization, the tail shape appears approximately continuous.

The tail deflection shapes achieved using synthesis based on the continuous model are shown in Fig. 7-26 for three frequencies across the total 1 Hz to 3.5 Hz range considered. In this figure, the deflected tail shapes are overlaid at the point when the end of the tail reaches its maximum deflection. The largest simulated tip deflection of 14.46 mm is shown in the center plot and occurs when $f = 1.75$ Hz, which corresponds to the first natural frequency of vibration. However, note that in the top and the

Table 7.3: Voltage parameters for modal input synthesis method for $r = 7$ and $n = 20$.

Amplitude Scale Parameter $\alpha_{r,i}$	**Phase Delay Parameter** $\delta_{d,i}$ (rad)
0.81	-
0.93	0.031
1.00	0.132
0.78	0.236
0.40	0.310

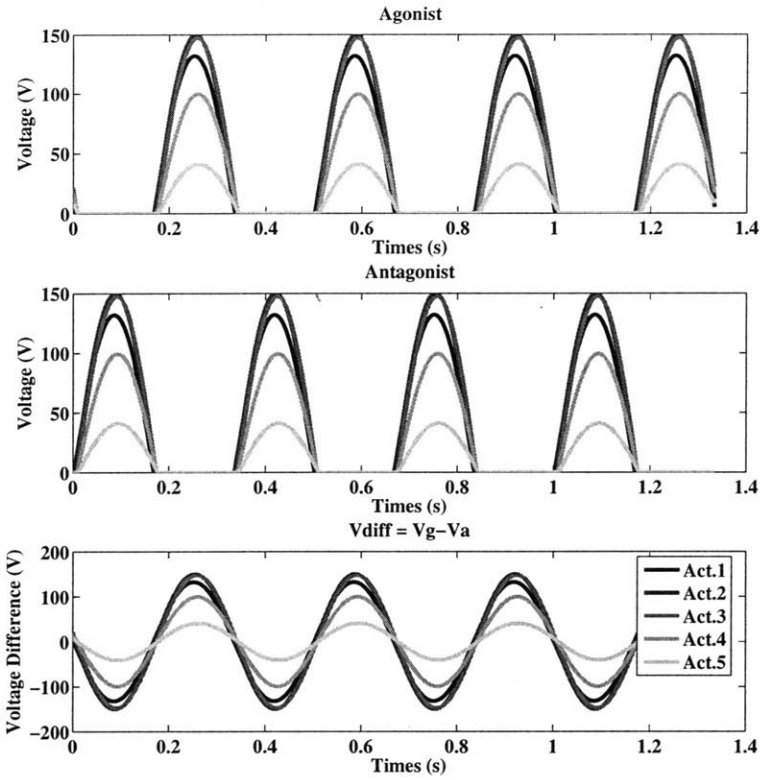

Figure 7-24: Synthesized voltage waveforms for modal decomposition method at 3 Hz tail beat frequency.

center plots, the tail centerline crosses itself, which is an indication that higher modes of vibration are also present.

Fig. 7-27 shows the simulated tail deflection for the modal decomposition method of voltage synthesis. As in the previous case, the deflected tail shapes are overlaid at the point when the end of the tail reaches its maximum deflection. The largest simulated tip deflection of 13.98 mm is shown in the center plot and again occurs when $f = 1.75$ Hz. Similarly, Fig. 7-28 shows the simulated tail deflection for the heuristic decomposition method of voltage synthesis wherein the maximum tail beat amplitude is 14.27 mm.

The complete simulation results of both tail beat amplitude and tail maximum caudal curvature are shown in Fig. 7-29. The curvature is included as an additional metric that could be correlated to swimming performance [110]. The results indicate that, with respect to tail beat amplitude, the fish will achieve the highest amplitude using the voltages synthesized with the continuous method. The next highest amplitude result is achieved using the heuristic method. The modal method provides the smallest amplitude of displacement.

Although these results seem to suggest that the continuous method should be universally employed, followed by the heuristic method, it is insightful to consider

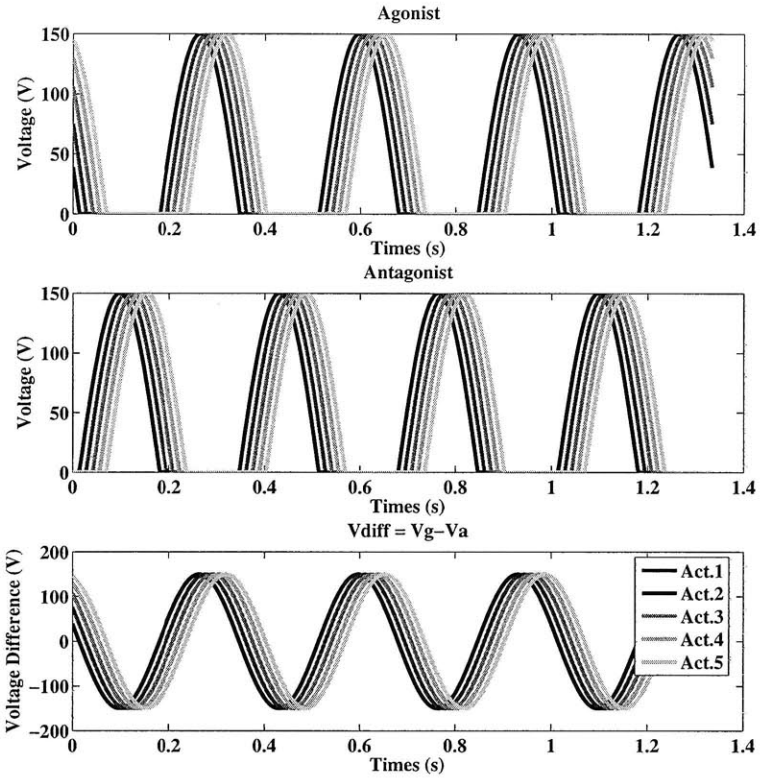

Figure 7-25: Voltage waveforms for a at 3 Hz tail beat frequency based on a heuristic activation method.

the power requirements for each method. The reactive (i.e. capacitive charging) power P_{VAR} for each method can be approximated by using the non resonant power analysis in Section 4.10.

$$P_{VAR} = 2\pi f (V_{pzt}^{max})^2 C \sum_{i=1}^{N} \alpha_{r,i}^2 \tag{7.77}$$

The results of power versus frequency for each method are shown in Fig. 7-30. Note that the listed power values represent reactive power requirements only for conditions where the charge on the capacitor must be sourced from an amplifier on each cycle. In reality, this power requirement can be drastically reduced using the techniques outlined in Chapter 8. From the figure, note that the heuristic method performs very poorly in terms of power consumption. Furthermore, the continuous method and modal methods compare favorably. Thus, if the power budget is a strict design constraint, either the modal method or heuristic methods may be expected to perform similarly. The remaining question is how each of the inputs performs in the physical prototype. This question will occupy the next section.

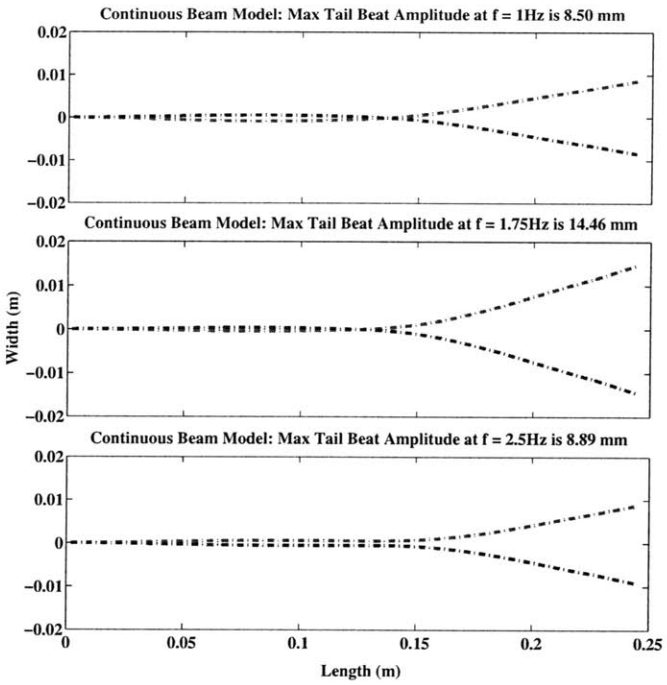

Figure 7-26: Comparison of simulated extreme tail beat shape at various frequencies for the continuous beam synthesis method.

Table 7.4: Voltage parameters for a heuristic input synthesis method

Amplitude Scale Parameter $\alpha_{r,i}$	**Phase Delay Parameter** $\delta_{d,i}$ (rad)
1.00	-
1.00	0.353
1.00	0.504
1.00	0.856
1.00	1.058

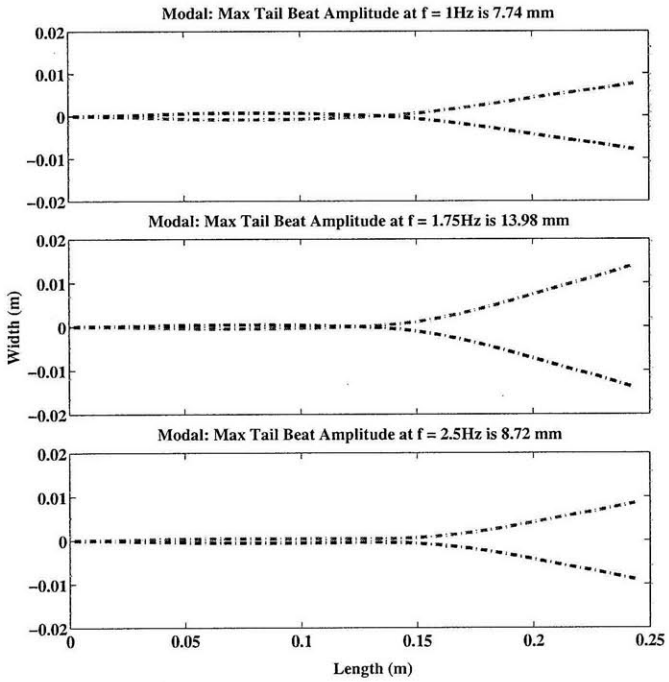

Figure 7-27: Comparison of simulated extreme tail beat shape at various frequencies for the modal decomposition method.

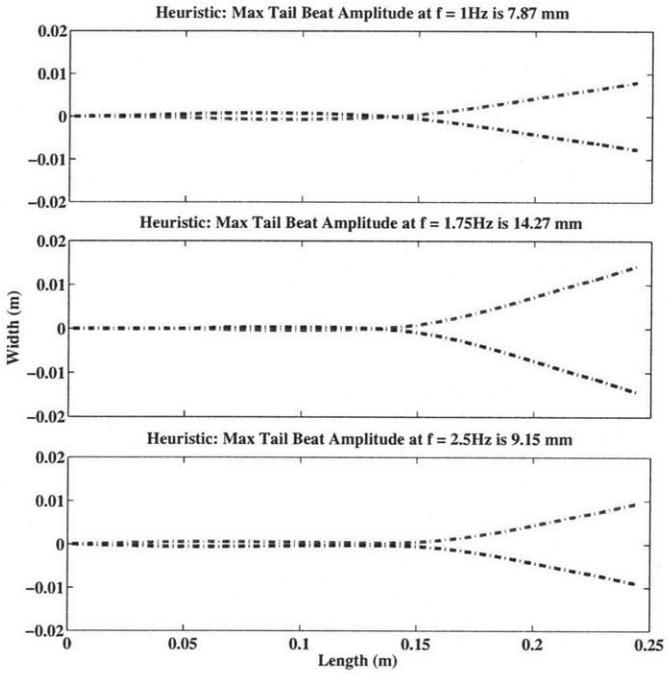

Figure 7-28: Comparison of simulated extreme tail beat shape at various frequencies for the heuristic method.

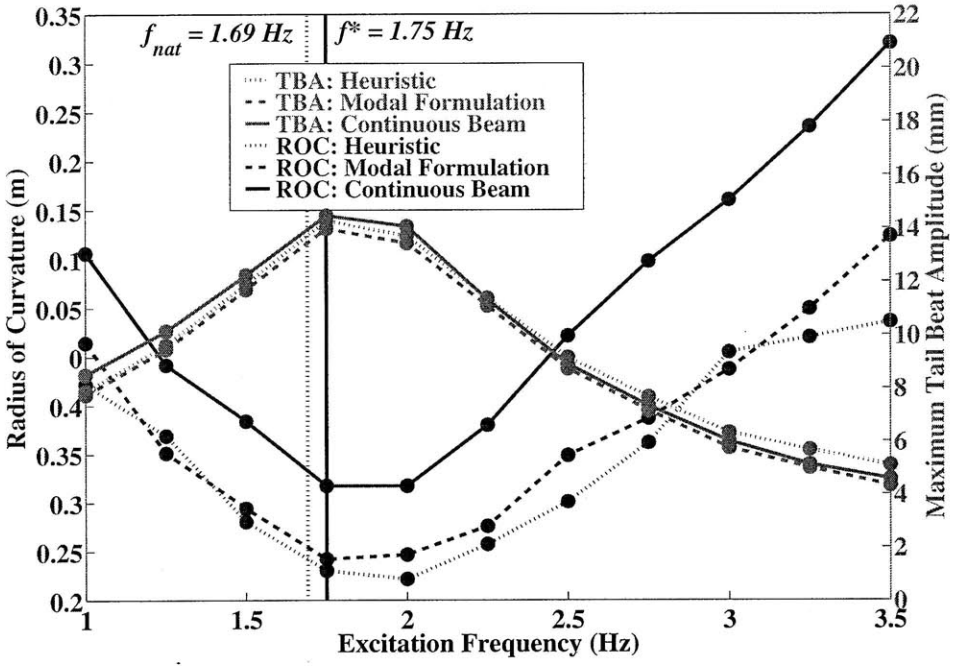

Figure 7-29: Simulation results for the frequency dependence of tail beat amplitude and curvature.

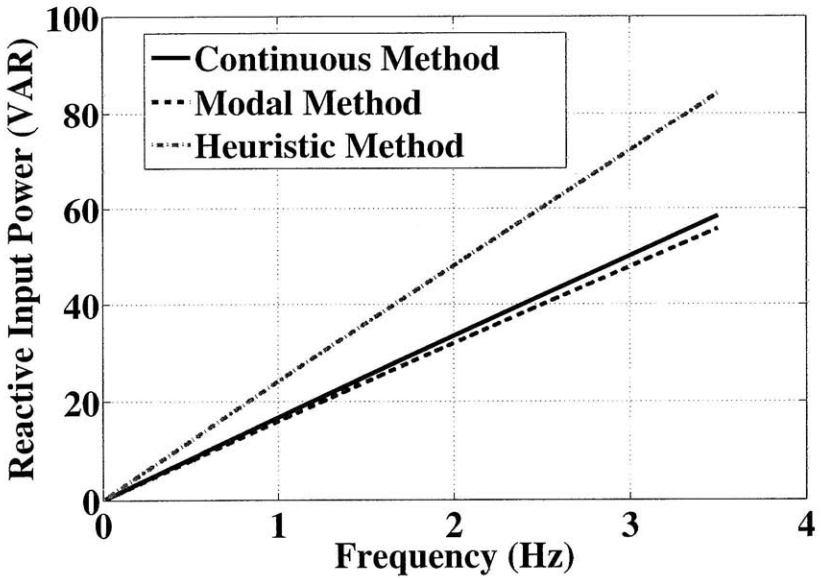

Figure 7-30: Simulation results for the power required to drive the robot at a given frequency using the different input synthesis methods.

7.7 Experimental Validation of the Fish Robot

The prototype fish described in Section 7.3 was used to test each of the input synthesis methods. The methods were assessed based on swimming velocity and power requirements. The results of the experiments are compared to the expected results from the numerical analysis in the preceding section.

The apparatus for these experiments is shown in Fig. 7-31. The test setup is composed of a cylindrical tank having a diameter of 1.52 m. The tank was filled with water to a height of 0.56 m. A LabVIEW program was used to convert user-defined amplitude ratios, phase lags, and frequency into analog output waveforms that matched the synthesized waveforms from the preceding section. These analog waveforms were then sent to the digital to analog output modules in a cRIO system (National Instruments). The voltage waveforms were then sent to the custom design amplifiers and then to the PZT electrodes extending out of the gantry rod. The gantry rod that supported the fish was connected to the aluminum gantry arm. The gantry arm was supported on two low friction roller bearings and was free to rotate throughout the tank. The gantry arm rotation was recorded using a non-contacting magnetic encoder. The angular position from the encoder was sampled at 500 Hz and converted to the tangential velocity at the attachment point of the fish using a least squares fit to the steady state slope.

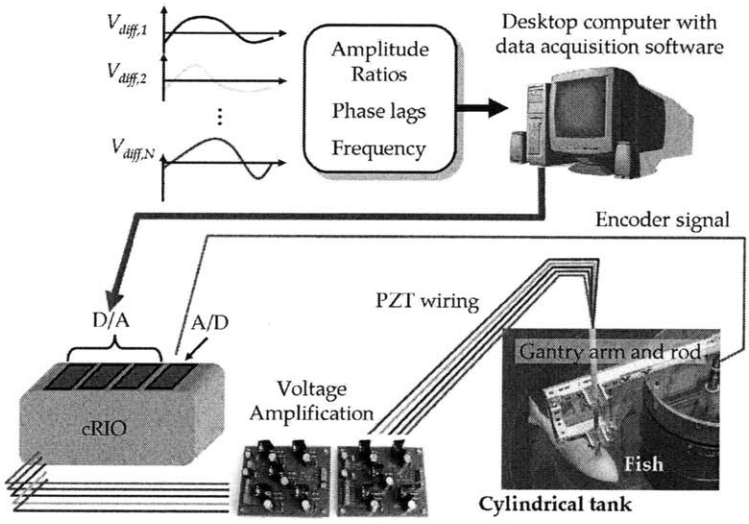

Figure 7-31: Schematic representation of robotic fish testing system.

7.7.1 Swimming Performance

The swimming velocity was measured at 7 frequencies ranging from 1 Hz to 4 Hz for all three input synthesis methods. Each experiment was repeated three times and the results were averaged. The complete experimental results are summarized in Fig. 7-32, which shows the swimming velocity in body lengths/second (BL/s) versus

the driving frequency. Note that for each experiment, the velocities at 1 Hz and 4 Hz were below the noise floor of the encoder and were therefore taken to be zero. The complete results are in agreement with what would be expected based on the ranking of peak tail beat amplitudes from the numerical simulation. That is, the continuous method performed the best with regard to amplitude and also performed the best with respect to swimming velocity. The heuristic method was the next best performing method, while the modal method achieved the slowest velocities. One notable difference between the simulation and the experiments is that the first fundamental frequency of the fin system appears to reside near 2.5 Hz, while the theoretical model predicted 1.7 Hz. This discrepancy is likely due to errors in the added mass approximation in (7.15) as well as uncertainty in the stiffness system parameters.

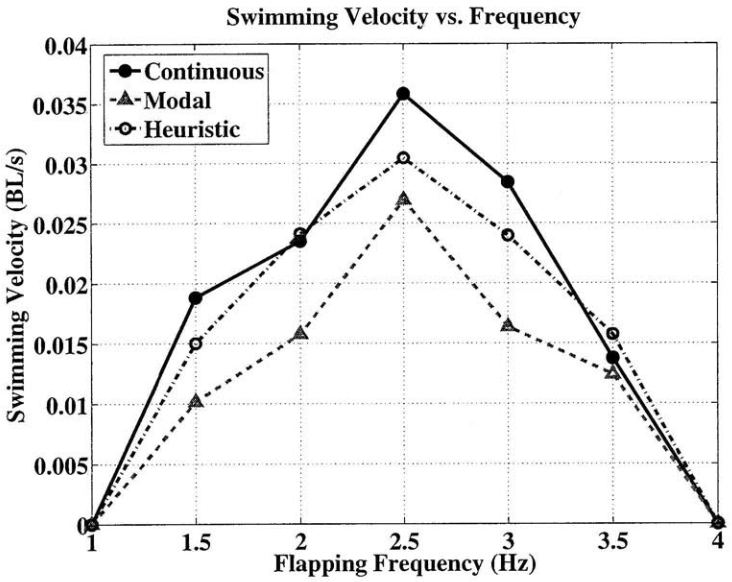

Figure 7-32: Robotic fish velocity versus frequency using three different input synthesis methods.

In order to more completely assess the swimming performance, video of each swimming method was captured from above the tank. The fastest swimming segments were used to examine tail beat amplitudes using a frame overlay technique. For each input driving method, the maximum tail deformation was found in one direction. A semi-transparent frame one half period later was then overlaid on the first deflected shape. Based on a calibration of the pixel size to distance in the plane of the fin, the tail beat amplitudes were computed. The results for each method are shown in Figures 7-33 to 7-35. The modal method achieved a maximum tail beat amplitude of 22 mm while the modal and heuristic methods achieved approximate tail beat amplitudes of 19 mm. These amplitudes were higher than that predicted by the model. This discrepancy is believed to arise from the large uncertainty in the effects of viscous dissipation in the polymer material that may overestimate the internal energy dissipation.

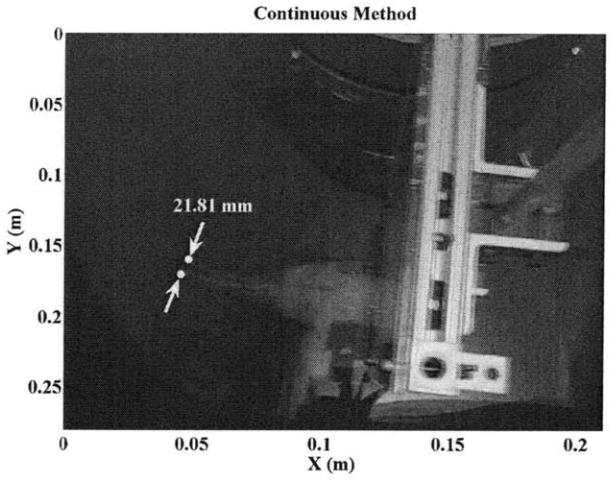

Figure 7-33: Video frame overlays showing 2.5 Hz tail beat amplitude using the continuous beam synthesis method.

Several dimensionless parameters can be used to characterize fish swimming performance. Some of the key parameters include the Reynolds number:

$$Re = \frac{LU}{\nu} \tag{7.78}$$

which establishes the ratio of inertial and viscous forces. In (7.78), ν is the kinematic viscosity of water and the other terms remain as previously defined. Typically this number is greater than 10^3 for fish swimming [95]. The Strouhal number, St, is also an important parameter in fish swimming. This parameter is computed using

$$St = \frac{fA}{U} \tag{7.79}$$

where A is the tail beat amplitude. This parameter has been shown to indicate how often vortices are created in the wake and how close together they are. The most efficient swimmers have values of this number in the range of 0.25 to 0.35 [12]. The final parameter is the tail beat amplitude A normalized by the body length. This parameter is typically near 0.1 for most carangiform fish [95]. Based on the swimming performance at 2.5 Hz, the values of these numbers were computed and are listed in Table 7.5.

7.7.2 Actuation Power Comparison

The relative merits of each driving method are best established by considering not only swimming velocity but also the power required to achieve a given velocity. For the ascending part of each curve in Fig. 7-32, the power at a given velocity was estimated using (7.77). The results are plotted in Fig. 7-36 as required power versus swimming velocity. For a given method, the resulting data points were fit using a linear regression. The best fit line is also included as part of Fig. 7-36. The

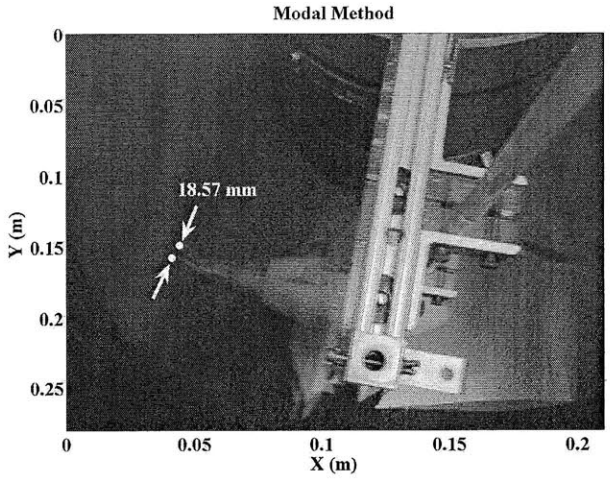

Figure 7-34: Video frame overlays showing 2.5 Hz tail beat amplitude using the modal decomposition synthesis method.

power results shown that the continuous method performed the best with respect to achieving a given swimming velocity at low power. The modal method performed similarly as predicted based on the amplitude of displacement obtained from the numerical simulations. The heuristic method is shown to be vastly inferior to the model-based synthesis methods.

Some of the sources of error and confounding factors in this section include standing waves in the tank caused by the fin motion, friction in the gantry system, loading imposed by the wires, vibrations in the gantry, and gravitational effects in the gantry. Of these effects, it is believed that the wire loading had the most profound effect on swimming velocity. The velocity data is likely to underestimate the actual velocity that would be achieved in a lower friction gantry or completely tetherless system. Furthermore, the results are not expected to compete with existing robotic fish, but rather to provide a starting point for using cellular actuators in underwater robotics. One of the additional features of this technology for underwater robotics is the ability to harvest energy and sense flow conditions, which is discussed in the next section.

Table 7.5: Key dimensionless parameters used to quantify swimming performance.

Dimensionless Number	**Continuous**	**Modal**	**Heuristic**	**Typical for Fish**
Reynolds Number	2.81×10^3	1.88×10^3	2.34×10^3	$10^3 - 10^8$
Strouhal Number	6.1	7.9	6.3	0.25 - 0.35
A/L	0.088	0.076	0.076	≈ 0.1

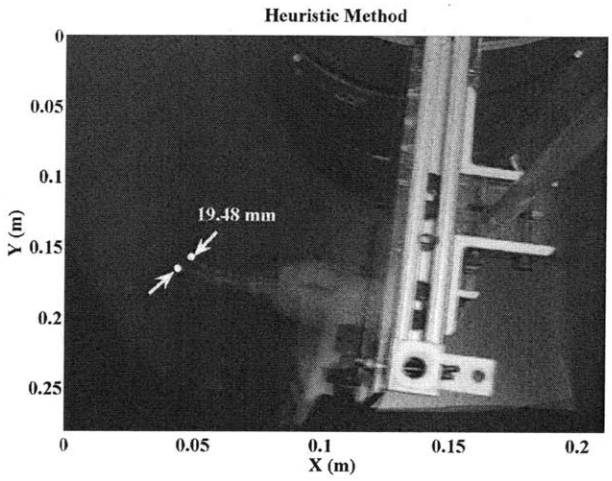

Figure 7-35: Video frame overlays showing 2.5 Hz tail beat amplitude using the heuristic synthesis method.

7.7.3 Energy Harvesting and Sensing

Chapter 6 first illustrated that the piezoelectric cells may be thought of as bidirectional actuation and energy generation devices. The nature of the flexure-based coupling is particularly well suited to creating large forces at the PZT stacks for relatively small forces applied at the output. To illustrate that the fish robot is capable of this bidirectional driving, the experimental setup shown in Fig. 7-37 was constructed. The experimental apparatus consists of Minn Kota Endura electric motor capable of generating 40 lbf thrust at maximum voltage. The motor was pulsed using square waves in order to create a time varying flow condition within the tank discussed previously. The pulsed flow is then routed around the tank to the back drive the fish caudal fin and thereby backdrive the actuators attached to the backbone structure.

Each of the 5 cells on the agonist side of the fin were connected to a pure resistance R_h. The voltage drop across each resistor was measured and sampled at 500 Hz in order to estimate the instantaneous current flow. The product of the voltage and current provided an estimate of the instantaneous power in the resistor. The results from an experiment at 2.0 Hz and various values of R_h are shown in Fig. 7-38. The peak in this figure occurs when the resistance is set according to (6.12), which is the closest possible impedance match using a pure resistance. Although this power level is on the order of μW, it would be sufficient to indefinitely power certain computational circuits. Furthermore, by utilizing an storage element such as an external capacitor, periodic data transmission could be readily achieved.

An additional function of the actuators is to serve as a flow sensor. As discussed, the flexure based cells are very sensitive to small changes in the externally applied forces. These external forces, if acting dynamically, can be estimated very accurately using the PZT voltage signals. The voltage signals acquired across the harvesting resistors have a high signal to noise ratio and can be used to estimate aspects of the flow such as velocity or frequency content. An example of power spectrum estimation is shown Fig. 7-39 for a motor drive frequency of 1.5 Hz. The power spectrum in

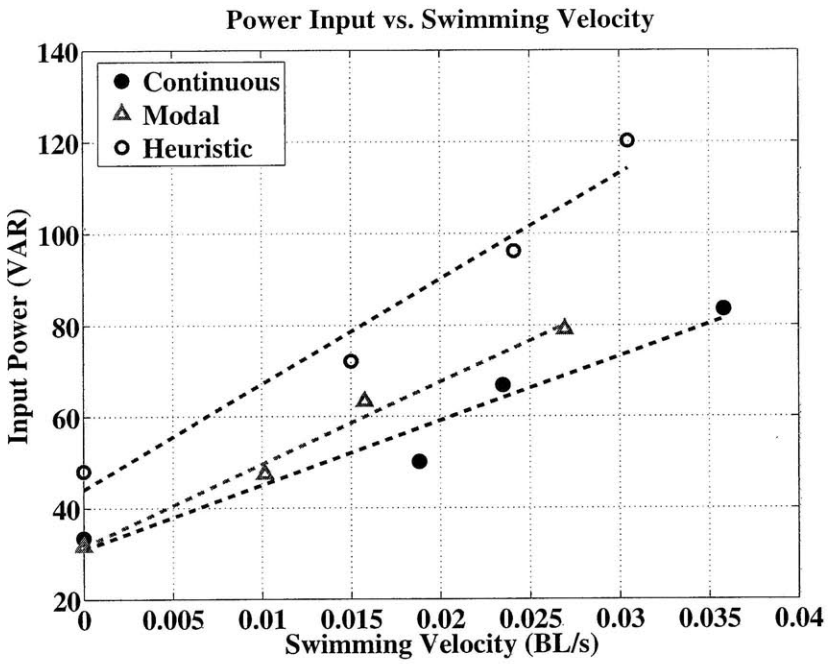

Figure 7-36: Linear regression to describe computed input power as a function of swimming velocity for each of the different input synthesis methods.

Fig. 7-39 was computed from 10 seconds of resistor voltage data acquired at the first agonist cell. Prior to computing the power spectrum, the signal was high pass filtered to remove any DC component. The resulting frequency content has a very clear peak near 1.5 Hz, which represents the frequency of the motor. Thus, with simple FFT algorithms, the flow frequency content can be ascertained accurately and used as the basis for future research in underwater adaptive energy harvesting.

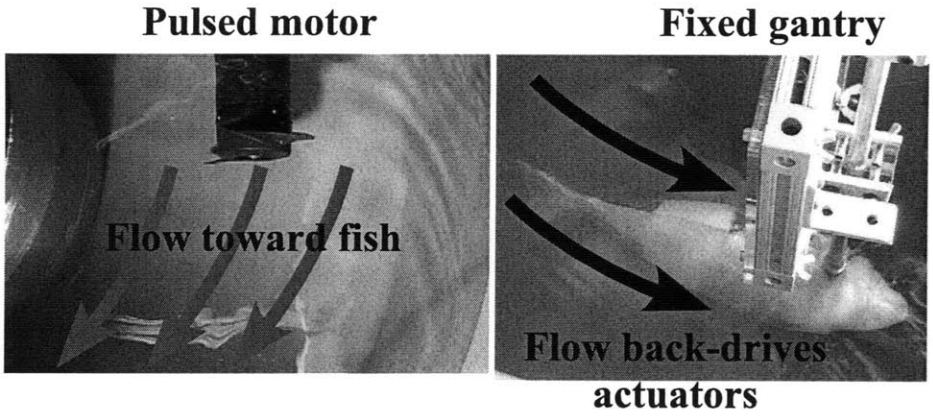

Figure 7-37: Apparatus for testing flow sensing and energy harvesting using the robotic system.

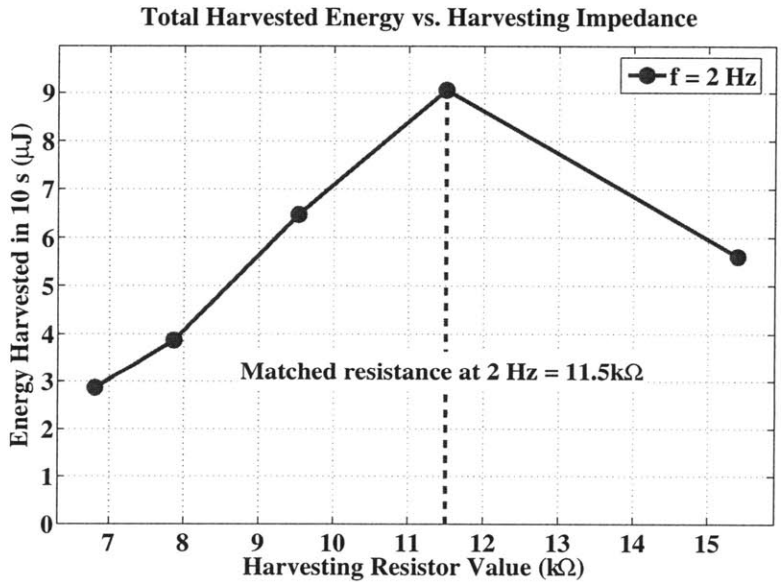

Figure 7-38: Change in harvested energy performance for changes in the harvesting resistance. Flow conditions were created using a 2 Hz square wave applied to the motor.

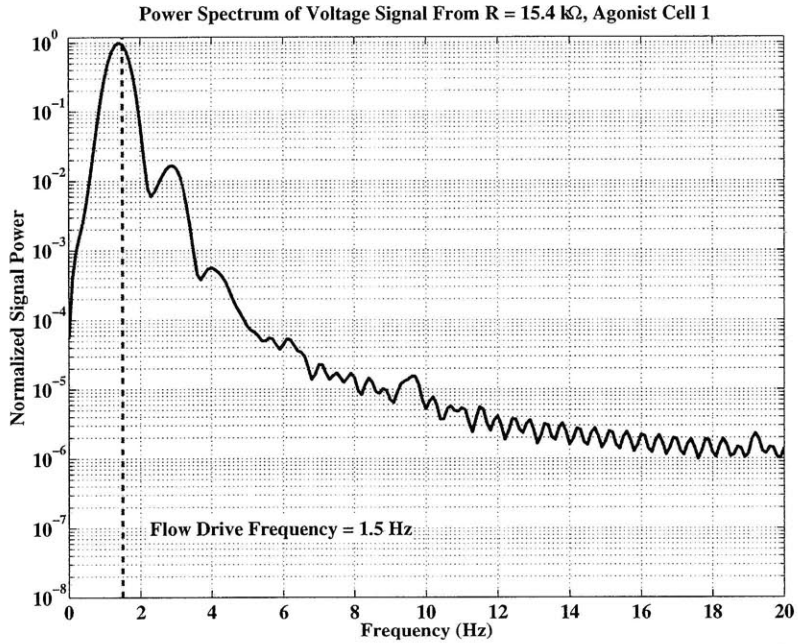

Figure 7-39: Power spectrum of high pass filtered voltage signal across the first agonist cell's harvesting resistance with motor driven at 1.5 Hz.

Chapter 8

Conclusions and Extensions of the Research

Actuators are devices that fundamentally influence the motion of any robotic or mechatronic system. The importance of a suitable actuator is especially apparent in biorobotics where the required motions are often periodic (e.g. walking, running, hopping, swimming, flapping). Furthermore, biorobotic systems are required to interact with external environment and, in doing so, must exhibit smooth motion, backdriveability, elastic energy storage, and scalability. All of these competing performance requirements have not yet been addressed existing artificial muscle technology.

The purpose of this thesis is to address as many of the existing performance hurdles as possible using a novel, yet reliable, technology. The three primary performance objectives in this thesis are classified as modularity and scaling, tunable stiffness and dynamics, and friction and backdriveability. These performance objectives are met using a subdivided, cellular architecture inspired by natural muscle. The primary contributions of this work stem from three sequential aims. The first aim is to develop the operating principles and design of the actuator cellular units. The basic operating principle of the actuator involves nested flexural amplifiers applied to piezoelectric stacks thereby creating an output length strain commensurate with natural muscle. The second aim is to further improve performance of the actuator design by imparting tunable stiffness and resonance capabilities. This work demonstrates a previously unavailable level of tunability in both stiffness and resonance. The final aim is to showcase the capabilities of the actuator design by developing an underwater biorobotic fish that utilizes the actuators for resonance-based periodic locomotion.

8.1 Summary of Contributions

8.1.1 Design

Contributed to the development of the nested rhombus, amplification mechanism concept for PZT-based artificial muscle design.
The concept of nested amplification is central to the design of the cells and represents a major innovation for converting the small expansion displacement of piezoelectric stack actuators into a tensile displacement needed for artificial muscle.

Developed general static and dynamic analysis methods for multilayer and cellular flexure systems.
These models are sufficiently general to be applied to any multilayer flexure systems at all levels of required detail, ranging from simple kinematic analysis to detailed finite element modeling.

Defined scaling properties of various cell performance metrics and defined optimum scale with respect to work density.
The models for the nested amplification mechanism were successfully applied to determine the best scale for a single actuator building block or cell. The results of the analysis indicate that displacement amplification flexures should be produced in a compact package at a scale that favors and further justifies the cellular approach.

Developed cell design procedure and best practices for manufacturing and assembly.
Chapter 4 discusses the detailed design procedure, manufacturing techniques, and reliability analysis associated with rigorously characterizing the properties of each cell design.

Created several functioning actuator cell prototypes.
In addition to the rigorous design analysis, several different cell prototypes were constructed and tested extensively. These cells were found to produce strain commensurate with the 20% natural muscle benchmark.

8.1.2 Extended Design

Utilized cellular architecture to obtain widely tunable resonance and tunable stiffness properties.
The idea of using a cellular architecture applied to the flexure based cells gives rise to two unique and useful properties of tunable stiffness and tunable resonance. The concept of using simple ON-OFF control to independently tune stiffness and resonance characteristics is broadly applicable to many other smart material systems.

Established general theory for resonance extrema in binary tunable vibration systems.
The proposed method of tuning stiffness and resonance was thoroughly quantified using the theory of generalized eigenvalue problems. The maximum and minimum resonant frequencies for serial strands are found and the associated ON-OFF configurations are provably unique. The analysis is also extended to include systems driving a general mass and stiffness load.

Demonstrated tunable stiffness and resonance experimentally.
The concepts of tunable stiffness and resonance were demonstrated to be highly effective and yielded wide range tunability in the respective properties. The partial decoupling of static stiffness from resonant frequencies is also demonstrated experimentally. Two separate designs for tunable stiffness and resonance are proposed: a normally compliant design (nC) and a normally stiff design (nS). These designs are shown to perform similarly, but with different advantages with respect to passive backdriveability.

8.1.3 Application Demonstration

Created a swimming robot utilizing distributed cellular artificial muscles.
The paradigm of using distributed cellular actuators within a fish robot is unique and leads to several interesting properties such as approximation of continuous muscle moment distributions, modal excitation, internal power optimization, energy harvesting, and flow sensing.

Extended and applied modal decomposition methods to solve the inverse dynamics problem in single wavelength vibrating structures.
This approach to inverse dynamics is shown to be a promising, low power, computationally favorable technique for producing desired structural vibrations.

Demonstrated that continuous model and modal decomposition methods are energetically favorable to heuristic approaches.
Although a simple heuristic can be shown to produce a faster velocity that modal methods, it is energetically unfavorable. The methods based on dynamic modeling are shown to perform much better with respect to achieving a given swimming velocity at lower power.

Demonstrated multifunctional actuation, harvesting, and sensing properties of the actuator technology.
In addition to the actuation property of the robot, the robot is also capable of passively harvesting energy from a surrounding flow. The conditions of the flow may also be monitored using, for example, Fourier analysis.

Provided technology platform for several robotics and mechatronics applications
The technology from the first two parts of this thesis provides a solid foundation for many future applications. Furthermore, many opportunities exist to refine both the cell technology and the underwater robotic system. Certain possible refinements and applications are discussed briefly in the following section.

8.2 Future Research Directions

8.2.1 Technology Refinement

The scaling analysis in Chapter 4 revealed that composite materials could possibly outperform metallic flexures and lead to reduced scale cells. Therefore, one possible future research direction would involve developing new composite structures and manufacturing processes for reducing the cell scale while increasing reliability. Once miniaturized, the cells would then have a much broader range of applications within biorobotics.

Several opportunities also exist in electronics design for piezoelectric systems. The most prevalent design paradigm for actuator amplifiers is centered on inductive electromagnetic actuators, which require substantially different circuit topologies than amplifiers for driving capacitive piezoelectric systems. For example, pulse-width-modulation techniques are not suitable for piezoelectric systems. For two cells operating at voltages that are perfectly anti-phased, the energy stored in one cell's capacitance can be effectively transferred to the other cell's capacitance by means of a circuit similar to that shown in Fig. 8-1 [17]. This technique can be explored for

vast connections of cellular systems. Another possible design challenge would involve creating individual on-board cell electronics. The cells could then be interconnected on a modular and reconfigurable bus network. Algorithms for time sharing, sensing and actuation, and energy recovery would all be required.

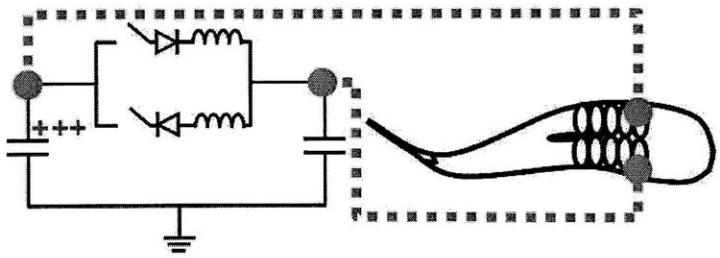

Figure 8-1: Possible transfer circuit used to transfer charge from anti-phased capacitors.

As discussed in Chapter 7, the back-driven actuator cells can be used as a distributed sensor network to sense the ambient conditions (e.g. local fluid flow). When combined with the tunable resonance energy harvesting techniques in Chapter 6, the sensing provides the basis for adaptive energy harvesting. The system could tune its structural resonant frequencies online in order to match that of the ambient conditions. A closed loop control scheme would require a complete examination of sensing calibration, ON-OFF activation and impedance tuning, and harvesting performance.

In the context of underwater systems, it may also be possible to add acoustic data transfer as a function in the system. It is well known that ultrasonic transducers can transmit data at great distances underwater. Many existing transceivers are based on piezoelectric technology. One possible realization of an underwater transmitter is shown in Fig. 8-2.

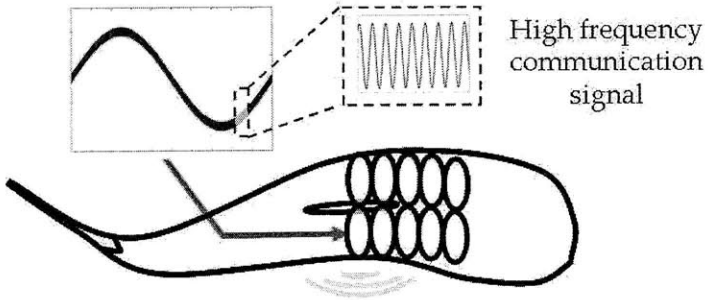

Figure 8-2: Possible design strategy for using PZT-cells as underwater communication devices. A high frequency communication signal is added to the low frequency, large amplitude actuation signal.

A more theoretical combinatoric analysis would also be required if non-uniform cell distributions were considered in the context of tunable stiffness and resonance. There is undoubtedly rich vibrations theory to be explored with regard to non-uniform cell distributions and parallel connection topologies for tunable resonance. For such systems, it is expected that a much more uniform spacing between the resonant peaks could be achieved throughout the entire tunable range.

8.2.2 Example Applications

Underwater robotics is one particularly exciting area of application for the piezoelectric technology for the reasons discussed in Chapter 7. Two example systems are shown in Fig. 8-3. Fig. 8-3 (a) shows the design of a stingray robot that can be used to create traveling waves along a flexible fin body. Fig. 8-3 (b) shows the design of a small robot that could be used for inspection of water-filled piping in offline nuclear reactors. In this design, single piezoelectric cells could be used to rapidly actuate valves for directing flow out of ports in the robot.

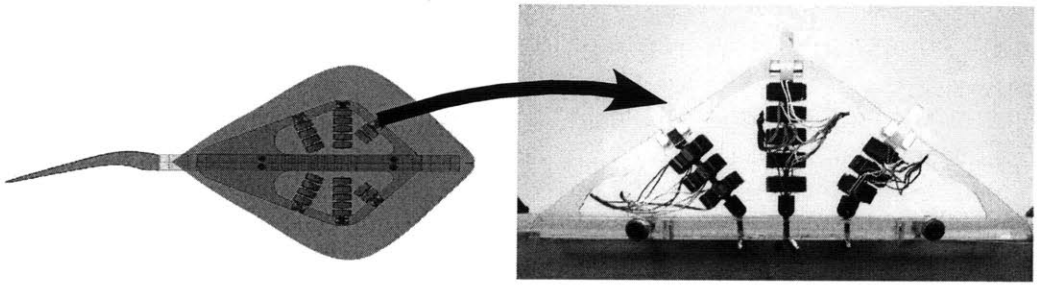

(a)

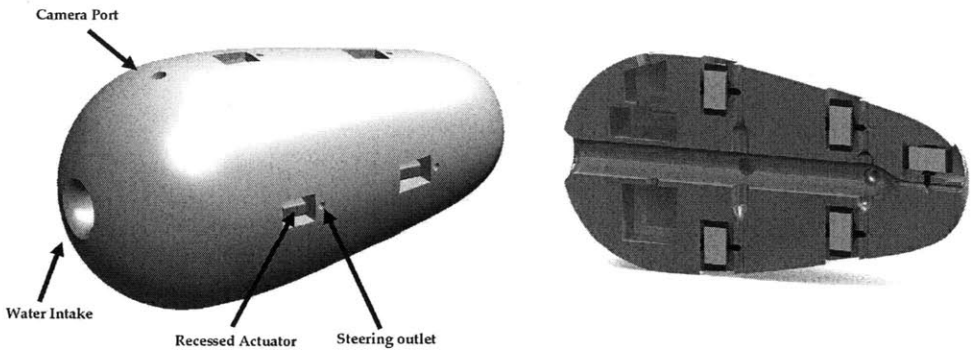

(b)

Figure 8-3: (a) Basic prototype illustrating muscle-like actuation in a robotic stingray. (b) Rendering of a nuclear power plant inspection robot that uses PZT actuators for high bandwidth valve control.

In aircraft manufacturing, a major research challenge is to automate fastener installation operations inside of an airplane wing box. In the operation, a sleeve must placed over a fastener pin that may have a certain degree of misalignment with respect

to the plane of the wing skin. Therefore, a precise positioning system is needed to adjust for angular alignment errors. An example two degree of freedom stage system designed using the PZT cells is shown in Fig. 8-4.

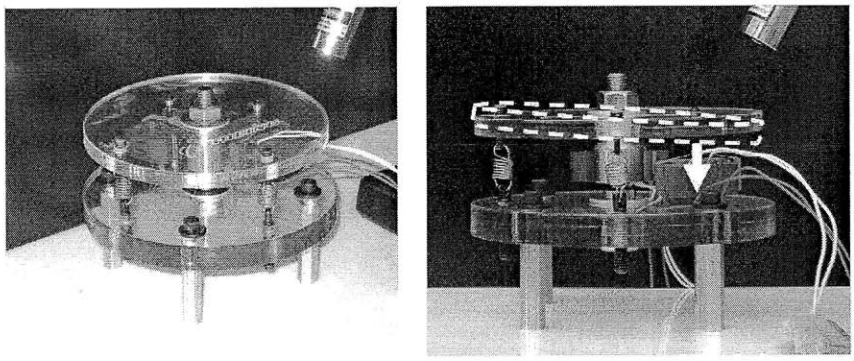

Figure 8-4: Two degree of freedom angular positioning stage.

One of the long-standing challenge in robotics is to develop an anthropomorphic hand that contains all of the necessary actuation within the hand itself. Such a self-contained design obviates the need for complex wrist systems. A related challenge is to achieve slow gross motions and fine rapid motions with the same actuators. To achieve self-containment of the actuators and handle the tradeoff in bandwidth and amplitude, the hybrid actuation design in Fig. 8-5 is proposed. This hand uses a single motor to drive the four primary fingers and two motors to drive the thumb. The motors achieve the desired gross motions of the hand In order to improve speed, agility, and compliance in the grasps, the index and middle fingers are actuated using PZT cells. The construction and analysis of this design would also be an exciting application for the PZT technology.

Rehabilitation robotics is also an exciting area to apply the PZT actuator technology developed in this thesis. An example of a stroke rehabilitation robot that guides patient arm motions is shown in Fig. 8-6. The advantages of the PZT actuators in this scenario would be zero backlash and tunable output compliance. Furthermore, by adding or removing cells the system could be scaled to meet the demands of rehabilitation for different patients.

Surgical robotics is another area where current systems may be limited by actuator technology. Despite certain initial successes, surgical robot technology still requires many fundamental technological improvements. In particular, the most commonly selected actuator for surgical applications is the rotary electric motor because of its predictability and commercial availability. Introducing these conventional motors into the operating room has many drawbacks including lack of backdriveability, limited capability for creating haptic (touch sense) feedback loops, poor sterilization properties, and limited accuracy due to backlash in gearing or transmission mechanisms. Furthermore, many surgical tasks require translational motion and compliant contact, which are difficult to provide with conventional actuators yet are two of the main features the present cellular actuator design. Other research opportunities include

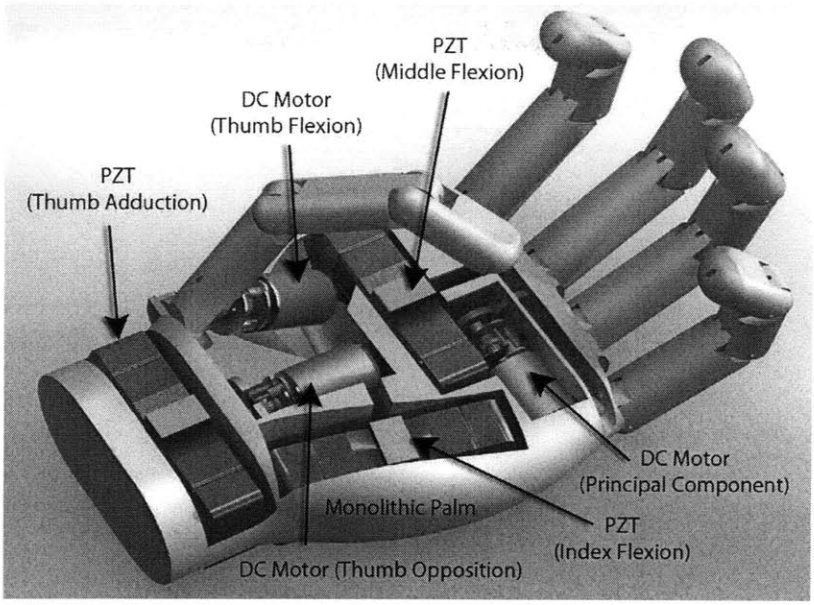

Figure 8-5: Example of a self-contained anthropomorphic hybrid hand using DC motors and piezoelectric cellular actuators.

active heart stabilization devices for minimally invasive bypass surgery and actuators for catheter steering devices. Overall, piezoelectric actuators could greatly expand the capabilities of current surgical robots by providing robustness, precision linear motion, large control bandwidths, and scalability to different force and displacement needs.

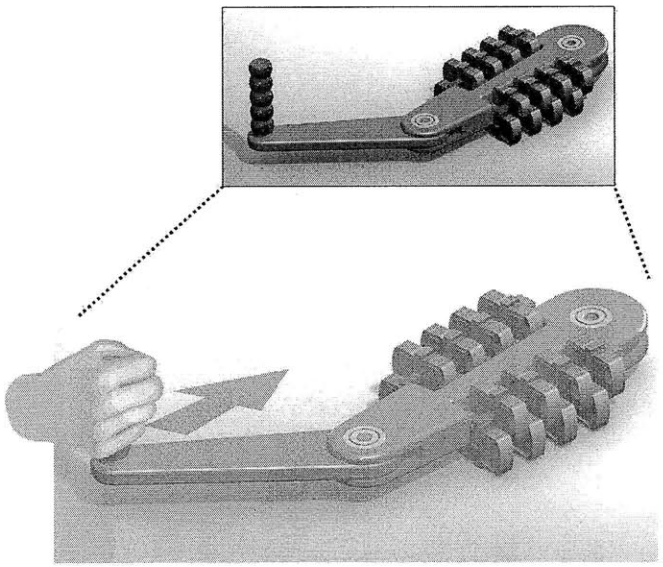

Figure 8-6: Example of a PZT-based stroke rehabilitation robot.

Appendix A

Review of Electrostatics and Piezoelectric Constitutive Behavior

A.1 Physics Preliminaries

To fully understand piezoelectric materials, one must first understand the underlying physics. As described in Chapter 2, piezoelectric materials respond to electric fields. Therefore, a review of some basic concepts from electrostatics is presented in this appendix. First, the basic concepts of electric fields are considered. This appendix then discusses charge distributions where Gauss's law for electrostatics plays a central role in determining electric fields. With a solid understanding of electric fields, the concepts of electrical potential, electrostatic energy, and capacitance are then considered. The following treatment of electrostatics parallels that of conventional physics texts (e.g. [45]).

A.1.1 Electric Fields due to Continuous Charge Distributions

The computation of electric fields due to continuous distributions of charge is often required for computing the response of piezoelectric materials. To derive expressions for electric fields due to continuous distributions of charge, one only needs to consider Coulomb's law and integral calculus. One can derive electric field distributions using integrals along lines, over surfaces, and throughout volumes. One useful relationship for calculating $\mathbf{E}$ due to a charge distribution is Gauss's Law for Electric Flux. Gauss's Law for Electric Flux can be derived from Coulomb's Law. Or, perhaps more fundamentally, Coulomb's law can be derived from Gauss's law.

The central idea when finding the electric field due to a continuous charge distribution is to choose an appropriate charge density: $\lambda = \Delta Q/L$ for linear distributions, $\sigma = \Delta Q/A$ for area distributions, and $\rho = \Delta Q/V$ for volume distributions and apply Gauss's law. For use in Gauss's law, flux can be defined for a closed surface as

$$\Phi_E = \oint \mathbf{E} \cdot d\mathbf{A}. \tag{A.1}$$

Gauss's law states that the flux through a closed surface is proportional to the

net charged enclosed by the surface. The closed surfaces are referred to as Gaussian surfaces. Gauss's law can be stated mathematically as

$$\epsilon_0 \oint \mathbf{E} \cdot d\mathbf{A} = q_{net,encl} \tag{A.2}$$

Gaussian surfaces are chosen so that calculation of the integral in Equation A.2 is as simple as possible.

A.1.2 Electrostatic Potential and Capacitance

The electric field can not only be defined by the vector field $\mathbf{E}$, but can also be described by the scalar quantity called the electric potential, V. To define the electrical potential difference, consider moving a test charge q_0 from position A to position B always keeping the charge in equilibrium. Then the potential difference is the work done by the agent moving the charge divided by the charge.

$$V_B - V_A \triangleq \frac{W_{AB}}{q_0} \tag{A.3}$$

If the potential difference is considered at a point, the potential difference is typically taken as zero at infinity. Or, in many circuit problems, the earth is taken as the zero reference. From the fundamental definition of work ($dW = \mathbf{F} \cdot d\mathbf{l}$),

$$V = -\int_A^B \mathbf{E} \cdot d\mathbf{l} \tag{A.4}$$

where in the line integral the integral is taken from the point of negative charge (or ∞) to the point of interest. The line integral is path independent. For example, to find the potential difference between two parallel conducting plates where the field is $\mathbf{E}$ and the separation distance is d, one can consider the simplest path between the plates: a straight line. For this example, Equation (A.4) then yields $V = Ed$.

What if, instead of finding V from a know $\mathbf{E}$, an expression for $\mathbf{E}$ from a known V is required? In this instance, the following relation is used:

$$\begin{aligned} \mathbf{E} &= -\nabla V \\ &= -\left(\frac{\partial V}{\partial x}\hat{\mathbf{i}} + \frac{\partial V}{\partial y}\hat{\mathbf{j}} + \frac{\partial V}{\partial z}\hat{\mathbf{k}}\right) \end{aligned} \tag{A.5}$$

In words, $\mathbf{E}$ points in the direction of the greatest decrease in potential. From the above definition, equipotential surfaces will lie at right angles to the electric field.

The previous discussion now allows electrical capacitance to be defined as

$$C \triangleq \frac{q}{V} \tag{A.6}$$

Any two nearby conductors carrying equal and opposite charges are a capacitor. V is the potential difference between the conductors. The potential goes down as the plates get closer together since the positive charges on an isolated object raise its potential whereas negative charges reduce it. Thus, the negative charges reduce the

potential difference between the conductors in a capacitor due to their proximity to the positive charges. The capacitance C is determined by the geometry of the conductors, their spatial relationship to one another, and the medium between the conductors.

For piezoelectric materials, the foremost capacitor geometry consists of parallel plate conductors. For a parallel plate configuration with a vacuum in between plates separated by a distance d, the potential difference is $V = Ed$. Using Gauss's law, the magnitude of the charge on one plate is $q = \epsilon_0 EA$ where A is the area of the plates. Thus, from the definition in Equation (A.6), the parallel plate equation emerges:

$$C = \frac{\epsilon_0 A}{d}. \tag{A.7}$$

By placing a nonconducting material (i.e. a dielectric) between the plates of the capacitor, the capacitance is greatly increased. When a dielectric is placed between the plates of a capacitor, the slab becomes polarized and surface charges arise. These surface charges set up a field that opposes the original field and reduces it. Since $V = Ed$ and $C = q/V$, C increases with a dielectric present. Therefore the dielectric constant κ is defined as

$$\kappa = \frac{V_{\text{w/o dielectric}}}{V_{\text{w dielectric}}} \tag{A.8}$$

where $\kappa > 1$. So, for a parallel plate capacitor,

$$C = \frac{\kappa \epsilon_0 A}{d}. \tag{A.9}$$

Using Gauss's law, the induced surface charge q' on the dielectric is given by

$$q' = q\left(1 - \frac{1}{\kappa}\right) \tag{A.10}$$

For a parallel plate capacitor,

$$\frac{q}{A} = \epsilon_0 \left(\frac{q}{\kappa \epsilon_0 A}\right) + \frac{q'}{A}, \tag{A.11}$$

where the term in parentheses is the electric field strength in the dielectric and the second term is the free charge per unit area of the plate. A preferable way to view the second term in Eq. (A.11) is the induced dipole moment per unit volume. One can see this by noting $\frac{q'}{A} = \frac{q'd}{Ad}$ is the induced dipole divided by the volume between the plates. Formally, this term is called the polarization P. Thus,

$$\frac{q}{A} = \epsilon_0 E + P \tag{A.12}$$

This sum occurs so often in electrostatic problems that is given the name electric displacement, D. More generally, these quantities are vectors and therefore

$$\mathbf{D} = \epsilon_0 \mathbf{E} + \mathbf{P}. \tag{A.13}$$

The name, electric displacement has historical significance and is related to the

idea of displacement current. Note that $\mathbf{D}$ is connected with the free charge only, $\mathbf{E}$ is connected with both the polarization and free charges, and $\mathbf{P}$ is connected with the polarization charge only. For an isotropic material with a single scalar dielectric constant κ,

$$\mathbf{D} = \kappa\epsilon_0\mathbf{E}. \tag{A.14}$$

Thus, Gauss's law when a dielectric media are present can be written as

$$\oint D \cdot d\mathbf{A} = q \tag{A.15}$$

where q represents the free charge only. Ultimately, D accounts for the effects of bound charges within materials.

Another important concept is that of energy storage in an electric field. The electrical potential energy U stored on a capacitor is given by

$$U = \frac{1}{2}CV^2 \tag{A.16}$$

On a per unit volume basis in an electric field the electrical energy density u is given by

$$u = \frac{1}{2}\kappa\epsilon_0 E^2. \tag{A.17}$$

A.2 Piezoelectric Static Constitutive Behavior

A.2.1 Basic Tensor Equations

For piezoelectric and electrostrictive behavior in the absence of stress, the following tensor equation applies.

$$S_{kl} = d_{ikl}\mathbf{E}_i + M_{ijkl}\mathbf{E}_i\mathbf{E}_j \tag{A.18}$$

which could also be written as

$$S_{kl} = g_{ikl}\mathbf{P}_i + Q_{ijkl}\mathbf{P}_i\mathbf{P}_j, \tag{A.19}$$

where S_{kl} is a second rank tensor representing strain, d_{ikl} and g_{ikl} are third rank tensors containing the piezoelectric coefficients, M_{ijkl} and Q_{ijkl} are fourth rank tensors that contain the electrostrictive coefficients, and $\mathbf{E}$ and $\mathbf{P}$ are the electric field and polarization. The above equations can be simplified by considering the crystallographic planar symmetry of PZT. With this simplification, matrix, rather than tensor, notation can be employed. In converting to matrix notation, the matrices are not second rank tensors because they do not obey the appropriate rules of transformation. However, the matrix representation is generally preferred for most simplified piezoelectric actuator geometries. The matrix notation will be discussed in the following subsection.

Considering now piezoelectric effects and effects of a mechanically applied stress tensor T_{jk}, the following represents the most common form for the piezoelectric system

of equations:

$$S_{ij} = \underline{d_{ijk}}^T E_j + s_{ijkl}{}^E T_{jk} \tag{A.20}$$

$$D_i = \epsilon_{ij}{}^T E_j + d_{ijk} T_{jk}. \tag{A.21}$$

where $\underline{d_{ijk}}^T$ is the third rank tensor containing the piezoelectric coefficients (the underline represents transposition), $s_{ijkl}{}^E$ is the compliance tensor measured at constant electric field, and $\epsilon_{ij}{}^T$ is the permittivity tensor.

A.3 Simplified Matrix Representations

PZT possesses crystallographic symmetry which therefore greatly simplifies the governing equations. The coordinate system shown in Figure A-1 defines the numbered directions used in the representations.

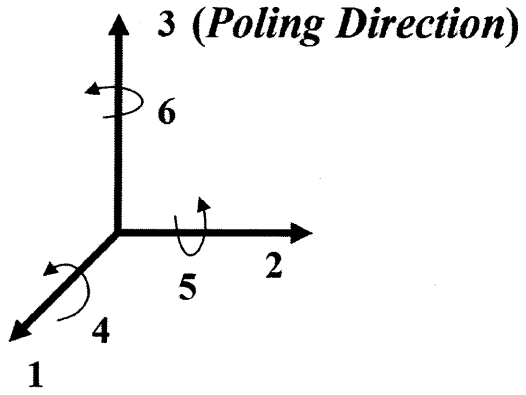

Figure A-1: Coordinate system used to establish matrix equations.

By convention, 3 is taken as the poling direction. In matrix notation, the first subscript gives the "electrical" direction (field or electric displacement) while the second gives the "mechanical" direction (deformation or stress). There is planar isotropy in poled ceramics and thus $d_{32} = d_{31}$ and $d_{24} = d_{15}$. The piezoelectric matrix equations are thus

$$\mathbf{S} = \mathbf{s}^E\mathbf{T} + \mathbf{d}^t\mathbf{E} \tag{A.22}$$

$$\mathbf{D} = \mathbf{d}\mathbf{T} + \epsilon^T\mathbf{E} \tag{A.23}$$

where the terms follow from previous definitions, however the superscript t refers to matrix transpose. These equations can be referred to as the strain-charge piezoelectric constitutive equation. More explicitly, the relationships of interest can be written in matrix form as follows:

$$\begin{pmatrix} S_1 \\ S_2 \\ S_3 \\ S_4 \\ S_5 \\ S_6 \end{pmatrix} = \begin{pmatrix} s_{11}^E & s_{12}^E & s_{13}^E & 0 & 0 & 0 \\ s_{11}^E & s_{12}^E & s_{13}^E & 0 & 0 & 0 \\ s_{11}^E & s_{12}^E & s_{13}^E & 0 & 0 & 0 \\ 0 & 0 & 0 & s_{55}^E & 0 & 0 \\ 0 & 0 & 0 & 0 & s_{55}^E & 0 \\ 0 & 0 & 0 & 0 & 0 & 2(s_{11}^E - s_{12}^E) \end{pmatrix} \begin{pmatrix} T_1 \\ T_2 \\ T_3 \\ T_4 \\ T_5 \\ T_6 \end{pmatrix} + \begin{pmatrix} 0 & 0 & d_{31} \\ 0 & 0 & d_{31} \\ 0 & 0 & d_{33} \\ 0 & d_{15} & 0 \\ d_{15} & 0 & 0 \\ 0 & 0 & 0 \end{pmatrix} \begin{pmatrix} E_1 \\ E_2 \\ E_3 \end{pmatrix} \tag{A.24}$$

and

$$\begin{pmatrix} D_1 \\ D_2 \\ D_3 \end{pmatrix} = \begin{pmatrix} 0 & 0 & 0 & 0 & d_{15} & 0 \\ 0 & 0 & 0 & d_{15} & 0 & 0 \\ d_{31} & d_{31} & d_{33} & 0 & 0 & 0 \end{pmatrix} \begin{pmatrix} T_1 \\ T_2 \\ T_3 \\ T_4 \\ T_5 \\ T_6 \end{pmatrix} + \begin{pmatrix} \epsilon_{11}^T & 0 & 0 \\ 0 & \epsilon_{11}^T & 0 \\ 0 & 0 & \epsilon_{33}^T \end{pmatrix} \begin{pmatrix} E_1 \\ E_2 \\ E_3 \end{pmatrix} \tag{A.25}$$

The four state variables **S**, **T**, **D**, and **E** can be rearranged to give an additional 3 forms for the piezoelectric constitutive equation. Upon rearrangement, **e**, **g** or **q** coupling matrices arise, which are defined in the following paragraphs.

The other forms for the piezoelectric constitutive equations are shown in Equations (A.26) to (A.31). First, the stress-charge form is considered:

$$\mathbf{T} = \mathbf{c}^E\mathbf{S} + \mathbf{e}^t\mathbf{E} \tag{A.26}$$

$$\mathbf{D} = \mathbf{e}\mathbf{S} + \epsilon^S\mathbf{E} \tag{A.27}$$

Similarly, the strain voltage form is written as follows:

$$\mathbf{S} = \mathbf{s}^D\mathbf{T} + \mathbf{g}^t\mathbf{D} \tag{A.28}$$

$$\mathbf{E} = -\mathbf{g}\mathbf{T} + (\epsilon^T)^{-1}\mathbf{D} \tag{A.29}$$

Finally, stress-voltage form is expressed as:

$$\mathbf{T} = \mathbf{c}^D\mathbf{S} - \mathbf{q}^t\mathbf{D} \tag{A.30}$$

Table A.1: Definition of terms in piezoelectric matrix equations.

Symbol	Type	Size	Units	Meaning
$\mathbf{T}$	Vector	6×1	$\frac{N}{m^2}$	Stress components
$\mathbf{S}$	Vector	6×1	$\frac{m}{m}$	Strain components
$\mathbf{E}$	Vector	3×1	$\frac{N}{C}$	Electric Field components
$\mathbf{D}$	Vector	3×1	$\frac{C}{m^2}$	Electric charge density displacement components
$\mathbf{s}$	Matrix	6×6	$\frac{m^2}{N}$	compliance coefficients
$\mathbf{c}$	Matrix	6×6	$\frac{N}{m^2}$	stiffness coefficients
ϵ	Matrix	3×3	$\frac{F}{m}$	electric permittivity
$\mathbf{d}$	Matrix	3×6	$\frac{C}{N}$	piezo coupling coeff. for the strain-charge form
$\mathbf{e}$	Matrix	3×6	$\frac{C}{m^2}$	piezo coupling coeff. for the stress-charge form
$\mathbf{g}$	Matrix	3×6	$\frac{m^2}{C}$	piezo coupling coeff. for the strain-voltage form
$\mathbf{q}$	Matrix	3×6	$\frac{N}{C}$	piezo coupling coeff. for the stress-voltage form

$$\mathbf{E} = -\mathbf{qS} + (\epsilon^S)^{-1}\mathbf{D} \tag{A.31}$$

The parameters in the above matrix equations are defined in Table A.1.

A.4 Further Simplification

Equations (A.24) and (A.25), can be distilled for use in describing practical actuator behavior. In stack actuators, the electric field is applied along the 3 axis and, in the absence of stress,

$$S_3 = d_{33}E_3. \tag{A.32}$$

In the absence of an applied electrical field, the corresponding d_{33} coupling when a stress is applied along the 3 axis is

$$D_3 = d_{33}T_3. \tag{A.33}$$

Hence, the d coupling constant can be viewed in two equivalent ways: strain per unit electric field or charge density per unit stress. A related constant g is used to express similar relationships. In the absence of stress,

$$S_3 = g_{33}D_3. \tag{A.34}$$

In the absence of an applied electrical field, the corresponding g_{33} coupling when a stress is applied along the 3 axis is

$$E_3 = g_{33} T_3. \tag{A.35}$$

Hence, the g coupling constant can be viewed in two equivalent ways: strain per unit applied charge density or electric field per unit stress. These two constants are related through the dielectric properties of the ceramic. To make this more explicit consider Equation (A.33). First, rewrite the electric displacement as $D_3 = \frac{Q}{A}$ where A is the area of the ceramic perpendicular to the 3 axis and Q is the induced charge from the applied stress. Then, using $Q = CV$ and $C = \frac{\epsilon_{33} A}{d}$ (where d is the thickness of the ceramic), one finds that

$$\begin{aligned} D_3 &= \frac{\epsilon_{33}^T V}{d} \\ &= d_{33} T_3 \end{aligned} \tag{A.36}$$

where V is the voltage difference between the ceramic surfaces. Thus, using $E_3 = \frac{V}{d}$,

$$E_3 = \frac{d_{33}}{\epsilon_{33}^T} T_3. \tag{A.37}$$

Comparing (A.35) and (A.37), it follows that $d_{33} = \epsilon_{33}^T g_{33}$.

When viewed from the electrical input perspective, d is the most direct indication of how well the ceramic will work as an actuator because d dictates the length change in for a given applied voltage. Similarly, when a piezoelectric ceramic is viewed from the mechanical input perspective, g directly indicates how well the ceramic will work as a sensor because g dictates the voltage resulting from an applied stress. The d constants are referred to as the piezoelectric charge constants while the g constants are referred to as the piezoelectric voltage constants.

Appendix B

Cellular Actuator Design Drawings

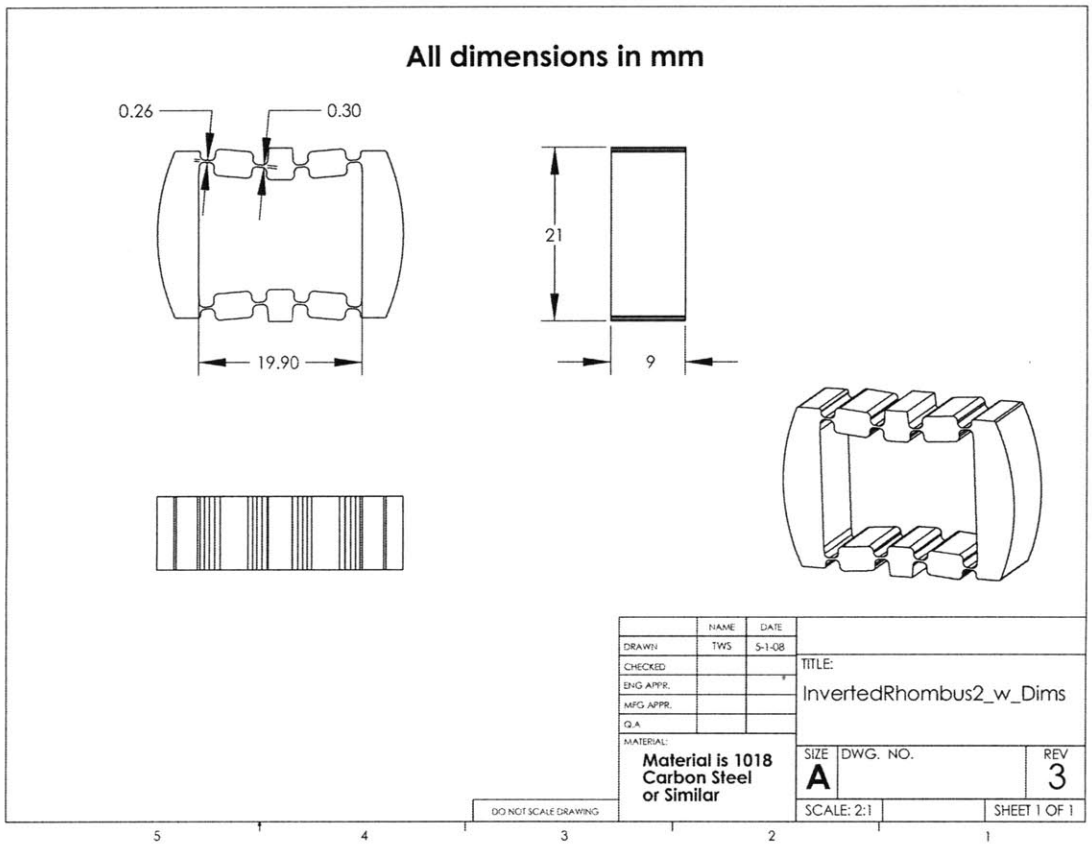

Figure B-1: Cell 1 Layer 1.

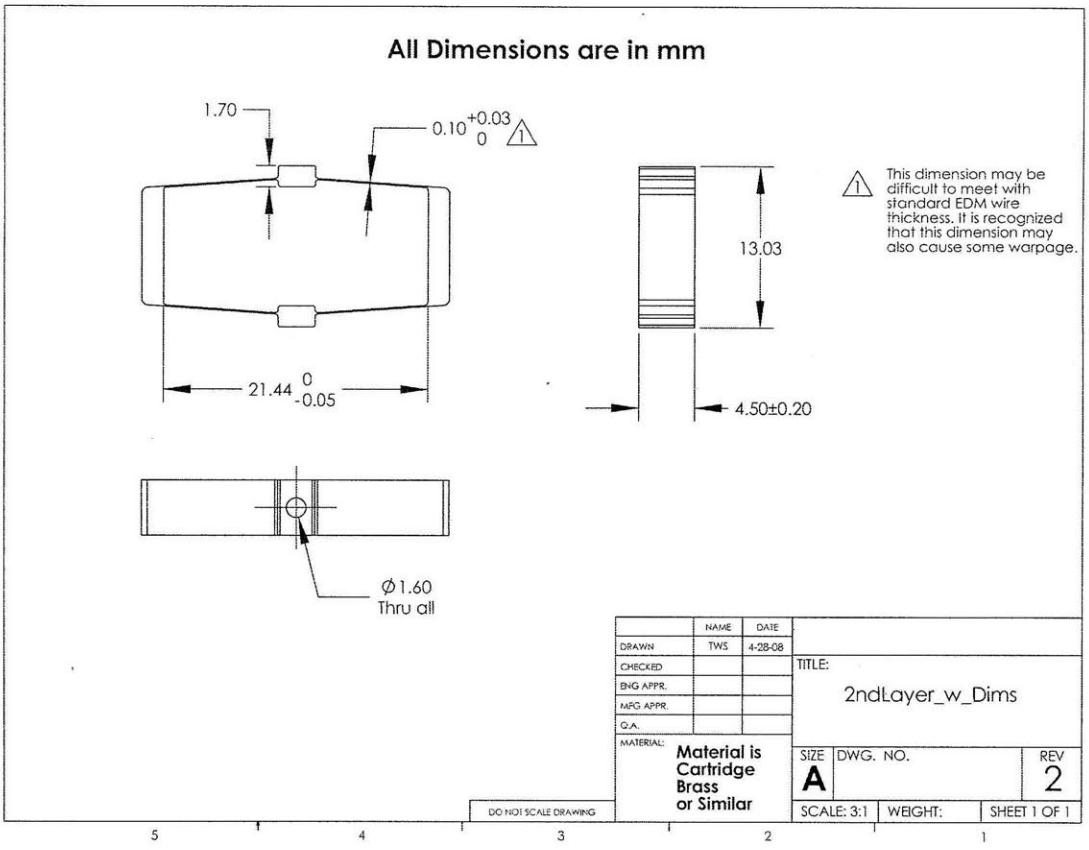

Figure B-2: Cell 1 Layer 2.

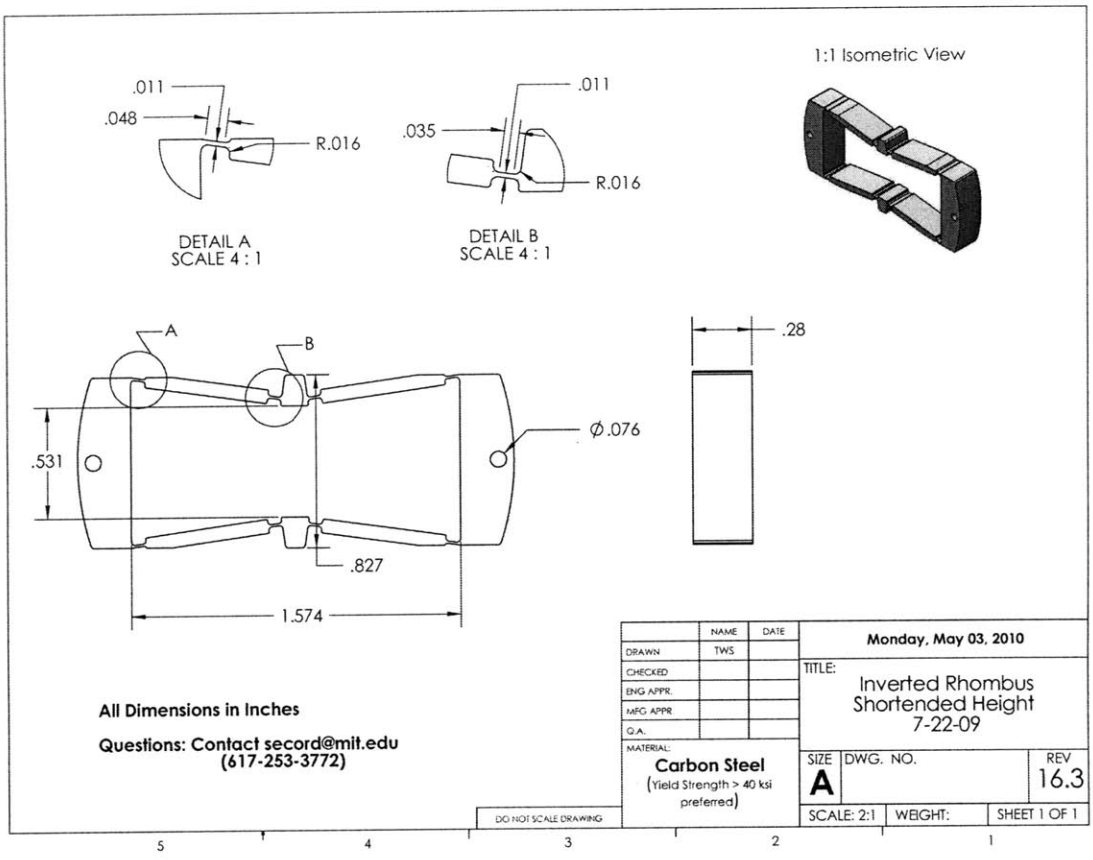

Figure B-3: Cell 2 Layer 1.

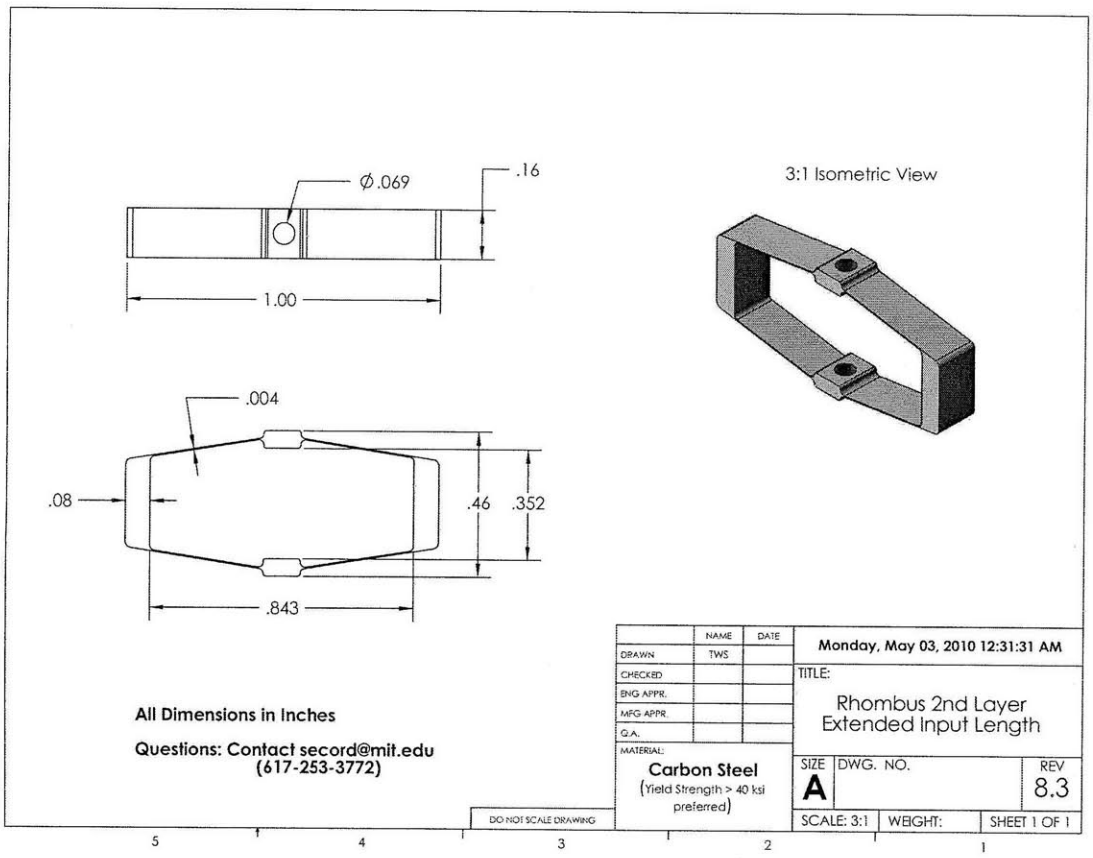

Figure B-4: Cell 2 Layer 2.

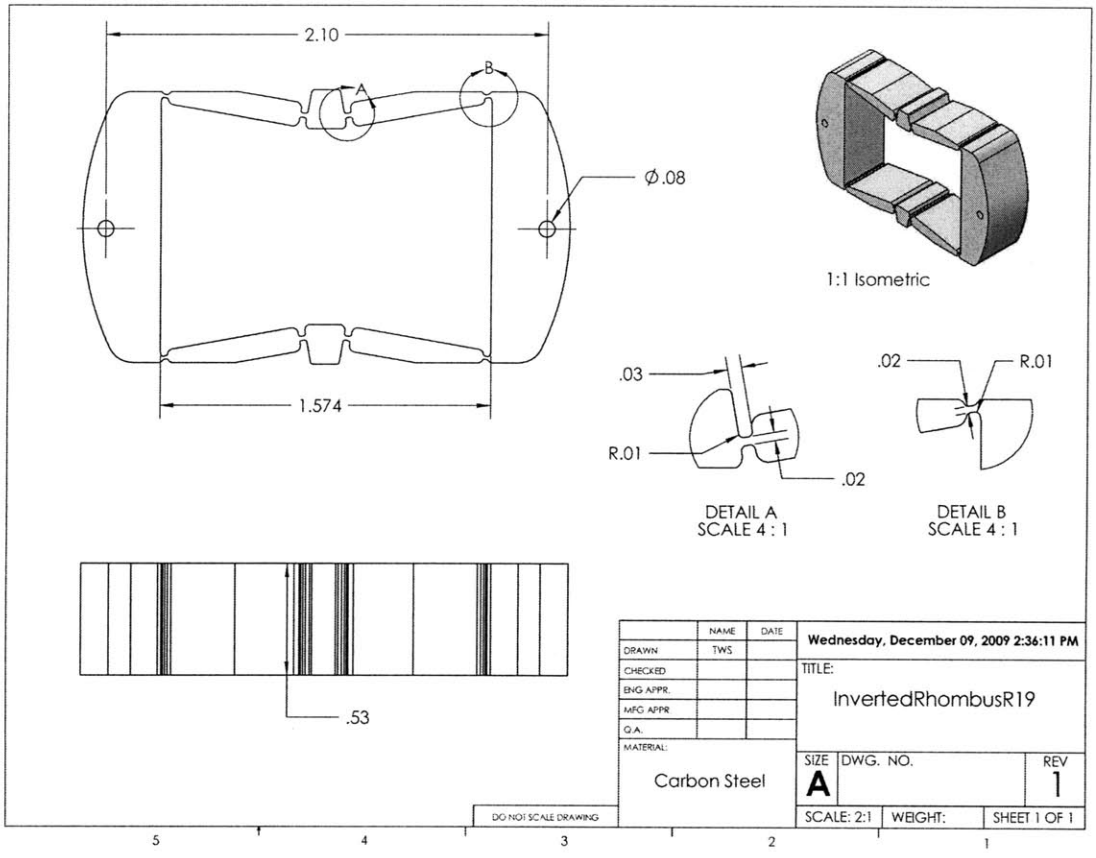

Figure B-5: Cell 3 Layer 1.

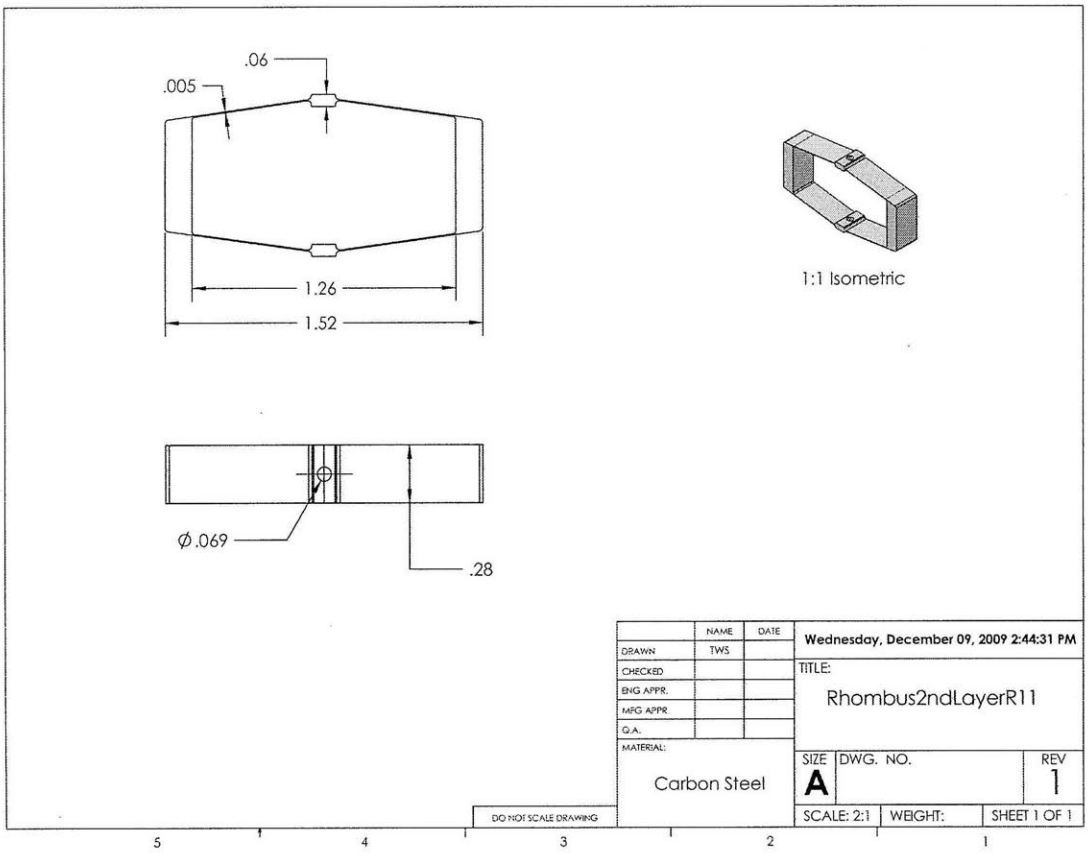

Figure B-6: Cell 3 Layer 2.

Appendix C

Drive Amplifier Design and Analysis

The drive amplifier shown in Fig. 7-9 in Chapter 7 was designed to have five channels, each with a nominal voltage gain of 30. The board was designed using Eagle layout software and the schematic is shown in Fig. C-1. The core of the design is a standard non-inverting amplifier topology based on resistive feedback. This topology by itself, however, is inherently unstable when the load is capacitive. To appreciate this instability, consider removing the 100 Ω resistance (R_D) and the 22 μF capacitance (C_D). Removing these compensating elements from the input terminals greatly reduces the stability as discussed below.

A model of the op-amp that includes its output impedance, but does not include the input terminal compensation elements R_D and C_D, leads to the following transfer function from input voltage V_{in} to output voltage V_{pzt}:

$$\frac{V_{pzt}(s)}{V_{in}(s)} = \frac{G_0 K}{G_0(\tau s + 1)(R_{out} C s + 1) + K} \tag{C.1}$$

where G_0 is the gain that is set by the feedback resistors (nominally 30), K is the open loop gain of the Apex PA240 high voltage amplifier, τ is the time constant of the dominant pole in the open loop response of the op-amp, R_{out} is the output resistance of the op-amp, and C is the capacitance of the PZT load. The dominant pole locations for this system are close to the imaginary axis because the high value of the gain K acts in closed loop to move the real axis open loop poles at $s = -\frac{1}{R_{out}C}$ and $s = -\frac{1}{\tau}$ to values at a high natural frequency and with a small damping ratio. A frequency response plot of this system is shown in Fig. C-2. The resonant peak in the kilohertz range leads to an audible ring in the circuit where small noise signals at this frequency are amplified immensely.

Reintroducing the input terminal resistance and capacitance lead to the compensated system shown in Fig. C-3. Note that there is a severe reduction in the bandwidth of the amplifier, but the resulting bandwidth is still well above the required frequency range for any of the target applications considered for this thesis.

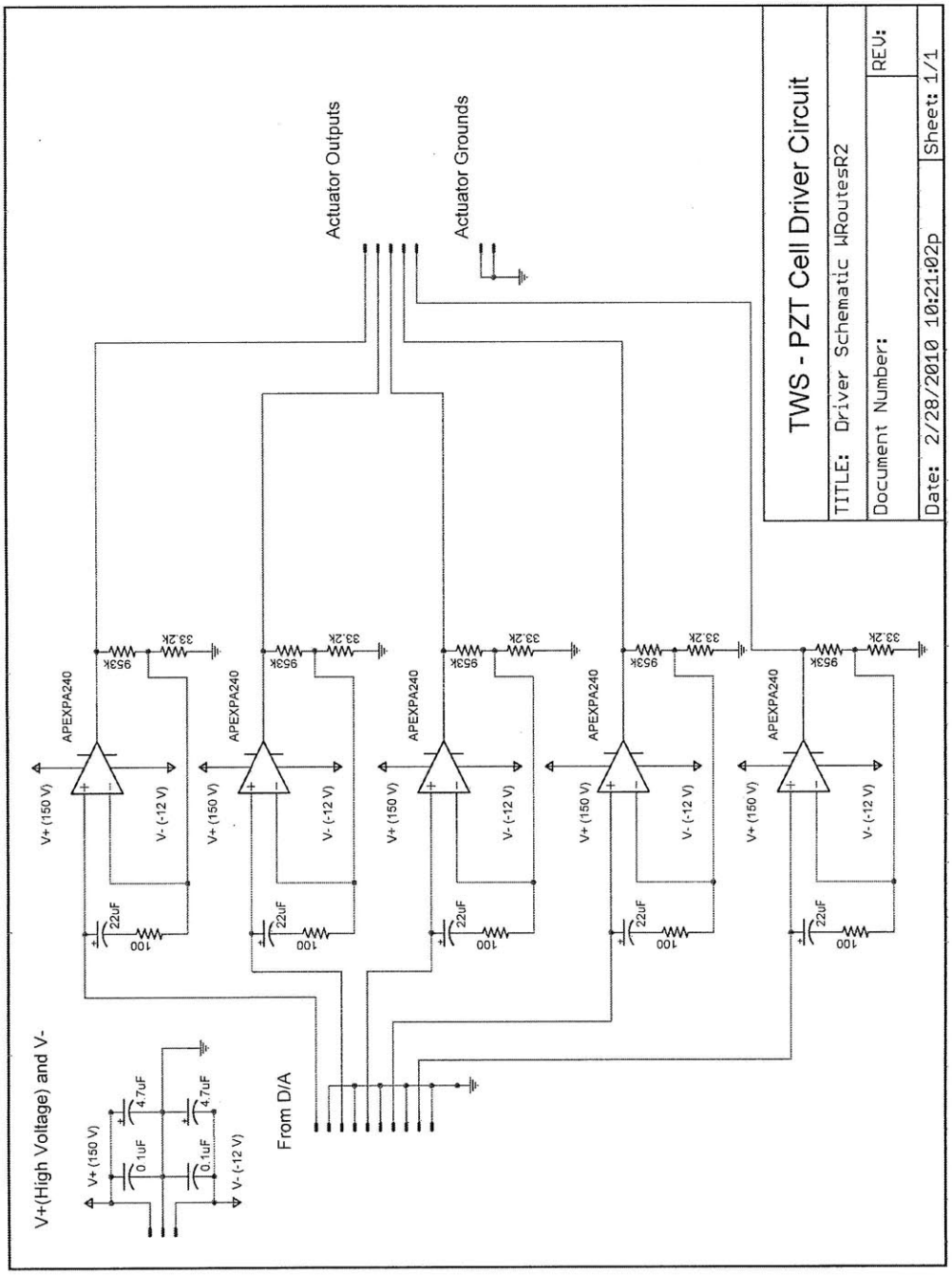

Figure C-1: Circuit schematic for the piezoelectric cell five channel amplifier.

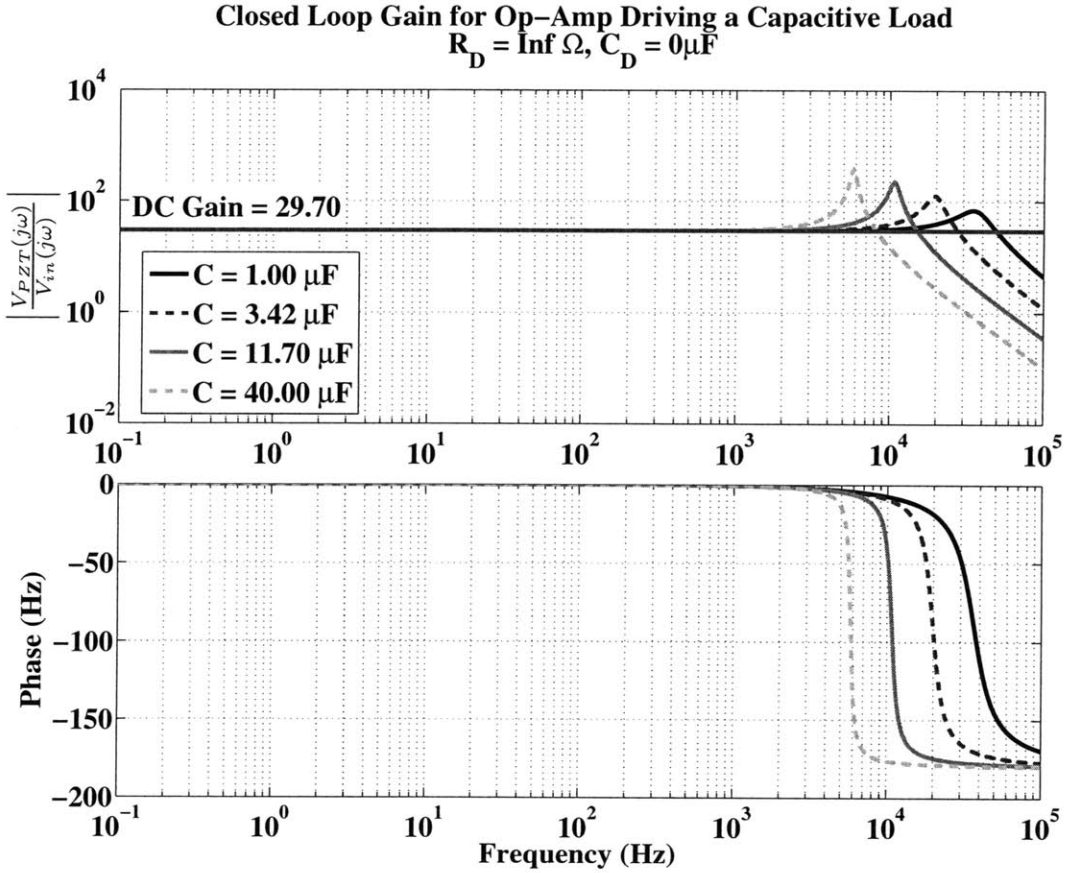

Figure C-2: Frequency response of the uncompensated PZT amplifier that has a lightly damped resonance in the kHz range when loaded with typical values of C.

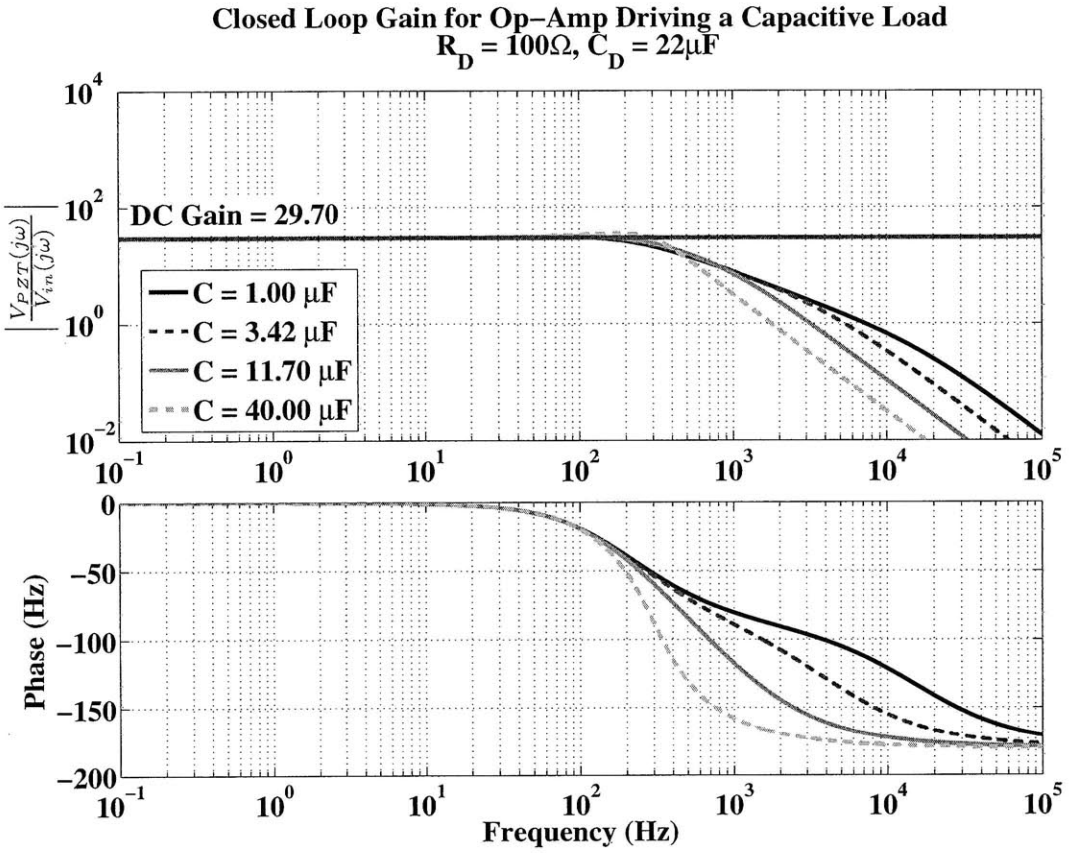

Figure C-3: Frequency response of the compensated PZT amplifier that has a reduced bandwidth, but a flat frequency response characteristic.

Bibliography

[1] Apparatus and process for optimizing work from a smart material actuator product. US Patent 7,368,856.

[2] Flexural-extensional electromechanical transducer. US Patent 3,277,433.

[3] High-efficiency, large stroke electromechanical actuator. US Patent 5,907,211.

[4] Lever actuator comprising a longitudinal-effect electroexpansive transducer. US Patent 4,435,666.

[5] Nonlinear, large-strain pzt actuators using controlled structural buckling.

[6] Shape memory alloy actuators and control methods. US Patent 6,574,958.

[7] Designing with piezoelectric transducers - application notes. *Physik Instrumente*, 2007.

[8] B. Ahlborn. *Zoological Physics.* Chapter 6, Springer, 2004.

[9] M.F. Ashby. *Materials Selection in Mechanical Design.* Butterworth-Heinemann, 3rd edition, 2005.

[10] S.K. Au and H.M. Herr. Powered ankle-foot prosthesis. *IEEE Robotics and Automation Magazine*, 15(3):52–59, 2008.

[11] P.R. Bandyopadhyay. Trends in biorobotic autonomous undersea vehicles. *IEEE Journal of Oceanic Engineering*, 30(1):109–139, 2005.

[12] D.S. Barrett, M.S. Triantafyllou, D.K.P. Yue, M.A. Grosenbaugh, and M.J. Wolfgang. Drag reduction in fish-like locomotion. *Journal of Fluid Mechanics*, 392:183–212, 1999.

[13] K.J. Bathe. *Finite Element Procedures.* Prentice Hall, 1996.

[14] D.N. Beal, F.S. Hover, M.S. Triantafyllou, J.C. Liao, and G.V. Lauder. Passive propulsion in vortex wakes. *Journal of Fluid Mechanics*, 549:385–402, 2006.

[15] J. Brufau-Penella and M. Puig-Vidal. Piezoelectric energy harvesting improvement with complex conjugate impedance matching. *Journal of Intelligent Material Systems and Structures*, 20(5):597, 2009.

[16] D.G. Caldwell, G.A. Medrano-Cerda, and M.J. Goodwin. Braided pneumatic actuator control of a multi-jointed manipulator. In *Systems, Man and Cybernetics, 1993.'Systems Engineering in the Service of Humans', Conference Proceedings.*, pages 423–428, 1993.

[17] D. Campolo, M. Sitti, and R.S. Fearing. Efficient charge recovery method for driving piezoelectric actuators with quasi-square waves. *IEEE Transactions on Ultrasonics, Ferroelectrics, and Frequency Control*, 50(3):237–244, 2003.

[18] V.R. Challa, M.G. Prasad, Y. Shi, and F.T. Fisher. A vibration energy harvesting device with bidirectional resonance frequency tunability. *Smart Materials and Structures*, 17(1), 2008.

[19] S.F. Chen and I. Kao. Conservative congruence transformation for joint and cartesian stiffness matrices of robotic hands and fingers. *The International Journal of Robotics Research*, 19(9):835–847, 2000.

[20] J.Y. Cheng. A continuous dynamic beam model for swimming fish. *Philosophical Transactions of the Royal Society B: Biological Sciences*, 353(1371):981, 1998.

[21] K. Cho, E. Hawkes, C. Quinn, and R.J. Wood. Design, fabrication and analysis of a body-caudal fin propulsion system for a microrobotic fish. In *Proceedings - IEEE International Conference on Robotics and Automation*, pages 706–711, 2008.

[22] K. Cho, J. Rosemarin, and H. Asada. Design of vast dof artificial muscle actuators with a cellular array structure and its application to a five-fingered robotic hand. *Proceedings - IEEE International Conference on Robotics and Automation*, pages 2214 – 2219, 2006.

[23] K. Cho, J. Rosmarin, and H. Asada. Sbc hand: A lightweight robotic hand with an sma actuator array implementing c-segmentation. In *Proceedings - IEEE International Conference on Robotics and Automation*, pages 921–926, 2007.

[24] J. Choi, S. Park, W. Lee, and S. Kang. Design of a robot joint with variable stiffness. *Proceedings - IEEE International Conference on Robotics and Automation*, pages 1760 – 1765, 2008.

[25] J.E. Colgate and K.M. Lynch. Mechanics and Control of Swimming: A Review. *IEEE Journal of Oceanic Engineering*, 29(3):660–673, 2004.

[26] N.J. Conway, Z.J. Traina, and S.G. Kim. A strain amplifying piezoelectric mems actuator. *Journal of Micromechanics and Microengineering*, 17(4):781–787, 2007.

[27] J.M. Cruz-Hernandez and V. Hayward. Phase control approach to hysteresis reduction. *IEEE Transactions on Control Systems Technology*, 9(1):17–26, 2001.

[28] J.A. Dantzig and C.L. Tucker. *Modeling in Materials Processing.* Cambridge Univ Press, 2001.

[29] MatWeb Material Property Data. Aisi 1010 steel, cold drawn. `http://www.matweb.com/`.

[30] B.S. Dhillon. *Applied Reliability and Quality: Fundamentals, Methods and Procedures.* Springer Verlag, 2007.

[31] M.H. Dickinson, C.T. Farley, et al. How Animals Move: An Integrative View. *Science*, 288(5463):100, 2000.

[32] A. Dogan, K. Uchino, and R.E. Newnham. Composite piezoelectric transducer with truncated conical endcaps 'cymbal'. *IEEE Transactions on Ultrasonics, Ferroelectrics, and Frequency Control*, 44(3):597–605, 1997.

[33] A. Dogan, Q. Xu, K. Onitsuka, S. Yoshikawa, K. Uchino, and R.E. Newnham. High displacement ceramic metal composite actuators (moonies). *Ferroelectrics*, 156(1):1–6, 1994.

[34] N.E. Dowling. *Mechanical Behavior of Materials: Engineering Methods for Deformation, Fracture, and Fatigue.* Prentice Hall Upper Saddle River, NJ, 1999.

[35] LLC Dynamic Structures & Materials. Dsm - mission critical motion control. `http://www.dynamic-structures.com/index.html`.

[36] B.P. Epps, P. Valdivia y Alvarado, K. Youcef-Toumi, and A.H. Techet. Swimming Performance of a Biomimetic Compliant Fish-Like Robot. *Experiments in Fluids*, 47(6):927–939, 2009.

[37] J.D. Ervin and D. Brei. Recurve piezoelectric-strain-amplifying actuator architecture. *IEEE/ASME Transactions on Mechatronics*, 3(4):293–301, 1998.

[38] J. Feenstra, J. Granstrom, and H. Sodano. Energy harvesting through a backpack employing a mechanically amplified piezoelectric stack. *Mechanical Systems and Signal Processing*, 22(3):721–734, 2008.

[39] R. Gabai and I. Bucher. Spatial and temporal excitation to generate traveling waves in structures. *Journal of Applied Mechanics*, 77:021010, 2010.

[40] M.V. Gandhi and B.S. Thompson. *Smart Materials and Structures.* Springer, 1992.

[41] F. Gantmacher and M. Krein. *Oscillation Matrices.* Revised Edition, American Mathematical Society, 2002.

[42] G.M.L Gladwell. *Inverse Problems in Vibration.* Martinus Nijhoff, Dordrecht, 1986.

[43] Cedrat Groupe. Guiding your technical innovation. http://www.cedrat.com.

[44] G.H. Haertling. Rainbow ceramics- a new type of ultra-high-displacement actuator. *American Ceramic Society Bulletin*, 73(1):93–96, 1994.

[45] D. Halliday, R. Resnick, J. Walker, J.R. Christman, and E. Derringh. *Fundamentals of Physics*. Wiley New York, 1997.

[46] A.M.A. Hamdan and A.H. Nayfeh. Measures of modal controllability and observability for first- and second- order linear systems. *Journal of Guidance, Control, and Dynamics*, 12(3):421–428, 1989.

[47] H. Hanafusa and H. Asada. A robotic hand with elastic fingers and its application to assembly processes. *Proceedings - FAC Symp. on Information Control Problems in Production Engineering*, pages 127–138, 1977.

[48] H. Hanafusa and H. Asada. Stable pretension by a robotic hand with elastic fingers. *Proceedings - 7th Int. Symp. on Industrial Robots*, pages 361–367, 1977.

[49] N. Hogan. Adaptive control of mechanical impedance by coactivation of antagonist muscles. *IEEE Transactions on Automatic Control*, AC-29(8):681–690, 1984.

[50] N. Hogan. Impedance control: An approach to manipulation: Part i - theory. *Journal of Dynamic Systems, Measurement and Control, Transactions of the ASME*, 107(1):1 – 7, 1985.

[51] L.L. Howell. *Compliant Mechanisms*. Wiley-Interscience, 2001.

[52] L.L. Howell and A. Midha. A Method for the Design of Compliant Mechanisms with Small-Length Flexural Pivots. *Journal of Mechanical Design*, 116:280, 1994.

[53] J.E. Huber, N.A. Fleck, and M.F. Ashby. The selection of mechanical actuators based on performance indices. *Proceedings: Mathematical, Physical and Engineering Sciences*, pages 2185–2205, 1997.

[54] I.W. Hunter and S. Lafontaine. A comparison of muscle with artificial actuators. In *IEEE Solid-State Sensor and Actuator Workshop, 1992. 5th Technical Digest.*, pages 178–185, 1992.

[55] J.W. Hurst, J.E. Chestnutt, and A.A. Rizzi. An actuator with physically variable stiffness for highly dynamic legged locomotion. *Proceedings - IEEE International Conference on Robotics and Automation*, 2004(5):4662–4667, 2004.

[56] Physik Instrumente. The world of nano- and micro- positioning. http://www.physikinstrumente.com/.

[57] K.K. Issac and S.K. Agrawal. An investigation into the use of springs and wing motions to minimize the power expended by a pigeon-sized mechanical bird for steady flight. *Journal of Mechanical Design, Transactions of the ASME*, 129(4):381–389, 2007.

[58] P. Janker, M. Christmann, F. Hermle, T. Lorkowski, and S. Storm. Mechatronics using piezoelectric actuators. *Journal of the European Ceramics Society*, 19(6):1127–1131, 1999.

[59] S. Kalpakjian, S.R. Schmid, and Chi-Wah. Kok. Manufacturing processes for engineering materials. 1991.

[60] K.Cho and H. Asada. Architecture design of a multiaxis cellular actuator array using segmented binary control of shape memory alloy. *IEEE Transactions on Robotics*, 22(4):831–843, 2006.

[61] S.J. Kline. *Similitude and Approximation Theory.* Springer Verlag, 1986.

[62] G.K. Klute, J.M. Czerniecki, and B. Hannaford. Artificial muscles: Actuators for biorobotic systems. *The International Journal of Robotics Research*, 21(4):295, 2002.

[63] R. Kornbluh, R. Pelrine, J. Eckerle, and J. Joseph. Electrostrictive polymer artificial muscle actuators. *Proceedings - IEEE International Conference on Robotics and Automation*, 3:2147–2154, 1998.

[64] D. Lachat, A. Crespi, and A.J. Ijspeert. Boxybot: A swimming and crawling fish robot controlled by a central pattern generator. In *Proceedings - IEEE/RAS-EMBS International Conference on Biomedical Robotics and Biomechatronics*, pages 643–648, 2006.

[65] E.S. Leland and P.K. Wright. Resonance tuning of piezoelectric vibration energy scavenging generators using compressive axial preload. *Smart Materials and Structures*, 15(5):1413–1420, 2006.

[66] W.S. Levine, editor. *The Control Handbook.* CRC Press, 1996.

[67] C. Liang, F.P. Sun, and C.A. Rogers. Coupled electro-mechanical analysis of adaptive material systems–determination of the actuator power consumption and system energy transfer. *Journal of Intelligent Material Systems and Structures*, 5(1):12, 1994.

[68] R.L. Lieber. Skeletal muscle is a biological example of a linear electro-active actuator. In *Proceedings of SPIE's 6th Annual International Symposium on Smart Structures and Materials*, volume 1, page 5, 1999.

[69] M.J. Lighthill. Note on the Swimming of Slender Fish. *Journal of Fluid Mechanics*, 9:305–317, 1960.

[70] N. Lobontiu and E. Garcia. Analytical model of displacement amplification and stiffness optimization for a class of flexure-based compliant mechanisms. *Computers and Structures*, 81(32):2797–2810, 2003.

[71] N. Lobontiu, M. Goldfarb, and E. Garcia. Maximizing the resonant displacement of piezoelectric beams. *Proceedings of SPIE - The International Society for Optical Engineering*, 3668(I):154 – 163, 1999.

[72] J.D. Madden and L. Filipozzi. Web-based actuator selection tool. In *Proceedings of SPIE*, volume 5759, page 9, 2005.

[73] J.D.W. Madden, N.A. Vandesteeg, P.A. Anquetil, P.G.A. Madden, A. Takshi, R.Z. Pytel, S.R. Lafontaine, P.A. Wieringa, and I.W. Hunter. Artificial muscle technology: Physical principles and naval prospects. *IEEE Journal of Oceanic Engineering*, 29(3):706–728, 2004.

[74] A. Menozzi, H.A. Leinhos, D.N. Beal, and P.R. Bandyopadhyay. Open-loop control of a multifin biorobotic rigid underwater vehicle. *IEEE Journal of Oceanic Engineering*, 33(2):59–68, 2008.

[75] S.O.R. Moheimani and A.J. Fleming. *Piezoelectric Transducers for Vibration Control and Damping (Advances in Industrial Control)*. Springer, 2006.

[76] G.E. Moore. Lithography and the future of moore's law. In *Proceedings of SPIE*, volume 2438, page 2, 1995.

[77] K.A. Morgansen, V. Duindam, R.J. Mason, J.W. Burdick, and R.M. Murray. Nonlinear control methods for planar carangiform robot fish locomotion. In *IEEE International Conference on Robotics and Automation*, volume 1, pages 427–434, 2001.

[78] A.J. Moskalik and D. Brei. Quasi-static behavior of individual c-block piezoelectric actuators. *Journal of Intelligent Material Systems and Structures*, 8(7):571–587, 1997.

[79] P. Mottard and Y. St-Amant. Analysis of flexural hinge orientation for amplified piezo-driven actuators. *Smart Materials and Structures*, 18:035005, 2009.

[80] R.E. Newnham, A. Dogan, Q.C. Xu, K. Onitsuka, J. Tressler, and S. Yoshikawa. Flextensional "moonie" actuators. In *Proceedings - IEEE 1993 Ultrasonics Symposium.*, pages 509–513.

[81] Q.S. Nguyen, S. Heo, H.C. Park, N.S. Goo, T. Kang, K.J. Yoon, and S.S. Lee. A fish robot driven by piezoceramic actuators and a miniaturized power supply. *International Journal of Control, Automation and Systems*, 7(2):267–272, 2009.

[82] C. Niezrecki, D. Brei, S. Balakrishnan, and A. Moskalik. Piezoelectric actuation: State of the art. *The Shock and Vibration Digest*, 33(4):269–280, 2001.

[83] L. Odhner and H. Asada. Equilibrium point control of artificial muscles using recruitment of many motor units. *Proceedings of the 2nd Biennial IEEE/RAS-EMBS International Conference on Biomedical Robotics and Biomechatronics*, pages 121–126, 2008.

[84] J.W. Paquette, K.J. Kim, and W. Yim. Aquatic robotic propulsor using ionic polymer-metal composite artificial muscle. In *Proceedings - IEEE/RSJ International Conference on Intelligent Robots and Systems*, volume 2, 2004.

[85] J.S. Plante and S. Dubowsky. On the performance mechanisms of dielectric elastomer actuators. *Sensors & Actuators: A. Physical*, 137(1):96–109, 2007.

[86] G.A. Pratt and M.M. Williamson. Series elastic actuators. *IEEE International Conference on Intelligent Robots and Systems*, 1:399 – 406, 1995.

[87] U. Rabe, M. Kopycinska, S. Hirsekorn, J.M. Saldana, GA Schneider, and W. Arnold. Characterization of piezoelectric ceramics. *Journal of Physics D: Applied Physics*, 35:2621–2635, 2002.

[88] M.H. Raibert. *Legged Robots that Balance*. Massachusetts Institute of Technology, Cambridge, MA, USA, 1986.

[89] J.M. Renno, M.F. Daqaq, and D.J. Inman. On the optimal energy harvesting from a vibration source. *Journal of Sound and Vibration*, 320(1-2):386–405, 2009.

[90] B. Richter, J. Twiefel, and J. Wallaschek. *Energy Harvesting Technologies*, chapter Piezoelectric Equivalent Circuit Models, pages 107–128. Springer, 2008.

[91] R. Schiavi, G. Grioli, S. Sen, and A. Bicchi. Vsa-ii: A novel prototype of variable stiffness actuator for safe and performing robots interacting with humans. *Proceedings - IEEE International Conference on Robotics and Automation*, pages 2171 – 2176, 2008.

[92] Thomas W. Secord and H. Harry Asada. Cellular muscle actuators with variable resonant frequencies. *To appear in Proceedings - Robotics Science and Systems*, 2009.

[93] T.W. Secord and H.H. Asada. A variable stiffness pzt cellular actuator with tunable resonance for cyclic motion tasks. *To appear in Proceedings - IEEE International Conference on Robotics and Automation*, 2009.

[94] K.A. Seffen and E. Toews. Hyperhelical actuators: Coils and coiled-coils. In *45th AIAA/ASME/ASCE/AHS/ASC Structures, Structural Dynamics and Materials Conference*, pages 19–22, 2004.

[95] M. Sfakiotakis, D.M. Lane, and J.B.C. Davies. Review of fish swimming modes for aquatic locomotion. *IEEE Journal of Oceanic Engineering*, 24(2):237–252, 1999.

[96] I.H. Shames and J.M. Pitarresi. *Introduction to Solid Mechanics.* Prentice Hall, 3rd edition, 2000.

[97] B. Singh and S. Singh. State of the art on permanent magnet brushless dc motor drives. *Journal of Power Electronics*, 9(1), 2009.

[98] H.A. Sodano, D.J. Inman, and G. Park. A review of power harvesting from vibration using piezoelectric materials. *Shock and Vibration Digest*, 36(3):197–206, 2004.

[99] MS Triantafyllou, FS Hover, AH Techet, and DKP Yue. Review of hydrodynamic scaling laws in aquatic locomotion and fishlike swimming. *Applied Mechanics Reviews*, 58:226, 2005.

[100] M.S. Triantafyllou and G.S. Triantafyllou. An efficient swimming machine. *Scientific American*, 272(3):64–71, 1995.

[101] Y.C. Tung, S.L. Jeng, and W.H. Chieng. Multi-level balanced isolated floating difference amplifier. *IEEE Transactions on Circuits and Systems I: Regular Papers*, 55(10):3016–3022, 2008.

[102] K. Uchino. *Piezoelectric Actuators and Ultrasonic Motors.* Kluwer Academic Publications, 1997.

[103] J. Ueda, T. Secord, and H. Asada. Design of pzt cellular actuators with power-law strain amplification. *IEEE International Conference on Intelligent Robots and Systems*, pages 1160–1165, 2007.

[104] Mitsunori Uemura, Katsuya Kanaoka, and Sadao Kawamura. A new control method utilizing stiffness adjustment of mechanical elastic elements for serial link systems. *Proceedings - IEEE International Conference on Robotics and Automation*, pages 1437 – 1442, 2007.

[105] P. Valdivia y Alvarado and K. Youcef-Toumi. Design of machines with compliant bodies for biomimetic locomotion in liquid environments. *Journal of Dynamic Systems, Measurement and Control, Transactions of the ASME*, 128(1):3 – 13, 2006.

[106] R. Van Ham, B. Vanderborght, M. Van Damme, B. Verrelst, and D. Lefeber. Maccepa, the mechanically adjustable compliance and controllable equilibrium position actuator: Design and implementation in a biped robot. *Robotics and Autonomous Systems*, 55(10):761–768, 2007.

[107] JL Van Leeuwen. The action of muscles in swimming fish. *Experimental physiology*, 80(2):177, 1995.

[108] J.J. Videler. *Fish Swimming.* Cahpman & Hall, 1993.

[109] W. Weaver, S. Timoshenko, and D.H. Young. *Vibration Problems in Engineering.* Wiley-Interscience, 1990.

[110] P.W. Webb. 'steady' swimming kinematics of tiger musky, an esociform accelerator, and rainbow trout, a generalist cruiser. *Journal of Experimental Biology*, 138(1):51, 1988.

[111] S. Wolf and G. Hirzinger. A new variable stiffness design: Matching requirements of the next robot generation. *Proceedings - IEEE International Conference on Robotics and Automation*, pages 1741 – 1746, 2008.

[112] W.J. Wu, Y.Y. Chen, B.S. Lee, J.J. He, and Y.T. Peng. Tunable rresonant frequency power harvesting devices. In *Proceedings of SPIE*, volume 6169, page 61690A, 2006.

[113] P. Valdivia y Alvarado. *Design of Biomimetic Compliant Devices for Locomotion in Liquid Environments.* Phd thesis, Massachusetts Institute of Technology, January 2007.

[114] K. Yamato, K. Tominaga, W. Takashima, and K. Kaneto. Stability of electrochemomechanical strains in polypyrrole films using ionic liquids. *Synthetic Metals*, 159(9-10):839–842, 2009.

[115] J. Yan, R.J. Wood, S. Avadhanula, M. Sitti, and R.S. Fearing. Towards flapping wing control for a micromechanical flying insect. *Proceedings - IEEE International Conference on Robotics and Automation*, 4:3901 – 3908, 2001.

[116] W. Yim, J. Lee, and K.J. Kim. An artificial muscle actuator for biomimetic underwater propulsors. *Bioinspiration & Biomimetics*, 2:S31–S41, 2007.

[117] D.F. Young, B.R. Munson, and T.H. Okiishi. *A Brief Introduction to Fluid Mechanics.* Wiley, 3rd edition, 2007.

[118] J. Yu, L. Liu, and L. Wang. Dynamic modeling and experimental validation of biomimetic robotic fish. In *American Control Conference*, page 6, 2006.

[119] D. Zhang, D. Hu, L. Shen, and H. Xie. A bionic neural network for fish-robot locomotion. *Journal of Bionic Engineering*, 3(4):187–194, 2006.

[120] D. Zhou, M. Kamlah, and D. Munz. Effects of uniaxial prestress on the ferroelectric hysteretic response of soft pzt. *Journal of the European Ceramic Society*, 25(4):425–432, 2005.